University of Trento
University of Brescia
University of Bergamo
University of Padova
University of Trieste
University of Udine
University IUAV of Venezia

Luca Gambirasio

LARGE STRAIN COMPUTATIONAL MODELING OF HIGH STRAIN RATE PHENOMENA IN PERFORATING GUN DEVICES BY LAGRANGIAN/EULERIAN FEM SIMULATIONS

Egidio Rizzi (Tutor)
University of Bergamo

2013

UNIVERSITY OF TRENTO
Doctoral School in Engineering of Civil and Mechanical Structural Systems

Ph.D. Head's: Davide Bigoni

Final Examination: 29 April 2013

Board of Examiners
Prof. Egidio Rizzi (University of Bergamo, Italy)
Prof. Spyros Karamanos (University of Thessaly, Greece)
Prof. Dennis Kochmann (California Institute of Technology, USA)
Prof. Giovanna Concu (University of Cagliari, Italy)

SUMMARY

The present doctoral thesis deals with the study and the analysis of large strain and high strain rate behavior of materials and components. Theoretical, experimental and computational aspects are taken into consideration. Particular reference is made to the modeling of metallic materials, although other kinds of materials are considered as well. The work may be divided into three main parts.

The first part of the work consists in a critical review of the constitutive modeling of materials subjected to large strains and high to very high strain rates. Specific attention is paid to the opportunity of adopting so-called strength models and equations of state. Damage and failure modeling is discussed as well. In this part, specific interest is addressed to reviewing the so-called Johnson-Cook strength model, by critically highlighting its positive and negative aspects. One of the main tackled issue consists in a reasoned assessment of the various procedures adoptable in order to calibrate the parameters of the model. This phase is enriched and clarified by applying different calibration strategies to a real case, i.e. the evaluation of the model parameters for a structural steel. The consequences determined by each calibration approach are then carefully evaluated and compared.

The second part of the work aims at introducing a new strength model, that consists in a generalization of the Johnson-Cook model. The motivations for the introduction of this model are first exposed and discussed. The features of the new strength model are then described. Afterwards, the various procedures adoptable for the determination of the material parameters are presented. The new strength model is then applied to a real case, i.e. a structural steel as above, and the results are compared to those obtained from the original Johnson-Cook model. Comparing to that, the obtained outcomes show that the new model displays a better capacity in reproducing experimental data. Results are discussed and commented.

The third and final part of the work deals with an application of the studied topics to a real industrial case of interest. A device called perforating gun is analyzed in its structural problematics and critical aspects. This challenging application involves the modeling of several typologies of material, large strains, very high strain rate phenomena, high temperatures, explosions, hypervelocity impacts, damage, fracture and phase changes. In this regard, computational applications of the studied theories are presented and their outcomes are assessed and discussed. Several finite element techniques are considered. In particular, tridimensional Eulerian simulations are presented. The obtained results appear to be very promising in terms of the possibilities of a fruitful use in the design process of the device, in particular in order to achieve an optimization of its key features.

SOMMARIO

Questa tesi di dottorato tratta lo studio e l'analisi del comportamento di materiali e componenti soggetti a grandi deformazioni ed alte velocità di deformazione. Vengono discussi aspetti teorici, sperimentali e computazionali, con particolare riferimento alla modellazione di materiali metallici, sebbene altre tipologie di materiale siano altresì considerate. Il lavoro può essere diviso in tre parti principali.

La prima parte del lavoro consiste in una revisione critica della modellazione costitutiva di materiali soggetti a grandi deformazioni ed alte o molto alte velocità di deformazione. Specifica attenzione è rivolta all'opportunità di utilizzare i cosiddetti modelli di resistenza ed equazioni di stato. La modellazione del danneggiamento e della rottura è altresì discussa. In questa parte, specifico interesse è indirizzato alla revisione del cosiddetto modello di resistenza di Johnson-Cook, sottolineandone entrambi gli aspetti positivi e negativi. Uno dei punti principali presentati consiste in una valutazione ragionata delle varie procedure adottabili ai fini della calibrazione dei parametri del modello. Questa fase è arricchita e chiarificata dall'applicazione delle strategie di calibrazione ad un caso reale, consistente nella valutazione dei parametri del modello per un acciaio strutturale. Le conseguenze determinate da ogni approccio di calibrazione sono poi attentamente valutate.

La seconda parte del lavoro mira ad introdurre un nuovo modello di resistenza, consistente in una generalizzazione del modello di Johnson-Cook. Le motivazioni per l'introduzione di tale modello sono discusse, insieme alle sue principali caratteristiche. In seguito, vengono presentate le varie procedure utilizzabili per la determinazione dei parametri del modello. Il nuovo modello è poi applicato ad un caso reale, l'acciaio strutturale di cui sopra, ed i risultati sono comparati a quelli ottenuti con il modello di Johnson-Cook originale. Comparandosi a tale modello, le previsioni ottenute dimostrano come il nuovo modello presenti una migliore capacità di riprodurre i dati sperimentali. I risultati sono quindi discussi e commentati.

La terza e ultima fase del lavoro tratta un'applicazione degli argomenti studiati ad un caso reale di interesse industriale. Un dispositivo chiamato perforating gun è analizzato nelle sue problematiche strutturali ed aspetti critici. Questa applicazione coinvolge la modellazione di diverse tipologie di materiali, grandi deformazioni, fenomeni ad alta velocità di deformazione, alte temperature, esplosioni, impatti iperveloci, danneggiamento, frattura e cambi di fase. Si propongono applicazioni computazionali delle teorie studiate ed i risultati sono valutati e discussi. In particolare, si presentano simulazioni Euleriane agli elementi finiti. I risultati ottenuti appaiono molto promettenti in termini di un loro uso proficuo nella fase di progettazione del dispositivo, in particolare riguardo l'ottimizzazione di alcune sue caratteristiche chiave.

ACKNOWLEDGMENTS

The doctoral candidate thanks his family for supporting the doctoral activities and prof. Egidio Rizzi at the University of Bergamo for tutoring the whole program.

The members of the Board of Examiners are thanked, together with the PhD School Coordinator, prof. Davide Bigoni.

Gratitude is expressed also to prof. David J. Benson at the University of California at San Diego for offering kind hosting and scientific support from September 2011 to July 2012.

Thanks go also to DYNAmore GmbH (Stuttgart, Germany), and in particular to dr. Thomas Münz, for kind hosting and providing a LSTC LS-DYNA license, for a two week period during January and February 2011.

Thanks go to the Lombardia Region, the company TenarisDalmine and the University of Bergamo for granting financial support to this research, through a two-year DRA ("Dote Ricerca Applicata") research contract ("Assegno di Ricerca").

CONTENTS

FOREWORD

This doctoral thesis originates from a research program conceived between academia and industry. The research activity has been supported halfway by the Lombardy region, through the University of Bergamo (Department of Engineering, Dalmine), and halfway from the R&D department of the company TenarisDalmine, nearby located. This arrangement has taken place in the context of a regional project called *Dote Ricerca Applicata (DRA)*. Therefore, the targets of the research activity have been established in order to meet the expectations of both academic and industrial partners.

The company TenarisDalmine, strongly involved in the production of seamless pipes and specifically in their applications in the oil and gas industry business, was contacted for possible cooperations on research themes related to computational mechanics. It proposed the analysis and study of a specific device, called perforating gun, which finds use in a critical phase of the extraction process of oil or natural gas from underground deposits, i.e. the radial perforation of rocks and soil surrounding wells. This process allows for and favors the subsequent pumping to the surface of the fluid hydrocarbons. The practical consequences of this perforating phase are of utter importance relatively to the well integrity and productivity. In order to successfully accomplish this process, the perforating gun device plays a role of absolute importance. Hence, the necessity of achieving a good industrial design arises, together with a possible optimization of its key parameters, which may be of different nature, e.g. geometrical, structural, technological or related to the characteristics of the involved materials. The main issue considered in this work regards the structural performance of a particular component of the perforating gun device, technically called carrier.

On the other side, the academic targets were those of achieving original research results in the field of continuum mechanics, with particular reference to large strain and high strain rate behavior of materials. The possibility of proposing some new ideas suitable for the description of such phenomena was evaluated and studied.

In this scenario, the academic and industrial objectives merged successfully by means of an in-deep analysis of the perforating gun device, which naturally led to the study and investigation of the complex physical phenomena related to its functionality. Large strains, very high strain rates, high temperatures, explosions, hypervelocity impacts, damage, fracture and phase changes are the most challenging aspects involved and considered in the present treatment.

Regarding the organization of this work, Chapter 1 briefly introduces some assumptions that are used throughout the exposition. Appropriate considerations about the adopted notation are presented as well. Furthermore, appropriate simplifying assumptions are introduced and motivated.

Chapter 2 presents a brief overview of the constitutive modeling pertinent to large strain and high strain rate material behaviors, in order to critically expose the most popular models suitable for the description of such phenomena. Particular attention is paid to the so-called Johnson-Cook strength model. As a matter of fact, the major part of the presented review deals with this model. This choice is due to the following three main facts. First of all, the Johnson-Cook model appears to be the most implemented and used model when there is the need to model large strain and high strain rate material behavior over a possible wide range of strain rates and temperatures. Second, a new strength model is later introduced in the present work and it actually originates from the Johnson-Cook model, since it considers an enhancement based on the same framework and the same variables. Third, the industrial application examined later in this work makes wide use of the Johnson-Cook model. Different materials are modeled through this specific strength model, although other models are used as well. More in detail, all the key components of the studied perforating gun device are modeled by using the Johnson-Cook model. These salient facts determine the importance of this specific strength model in the context of the present work. The main issue investigated in this section regards a reasoned assessment of the various procedures adoptable for calibrating the parameters of the Johnson-Cook model. This phase is enriched and clarified by applying the calibration strategies to a real case, i.e. the evaluation of the model parameters of a structural steel, by relying on experimental data available from the literature. The consequences determined by each calibration approach are then carefully evaluated, together with a final discussion on the positive and negative aspects of such strategies and some suggestions on how to choose the best calibration approach, by considering the available experimental data and the objectives of the modeling process.

Chapter 3 aims at presenting a new strength model. It is conceived as a generalization of the Johnson-Cook model. The introduction of this new model is motivated and accurately described. This strength model aims at improving the coherency of the original Johnson-Cook model. As for the original Johnson-Cook model, the proposed model pays attention to the fact of keeping the formulation suitable for computational applications, with particular reference to Finite Element Method (FEM from now on) applications. In fact, the new model may collocate itself as a direct competitor of the Johnson-Cook model. The model is also applied to a real case, i.e. the modeling of the elastoplastic response of a structural steel tested throughout wide ranges of strain rates and temperatures, and the obtained results

are compared to the results provided by the original Johnson-Cook model. This comparison allows to assess the positive features of the proposed model. The differences between the two compared models are highlighted and discussed. Furthermore, appropriate considerations about the possibility of implementing this new model into FEM codes are pointed-out.

Chapter 4 deals with an application of the studied theories and models to the practical industrial case suggested by the industrial partner TenarisDalmine, i.e. a specific perforating gun device. This chapter provides a brief introductory description of perforating gun devices, in particular by identifying the most important components of such devices. After this phase, the specific perforating gun under target is analyzed. Appropriate considerations regarding the constitutive modeling options are introduced and discussed. Whenever possible, reference is made to the experimental and technical data supplied by the industrial partner. Moreover, a series of preliminary considerations relative to the adopted computational strategies are presented. The difficulties and the objectives of appropriate FEM simulations of perforating gun devices are debated. Finally, a campaign of FEM computational simulations is presented, with the target of reproducing, as coherently as possible, the phenomena involved during the practical application of a perforating gun. The FEM code LS-DYNA is used extensively in this phase, after a comprehensive study that has concerned several FEM codes and their potentialities in the present challenging computational context. Both tridimensional Lagrangian and Eulerian FEM simulations are presented and discussed.

1. BASIC ASSUMPTIONS AND NOTATIONS

The central aspect analyzed in the present work consists in the large strain and high strain rate constitutive modeling of continuous media, in particular by considering metallic materials. In continuum mechanics, the wording constitutive model tipically refers to a function that relates a measure of strain to a measure of stress, and conversely. Constitutive modeling is one of the most challenging branch of continuum mechanics and its study involves a lot of aspects and considerations. A comprehensive review of these arguments is not an aim of this work. However, it is necessary to point-out some preliminary considerations about a number of basic concepts and notations, as they are adopted throughout the present work.

Ordered arrays of numerical elements are referred to here as tensors, and the number of distinct ordering levels is referred to as the valence or the order of the tensor. A tensor with valence equal to n is denoted by the wording n-tensor. The number of elements in a specific valence is referred to as its cardinality. Given a n-tensor, with n strictly greater than 2, it is said to be a square n-tensor if all its cardinalities are equal.

It is recognized that an abuse of notation may be made here. A n-tensor is indeed something more specific than a simple set of ordered arrays of numbers. Generally speaking, the definition of n-tensor is related to the way in which these numbers describe a quantity in an underlying space and how they transform when passing from one space observer to another. Examples of references on these topics are Levi-Civita, 1926, Struik, 1953, Synge and Schild, 1969, and Moon and Spencer, 1986. Anyway, in order to develop a flowing exposition, the wording n-tensor is used here to refer only to a set of ordered arrays of numbers, without specifying anything particular relatively to its transformation law. This assumption favors simplicity and allows to avoid the involvement of a quite long preliminary treatment of some basic assumptions on which large strain continuum mechanics is implicitly founded, a task that would be too heavy to be presented here and actually not strictly necessary for the achievement of the aims of this work. Furthermore, it appears that this assumption is tacitly assumed in many references, i.e. the wording n-tensor is used in a quite general context, without specifying strict limitations on the transformation rules. Therefore, the approach adopted in the present work allows to fit in this popular framework.

For the sake of simplicity, space and time are assumed to be independent quantities. Time is considered as absolute, equal for all the observers. Space is assumed to have three dimensions and to possess infinite extensions along these dimensions. This assumption implies that the relevant metric is a square 2-tensor of

cardinality 3. With further simplification, the space is assumed to be assessed by an observer characterized by having an atlas composed by only one chart. Moreover, this chart is assumed to be Euclidean, i.e. it imposes a metric field g_{ij} that is constant in space and equal to the identity 2-tensor, as defined in the following relation

$$g_{ij} = \delta_{ij} = \begin{bmatrix} [1,0,0] \\ [0,1,0] \\ [0,0,1] \end{bmatrix}. \tag{1}$$

The assumption of imposing an Euclidean metric implies having a vanishing linear connection, denoted by Γ_{ijk}, as specified in the following equation

$$\Gamma_{ijk} = \frac{g_{il}}{2} \cdot \left(\frac{\partial g_{lj}}{\partial x_k} + \frac{\partial g_{lk}}{\partial x_j} - \frac{\partial g_{jk}}{\partial x_l} \right) = 0_{ijk}. \tag{2}$$

As a consequence, any time spatial derivatives are used, the linear connection needs not to be introduced. More specifically, the covariant derivative reduces to the classical derivative. For a treatment on these topics, see, e.g., Marsden and Hughes, 1983, Moon and Spencer, 1986, and Marsden et al., 2007.

Euclidean observers imply the equality of the two natural local bases fields, i.e. the covariant and contravariant local bases field become coincident. This fact leads to the definition of a unique natural local bases field, thus allowing to avoid the need to use subscripts and superscripts in order to distinguish contravariant and covariant n-tensors. Therefore, n-tensors will be denoted by using subscripts only. The choice of limiting the analysis to Euclidean observers only is quite restricting but also favors simplicity and does not hinder the achievement of the targets of the present work.

Functions are denoted by writing first the dependent variable and then the independent variables, gathered by curly brackets and separated by commas. For instance, if A is a function of B and C, the following symbol holds

$$A\{B,C\}. \tag{3}$$

The next concise summary exposes the adopted notation for the basilar continuum mechanics quantities involved in this work.

Generic evolutions are delimited in time by an initial instant and a current instant. The positions of a point in the initial and in the current instants are denoted by X_i and x_i, respectively, and are called initial and current positions, respectively. Motion can then be defined by considering the current position as a function of the initial position and time, as exposed in the following, where time is denoted by the symbol t

$$x_i\{X_i,t\}. \tag{4}$$

This function is also called mapping. The deformation gradient, or tangent mapping, is a 2-tensor denoted by F_{ij} and defined in the following way

$$F_{ij}=\frac{\partial x_i}{\partial X_j}. \tag{5}$$

The right stretch 2-tensor, denoted by U_{ij}, the left stretch 2-tensor, denoted by V_{ij}, and the rotation 2-tensor, denoted by R_{ij}, arise from the right and left polar decompositions of the deformation gradient, reported respectively in the following equations

$$F_{ij}=\sum_{k=1}^{3}R_{ik}\cdot U_{kj}, \tag{6}$$

$$F_{ij}=\sum_{k=1}^{3}V_{ik}\cdot R_{kj}. \tag{7}$$

It is also possible to define the velocity of the motion v_i, as specified in the following equation

$$v_i=\frac{\partial x_i}{\partial t}. \tag{8}$$

The velocity gradient is another 2-tensor denoted by L_{ij} and defined as follows

$$L_{ij}=\frac{\partial v_i}{\partial x_j}. \tag{9}$$

The symmetric part of the velocity gradient is a 2-tensor called rate of deformation and denoted by D_{ij}, while its skew-symmetric part is a 2-tensor called spin and denoted by W_{ij}. Therefore, the following equations hold

$$D_{ij} = \frac{1}{2} \cdot \left(L_{ij} + L_{ji} \right), \tag{10}$$

$$W_{ij} = \frac{1}{2} \cdot \left(L_{ij} - L_{ji} \right). \tag{11}$$

It is assumed here that when a 2-tensor is indicated with subscripts arranged inversely to the alphabetical order, the valences indicated by these subscripts are intended as swapped, i.e. the 2-tensor is transposed in these valences. The right stretch and the left stretch allow for defining two sets, each of which is composed by an infinite number of 2-tensors called strain measures. One set defines the so-called Lagrangian strain measures, whilst the other defines the so-called Eulerian strain measures. These strain measures are denoted by E_{ij} and G_{ij} and defined respectively by the following relations

$$E_{ij}^{(m)} = \begin{cases} \dfrac{U_{ij}^{m} - \delta_{ij}}{m} & \text{if} \quad m \neq 0 \\ \ln U_{ij} & \text{if} \quad m = 0 \end{cases}, \tag{12}$$

$$G_{ij}^{(m)} = \begin{cases} \dfrac{V_{ij}^{m} - \delta_{ij}}{m} & \text{if} \quad m \neq 0 \\ \ln V_{ij} & \text{if} \quad m = 0 \end{cases}. \tag{13}$$

The parameter m is assumed to be an integer.

In the present work, a generic strain measure, that could be either Lagrangian or Eulerian, is denoted by the symbol ε_{ij}. It is possible to decompose any strain measure into its volumetric and deviatoric parts, through the following equation

$$\varepsilon_{ij} = \varepsilon_{ij}^{dev} + \varepsilon^{vol} \cdot \delta_{ij} = \varepsilon_{ij}^{dev} + \frac{\mathrm{tr}\varepsilon_{ij}}{3} \cdot \delta_{ij}, \tag{14}$$

where the first term in the right member is referred to as deviatoric strain or strain deviator and the second term is referred to as volumetric strain. Moreover, given a

strain measure ε_{ij}, it is possible to define an associated scalar quantity called equivalent or effective strain, denoted by $\bar{\varepsilon}$ and defined as follows

$$\bar{\varepsilon} = \sqrt{\frac{2}{3} \cdot \sum_{i=1}^{3} \sum_{j=1}^{3} \varepsilon_{ij} \cdot \varepsilon_{ij}} \,. \tag{15}$$

Sometimes, the equivalent strain is calculated by using a time integral of the rate of deformation, in particular in FEM code implementations. It is then defined by the following equation

$$\bar{\varepsilon} = \int_t \sqrt{\frac{2}{3} \cdot \sum_{i=1}^{3} \sum_{j=1}^{3} D_{ij} \cdot D_{ij}} \, dt \,. \tag{16}$$

It is worthwhile to point-out that this time integral may not give an equivalent strain attributable to any known strain measure. In this regard, see, e.g. Hoger, 1986.

The time derivative of a strain measure is called strain rate (referred to the considered strain measure) and is denoted by $\dot{\varepsilon}_{ij}$. Analogously, the time derivative of an equivalent strain is called equivalent strain rate (referred to the considered strain measure) and is denoted by $\dot{\bar{\varepsilon}}$. If elastic and plastic strains are identified, the quantities defined above for a generic strain measure can be specialized to these two cases.

The Cauchy stress is a 2-tensor that stems from considerations on the equilibrium of a continuum body (see, e.g., Bigoni, 2012). It is denoted by T_{ij} and is assumed to be symmetric. It defines a field on a body that describes its stress state. Furthermore, the Kirchhoff stress is another 2-tensor, denoted by τ_{ij}, still symmetric and defined by the following equation

$$\tau_{ij} = \det\left(F_{ij}\right) \cdot T_{ij} \,. \tag{17}$$

The stress power per unit volume of a continuous body is a scalar denoted by w and defined by the following equation

$$w = \sum_{i=1}^{3} \sum_{j=1}^{3} \tau_{ij} \cdot D_{ij} \,. \tag{18}$$

It is then said that the Kirchhoff stress and the rate of deformation are work-conjugate variables (see, e.g., Hill, 1978). For each of the previously introduced Lagrangian and Eulerian strain measures, it is possible to define a work-conjugate stress measure. To this end, the next two relations are introduced, in order to define the so-called Lagrangian and Eulerian stress measures, denoted by $T_{ij}^{(m)}$ and $Z_{ij}^{(m)}$, respectively

$$w = \sum_{i=1}^{3}\sum_{j=1}^{3} \tau_{ij} \cdot D_{ij} = \sum_{i=1}^{3}\sum_{j=1}^{3} T_{ij}^{(m)} \cdot \frac{\partial E_{ij}^{(m)}}{\partial t}, \tag{19}$$

$$w = \sum_{i=1}^{3}\sum_{j=1}^{3} \tau_{ij} \cdot D_{ij} = \sum_{i=1}^{3}\sum_{j=1}^{3} Z_{ij}^{(m)} \cdot \frac{\partial G_{ij}^{(m)}}{\partial t}. \tag{20}$$

In the present work, a generic stress measure, that may be either Lagrangian or Eulerian, is denoted by the symbol σ_{ij}. Analogously to what said for strain measures, it is possible to decompose any stress measure in its volumetric and deviatoric parts, through the following relation

$$\sigma_{ij} = s_{ij} + p \cdot \delta_{ij} = s_{ij} + \frac{tr\sigma_{ij}}{3} \cdot \delta_{ij}, \tag{21}$$

where the first term in the right member is referred to as deviatoric stress or stress deviator, denoted by s_{ij}, and the second term is referred to as volumetric stress. The scalar p is called pressure. Moreover, given a stress measure σ_{ij}, it is possible to define an associated scalar quantity called equivalent or effective stress, denoted by $\bar{\sigma}$ and defined as follows

$$\bar{\sigma} = \sqrt{\frac{3}{2} \cdot \sum_{i=1}^{3}\sum_{j=1}^{3} \sigma_{ij} \cdot \sigma_{ij}}. \tag{22}$$

The equivalent stress of the deviatoric part of a stress measure is called von Mises equivalent stress of such stress measure. It is denoted by $\bar{s}$ and is obtained accordingly

$$\bar{s} = \sqrt{\frac{3}{2} \cdot \sum_{i=1}^{3} \sum_{j=1}^{3} s_{ij} \cdot s_{ij}} = \sqrt{3 \cdot J_2} \,. \tag{23}$$

In this equation, J_2 represents the second invariant of the stress deviator of the considered stress measure, defined as follows

$$J_2 = \frac{1}{2} \cdot \sum_{i=1}^{3} \sum_{j=1}^{3} s_{ij} \cdot s_{ij} \,. \tag{24}$$

The time derivative of a stress measure is called stress rate (referred to the considered stress measure) and is denoted by $\dot{\sigma}_{ij}$. Analogously, the time derivative of an equivalent stress is called equivalent stress rate (referred to the considered stress measure) and is denoted by $\dot{\bar{\sigma}}$.

Furthermore, given a stress measure, it is possible to define a scalar known as stress triaxiality of such stress measure (see, e.g., Meyers, 1994), denoted by x, by introducing the ratio of its pressure and its von Mises stress, as reported in the following equation

$$x = \frac{p}{\bar{s}} \,. \tag{25}$$

The temperature field is denoted by symbol T throughout the work. A final consideration is related to the choice of the strain and stress measures to be related through a constitutive model. In this work, constitutive models are presented in a general way in which strain and stress measures are not forcedly defined a priori. However, when a generic strain measure and a generic stress measure or their time derivative are related through a constitutive model, it is always assumed that they form a couple of work-conjugate strain and stress measures. This hypothesis ensures the fulfillment of some technical requirements which are at the base of the constitutive modeling theory of continuum mechanics.

As already stated, this very brief summary aims only at introducing some quantities used in the present work and at clarifying their notation. Additional information and further comments on these topics, together with their notation, may be found, e.g., in Fung, 1965, Malvern, 1969, Gurtin, 1981, Marsden and Hughes, 1983, Holzapfel, 2001, Lubarda, 2002, Truesdell and Noll, 2004, Asaro and Lubarda, 2006, and Bigoni, 2012. Some considerations regarding the use of alternative compact tensor notation may be found, e.g., in Rizzi and Carol, 2001.

2. BRIEF OVERVIEW OF THE CONSTITUTIVE MODELING OF LARGE STRAIN AND HIGH STRAIN RATE PHENOMENA

Large strain and high strain rate phenomena may be defined as events that occur in a short time, say in the order of fractions of a second, which involve large strains and therefore high strain rates. Plastic strains, damage and fracture are usually present in this kind of processes.

A first aspect of the study of material behavior under dynamic loading involves the analysis of stress wave propagations in solid and fluid materials, for both elastic and plastic regimes. Stress propagates through continuous media as waves with finite velocity. Therefore, a certain time is required in order to allow these waves to spread through the matter. Elastic wave, plastic wave and shock wave propagations are phenomena of utter importance for the study of the dynamic behavior of materials. However, reviewing this entire argument is not on aim of this work. Among others, general treatments are provided in Meyers, 1994, and Wang, 2007. Treatments on elastic wave propagation can be found in Graff, 1965, and Achenbach, 1973. Studies on shock waves and high-pressure shock compression of solids are provided in Asay and Shahinpoor, 1993, Graham, 1993, Horie et al., 2003, Ben-Dor, 2007 and Davison, 2008.

A second key aspect of the study of the dynamic behavior of materials consists in the study of experimental procedures capable to expose the material response to such dynamic conditions. Throughout the years, some particular experimental procedures have emerged over others, thanks to their better feasibility and effectiveness. Dropweight machines, Hopkinson bars, Taylor tests and plate impact tests have become fairly popular. Nowadays, their use is common in many situations, both academic and industrial. Procedures to carry-out these tests and efficiently measure material responses keep on being elaborated and improved as well. A review of these experimental techniques is also not a target of the present work. However, general treatments are provided in Meyers, 1994, and Field et al., 2004. The Taylor test is presented in Taylor, 1948, and Whiffin, 1948. A review on the use of Hopkinson bars is supplied by Jiang and Vecchio, 2009. Some considerations on the procedures necessary to technically execute such tests and relevant test results for different materials are provided in Rajendran and Bless, 1985, and Rajendran, 1992.

Beyond these aspects, the focus of this work is on the constitutive modeling of dynamically loaded materials. Since decades ago, the study of such argument has been a leading research theme in the fields of solid and structural mechanics. Usually, a constitutive model exposed within classical continuum mechanics

contexts involves stress and strain 2-tensor measures as a whole, i.e. it involves the presence of both the deviatoric and volumetric parts. When large strain and high strain rate phenomena are addressed, it is a common practice to decompose these 2-tensors in their volumetric and deviatoric parts and then define two constitutive models, one for the deviatoric part and one for the volumetric part. This practice derives basically from deductions suggested by experimental evidences. An ad-hoc relation between the stress deviator and the strain deviator needs to be established, possibly involving also the strain rate, the temperature and the pressure. Similarly, an ad-hoc relation between the pressure, the volumetric strain and possibly other thermodynamic parameters needs to be established. Basically, the stress deviator is not assumed to be a function of the sole deviatoric strain, in particular when plastic regimes are involved. Similarly, the pressure is no longer a function of the sole volumetric strain. In this context, the wording strength model refers to a function that has the deviatoric part of the stress as dependent variable, while the quite general wording equation of state (also denoted by the acronym EOS) refers to a function that has the pressure as dependent variable.

Beyond strength models and equations of state, an ad-hoc description is also necessary for the modeling of damage and fracture of materials subjected to large strain and high strain rate phenomena. Such models usually need to include the strain rate, the temperature and possibly other parameters. Particular importance is given to the role of stress triaxiality. This parameter does not appear to be widely used in the quasi-static modeling of materials under damage and fracture processes. However, when high strain rates and large strains are involved, the stress triaxiality appears to play an important role in the evaluation of the damage and fracture of the materials.

In the following, some considerations on strength models, equations of state and damage and fracture models are presented, in order to briefly describe the nature of the most used models. In this context, the aim of this chapter is that of analyzing the pertinent literature seeking for the most interesting and successful constitutive models suitable for describing large strain and high strain rate phenomena. Particular reference is made here to the modeling of metallic materials. A brief review of such models and of some references will be made, together with the presentation of some original comments.

2.1. Strength Models

Several strength models suitable for the modeling of materials subjected to large strains and high strain rates have been proposed in the literature. One of the first references that treated these topics was probably Zener and Hollomon, 1944, in which the plastic behavior of steel was investigated, with particular attention to the

effects of the strain rate and the temperature. Afterwards, many authors have contributed to the development of the knowledge on strength models. In this work, some of the most popular strength models are analyzed and considered, namely the Johnson-Cook model (Johnson and Cook, 1983), the Zerilli-Armstrong model (Zerilli and Armstrong, 1987), the Steinberg-Cochran-Guinan model (Steinberg et al., 1980) and the Steinberg-Lund model (Steinberg and Lund, 1988). These constitutive models are believed to represent some of the most suitable options for the description of high to very high strain rate behavior of materials, in particular for metallic materials, i.e. the materials of highest interest for the industrial application considered in the present research project. More in detail, these models are potentially suitable for the description of materials subjected to the strain rate ranges involved in the considered industrial application. In the following, these models are briefly described and some relevant references are introduced. As previously stated, more attention is paid to the Johnson-Cook strength model, for the following reasons. First of all, it appears to be the most implemented and used material model when there is the need to model large strain and high strain rate material behavior over a possible wide range of strain rates and temperatures. Also, the new strength model introduced later in the present work (Chapter 3) actually originates as an enhancement of the Johnson-Cook model. Furthermore, the industrial application examined later in this work makes wide use of the Johnson-Cook model.

2.1.1. Johnson-Cook Strength Model

The wording Johnson-Cook strength model (also referred to as JC strength model) refers to the hardening function proposed in Johnson and Cook, 1983. The two authors proposed a form for the evaluation of the yield stress as a function of the equivalent plastic strain, the equivalent plastic strain rate and the temperature. Since its first proposal in 1983, this model has gained popularity and nowadays it appears as the most used strength model for the modeling of strain rate dependent phenomena.

For what it concerns the diffusion of the model in the scientific community, the Johnson-Cook strength model has been widely used by many authors throughout the years. Examples of such use, together with material data, can be found in several references, starting from the original Johnson-Cook paper (Johnson and Cook, 1983), which provided data and model parameters for 12 different materials. Noble et al., 1999, studied the application of the Johnson-Cook model to iron. Kay, 2003, considered applications to a titanium alloy and an aluminum alloy. Nemat-Nasser and Guo, 2003, evaluated the use of the Johnson-Cook model for a naval structural steel. Klepaczko et al., 2009, considered the application of the

Johnson-Cook model to two diverse structural steels. Scapin et al., 2012, presented an application of the model to an alumina dispersion strengthened copper. These are only some illustrative examples of the many applications of the Johnson-Cook model that may be found in the literature.

The Johnson-Cook strength model operates in the classic elastoplastic framework, in which an elastic constitutive model defines the elastic response, a yield criterion defines the delimitation of the elastic regime, and the plastic flow is determined by a flow rule and a hardening function. A review of these classic plasticity concepts is not an aim of this work. Reference is made to, e.g., Hill, 1950, Kachanov, 1971, Lubliner, 2006, and Bigoni, 2012. The Johnson-Cook strength model specifies this classical elastoplastic model by introducing a hardening function capable to model the yield stress dependence on the equivalent plastic strain rate and the temperature. In this context, the Johnson-Cook hardening function is used for updating the stress deviator only. The volumetric response of the material needs to be determined by an equation of state.

When quasi-static regimes are involved, hardening functions are tipically conceived as function of the sole equivalent plastic strain, e.g. through a power function. The contribution presented in Johnson and Cook, 1983, was that of proposing a more general hardening function, suitable for the description of the hardening of materials subjected to large strains, within a certain range of equivalent plastic strain rates and temperatures. Only isotropic hardening was considered, without the introduction of more complicated kinematic or combined hardening rules. Furthermore, one of the main aims of the authors was that of keeping the formulation in a fashion well suitable for implementations in FEM codes.

The form of the proposed hardening function was derived through a totally empiric approach, based on a quite high amount of experimental data collected by the two authors. Tensile and torsion tests were carried-out, considering experimental tests at different strain rates (through an Hopkinson bar) and temperatures. Several metallic materials were tested and analyzed. Results were presented in terms of the Cauchy stress and of the so-called true strain, i.e. the logarithmic strain measure.

On the basis of the obtained experimental results, Johnson and Cook, 1983, introduced a hardening function in which the yield stress manifested a power dependence on the equivalent plastic strain. Furthermore, they pointed-out that the yield stress presented a natural logarithmic dependence on the so-called dimensionless equivalent plastic strain rate, denoted by $\dot{\bar{\varepsilon}}_p^*$ and defined as follows

$$\dot{\bar{\varepsilon}}_p^* = \frac{\dot{\bar{\varepsilon}}_p}{\dot{\bar{\varepsilon}}_p^0}, \tag{26}$$

where $\dot{\bar{\varepsilon}}_p$ represents the current equivalent plastic strain rate and $\dot{\bar{\varepsilon}}_p^0$ represents a fixed equivalent plastic strain rate, taken as reference value. This value varies accordingly to the available experimental data.

Johnson and Cook, 1983, also pointed-out the fact that the current yield stress exhibited a power dependence on the so-called homologous or homogeneous temperature, denoted by T* and defined as follows

$$T^* = \frac{T - T_0}{T_m - T_0}, \tag{27}$$

where T_m represents the melting temperature and T_0 a fixed temperature, taken as reference value. As for the reference equivalent plastic strain rate, this value varies accordingly to the available experimental data.

On the basis of these observations, the proposed hardening function assumed the following form, in which the yield stress, interpreted as the von Mises stress, is a function of the equivalent plastic strain, the dimensionless equivalent plastic strain rate and the homologous temperature, together with other material parameters

$$\bar{s} = \left(A + B \cdot \bar{\varepsilon}_p^n\right) \cdot \left(1 + C \cdot \ln \frac{\dot{\bar{\varepsilon}}_p}{\dot{\bar{\varepsilon}}_p^0}\right) \cdot \left(1 - \left(\frac{T - T_0}{T_m - T_0}\right)^m\right). \tag{28}$$

The 8 parameters denoted by A, B, n, C, $\dot{\bar{\varepsilon}}_p^0$, T_0, T_m and m are referred to as the parameters of the Johnson-Cook strength model. They need to be calibrated through appropriate experimental tests. Following Table 1 reports their dimensions and possible units.

A	Stress, e.g. [MPa]	m	Non-dimensional
B	Stress, e.g. [MPa]	$\dot{\bar{\varepsilon}}_p^0$	Strain rate, e.g. [s^{-1}]
N	Non-dimensional	T_0	Temperature, e.g. [K]
C	Non-dimensional	T_m	Temperature, e.g. [K]

Table 1
Dimensions and possible units of the Johnson-Cook parameters.

It is worthwhile to note that the Johnson-Cook hardening function is conceived in a multiplicative fashion, in which the terms contained in the three outer round brackets act together to set the value of the current yield stress.

The first multiplicative term represents a power hardening law, characterized by the three parameters A, B and n. This form is widely used for describing metallic hardening functions in quasi-static modeling contexts. It may then be said that the first multiplicative term represents the quasi-static part of the hardening function and thus it is referred to here as the quasi-static term of the Johnson-Cook strength model.

The second multiplicative term introduces the natural logarithmic dependence on the dimensionless equivalent plastic strain rate and thus it is referred to here as the strain rate term of the Johnson-Cook strength model. This term is conceived in such a way that when the current equivalent plastic strain rate is equal to the reference equivalent logarithmic plastic strain rate it becomes equal to 1 and therefore there are no strain rate effects on the computation of the current yield stress. In such conditions, the hardening response of the material is then ruled by the two other multiplicative terms. Otherwise, the effect of the strain rate on the yield stress is determined by the current value of the equivalent plastic strain rate and ruled by the reference equivalent plastic strain rate and by the parameter C.

The third and last multiplicative term introduces the power dependence on the homologous temperature and thus it is referred to here as the temperature term of the Johnson-Cook strength model. This term is conceived in a way such that when the current temperature is equal to the reference temperature it becomes equal to 1 and therefore there are no temperature effects on the computation of the current yield stress. In such conditions, the hardening response of the material is then ruled by the other 2 multiplicative terms. Otherwise, the effect of the temperature on the yield stress is determined by the current value of the temperature and ruled by the reference temperature, the melting temperature and the parameter m. It is also worthwhile to note that when the current temperature reaches the melting temperature value, this term becomes equal to 0 and thus the current yield stress is assumed to be null and the material is assumed to offer no deviatoric resistance. Temperatures higher than the melting temperature are allowed to occur but then the yield stress is no longer computed with Eq. (28), which would lead to a negative yield stress. In such cases, the yield stress is just set equal to zero.

As pointed-out by the authors themselves (Johnson and Cook, 1983), the Johnson-Cook hardening function is a quite simple model that may not provide accurate descriptions of the hardening response of the material, thus leading to results that may lack in coherence. On the other hand, its simplicity implies some advantages. Indeed, the Johnson-Cook hardening function may be seen as a valid

compromise between simplicity, modeling coherency, requirement of experimental tests and need of computational capacities.

Regarding the positive features of the Johnson-Cook strength model, simplicity and readiness of computational implementation appear to be the most interesting. The model turns-out quite cheap in terms of demand of computational requirements. Furthermore, it is surely well suitable to fit FEM applications, since it uses variables that are readily available in most FEM codes or so-called hydrocodes, namely the equivalent plastic strain, the equivalent plastic strain rate and the temperature. In order to compute the current yield stress, these three variables are the only ones that need to be computed in each timestep of the calculation, since the 8 parameters of the model are fixed and established at the beginning of the calculation. Beyond this aspect, the Johnson-Cook strength model is capable of displaying a good coherence when adopted for the modeling of some basic high strain rate experimental tests, such as for the FEM modeling of Taylor tests. As exposed in Johnson and Cook, 1983, applications of the model in a FEM code (EPIC-2) showed a good matching between the Taylor test computed results and their experimental counterparts. It is often said that the Johnson-Cook model is a formulation able to provide results characterized by having a high enough grade of accuracy, capable to satisfy necessities required in common engineering practices. Actually, these features are the main factors that contributed to the large diffusion of the Johnson-Cook model among the scientific community, in particular towards computational applications.

Regarding the negative aspects, it may be said that the simplicity of the Johnson-Cook strength model is paid by introducing some drawbacks in the formulation. In particular, two main flaws can be identified. The first issue consists in the fact that the natural logarithmic dependence of the yield stress on the dimensionless equivalent plastic strain rate may not be suitable to coherently fit the strain rate dependence of some materials. Analogously, the power dependence of the yield stress on the homologous temperature may present the same shortcoming. These aspects might lead to heavy modeling errors in practical cases.

The second problem consists in the fact that the equivalent plastic strain, the equivalent plastic strain rate and the temperature effects on the yield stress are totally independent from each other. This is a direct consequence of the choice of adopting a hardening function conceived in a multiplicative fashion, in which the equivalent plastic strain, the equivalent plastic strain rate and the temperature terms aim at independently representing the three effects on the yield stress. For a given equivalent plastic strain, its effect on the yield stress is the same whatever values the equivalent plastic strain rate and the temperature take. Similarly, for a given equivalent plastic strain rate, its effect on the yield stress is the same whatever values the equivalent plastic strain and the temperature take. Similarly again, for a

given temperature, its effect on the yield stress is the same whatever value the equivalent plastic strain and the equivalent plastic strain rate take. The main problem due to this aspect may be the fact that the effects of the equivalent plastic strain rate and the temperature need to be assumed as equal for each equivalent plastic strain. As a matter of fact, this effect may instead be quite different by passing from a condition in which the equivalent plastic strain is null (i.e., the first yielding stress of the material, called also lower yield stress), to conditions with non zero equivalent plastic strain. This point may imply the introduction of heavy coherency errors in the modeling, either of the lower yield stress or of the plastic flow. The more these two aspects present a different dependence on the equivalent plastic strain rate and on the temperature, the more errors are to be introduced, since a compromise between these aspects necessarily needs to be adopted. This simplistic approach may lead to considerable modeling errors, which might actually add to the ones due to the first issue.

At this point, there arise questions about the relevance of these flaws, i.e. how much they may negatively affect the coherency of the model. The point is that of assessing the magnitude of the errors in the prediction of the yield stress for a given equivalent plastic strain, and, accordingly, the magnitude of the errors in the prediction of the equivalent plastic strain for a given yield stress. The examination of the hardening characteristics of the steel adopted in the industrial application under analysis in the present work (i.e., a perforating gun device) suggested that this aspect may be central and heavily affect the computed results, although only a low amount of experimental data was made available. The point here is that the Johnson-Cook hardening function may not be capable to fit the available data with sufficient accuracy in order to produce results fruitfully usable for engineering purposes. Most of all, the fitting may be appropriate only for selected ranges of equivalent plastic strains, equivalent plastic strain rates and temperatures, but not overall.

Beyond the analysis of the material used in the particular industrial application considered in the present thesis, the belief that the Johnson-Cook model may sometimes produce strongly incoherent predictions appears to be confirmed by the analysis of other references, which investigate the strain rate and temperature hardening response of different materials. Some examples of such references are reported in the following: Krafft et al., 1954, which presented studies on iron and steel plastic flow in the dependence of the strain rate and temperature; Hoge and Mukherjee, 1977, which proposed an investigation on the temperature and strain rate dependence of the flow stress of tantalum; Nemat-Nasser and Guo, 2003, which proposed a wide strain rate and temperature investigation of the plastic flow behavior of a structural steel; Rusinek et al., 2009, which presented similar investigations for six high strength steels. It appears that the adoption of the

Johnson-Cook strength model may occasionally introduce heavy modeling errors, in particular when there is the aim of predicting material behaviors over wide ranges of equivalent plastic strain rates and temperatures.

The two previously presented main issues of the Johnson-Cook model did not pass unnoticed in the scientific community. Indeed, the original Johnson-Cook strength model has been the subject of a large number of reviews and modifications. The aims were that of solving or mitigating the negative effects due to the two main drawbacks described above. The following exposition aims at briefly reviewing the main proposed contributions. References that dealt with the first Johnson-Cook issue are presented first, while those which dealt with the second issue are presented second. In this regard, It may be said that the relevance of the Johnson-Cook strength model is further proven by the large number of revisions and enhancements that have been proposed since its first publication.

The first Johnson-Cook issue addresses the fact that a material may not present a natural logarithmic dependence of the yield stress on the dimensionless equivalent plastic strain rate and a power dependence on the homologous temperature. Many authors have contributed to a revision and possibly to a modification of the original Johnson-Cook strain rate and temperature multiplicative terms, in order to improve the coherence of the strength model.

For what it concerns the strain rate term, one of the earlier modifications was presented in Holmquist and Johnson, 1991. These authors pointed-out how the natural logarithmic dependence of the yield stress on the dimensionless equivalent plastic strain rate could be replaced by a power dependence in which the parameter C has now the role of the exponent. In detail, the original Johnson-Cook strength model was substituted by the following one

$$\bar{s} = \left(A + B \cdot \bar{\varepsilon}_p^{n}\right) \cdot \left(\frac{\dot{\bar{\varepsilon}}_p}{\dot{\bar{\varepsilon}}_p^{0}}\right)^{C} \cdot \left(1 - \left(\frac{T - T_0}{T_m - T_0}\right)^{m}\right). \tag{29}$$

This model still uses 8 parameters. Holmquist and Johnson, 1991, presented a FEM implementation of this modified Johnson-Cook model, with the aim of computationally reproduce experimental data from a number of Taylor tests. This modified model provided a better data fitting comparing to the original Johnson-Cook model, although the differences appeared actually marginal.

Couque et al., 1995, proposed another modification of the Johnson-Cook strain rate term. The authors pointed-out that the original Johnson-Cook model may be capable to provide satisfactory results when equivalent plastic strain rates lower than 10^3 s^{-1} are involved. However, these authors also pointed-out that the model may lack in coherence when higher equivalent plastic strain rates occur. In order to

better account for this effect, the original Johnson-Cook model was modified with the introduction of a power strain rate component added to the natural logarithm strain rate term, leading to a model with 11 parameters, as represented in the following equation

$$\bar{s} = \left(A + B \cdot \bar{\varepsilon}_p^{\,n}\right) \cdot \left(1 + C \cdot \ln \frac{\dot{\bar{\varepsilon}}_p}{\dot{\bar{\varepsilon}}_p^{0}} + D \cdot \left(\frac{\dot{\bar{\varepsilon}}_p}{\dot{\bar{\varepsilon}}_p^{1}}\right)^{k}\right) \cdot \left(1 - \left(\frac{T - T_0}{T_m - T_0}\right)^{m}\right). \qquad (30)$$

In this equation, $\dot{\bar{\varepsilon}}_p^{1}$ represents an equivalent plastic strain rate value which determines the transition between the so-called thermally activated regime and the so-called viscous regime. This value was stated to be about 10^3 s^{-1}. Two further parameters are introduced in the model, denoted by D and k. The modified model was evaluated through numerical simulations of Taylor tests for pure nickel and a high strength nickel alloy. Comparing to the original Johnson-Cook model, the outcomes proved the modified model to display an improved coherency in reproducing experimental data at high equivalent plastic strain rates.

Another modification of the strain rate multiplicative term was proposed by Rule and Jones, 1998. The point was that of modifying the original Johnson-Cook strain rate term, in order to more closely match observed material behavior at high strain rates. Similarly to what stated by Couque et al., 1995, the two authors pointed-out that the yield strength may increase more rapidly with the equivalent plastic strain rates than what determined by the original Johnson-Cook hardening function, in particular for equivalent plastic strain rates that exceed 10^3 s^{-1}. On this basis, Rule and Jones, 1998, proposed to modify the original Johnson-Cook model in the following way

$$\bar{s} = \left(A + B \cdot \bar{\varepsilon}_p^{\,n}\right) \cdot \left(1 + C \cdot \ln \frac{\dot{\bar{\varepsilon}}_p}{\dot{\bar{\varepsilon}}_p^{0}} + C_1 \left(\frac{1}{C_2 - \ln \frac{\dot{\bar{\varepsilon}}_p}{\dot{\bar{\varepsilon}}_p^{0}}} - \frac{1}{C_2}\right)\right) \cdot \left(1 - \left(\frac{T - T_0}{T_m - T_0}\right)^{m}\right). \qquad (31)$$

In this equation, C_1 and C_2 are additional parameters of the model, to be determined from experimental data. The number of parameters of the model amounts to 11. Rule and Jones, 1998, proposed also a procedure to calibrate the parameters of the model, with application to four metals, through the evaluation of quasi-static tests and Taylor tests. This new model was then proven to be capable

of providing a good fit of the yield stress at elevated equivalent plastic strain rates, referring to the capacity of fitting Taylor impact experimental data.

Kang et al., 1999, pointed-out that the original Johnson-Cook strain rate term, which determines a linear dependence of the yield stress on the natural logarithm of the dimensionless equivalent plastic strain rate, may need to be enriched with a term that adds a quadratic dependence of the yield stress on the natural logarithm of the dimensionless equivalent plastic strain rate. This assumption was motivated with reference to some presented experimental data. In particular, it was shown that the quadratic term may be necessary to correctly represent the material behavior at low equivalent plastic strain rates, i.e. rates lower than 1 s^{-1}. The Johnson-Cook hardening function was then modified in the following way

$$\bar{s} = \left(A + B \cdot \bar{\varepsilon}_p^{\,n}\right) \cdot \left(1 + C \cdot \ln \frac{\dot{\bar{\varepsilon}}_p}{\dot{\bar{\varepsilon}}_p^{\,0}} + C_1 \cdot \left(\ln \frac{\dot{\bar{\varepsilon}}_p}{\dot{\bar{\varepsilon}}_p^{\,0}}\right)^2\right) \cdot \left(1 - \left(\frac{T - T_0}{T_m - T_0}\right)^m\right). \tag{32}$$

This model uses 9 parameters. A new parameter is introduced in the model, denoted by C_1. It determines the weight of the quadratic strain rate term.

Johnson et al., 2006, proposed another modification of the strain rate term by introducing a power term that enriches the modeling of the yield stress dependence on the equivalent plastic strain rate. The following form was then proposed and called high-rate Johnson-Cook model

$$\bar{s} = \left(A + B \cdot \bar{\varepsilon}_p^{\,n}\right) \cdot \left(1 + C \cdot \ln \frac{\dot{\bar{\varepsilon}}_p}{\dot{\bar{\varepsilon}}_p^{\,0}} + C_1 \cdot \left(\ln \frac{\dot{\bar{\varepsilon}}_p}{\dot{\bar{\varepsilon}}_p^{\,0}}\right)^{C_2}\right) \cdot \left(1 - \left(\frac{T - T_0}{T_m - T_0}\right)^m\right). \tag{33}$$

It is worthwhile to point-out that this strength model is a generalization of the model proposed by Kang et al., 1999, i.e. that represented in Eq. (32). This approach introduces two additional parameters, denoted by C_1 and C_2, leading to a total of 10 parameters. Applications of this model and comparison to the original Johnson-Cook model have been provided in the same reference (Johnson et al., 2006). Referring to the original Johnson-Cook model, the high-rate Johnson-Cook model showed an improved modeling coherency.

Some modifications have been proposed for the Johnson-Cook temperature term as well. Maheshwari et al., 2009, proposed a modification of this term based on high temperature experimental data of the aluminum alloy Al-2024, considering also the strain rate term modification proposed by Holmquist and Johnson, 1991, i.e. the power dependence. The following hardening function was then proposed

$$\bar{s} = \left(A + B \cdot \bar{\varepsilon}_p^{n}\right) \cdot \left(\frac{\dot{\bar{\varepsilon}}_p}{\dot{\bar{\varepsilon}}_p^{0}}\right)^{C} \cdot \left(1 + \left(\frac{\bar{s}_m}{\bar{s}_y} - 1\right) e^{-\alpha\left(\frac{T - T_0}{T_m - T_0}\right)^{\beta}}\right). \tag{34}$$

In this equation, $\bar{s}_m$, $\bar{s}_y$, α and β represent additional model parameters, to be determined from experimental data. The total number of parameters becomes now 11. The two authors presented some applications of the model that demonstrated a more coherent fitting of the experimental data, when comparing to the original Johnson-Cook hardening function, in particular at high temperatures.

Hou and Wang, 2010, introduced a modification of the temperature term in order to better predict the material behavior when the range of temperatures involved is particularly wide. The focus was on a hot-extruded Mg-10Gd-2Y-0.5Zr alloy. Such modified hardening function uses the same 8 parameters of the original Johnson-Cook model. The proposed model is reported in the following equation

$$\bar{s} = \left(A + B \cdot \bar{\varepsilon}_p^{n}\right) \cdot \left(1 + C \cdot \ln \frac{\dot{\bar{\varepsilon}}_p}{\dot{\bar{\varepsilon}}_p^{0}}\right) \cdot \left(1 - \lambda \frac{e^{\frac{T}{T_m}} - e^{\frac{T_0}{T_m}}}{e - e^{\frac{T_0}{T_m}}}\right). \tag{35}$$

Other authors presented more complicated developments of the original Johnson-Cook strain rate and temperature terms. As instance, Duc-Toan et al., 2012, introduced a modification of the temperature term in order to enhance the model coherency when very high temperatures are involved.

As proven by the brief review presented here, many modifications of the original Johnson-Cook model have been proposed. In general, it may be said that the first issue of the Johnson-Cook model is partially solved, or mitigated, by the possibility of choosing between different strain rate and temperature terms, with the aim of better fitting the experimental data of the considered material, by taking into account specific equivalent plastic strain rate and temperature ranges. As a matter of fact, some commercial FEM codes allow to choose between some of the different strain rate and temperature terms described above.

For what it concerns the second Johnson-Cook issue, the point was that of considering the equivalent plastic strain, the equivalent plastic strain rate and the temperature effects on the yield stress as totally independent from each other. It appears that no contributions capable to mitigate this problem have ever appeared in the literature, unless some references which treated this aspect but only

marginally. In this regard, some authors proposed modifications capable to partially introduce the synergic dependence of the strain rate and the temperature effects.

For instance, Lin et al., 2010, proposed a modified Johnson-Cook model in which a mixed strain rate and temperature term is introduced. The proposed term is reported in the following equation

$$\bar{s} = \left(A + B_1 \cdot \bar{\varepsilon}_p + B_2 \cdot \bar{\varepsilon}_p^2\right) \cdot \left(1 + C \cdot \ln \frac{\dot{\bar{\varepsilon}}_p}{\dot{\bar{\varepsilon}}_p^0}\right) \cdot e^{\left(\lambda_1 + \lambda_2 \cdot \ln \frac{\dot{\bar{\varepsilon}}_p}{\dot{\bar{\varepsilon}}_p^0}\right) \cdot (T - T_r)} . \quad (36)$$

The power quasi-static term is replaced by a form that involves a second order trend on the equivalent plastic strain. The parameters B_1 and B_2 replace the original Johnson-Cook parameters B and n. Their role is that of describing the quasi-static behavior. However, this is only another form to fit data throughout the equivalent plastic strain. The point here is on the strain rate and temperature terms. The strain rate term is maintained the same as in the original Johnson-Cook model. The temperature term is substituted with an exponential term which involves both the dimensionless equivalent plastic strain rate and the temperature. Two new parameters are introduced, denoted by λ_1 and λ_2, while the parameters T_m and m are no longer present, thus keeping a total number of parameters equal to 8. The proposed model was applied to predict the tensile behavior of a typical high-strength alloy steel, showing a good fitting of experimental data. Furthermore, Wang et al., 2011, proposed a modification similar to the one introduced by Lin et al., 2010, with some variations to the quasi-static and the strain rate terms.

Despite these efforts, the second Johnson-Cook issue appears to be still present, in particular in its heaviest problematics, i.e. the fact that the effects of the equivalent plastic strain rate and the temperature need to be assumed as equal for each equivalent plastic strain, a point which may lead to heavy modeling errors for the prediction either of the lower yield stress or of the plastic flow. In this context, Chapter 3 presents a new formulation capable to mitigate this important shortcoming.

2.2.1.1. Johnson-Cook Model Calibration Strategies

The calibration of the 8 material parameters of the Johnson-Cook model (Eq. (28)) is strictly related to the problematics exposed above. The original paper that proposed the model (Johnson and Cook, 1983), did not actually provide a detailed description of the procedure necessary to calibrate them. It may be said that this fact has probably contributed to the appearance of uncertainties about the

calibration procedure. In this regard, some considerations can be found in Holmquist and Johnson, 1991, but it appears that several key points are still missing. Various other references treated this aspect, such as, e.g., Langrand et al., 1999, Schwer, 2004, Milani et al., 2008, and Scapin et al., 2012, just to cite a few. When it comes to the determination of the 8 Johnson-Cook model parameters, the first aspect to understand is that it is actually possible to define different calibration strategies. In this context, the following exposition aims at reviewing systematically the procedures for the calibration of the Johnson-Cook parameters, a process whose importance is crucial in order to correctly use the model, say at its best potentialities. The most popular calibration approaches are framed, described and discussed, together with the introduction of some original contributions.

For the sake of clarity, all the calibration strategies are illustrated with application to a practical material case, i.e. the 8 Johnson-Cook parameters are actually determined from a selected instance of true experimental data. To this end, literature experimental data are considered, since the experimental observations made available for the materials used in the industrial application considered in this work are very limited and therefore they are not complete enough to be successfully used for presenting calibration applicative examples. Experimental data are extracted from the work proposed by Nemat-Nasser and Guo, 2003, in which a high strength structural steel used for naval applications (associated to the nomenclature DH-36) has been widely tested. This choice is due to the fact that this work presents a wide amount of experimental observations, intended in terms of hardening functions of the material, capable to cover wide ranges of equivalent plastic strain rates and temperatures. The experimental data considered here consists in a set of nine hardening functions, evaluated at three different equivalent plastic strain rates and at three different temperatures. The considered equivalent plastic strain rates are 0.001 s^{-1}, 0.1 s^{-1} and 3000 s^{-1}, while the considered temperatures are 77 K, 296 K and 800 K. Although further data can be found in Nemat-Nasser and Guo, 2003, the extracted subset of data is surely enough to achieve the target of this chapter and also to avoid bringing up too much data, in order to favor exposition conciseness. The nine hardening functions considered have been obtained through compressive tests. Compressive Hopkinson bars, cooling systems and furnaces have been used. Reference is made to the presented adiabatic results. Results are provided in terms of Cauchy stress versus true (logarithmic) equivalent plastic strain. Following Figs. 1 to 3 report the nine hardening functions taken into consideration. These experimental data have been extracted from Nemat-Nasser and Guo, 2003, by means of appropriate digitalization. The scores visible in the figures represent the digitalized points. Clearly, this process implies the introduction of some uncertainties in the considered data, in particular for the determination of the lower yield stress. Of

course, this is not an important issue here, since the point under question is only that of showing the outcomes of different Johnson-Cook calibration strategies and not that of fitting the DH-36 steel data as best as possible. Furthermore, data are purified by possible oscillations or peaks near the lower yield stress that may appear in some case, in order to present clearer and more useful data.

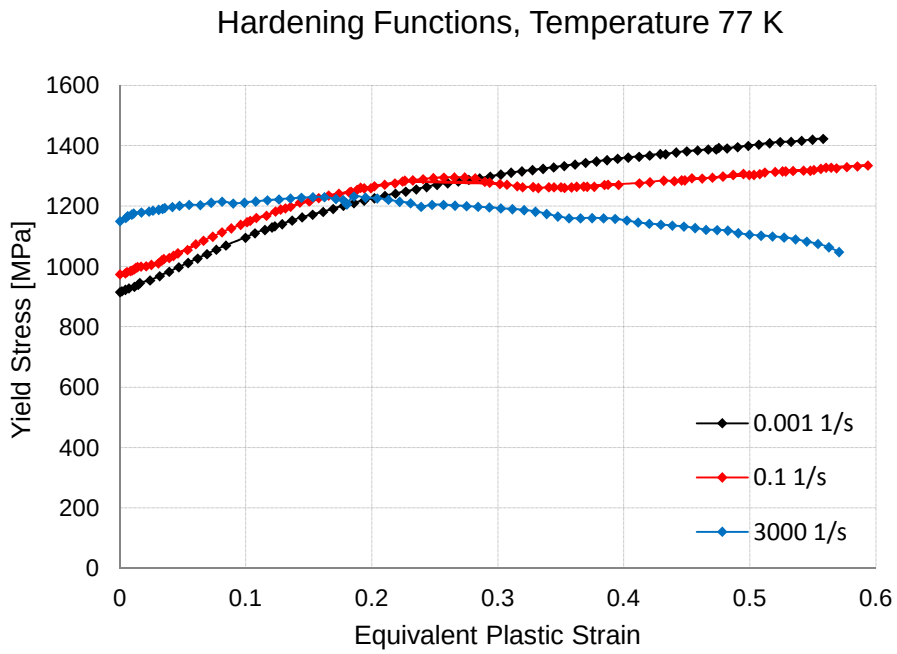

Figure 1. DH-36 structural steel hardening functions at temperature of 77 K and three different equivalent plastic strain rates. Material softening arises for data at 3000 s^{-1}. Data re-elaborated from Nemat-Nasser and Guo, 2003.

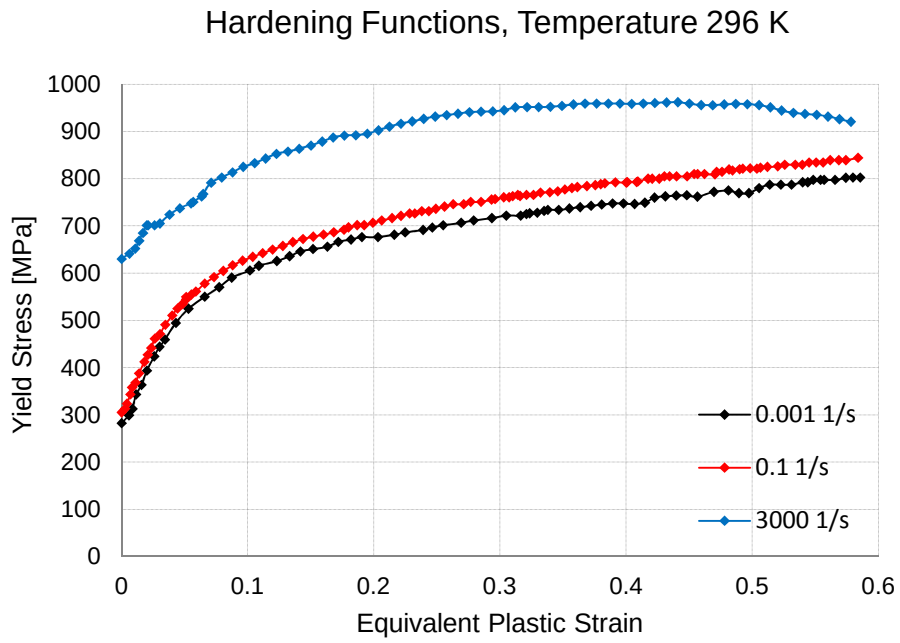

Figure 2. DH-36 structural steel hardening functions at temperature of 296 K and three different equivalent plastic strain rates. Data re-elaborated from Nemat-Nasser and Guo, 2003.

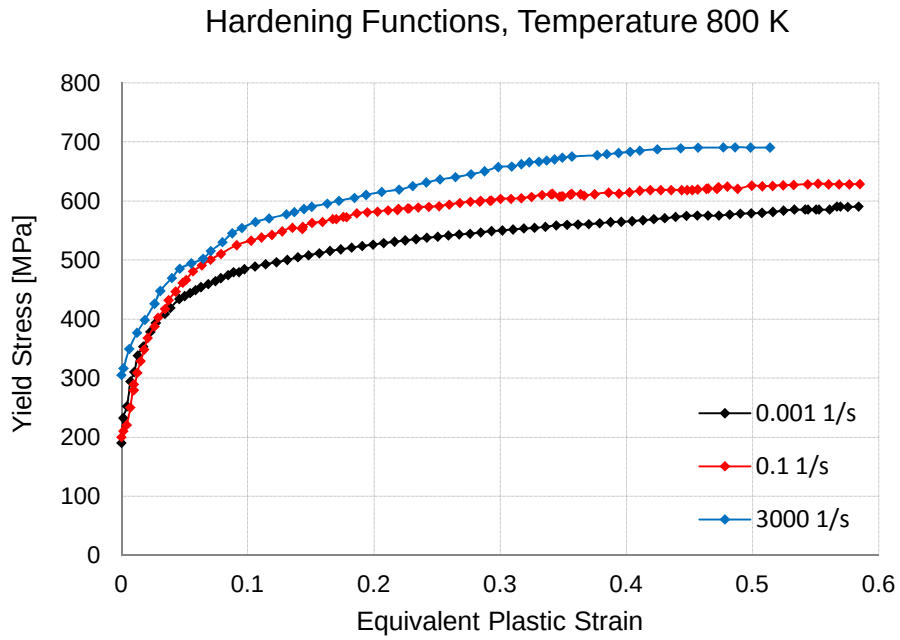

Figure 3. DH-36 structural steel hardening functions at temperature of 800 K and three different equivalent plastic strain rates. Data re-elaborated from Nemat-Nasser and Guo, 2003.

Following Table 2 summarizes the lower yield stresses for the nine hardening functions plotted above.

	0.001 s^{-1}	**0.1 s^{-1}**	**3000 s^{-1}**
77 K	915.555 MPa	974.565 MPa	1150.46 MPa
296 K	282.455 MPa	305.455 MPa	630.137 MPa
800 K	190.345 MPa	200.213 MPa	305.345 MPa

Table 2
DH-36 structural steel lower yield stresses at different equivalent plastic strain rates and temperatures. Data re-elaborated from Nemat-Nasser and Guo, 2003.

It is worthwhile to note that the lower yield stress is strictly increasing with the equivalent plastic strain rate, at each temperature, and that it is strictly decreasing with the temperature, at each equivalent plastic strain rate.

Following Figs. 4 and 5 show the trends of the lower yield stress versus the equivalent plastic strain rate and the temperature, respectively.

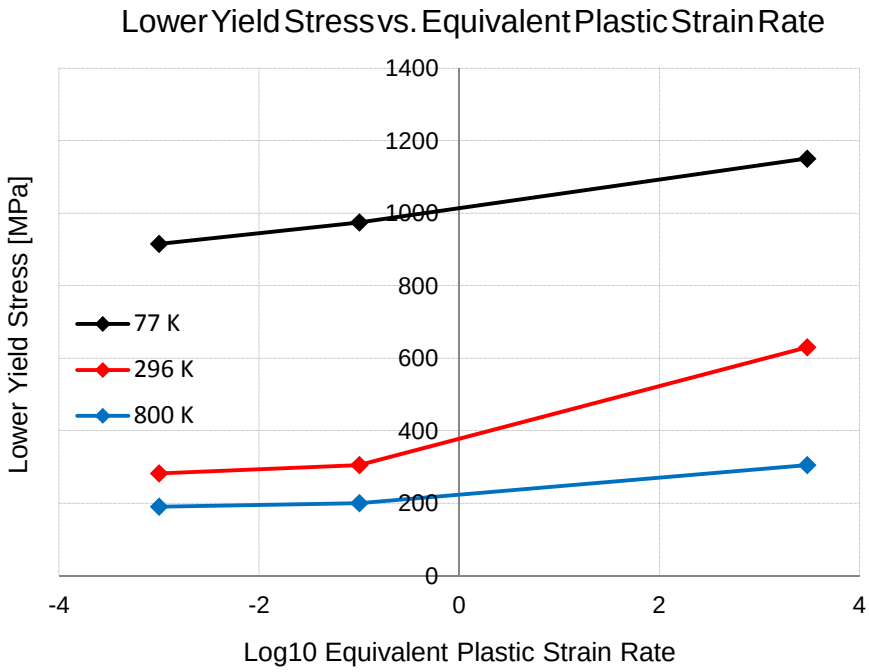

Figure 4. DH-36 structural steel lower yield stress versus equivalent plastic strain rate for the three considered temperatures. For representation convenience, the equivalent plastic strain rates are evaluated though their base 10 logarithm. Data re-elaborated from Nemat-Nasser and Guo, 2003.

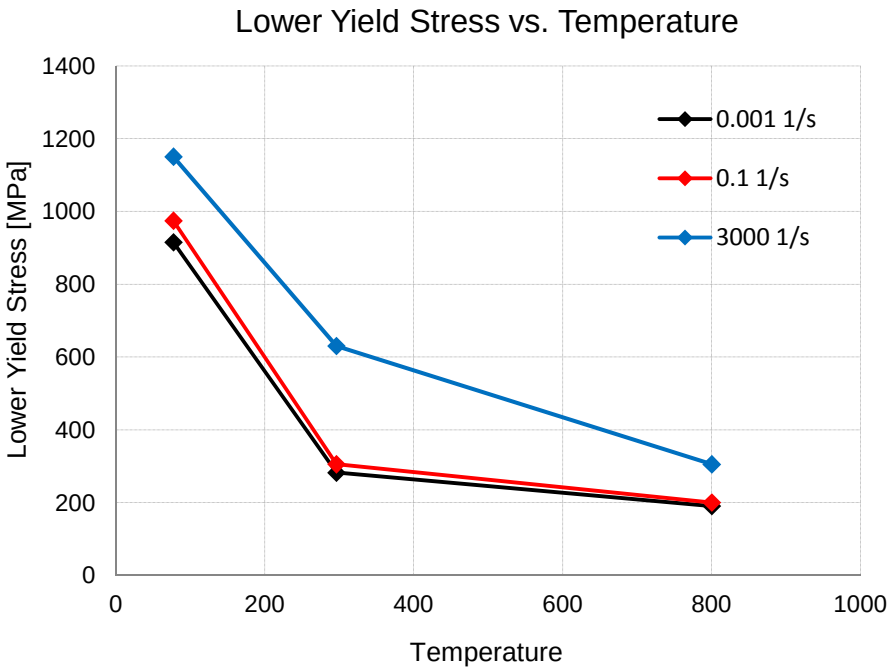

Figure 5. DH-36 structural steel lower yield stress versus temperature for the three considered equivalent plastic strain rates. Data re-elaborated from Nemat-Nasser and Guo, 2003.

In the following, five different calibration strategies are described and applied to the just presented experimental data. These approaches appear to be the most intuitive, although it is recognized that they are not the only possible ones and other calibration strategies may be defined. In order to ease their identification, a name is defined here and associated to each of them. The five exposed calibration strategies do not appear to be clearly identified and defined in the pertinent literature. Rather, it seems that different Johnson-Cook calibration strategies are not clearly distinguishable from each other. Thus, the following rigorous and systematic treatment aims at clarifying such situation, at least for the five calibration strategies considered here.

This exposition aims also at introducing some considerations about the experimental tests necessary to get the input for each calibration procedure. In this context, testing the material means to obtain experimental data intended in terms of hardening functions, i.e. curves relating the yield stress to the equivalent plastic strain. Since the Johnson-Cook model does not consider a dependence of the yield stress on the stress triaxiality, these data may come from tensile, compressive or torsion tests, provided that the obtained results are then transformed and evaluated in terms of the von Mises stress and the equivalent plastic strain. However, discrepancies through the parameters may be found when passing from one kind of

test to another, as pointed-out by the original paper that presented the strength model (Johnson and Cook, 1983). This may be related to a dependence of the yield stress on the stress triaxiality, although this appears to be a controversial point and it will not be treated in this work. In this regard, some considerations can be found in Hopperstad et al., 2003, and in Børvik et al., 2003, in which the combined effects of strain rate and stress triaxiality have been investigated.

2.2.1.1.1. LYS Calibration Strategy

The LYS (Lower Yield Stress) calibration strategy aims at determining the set of material parameters capable to achieve the best experimental data fitting for the lower yield stresses, i.e. at null equivalent plastic strain.

The first parameter to be determined is the melting temperature of the material. This phase is straightforward, provided that melting data are available. It is then necessary to identify the equivalent plastic strain rates and temperatures at which it is possible to test the considered material. This information allows to determine the reference values of the equivalent plastic strain rate and of the temperature. Regarding the reference equivalent plastic strain rate, it must be chosen as one of the equivalent plastic strain rates at which the material is tested. No other particular conditions are proposed here, therefore it is possible to choose any of them. A popular choice is that of taking the lowest considered value. Regarding the reference temperature, a sound option is that of taking it equal to the lowest temperature at which the material is tested. This choice is due to the fact that it is necessary to avoid the computation of negative homologous temperatures, since this term is then raised through the parameter m, that may be a non integer number, and therefore the calculation of this power may not be possible. This situation can lead to error terminations when the model is implemented in FEM codes and therefore needs to be avoided. As a consequence, the choice of identifying the reference temperature with the lowest temperature at which the material is tested, in order to avoid this problem. If a FEM simulation is involved, it may also be necessary to check also the fact that the material temperature shall never go below the reference value.

The next phase consists in the determination of the three quasi-static parameters, namely A, B and n. This point uses data obtained from the test conducted at the reference temperature and at the reference equivalent plastic strain rate. These data may be filtered from structural effects through an inverse analysis of the experimental tests, to be carried-out with a FEM code. The facts that the test is carried-out at the equivalent plastic strain rate and temperature reference values implies that the Johnson-Cook strength model assumes the following form, in which the second and third multiplicative terms become equal to 1

$$\bar{s} = A + B \cdot \bar{\varepsilon}_p^{\,n} . \tag{37}$$

Under these reference conditions, the parameter A corresponds to the lower yield stress, while the parameters B and n describe the successive hardening of the material. It is then possible to determine the parameters A, B and n by fitting the experimental points with the function shown in Eq. (37). A good strategy here is that of adopting a code that provides nonlinear regression capabilities. Following this strategy, the determination of the three quasi-static parameters, i.e. A, B and n, is due only to the material behavior at the so-called reference conditions, i.e. at reference equivalent plastic strain rate and temperature.

At this point, it is worthwhile to highlight a consideration about the choice of the reference equivalent plastic strain rate. As a matter of fact, the reference equivalent plastic strain rate must be taken as the value at which the quasi-static parameters are evaluated, following the procedure just shown. Otherwise, it is not possible to determine the three quasi-static parameters in the way just exposed, because the strain rate multiplicative term does not vanish. Assuming the reference equivalent plastic strain rate to be equal to 1 and determining the quasi-static parameters by fitting a hardening function which refers to an equivalent plastic strain rate that is actually different from this reference equivalent plastic strain rate may lead to errors. Schwer, 2004, provides a discussion on this aspect, in the context of FEM applications of the Johnson-Cook model.

The next step is relative to the determination of the strain rate parameter, i.e. the parameter C. This step involves experimental tests conducted at the reference temperature and at equivalent plastic strain rates different from the reference equivalent plastic strain, from the lowest one tested up to the highest one. These data are always to be intended as a hardening function relating the yield stress to the equivalent plastic strain. The value of the parameter C can be obtained by noting that the temperature term of the Johnson-Cook strength model becomes equal to 1 and thus vanishes, since the tests are carried-out at the reference temperature. Being the parameters A, B and n known, the only unknown remaining parameter is C, and it can be calculated through the hardening function by using the following equation

$$C = \frac{\dfrac{\bar{s}}{A + B \cdot \bar{\varepsilon}_p^{\,n}} - 1}{\ln \dfrac{\dot{\bar{\varepsilon}}_p}{\dot{\bar{\varepsilon}}_p^{\,0}}} . \tag{38}$$

In order to calculate the value of the parameter C, the values of the equivalent plastic strain rate, the yield stress and the equivalent plastic strain need to be introduced in Eq. (38). By considering experimental results at one determined equivalent plastic strain rate, the remaining unknown values are the yield stress and the equivalent plastic strain. It is clear that the yield stress is determined when an equivalent plastic strain value is chosen, thanks to the experimental hardening curve under analysis, which relates such quantities. Therefore, in order to obtain the value of the parameter C, it is necessary to choose one equivalent plastic strain and the corresponding yield stress. In general, choosing different couples of equivalent plastic strain and yield stress results in the calculation of different values of C. Since the LYS calibration strategy aims at achieving the best possible fit for the lower yield stresses, the parameter C is calculated by considering a null equivalent plastic strain and the correspondent yield stress, i.e. the lower yield stress. This strategy allows to model the strain rate effects coherently at first yield but then its modeling may not be coherent with the experimental results when the equivalent plastic strain increases. It is worthwhile to note that this approach does not need to carry-out an inverse analysis to purify the hardening function, because the only couple of yield stress and equivalent plastic strain values considered are those at the lower yield stress, for which possible structural effects can be considered as irrelevant.

The procedure above allows for the determination of the value of the parameter C for a given tested equivalent plastic strain rate. The same procedure must be followed for the other tested equivalent plastic strain rates, by considering the corresponding hardening functions. These tests are intended again as carried-out at the reference value of the temperature, thus allowing to use Eq. (38) for determining the parameter C, with the same procedure proposed above. Clearly, the more tests at different equivalent plastic strain rates can be conducted the better for the aim of determining the material behavior. Such data allow to better understand the trend of the yield stress on the equivalent plastic strain rate. If the material respects the natural logarithmic dependence of the yield stress on the dimensionless equivalent plastic strain rate, as assumed in the Johnson-Cook model, the same value of C must be recovered for all the available experimental data that cover the various tested equivalent plastic strain rates. This may not be the case, as previously mentioned. In this case, the value of C is taken as an average value of all the available values. As a result, the calibration of the parameter C for the LYS strategy may be inevitably flawed due to such aspect, that derives directly from the nature of the Johnson-Cook model. It may also be interesting to check if some of the modifications of the strain rate term proposed in the literature and previously reviewed may be more suitable for the description of the considered material.

The last step of the calibration procedure concerns the determination of the temperature parameter, i.e. the parameter m. This step involves experimental tests conducted at the reference equivalent plastic strain rate and at temperatures different from the reference temperature, from the lowest one tested up to the highest one. These data are always to be intended as a hardening function relating the yield stress to the equivalent plastic strain. The value of the parameter m can be obtained by noting that the strain rate term of the Johnson-Cook strength model becomes equal to 1 and thus vanishes, since the tests are carried-out at the reference equivalent plastic strain rate. Being the parameters A, B and n known, the only unknown remaining parameter is m, and it can be calculated through the hardening function by using the following equation

$$m = \frac{\ln\left(1 - \frac{\bar{s}}{A + B \cdot \bar{\varepsilon}_p^n}\right)}{\ln\left(\frac{T - T_0}{T_m - T_0}\right)}. \tag{39}$$

At this point, the situation is similar to the one that arises for the calculation of the parameter C. In order to calculate the value of the parameter m, the values of the temperature, the yield stress and the equivalent plastic strain need to be introduced in Eq. (39). By considering the experimental results at one determined temperature, the remaining unknown values are the yield stress and the equivalent plastic strain. Again, the yield stress is determined when an equivalent plastic strain value is chosen, thank to the experimental hardening curve under analysis. Therefore, in order to obtain the value of m, it is necessary to choose one equivalent plastic strain and the correspondent yield stress. In general, choosing different values of equivalent plastic strain results in calculating different values of m, similarly to what happened for the determination of the parameter C. Since the LYS calibration strategy aims at achieving the best possible fit for the lower yield stresses, the parameter m is calculated by introducing a null equivalent plastic strain and the corresponding yield stress, i.e. the lower yield stress. Considerations similar to those stated for the determination of the parameter C hold true.

The procedure above allows for determining the value of the parameter m for a given tested temperature. The same procedure must be followed for the other tested temperatures, by considering the corresponding hardening functions. These tests are intended again as carried-out at the reference value for the equivalent plastic strain rate, thus allowing to use Eq. (39) to determine the parameter m with the same procedure proposed above. Clearly, the more tests at different temperatures can be conducted, the better for the aim of determining the material

behavior. Such data allow to better understand the trend of the yield stress on the temperature. If the material respects the power dependence of the yield stress on the homologous temperature, as assumed in the Johnson-Cook model, the same value of m must be recovered for all the available experimental data that cover the various temperatures tested. This may not be the case, as previously mentioned. In this case, the value of m is taken as an average value of all the available values. Considerations similar to those stated for the determination of the parameters C hold true.

It is worthwhile to point-out some considerations about the procedure stated above. Following the LYS calibrations strategy, the experimental data necessary for the determination of the Johnson-Cook parameters can be resumed with the following list.

- One test conducted at the reference temperature and at the reference equivalent spatial plastic strain rate. These data allow to determine the reference equivalent plastic strain rate and temperature and the quasi-static parameters A, B and n.

- A series of tests conducted at the reference temperature and at equivalent plastic strain rates different from the reference equivalent plastic strain, from the lowest one tested up to the highest one. As instance, these tests can be carried-out with a Hopkinson bar. These data allow to determine the parameter C. Clearly, the more hardening functions can be obtained, the better, in order to cover the considered equivalent plastic strain rate range with a good resolution.

- A series of tests conducted at the reference equivalent plastic strain rate but at different temperatures, from the lowest tested up to the highest one. As instance, these tests can be conducted with a tensile test machine endowed with an oven or a furnace capable to heat the specimen and keep it at a constant temperature: Device capable to cool down the specimen may be adopted for testing at low temperatures. These data allow to determine the parameter m. Clearly, the more hardening functions can be obtained, the better, in order to cover the considered temperature range with a good resolution.

In the following, the LYS calibration strategy is applied to the nine experimental hardening functions extracted from Nemat-Nasser and Guo, 2003.

The reference equivalent plastic strain rate is chosen as the lowest equivalent plastic strain rate tested, i.e. 0.001 s^{-1}. The reference temperature is chosen as the lowest temperature tested, i.e. 77 K. By evaluating the experimental hardening function at these reference values, the quasi-static parameters are obtained,

through a fitting carried-out with Wolfram Mathematica 7. The obtained parameters A, B and n are equal to 915.555 MPa, 760.782 MPa and 0.60101, respectively.

Regarding the parameter C, it is obtained by introducing a null equivalent plastic strain in Eq. (38), thus obtaining the following form

$$C = \frac{\frac{\bar{s}}{A} - 1}{\ln \frac{\dot{\bar{\varepsilon}}_p}{\dot{\bar{\varepsilon}}_p^0}}. \tag{40}$$

The parameter C can be calculated with the two equivalent plastic strain rates different from the reference equivalent plastic strain rate, i.e. 0.1 s^{-1} and 3000 s^{-1}, at the reference temperature of 77 K. The computed values are equal to 0.01399 and 0.01720, for the equivalent plastic strain rates of 0.1 s^{-1} and 3000 s^{-1}, respectively. The fact of having obtained different values for the parameter C reveals that the material does not strictly respect the natural logarithm dependence of the lower yield stress on the dimensionless equivalent plastic strain rate. Following the procedure described above, the parameter C is set equal to their average value, namely 0.01560.

Regarding the parameter m, it is determined by introducing a null equivalent plastic strain in Eq. (39), thus obtaining the following form

$$m = \frac{\ln\left(1 - \frac{\bar{s}}{A}\right)}{\ln\left(\frac{T - T_0}{T_m - T_0}\right)}. \tag{41}$$

The parameter m can be calculated with the two temperatures different from the reference temperature, i.e. 296 K and 800 K, at the reference equivalent plastic strain rate of 0.001 s^{-1}. The computed values are equal to 0.18022 and 0.27336, for the temperatures of 296 K and 800 K, respectively. The fact of having obtained different values for the parameter m reveals that the material does not strictly respect the power dependence of the lower yield stress on the homologous temperature. Following the procedure described above, the parameter m is set equal to their average value, namely 0.22679.

The 8 Johnson-Cook parameters obtained through the LYS calibration strategy are summarized in following Table 3.

A	915.555 MPa	m	0.22679
B	760.782 MPa	$\dot{\bar{\varepsilon}}_0$	0.001 s^{-1}
n	0.60101	T_0	77 K
C	0.01560	T_m	1773 K

Table 3
Johnson-Cook parameters for the DH-36 structural steel calculated through the LYS calibration strategy.

Following Figs. 6 to 8 show the hardening functions predicted by the Johnson-Cook model calibrated with the LYS strategy. As expected, the curves of the model follow in the best possible way the first yield of the experimental hardening curves. However, this target is partially hindered by the fact that the material does not strictly respect the natural logarithm dependence of the lower yield stress on the dimensionless equivalent plastic strain rate and the power dependence on the homologous temperature. The fact of having chosen an average value of C and m implies that the predictions of the models lie in between the two cases.

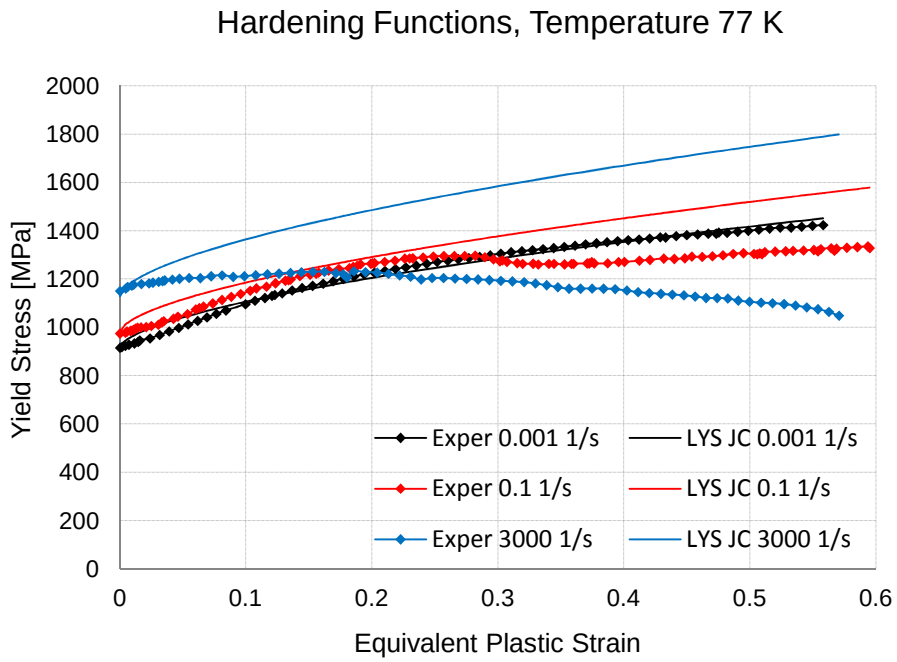

Figure 6. LYS calibrated Johnson-Cook fitting to DH-36 structural steel data at temperature of 77 K and at three different equivalent plastic strain rates.

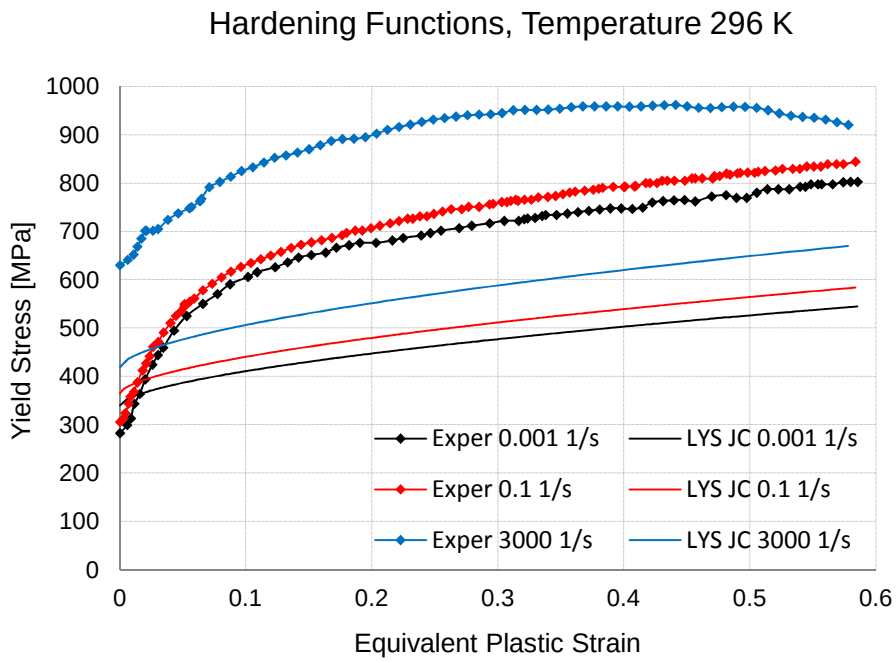

Figure 7. LYS calibrated Johnson-Cook fitting to DH-36 structural steel data at temperature of 296 K and at three different equivalent plastic strain rates.

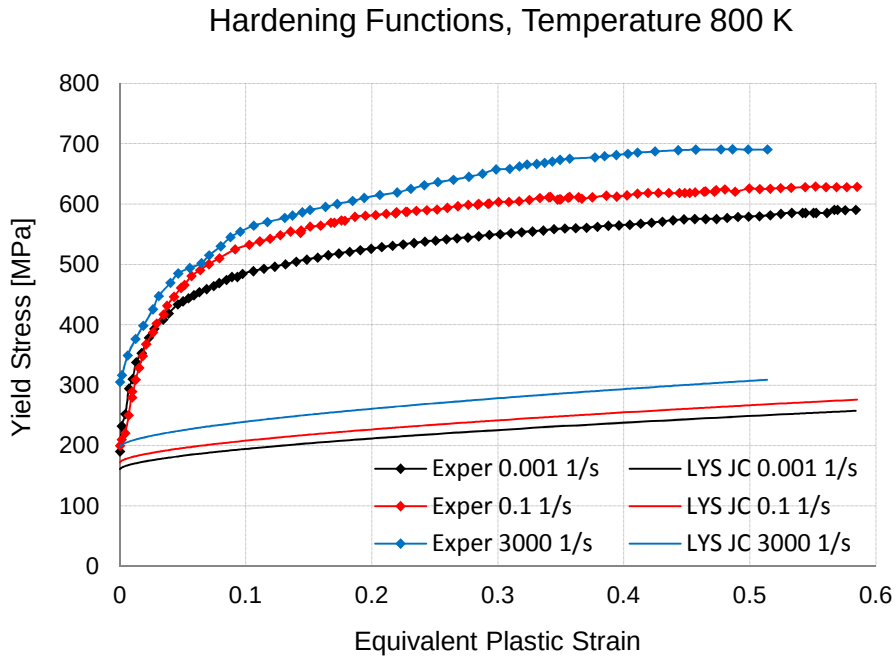

Figure 8. LYS calibrated Johnson-Cook fitting to DH-36 structural steel data at temperature of 800 K and at three different equivalent plastic strain rates.

Following Figs. 9 to 11 show the same results but this time the yield stress is visualized as a two-dimensional function of the equivalent plastic strain and the base 10 logarithm of the equivalent plastic strain rate, allowing to better understand the predictions of the model. Experimental data are reported with black dots whilst the predictions of the Johnson-Cook model are represented by red surfaces.

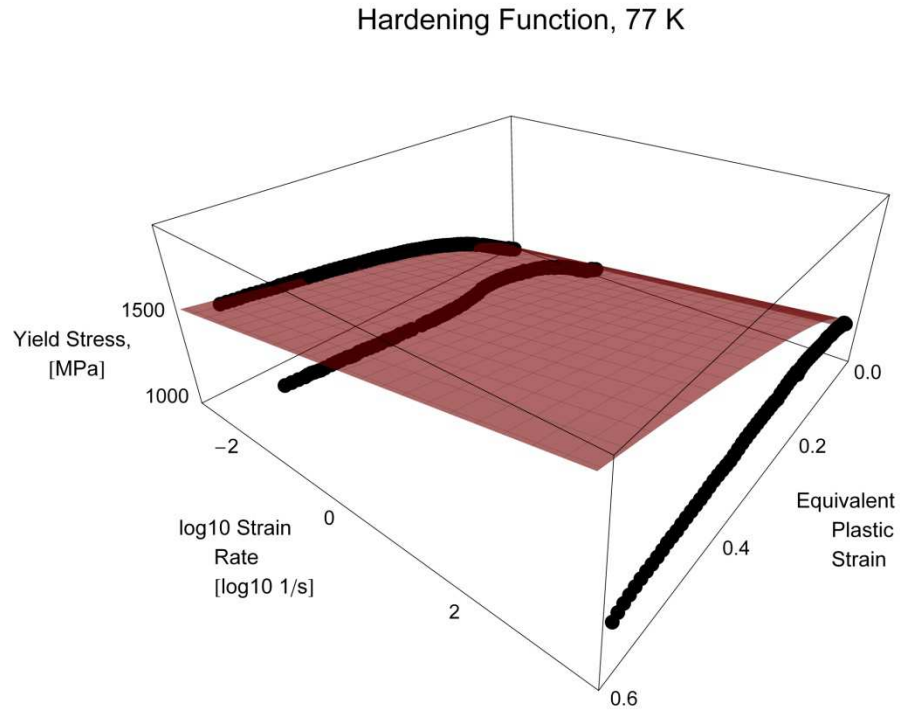

Figure 9. LYS calibrated JC model fitting to DH-36 steel data at temperature of 77 K.

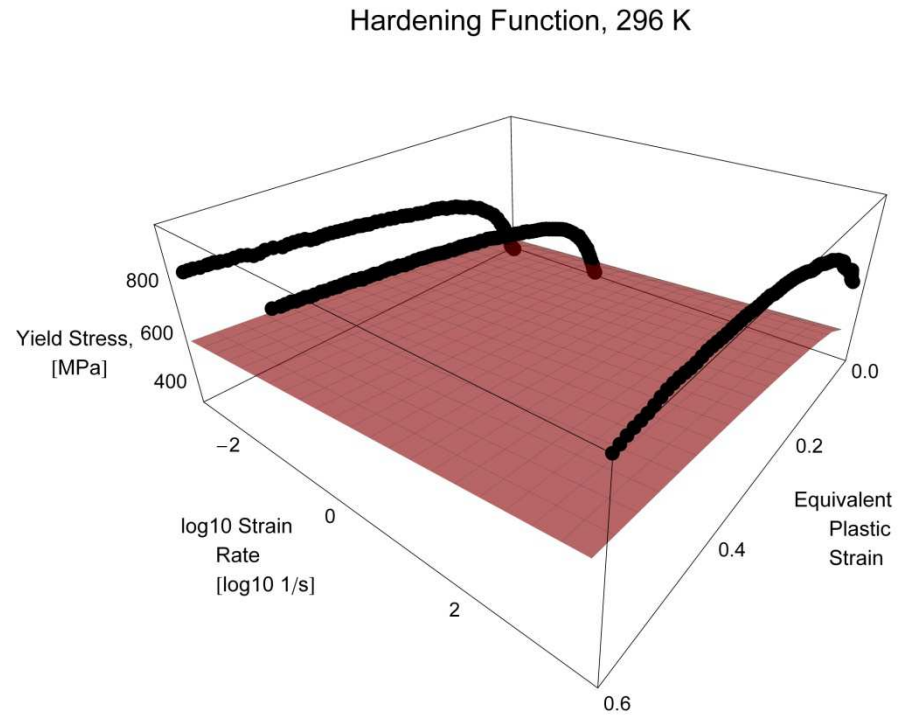

Figure 10. LYS calibrated JC model fitting to DH-36 steel data at temperature of 296 K.

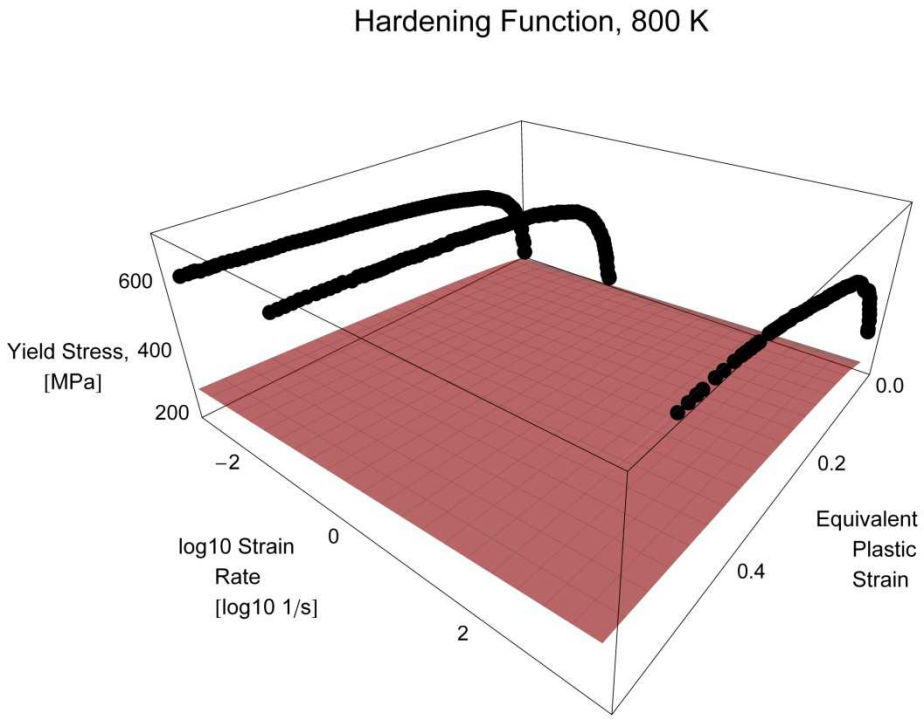

Figure 11. LYS calibrated JC model fitting to DH-36 steel data at temperature of 800 K.

As shown in Figs. 6 to 11, the fit to the lower yield stresses is very good for the hardening functions in which at least one reference condition is present, i.e. an equivalent plastic strain rate of 0.001 s^{-1} or a temperature of 77 K. On the other hand, when the model fits the four hardening functions that do not refer to at least one reference condition, i.e. 0.1 s^{-1} and 296 K, 3000 s^{-1} and 296 K, 0.1 s^{-1} and 800 K, and 3000 s^{-1} and 800 K, large errors may be introduced, as clearly visible in the plots. This fact is due to having calculated the parameters C and m by considering only experimental data at the reference temperature and at the reference equivalent plastic strain rate, respectively. As a matter of fact, the four hardening functions that do not refer to at least one reference condition are never used when the LYS calibration strategy is adopted. Following Table 4 reports a comparison between the LYS calibrated Johnson-Cook model predictions of the lower yield stresses and their experimental counterparts.

	Experimental Values	**LYS JC Values**
0.001 s^{-1}, 77 K	915.555 MPa	915.555 MPa
0.1 s^{-1}, 77 K	974.565 MPa	981.323 MPa
3000 s^{-1}, 77 K	1150.46 MPa	1128.545 MPa
0.001 s^{-1}, 296 K	282.455 MPa	340.015 MPa
0.1 s^{-1}, 296 K	305.455 MPa	364.439 MPa
3000 s^{-1}, 296 K	630.137 MPa	419.115 MPa
0.001 s^{-1}, 800 K	190.345 MPa	160.967 MPa
0.1 s^{-1}, 800 K	200.213 MPa	172.533 MPa
3000 s^{-1}, 800 K	305.345 MPa	198.417 MPa

Table 4
Comparison between experimental lower yield stresses and corresponding predicted lower yield stresses from the Johnson-Cook model calibrated with the LYS strategy.

Usually, when the LYS calibration strategy is adopted, predictions of the calibrated Johnson-Cook model are assessed only by comparing to hardening functions which refer to at least one reference condition. Indeed, often these hardening functions are the only ones that are experimentally investigated. It is clear that this kind of check may give good results, as readable in Figs. 6 to 11. However, the model should be checked even against hardening functions that do not refer to at least one reference condition, since large errors may be introduced. The relevance of this aspect should not be underestimated, as large modeling errors may be involved.

As a last observation, Figs. 6 to 11 clearly show how the requirement to best fit the first yield implies errors, sometimes of conspicuous magnitude, when the equivalent plastic strain increases. Such errors are obviously minimized for the

hardening function at the reference conditions, i.e. 0.001 s^{-1} and 77 K. The parameters A, B and n are indeed calibrated through a nonlinear regression to best fit this hardening function. On the other hand, when it comes to the fitting of other hardening functions, heavy modeling errors are introduced.

In order to better assess the errors of the LYS calibrated Johnson-Cook model throughout the considered equivalent plastic strain ranges, it is possible to calculate the yield stress Root Mean Square (RMS) error, denoted here by $\bar{s}_{err}$, for each of the nine hardening function predictions, through the following relation

$$\bar{s}_{err} = \sqrt{\frac{\sum_{i=1}^{n}\left(\bar{s}_i^{JC} - \bar{s}_i^{EXP}\right)^2}{n}}, \tag{42}$$

where $\bar{s}_i^{JC}$ and $\bar{s}_i^{EXP}$ represent the i-th Johnson-Cook yield stress prediction and the correspondent i-th experimental yield stress measurements, respectively. Of course, the i-th Johnson-Cook yield stress prediction is calculated by using the same equivalent plastic strain to which the i-th experimental yield stress refers to.

The errors of the LYS calibrated Johnson-Cook model throughout the equivalent plastic strain ranges considered can be further evaluated by introducing the percentage yield stress RMS error, denoted here by $\bar{s}_{\%err}$, for each of the nine hardening functions predictions, through the following relation

$$\bar{s}_{\%err} = \sqrt{\frac{\sum_{i=1}^{n}\left(100 \cdot \frac{\bar{s}_i^{JC} - \bar{s}_i^{EXP}}{\bar{s}_i^{EXP}}\right)^2}{n}}. \tag{43}$$

Following Table 5 reports both the yield stress and the percentage yield stress RMS errors for each one of the nine considered hardening functions, together with their algebraic mean value, i.e. their sum divided by nine. Heavy errors are introduced.

	$\bar{s}_{err}$	$\bar{s}_{\%err}$
0.001 s^{-1}, 77 K	19.5893 MPa	1.784%
0.1 s^{-1}, 77 K	136.732 MPa	10.63%
3000 s^{-1}, 77 K	404.147 MPa	35.74%
0.001 s^{-1}, 296 K	221.587 MPa	30.92%
0.1 s^{-1}, 296 K	221.711 MPa	29.56%
3000 s^{-1}, 296 K	315.801 MPa	35.85%
0.001 s^{-1}, 800 K	299.824 MPa	57.02%
0.1 s^{-1}, 800 K	327.546 MPa	56.91%
3000 s^{-1}, 800 K	337.807 MPa	55.24%
Average	*253.860 MPa*	*34.85%*

Table 5
Yield stress (central column) and percentage yield stress (right column) root mean square errors for the LYS calibrated Johnson-Cook model yield stress predictions.

2.2.1.1.2. OPTLYS Calibration Strategy

The OPTLYS (OPTimized Lower Yield Stress) calibration strategy aims at improving the LYS calibration strategy by optimizing the value of the parameters C and m. In order to achieve this target, this strategy introduces in the calibration procedure the experimental data relative to the hardening functions which do not refer to at least one reference condition, by trying to obtain values of the parameters C and m capable to provide the actual best fit for all the made available hardening functions.

For what it concerns the calibration of the melting temperature, the reference equivalent plastic strain rate, the reference temperature and the quasi-static parameters A, B and n, the procedure is exactly the same as that exposed for the LYS calibration strategy. Differences arise for the determination of the parameters C and m. In order to introduce all the lower yield stress data provided by all the available hardening functions, the Johnson-Cook strength model, Eq. (28), is recalled a number of times equal to the number of available hardening functions which do not refer to reference conditions for both the equivalent plastic strain rate and the temperature, i.e. all the available hardening functions except for the one which refers to both reference equivalent plastic strain rate and reference temperature. This approach leads to the construction of an overdetermined system of nonlinear equations, in which the unknowns are the parameters C and m and the number of equations is equal to the number of available hardening functions which do not refer to reference conditions for both the equivalent plastic strain rate and the temperature. Such system is reported in the following. Of course, the equivalent plastic strain is always set to zero, in order to reach the aims of the OPTLYS

calibration strategy, and thus only the lower yield stress is considered, resulting in the following equation

$$\bar{s}_i = A \cdot \left(1 + C \cdot \ln \frac{\dot{\bar{\varepsilon}}_{p_i}}{\dot{\bar{\varepsilon}}_p^0} \right) \cdot \left(1 - \left(\frac{T_i - T_0}{T_m - T_0} \right)^m \right). \tag{44}$$

In this equation, the subscript i refers to the values relative to the i-th hardening function. A system of this kind can be solved through a nonlinear least square method. The solution values for the parameters C and m are those characterized by being capable to minimize the square errors of the Johnson-Cook model predictions against experimental data at the lower yield stresses. A good strategy here is that of adopting a numerical tool capable to handle such problems.

It is worthwhile to point-out some considerations about the procedure stated above. Following the OPTLYS calibration strategy, the experimental data necessary for the determination of the Johnson-Cook parameters can be resumed with the following list.

- One test conducted at the reference temperature and at the reference equivalent plastic strain rate. These data allow to determine the reference equivalent plastic strain rate and temperature and the quasi-static parameters A, B and n.

- A series of tests conducted in such a way that at least one between the equivalent plastic strain and the temperature are different from their reference values. These data allow to simultaneously determine the parameters C and m. It is worthwhile to note that the OPTLYS calibration strategy does not compulsorily imply to carry-out separate tests at the reference temperature but at different equivalent plastic strain rates and then at the reference equivalent plastic strain rate but at different temperatures. Rather, any hardening function which does not refer to reference conditions for both the equivalent plastic strain rate and the temperature is actually useful for the determination of the parameters C and m. As previously stated for the LYS calibration strategy, a coherent approach would be that of testing the material throughout the equivalent plastic strain rate and temperature ranges of interest. As instance, tests at different equivalent plastic strain rates and temperatures can be carried-out with a Hopkinson bar endowed with an oven or a furnace capable to heat the specimen, or with a system able to cool it down if low temperatures need to be tested. Clearly, the more hardening functions can be obtained, the

better, in order to cover the considered equivalent plastic strain rate and temperature ranges with a good resolution.

In the following, the OPTLYS calibration strategy is applied to the nine experimental hardening functions extracted from Nemat-Nasser and Guo, 2003.

All the parameters are equal to the ones evaluated for the LYS calibration strategy, except for the parameters C and m, which are evaluated by solving the following overdetermined system of 8 nonlinear equations and 2 unknowns, i.e. the parameters C and m

$$
\begin{aligned}
282.455 &= 915.555 \cdot \left(1 - \left(\frac{296-77}{1773-77} \right)^{m} \right) \\
190.345 &= 915.555 \cdot \left(1 - \left(\frac{800-77}{1773-77} \right)^{m} \right) \\
974.565 &= 915.555 \cdot \left(1 + C \cdot \ln \frac{0.1}{0.001} \right) \\
305.455 &= 915.555 \cdot \left(1 + C \cdot \ln \frac{0.1}{0.001} \right) \cdot \left(1 - \left(\frac{296-77}{1773-77} \right)^{m} \right) \\
200.213 &= 915.555 \cdot \left(1 + C \cdot \ln \frac{0.1}{0.001} \right) \cdot \left(1 - \left(\frac{800-77}{1773-77} \right)^{m} \right) \\
1150.455 &= 915.555 \cdot \left(1 + C \cdot \ln \frac{3000}{0.001} \right) \\
630.137 &= 915.555 \cdot \left(1 + C \cdot \ln \frac{3000}{0.001} \right) \cdot \left(1 - \left(\frac{296-77}{1773-77} \right)^{m} \right) \\
305.345 &= 915.555 \cdot \left(1 + C \cdot \ln \frac{3000}{0.001} \right) \cdot \left(1 - \left(\frac{800-77}{1773-77} \right)^{m} \right).
\end{aligned}
\tag{45}
$$

This overdetermined system of nonlinear equations has been solved with a nonlinear least squares trust-region-reflective algorithm with MathWorks MatLab 2010b. A tolerance of 10^{-8} was set. This means that when the iterative solution provided by the algorithm changes of a value lower then 10^{-8} from one iteration step to the next, the algorithm is stopped and these values are taken as the final solution. The obtained values for the parameters C and m simultaneously minimize the square errors for the eight nonlinear equations of the system, through a multi-objective nonlinear optimization. Details on this algorithm can be found, e.g.,

in Coleman and Li, 1994. These optimized values are equal to 0.02049 and 0.26367 for the parameters C and m, respectively.

The 8 Johnson-Cook parameters obtained through the OPTLYS calibration strategy are summarized in following Table 6.

A	915.555 MPa	M	0.26367
B	760.782 MPa	$\dot{\bar{\varepsilon}}_0$	0.001 s^{-1}
N	0.60101	T_0	77 K
C	0.02049	T_m	1773 K

Table 6
Johnson-Cook parameters for the DH-36 structural steel calculated through the OPTLYS calibration strategy.

Following Figs. 12 to 14 show the hardening functions predicted by the Johnson-Cook model calibrated with the OPTLYS strategy.

The curves of the OPTLYS calibrated Johnson-Cook model follow in the best possible way the lower yield stresses of the experimental hardening curves, this time by considering not only the hardening functions which have at least one between the equivalent plastic strain and the temperature equal to the reference value, but all the nine hardening functions. As previously said, this target is partially hindered by the fact that the material does not strictly respect the natural logarithm dependence of the lower yield stress on the dimensionless equivalent plastic strain rate and the power dependence on the homologous temperature.

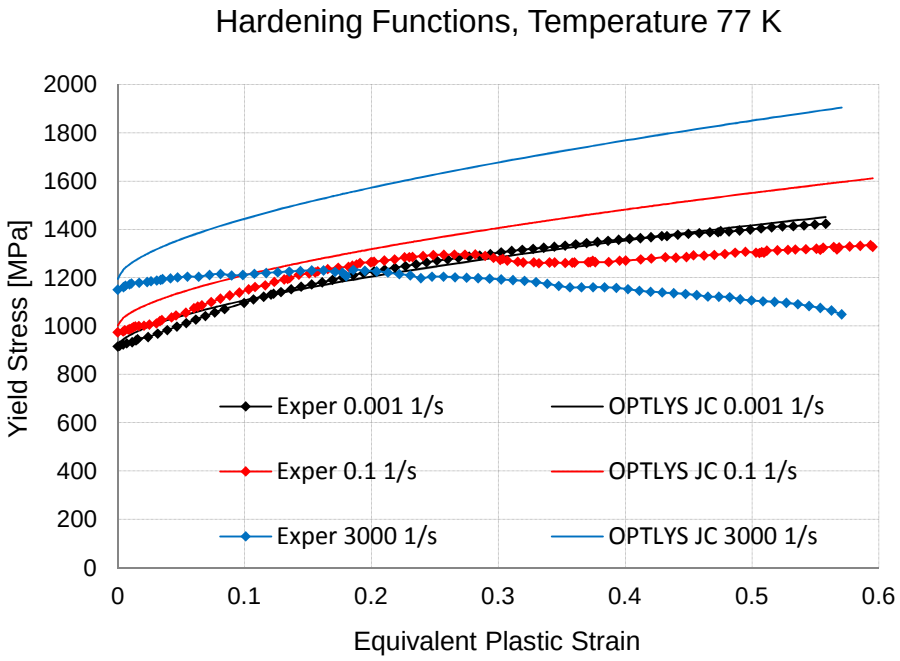

Figure 12. OPTLYS calibrated Johnson-Cook fitting to DH-36 structural steel data at temperature of 77 K and at three different equivalent plastic strain rates.

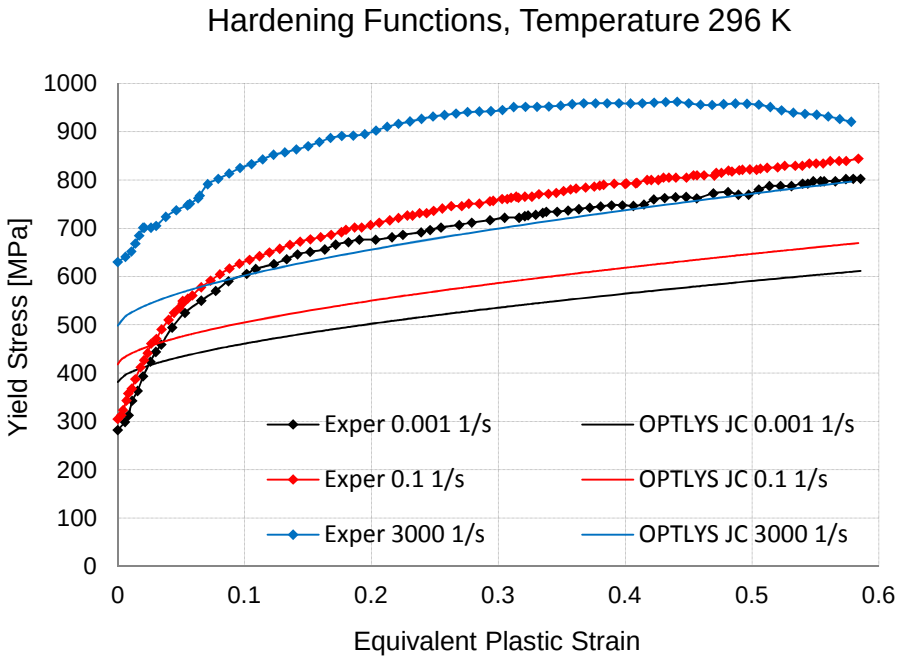

Figure 13. OPTLYS calibrated Johnson-Cook fitting to DH-36 structural steel data at temperature of 296 K and at three different equivalent plastic strain rates.

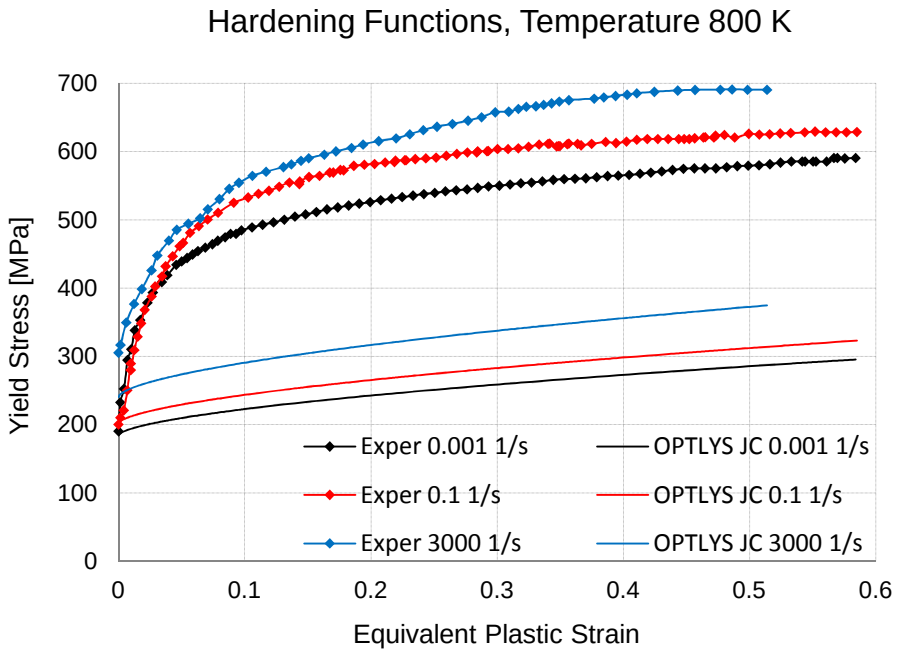

Figure 14. OPTLYS calibrated Johnson-Cook fitting to DH-36 structural steel data at temperature of 800 K and at three different equivalent plastic strain rates.

Following Figs. 15 to 17 further show the OPTLYS results by surface plots.

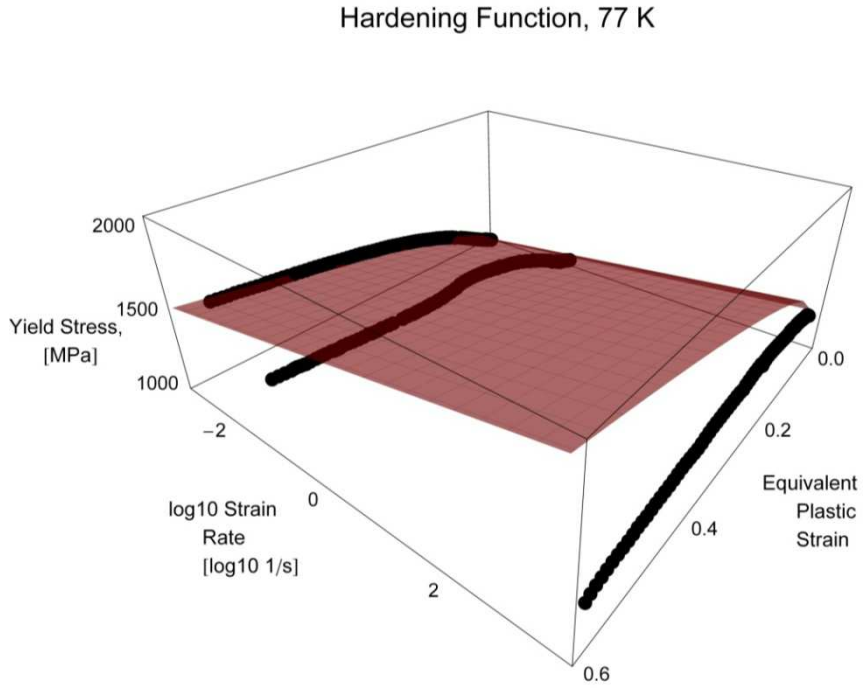

Figure 15. OPTLYS calibrated JC model fitting to DH-36 steel data at temperature of 77 K.

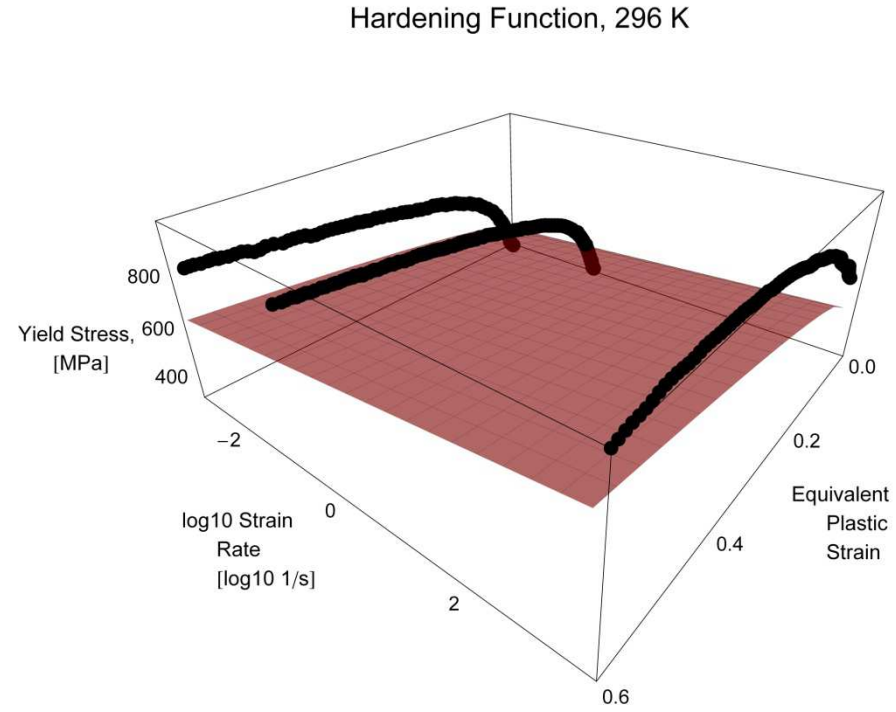

Figure 16. OPTLYS calibrated JC model fitting to DH-36 steel data at temperature of 296 K.

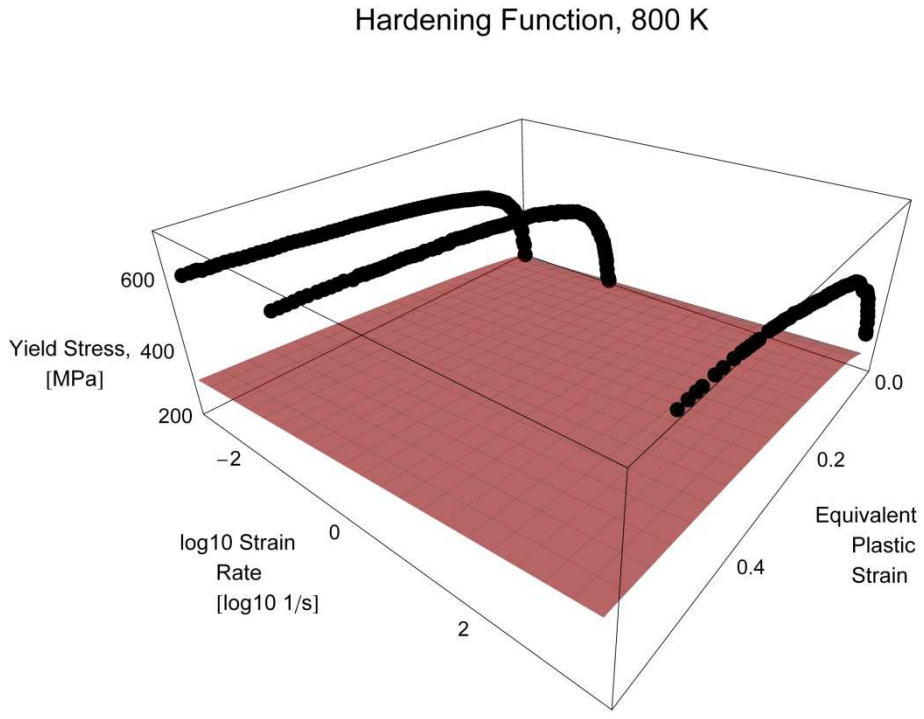

Figure 17. OPTLYS calibrated JC model fitting to DH-36 steel data at temperature of 800 K.

As displayed in Figs. 12 to 17, the fit to the lower yield stresses is now the result of a compromise between all the nine hardening functions. This point implies the fact that the fit with the hardening functions in which at least one reference conditions is present is less coherent than the one obtainable from the predictions of the LYS calibrated Johnson-Cook model. On the other hand, when the model fits the four hardening functions that do not refer to at least one reference condition, the errors are lower. Clearly, this is a consequence of having calculated the parameters C and m by considering experimental data from all the nine hardening functions. Following Table 7 reports a comparison between the OPTLYS calibrated Johnson-Cook model predictions of the lower yield stresses and their experimental counterparts.

	Experimental Values	**OPTLYS JC Values**
0.001 s^{-1}, 77 K	915.555 MPa	915.555 MPa
0.1 s^{-1}, 77 K	974.565 MPa	1001.95 MPa
3000 s^{-1}, 77 K	1150.46 MPa	1195.34 MPa
0.001 s^{-1}, 296 K	282.455 MPa	381.868 MPa
0.1 s^{-1}, 296 K	305.455 MPa	417.901 MPa
3000 s^{-1}, 296 K	630.137 MPa	498.563 MPa
0.001 s^{-1}, 800 K	190.345 MPa	184.331 MPa
0.1 s^{-1}, 800 K	200.213 MPa	201.724 MPa
3000 s^{-1}, 800 K	305.345 MPa	240.660 MPa

Table 7
Comparison between experimental lower yield stresses and correspondent predicted lower yield stresses from the Johnson-Cook model calibrated with the OPTLYS strategy.

Of course, the problem of having errors when the equivalent plastic strain increases is still present, since it is a consequence of the basic assumption of both the LYS and the OPTLYS calibration strategies. Following Table 8 reports both the yield stress and the percentage yield stress root mean square errors for each of the nine considered hardening functions, together with their algebraic mean value, i.e. their sum divided by nine. Conspicuous errors are introduced.

	$\bar{s}_{err}$	$\bar{s}_{\%err}$
0.001 s^{-1}, 77 K	19.5893 MPa	1.784%
0.1 s^{-1}, 77 K	161.790 MPa	12.65%
3000 s^{-1}, 77 K	486.710 MPa	42.86%
0.001 s^{-1}, 296 K	166.723 MPa	23.91%
0.1 s^{-1}, 296 K	152.704 MPa	21.14%
3000 s^{-1}, 296 K	209.812 MPa	23.82%
0.001 s^{-1}, 800 K	268.377 MPa	50.91%
0.1 s^{-1}, 800 K	288.575 MPa	49.90%
3000 s^{-1}, 800 K	282.324 MPa	45.84%
Average	*226.289 MPa*	*30.31%*

Table 8
Yield stress (central column) and percentage yield stress (right column) root mean square errors for the OPTLYS calibrated Johnson-Cook model yield stress predictions.

2.2.1.1.3. EPS Calibration Strategy

The EPS (Equivalent Plastic Strain) calibration strategy aims at determining the set of material parameters capable to achieve the best fitting of experimental data throughout the equivalent plastic strain ranges involved in the available hardening functions.

For what it concerns the calibration of the melting temperature, the reference equivalent plastic strain rate, the reference temperature and the quasi-static parameters A, B and n, the procedure is still the same as that previously exposed for the LYS calibration strategy. Differences arise again for the determination of the parameters C and m. In order to achieve the best fitting throughout the equivalent plastic strain ranges involved in the available hardening functions, data at each value of equivalent plastic strain need to be considered for the calculation of the two parameters.

The first step is relative to the determination of the strain rate parameter, i.e. the parameter C. As for the LYS and OPTLYS calibration strategies, this step involves experimental tests conducted at the reference temperature and at equivalent plastic strain rates different from the reference equivalent plastic strain, from the lowest one tested up to the highest one. These data are always to be intended as a hardening function relating the yield stress to the equivalent plastic strain. The value of the parameter C can be obtained by noting that the temperature term of the Johnson-Cook strength model becomes 1 and thus vanishes, since the tests are carried-out at the reference temperature. Therefore, Eq. (38) is used again, although this time the equivalent plastic strain is not set equal to zero, but rather it is left as an unknown. At this point, the procedure is that of performing a regression

of the hardening function data at a given equivalent plastic strain rate, of course different from the reference equivalent plastic strain rate, by considering the Johnson-Cook form presented in Eq. (38), i.e. a regression in which the only parameter to be determined is C.

This strategy allows to model coherently the strain rate effects throughout the equivalent plastic strain range but then the prediction of the lower yield stress may be somehow incoherent. It is worthwhile to note that this approach does need to carry-out an inverse analysis to purify the experimental hardening function, because all data are actually used in the calibration procedure, and thus structural effects cannot be considered as irrelevant. Furthermore, the inverse analysis is helpful in order to clean the results from temperature effects due to the plastic work converted into heat during the testing of the specimens. This last aspect is particularly relevant when the material is tested at high strain rates.

The procedure above allows to determine the value of the parameter C for a given tested equivalent plastic strain rate. The same procedure must be followed for the other tested equivalent plastic strain rates, by considering the corresponding hardening functions. These tests are intended again as carried-out at the reference value for the temperature, thus allowing to use Eq. (38) to determine the parameter C with the same procedure proposed above. Clearly, the more tests at different equivalent plastic strain rates can be conducted, the better for the aim of determining the material behavior, similarly to what said for the other calibration strategies. Such data allow to better understand the trend of the yield stress on the equivalent plastic strain rate. At this point, the same issue previously outlined for the LYS and OPTLYS calibration strategies arises. If the material respects the natural logarithmic dependence of the yield stress on the dimensionless equivalent plastic strain rate, as assumed in the Johnson-Cook model, the same value of C must be recovered for all the available experimental data that cover the various tested equivalent plastic strain rates. If this aspect is not respected, the value of C is taken as an average value of all the available values. As a result, the calibration of the parameter C for the EPS strategy may be inevitably flawed due to such aspect, that derives directly from the nature of the Johnson-Cook model. It may also be interesting to check if some of the modifications of the strain rate term proposed in the literature and previously reviewed may be more suitable for the description of the considered material.

The last step of the calibration procedure concerns the determination of the temperature parameter, i.e. the parameter m. As for the LYS and OPTLYS calibration strategies, this step involves experimental tests conducted at the reference equivalent plastic strain rates and at temperatures different from the reference temperature, from the lowest one tested up to the highest one. These data are always to be intended as a hardening function relating the yield stress to

the equivalent plastic strain. The value of the parameter m can be obtained by noting that the strain rate term of the Johnson-Cook strength model becomes equal to 1 and thus vanishes, since the tests are carried-out at the reference equivalent plastic strain rate. Hence, Eq. (39) is used again, although this time the equivalent plastic strain is not set to zero, but rather it is left as an unknown. At this point, the procedure is that of performing a regression of the hardening function data at a given temperature, of course different from the reference temperature, by considering the Johnson-Cook form presented in Eq. (39), i.e. a regression in which the only parameter to be determined is m.

As said for the strain rate effects, this strategy allows to model coherently the temperature effects throughout the equivalent plastic strain range but then the prediction of the lower yield stress may be somehow incoherent. The same considerations previously stated about the necessity to carry-out an inverse analysis of the experimental data hold true.

The procedure above allows for determining the value of the parameter m for a given tested temperature. The same procedure must be followed for the other tested temperatures, by considering the corresponding hardening functions. These tests are intended again as carried-out at the reference value for the equivalent plastic strain rate, thus allowing to use Eq. (39) to determine the parameter m with the same procedure proposed above. Clearly, the more tests at different temperatures can be conducted, the better for the aim of determining the material behavior, similarly to what said for the other calibration strategies. Such data allow to better understand the trend of the yield stress on the equivalent plastic strain rate. Once again, the same issue previously seen for the LYS and OPTLYS calibration strategies arises. If the material respects the power dependence of the yield stress on the homologous temperature, as assumed in the Johnson-Cook model, the same value of m must be recovered for all the available experimental data that cover the various tested temperatures. If this aspect is not respected, the value of m is taken as an average value of all the available values. Considerations similar to those stated for the determination of the parameters C hold true.

Regarding the experimental data necessary in order to carry-out the EPS calibration strategy, these are exactly the same required for the LYS calibration strategy. In the following, the EPS calibration strategy is applied to the nine experimental hardening functions extracted from Nemat-Nasser and Guo, 2003.

All the parameters are equal to the ones evaluated for the LYS calibration strategy, except for the parameters C and m, which are obtained by carrying-out a regression of the experimental data through Eq. (38). The parameter C can be calculated with the hardening functions that refer to the two equivalent plastic strain rates differing from the reference equivalent plastic strain rate, i.e. 0.1 s^{-1} and 3000 s^{-1}, at the reference temperature of 77 K. Wolfram Mathematica 7 has been

used to achieve such task. The computed values are equal to -0.00479 and -0.00407, for the equivalent plastic strain rates of 0.1 s^{-1} and 3000 s^{-1}, respectively. The two obtained values are quite similar, proving that the material somehow respects the natural logarithm dependence of the plastic flow on the dimensionless equivalent plastic strain rate. Following the procedure described above, the parameter C is set equal to the average value, namely -0.00443.

Regarding the parameter m, it is obtained by carrying-out a regression of the experimental data through Eq. (39). The parameter m can be calculated with the hardening functions that refer to the two temperatures differing from the reference temperature, i.e. 296 K and 800 K, at the reference equivalent plastic strain rate of 0.001 s^{-1}. Wolfram Mathematica 7 has been used again. The computed values are equal to 0.37849 and 0.62806, for the temperatures of 296 K and 800 K, respectively. The fact of having obtained quite different values for the two computed parameters m reveals that the material does not strictly respect the power dependence of the yield stress on the homologous temperature. Following the procedure described above, the parameter m is set equal to the average value, namely 0.50328.

The eight Johnson-Cook parameters obtained through the EPS calibration strategy are summarized in following Table 9.

A	915.555 MPa	m	0.50328
B	760.782 MPa	$\dot{\bar{\varepsilon}}_0$	0.001 s^{-1}
N	0.60101	T_0	77 K
C	-0.00443	T_m	1773 K

Table 9
Johnson-Cook parameters for the DH-36 structural steel calculated through the EPS calibration strategy.

Following Figs. 18 to 20 show the hardening functions predicted by the Johnson-Cook model calibrated with the EPS strategy. As expected, the curves of the model follow in the best possible way the experimental hardening curves throughout the equivalent plastic strain ranges. However, this target is partially hindered by the fact that the material does not strictly respect the natural logarithm dependence of the yield stress on the dimensionless equivalent plastic strain rate and the power dependence on the homologous temperature. The fact of having chosen an average value of C and m implies that the predictions of the model lie in between the two cases.

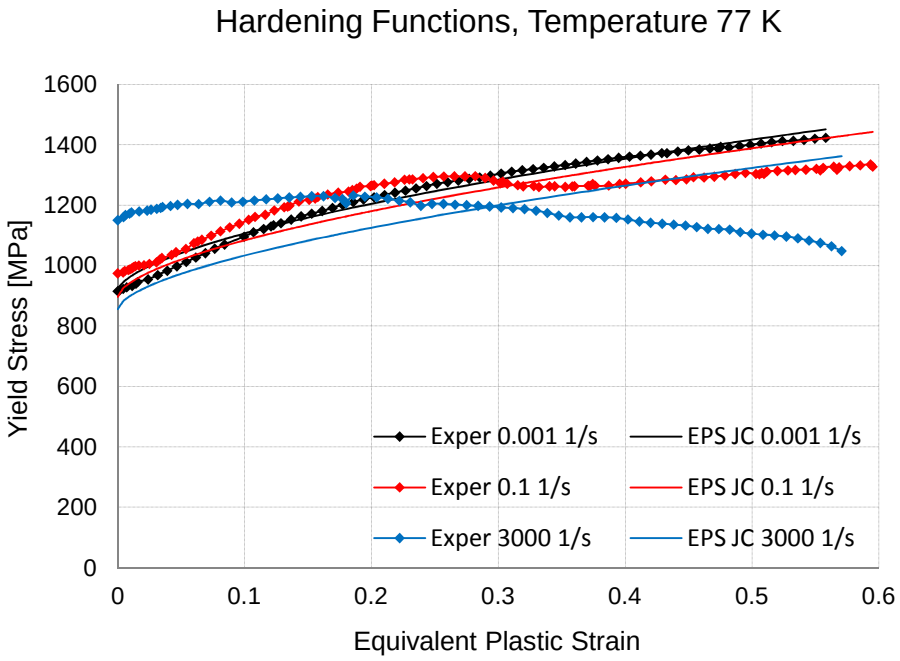

Figure 18. EPS calibrated Johnson-Cook fitting to DH-36 structural steel data at temperature of 77 K and at three different equivalent plastic strain rates.

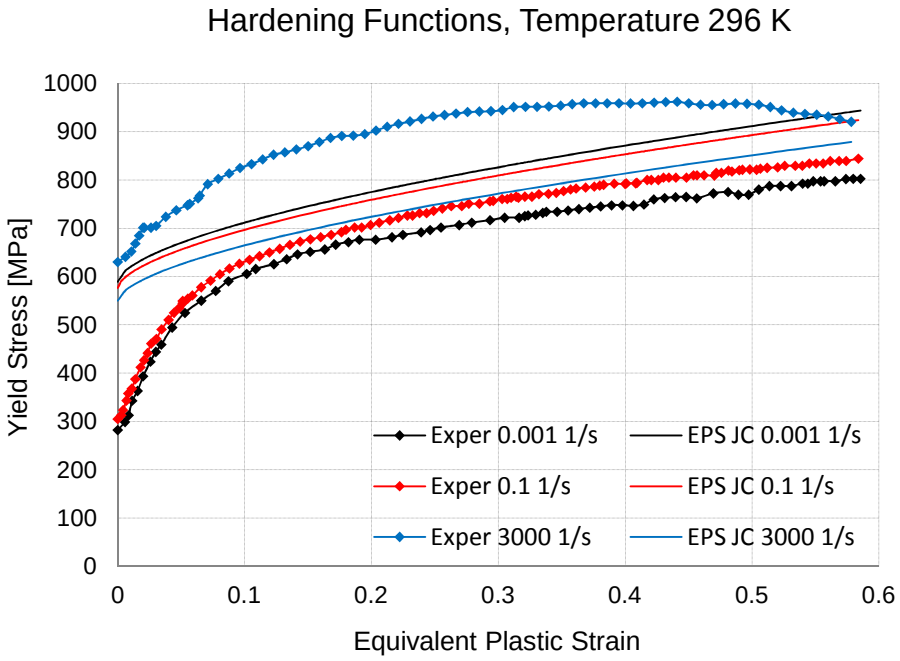

Figure 19. EPS calibrated Johnson-Cook fitting to DH-36 structural steel data at temperature of 296 K and at three different equivalent plastic strain rates.

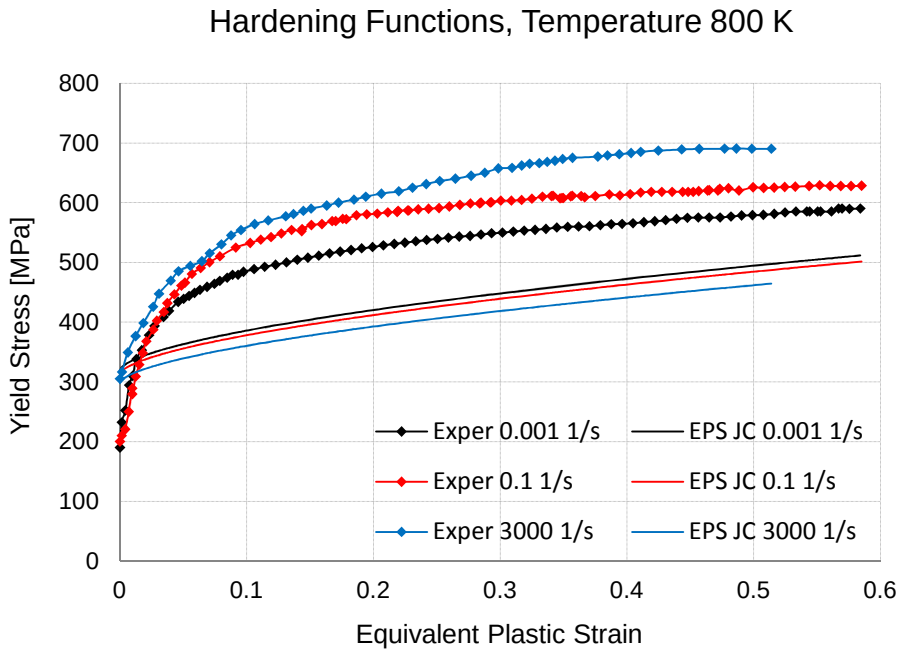

Figure 20. EPS calibrated Johnson-Cook fitting to DH-36 structural steel data at temperature of 800 K and at three different equivalent plastic strain rates.

Following Figs. 21 to 23 further show the EPS results by surface plots.

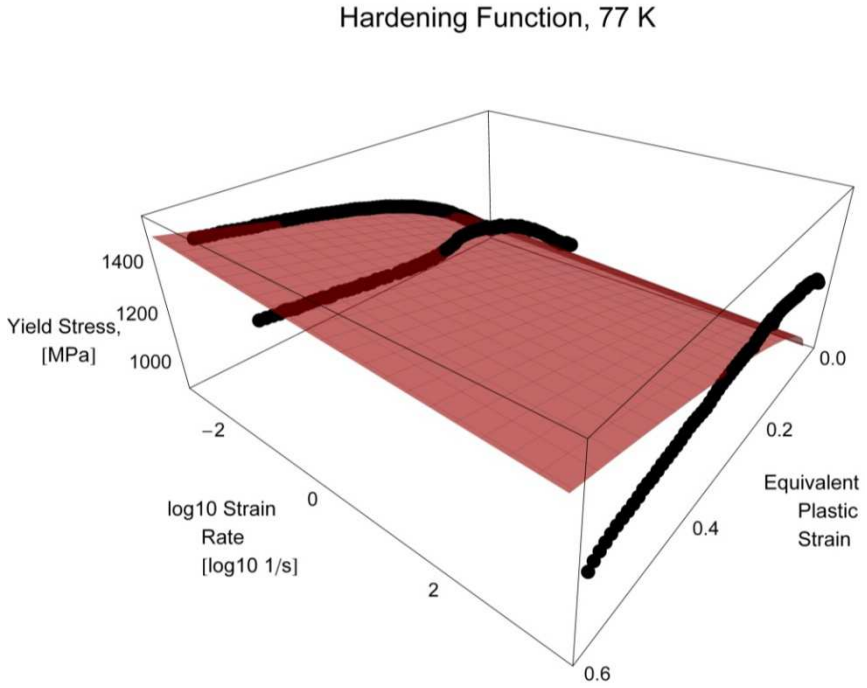

Figure 21. EPS calibrated JC model fitting to DH-36 steel data at temperature of 77 K.

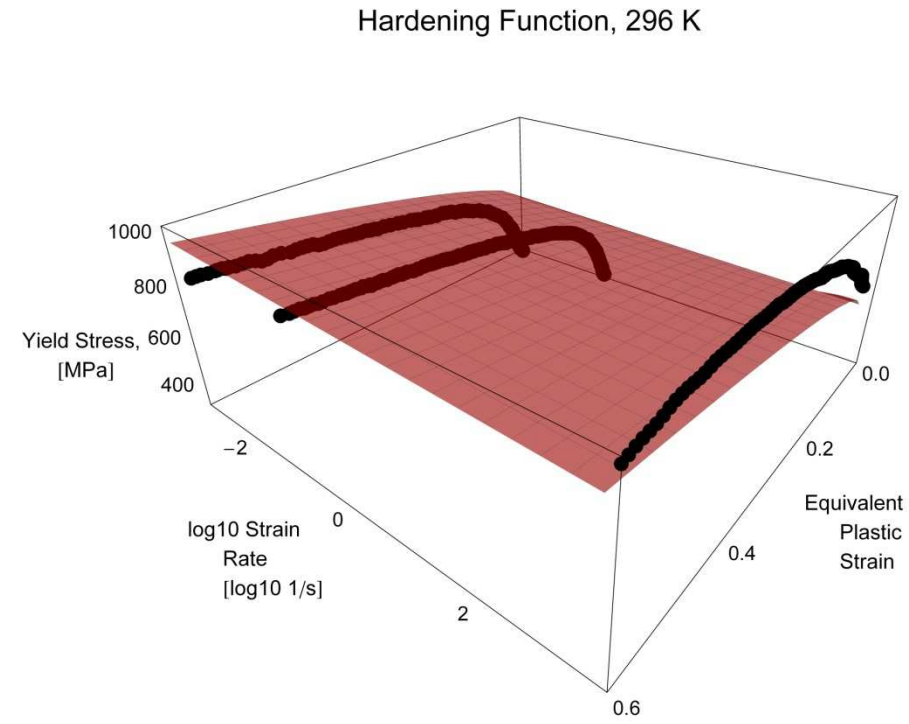

Figure 22. EPS calibrated JC model fitting to DH-36 steel data at temperature of 296 K.

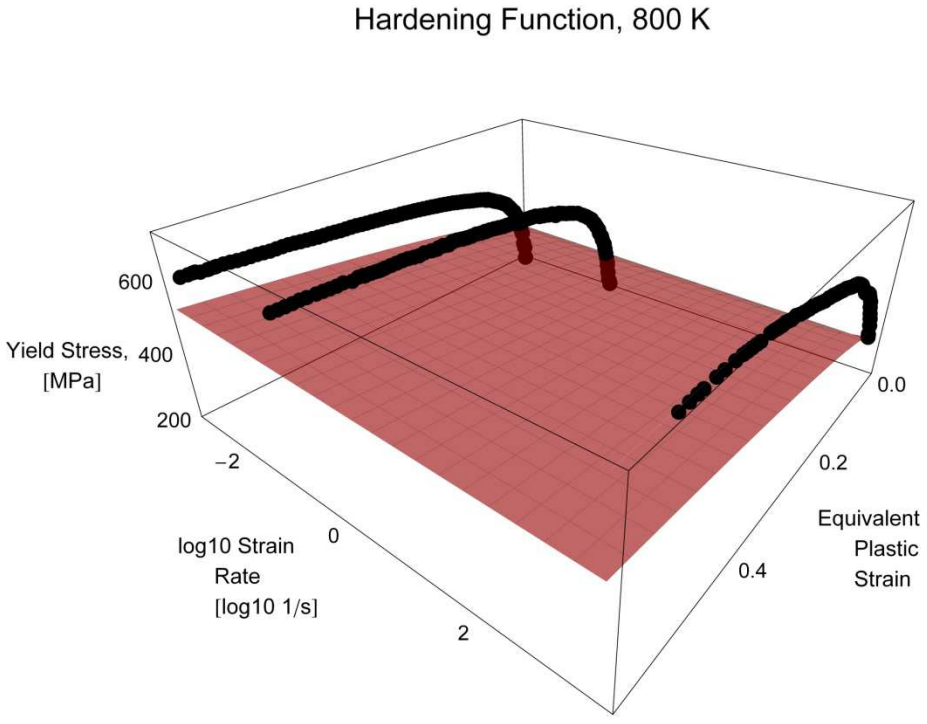

Figure 23. EPS calibrated JC model fitting to DH-36 steel data at temperature of 800 K.

As shown in Figs. 18 to 23, the hardening functions fit throughout the equivalent plastic strain ranges is improved, by comparing to the predictions of the LYS and OPTLYS calibrated Johnson-Cook models. Due to the nature of the EPS calibration strategy, the best fit is achieved for the hardening functions in which at least one reference conditions is present, i.e. an equivalent plastic strain rate of 0.001 s^{-1} or a temperature of 77 K. On the other hand, when the model fits the four hardening functions that do not refer to at least one reference condition, i.e. 0.1 s^{-1} and 296 K, 3000 s^{-1} and 296 K, 0.1 s^{-1} and 800 K, and 3000 s^{-1} and 800 K, wider errors may be introduced. This fact is due to having calculated the parameters C and m by considering only experimental data at the reference temperature and at the reference equivalent plastic strain rate, respectively. As a matter of fact, the four hardening functions that do not refer to at least one reference condition are never used when the EPS calibration strategy is adopted, as for the LYS calibration strategy.

Another important aspect that does contribute in creating fitting errors is the fact that the hardening parameters B and n are actually chosen as the ones capable to best fit the hardening function at the reference conditions only, i.e. at 0.001 s^{-1} and at 77 K. As clearly visible in Figs. 18 to 23, the parameters B and n capable to best fit the nine hardening functions vary strongly throughout the equivalent plastic strain rate and temperature ranges. In particular, the material softening that arises for the hardening function at 3000 s^{-1} and 77 K is very badly fitted, since the Johnson-Cook hardening function is not capable to fit trends which present a hardening phase followed by a softening one. In general, the more the best fit of the parameters B and n is dependent on the equivalent plastic strain rate and on the temperature, the more modeling errors are introduced, when trying to model hardening functions which do not refer to the reference conditions for both the equivalent plastic strain and the temperature.

As shown in Figs. 18 to 23, the requirement to best fit the data throughout the equivalent plastic strain ranges implies errors for the prediction of the lower yield stresses, sometimes of high magnitude. Such errors are obviously minimized for the hardening function at the reference conditions, i.e. 0.001 s^{-1} and 77 K. The parameters A, B and n are indeed calibrated through a nonlinear regression to best fit this hardening function. On the other hand, when it comes to the fitting of other hardening functions, heavy modeling errors are introduced. Following Table 10 reports a comparison between the EPS calibrated Johnson-Cook model predictions of the lower yield stresses and their experimental counterparts.

	Experimental Values	EPS JC Values
0.001 s^{-1}, 77 K	915.555 MPa	915.555 MPa
0.1 s^{-1}, 77 K	974.565 MPa	896.883 MPa
3000 s^{-1}, 77 K	1150.46 MPa	855.085 MPa
0.001 s^{-1}, 296 K	282.455 MPa	588.755 MPa
0.1 s^{-1}, 296 K	305.455 MPa	576.748 MPa
3000 s^{-1}, 296 K	630.137 MPa	549.869 MPa
0.001 s^{-1}, 800 K	190.345 MPa	319.443 MPa
0.1 s^{-1}, 800 K	200.213 MPa	312.928 MPa
3000 s^{-1}, 800 K	305.345 MPa	298.344 MPa

Table 10

Comparison between experimental lower yield stresses and correspondent predicted lower yield stresses from the Johnson-Cook model calibrated with the EPS strategy.

At this point, it is worthwhile to point-out the following consideration, similarly to what done for the LYS calibration strategy. Usually, when the EPS calibration strategy is adopted, predictions of the calibrated Johnson-Cook model are assessed only by comparing to hardening functions which refer to at least one reference condition. This kind of check may give good results, as readable in Figs. 18 to 23. However, the model should be checked even against hardening functions which do not refer to at least one reference condition, since large errors may be introduced.

Following Table 11 reports both the yield stress and the percentage yield stress root mean square errors for each of the nine considered hardening functions, together with their algebraic mean value. Heavy errors are introduced, although the situation is clearly improved by comparing to the LYS and OPTLYS strategies.

	$\bar{s}_{err}$	$\bar{s}_{\%err}$
0.001 s^{-1}, 77 K	19.5893 MPa	1.784%
0.1 s^{-1}, 77 K	68.1024 MPa	5.458%
3000 s^{-1}, 77 K	178.521 MPa	15.59%
0.001 s^{-1}, 296 K	145.517 MPa	31.88%
0.1 s^{-1}, 296 K	100.287 MPa	23.54%
3000 s^{-1}, 296 K	142.636 MPa	16.19%
0.001 s^{-1}, 800 K	90.808 MPa	19.20%
0.1 s^{-1}, 800 K	143.578 MPa	26.22%
3000 s^{-1}, 800 K	207.018 MPa	33.23%
Average	*121.784 MPa*	*19.23%*

Table 11

Yield stress (central column) and percentage yield stress (right column) root mean square errors for the EPS calibrated Johnson-Cook model yield stress predictions.

2.2.1.1.4. OPTEPS Calibration Strategy

The OPTEPS (OPTimized Equivalent Plastic Strain) calibration strategy aims at improving the EPS calibration strategy, by optimizing the value of the parameters C and m. In order to achieve this target, this strategy introduces in the calibration procedure the experimental data relative to the hardening functions which do not refer to at least one reference condition, by trying to obtain values of the parameters C and m capable to provide the actual best fit for all the hardening functions that are made available.

For what it concerns the calibration of the melting temperature, the reference equivalent plastic strain rate, the reference temperature and the quasi-static parameters A, B and n, the procedure is exactly the same as that exposed for the LYS calibration strategy. Differences arise for the determination of the parameters C and m. In order to introduce all the yield stress data provided by all the available hardening functions, the Johnson-Cook strength model, Eq. (28), is recalled a number of times equal to the number of available experimental observations, intended in terms of couples of yield stress and corresponding equivalent plastic strain values, throughout the equivalent plastic strain ranges experimentally investigated. These data refer to all the available hardening functions which do not refer to reference conditions for both the equivalent plastic strain rate and the temperature, i.e. all the available hardening functions except for the one which refers to the reference equivalent plastic strain rate and the reference temperature. This approach leads to the construction of a large overdetermined system of nonlinear equations, in which the unknowns are the parameters C and m and the number of equations is equal to the number of available couples of yield stress and corresponding equivalent plastic strain values, which depends on the number of experimental hardening functions that are made available and on the sampling frequency adopted for the experimental measurements. In order to avoid to set-up too large systems, it is obviously possible to consider data at a frequency inferior to that used for obtaining data during the experimental measurements, e.g. 10 times lower. Such system takes the following form

$$\bar{s}_i = \left(A + B \cdot \bar{\varepsilon}_{p_i}^{n}\right) \cdot \left(1 + C \cdot \ln \frac{\dot{\bar{\varepsilon}}_{p_i}}{\dot{\bar{\varepsilon}}_{p}^{0}}\right) \cdot \left(1 - \left(\frac{T_i - T_0}{T_m - T_0}\right)^{m}\right). \tag{46}$$

In these equations, the subscript i refers to the i-th couple of yield stress and corresponding equivalent plastic strain values. As said for the OPTLYS calibration strategy, a system of this kind can be solved through a nonlinear least square method. The solution values for the parameters C and m are those characterized by

being capable to minimize the square errors of the Johnson-Cook model predictions against experimental data at each couple of yield stress and corresponding equivalent plastic strain values.

Regarding the experimental data necessary in order to carry-out the OPTEPS calibration strategy, these are exactly the same required for the OPTLYS calibration strategy. In the following, the OPTEPS calibration strategy is applied to the nine experimental hardening functions extracted from Nemat-Nasser and Guo, 2003.

All the parameters are equal to the ones evaluated for the LYS calibration strategy, except for the parameters C and m, which are evaluated by solving the overdetermined system of nonlinear equations and 2 unknowns, i.e. the parameter C and m. Couples of yield stress and corresponding equivalent plastic strain values are taken with the same frequency of the experimental ones, i.e. for each digitalized couple of yield stress and corresponding equivalent plastic strain. Following this approach, a large overdetermined system of 664 nonlinear equations and 2 unknowns is created. It has been numerically solved with a nonlinear least squares trust-region-reflective algorithm within MathWorks MatLab 2010b, as previously done for the OPTLYS calibration strategy, with a tolerance of 10^{-8}. The obtained values for the parameters C and m simultaneously minimize the square errors for the 664 nonlinear equations of the system, through a multi-objective nonlinear optimization. These optimized values are equal to -0.00091 and 0.52988 for the parameters C and m, respectively.

The 8 Johnson-Cook parameters obtained through the OPTEPS calibration strategy are summarized in following Table 12.

A	915.555 MPa	m	0.52988
B	760.782 MPa	$\dot{\varepsilon}_0$	0.001 s^{-1}
n	0.60101	T_0	77 K
C	-0.00091	T_m	1773 K

Table 12
Johnson-Cook parameters for the DH-36 structural steel calculated through the OPTEPS calibration strategy.

Following Figs. 24 to 26 show the hardening functions predicted by the Johnson-Cook model calibrated with the OPTEPS strategy. The curves of the OPTEPS calibrated Johnson-Cook model follow in the best possible way the experimental hardening curves throughout the equivalent plastic strain ranges, this time considering not only the hardening functions which have at least one between the equivalent plastic strain and the temperature equal to the reference value, but all the nine hardening functions. As previously said, this target is partially hindered by

the fact that the material does not strictly respect the natural logarithm dependence of the yield stress on the dimensionless equivalent plastic strain rate and the power dependence on the homologous temperature, together with the fact that the hardening parameters B and n are actually chosen as the ones capable to best fit the hardening functions at the reference conditions only.

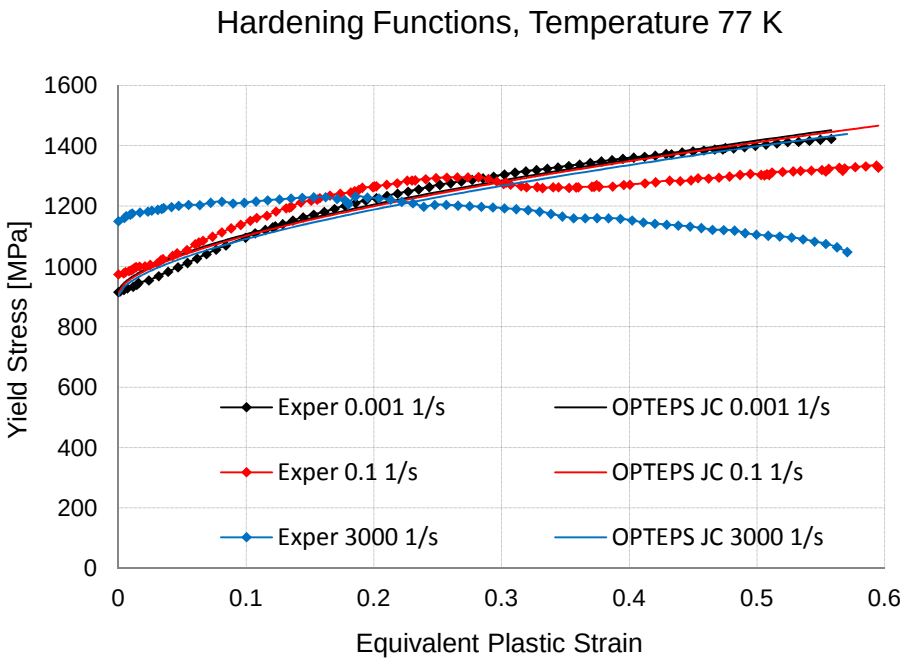

Figure 24. OPTEPS calibrated Johnson-Cook fitting to DH-36 structural steel data at temperature of 77 K and at three different equivalent plastic strain rates.

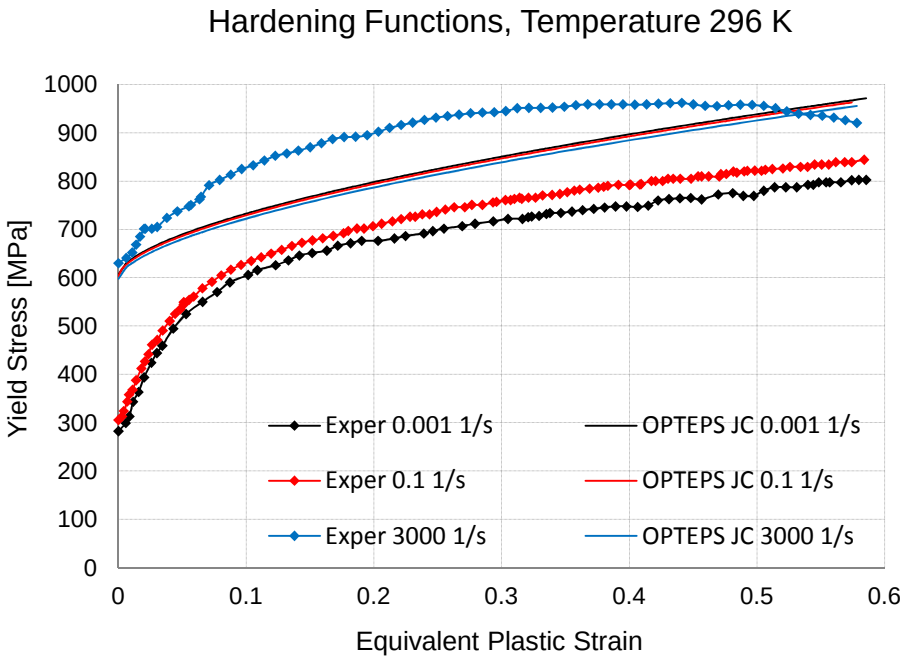

Figure 25. OPTEPS calibrated Johnson-Cook fitting to DH-36 structural steel data at temperature of 296 K and at three different equivalent plastic strain rates.

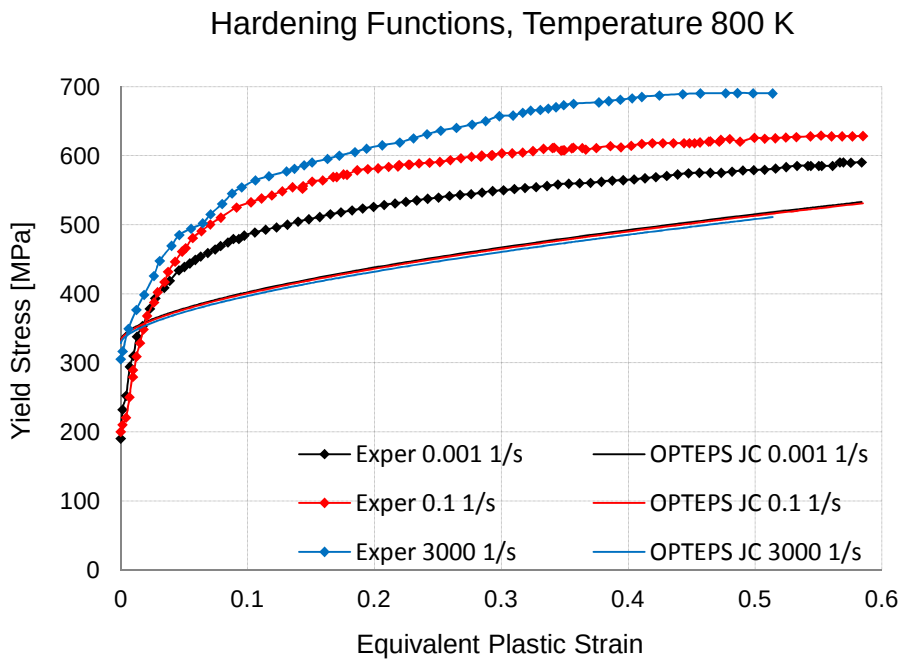

Figure 26. OPTEPS calibrated Johnson-Cook fitting to DH-36 structural steel data at temperature of 800 K and at three different equivalent plastic strain rates.

Following Figs. 27 to 29 further show the OPTEPS results by surface plots.

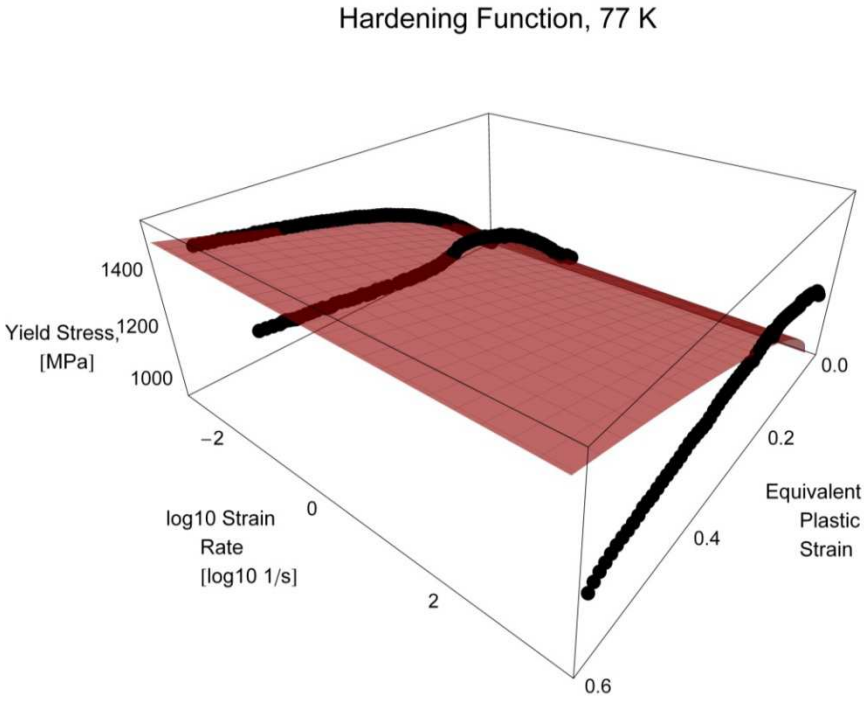

Figure 27. OPTEPS calibrated JC model fitting to DH-36 steel data at temperature of 77 K.

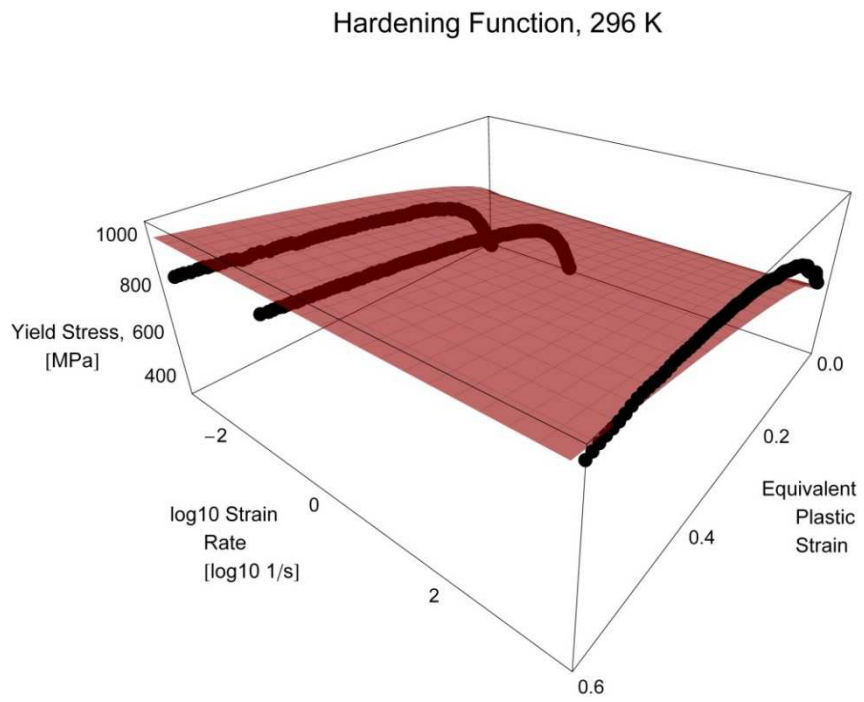

Figure 28. OPTEPS calibrated JC model fitting to DH-36 steel data at temperature of 296 K.

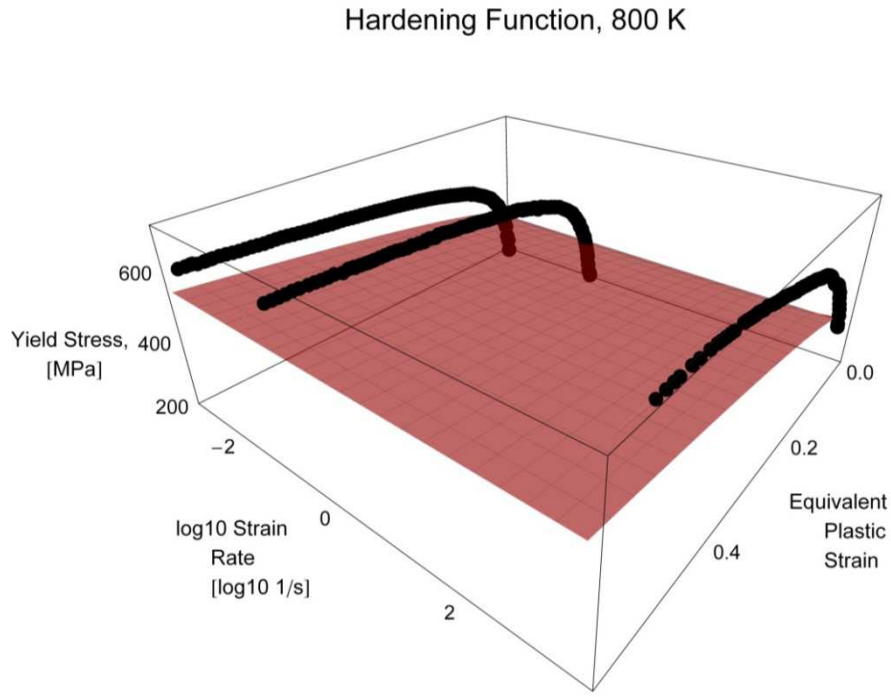

Figure 29. OPTEPS calibrated JC model fitting to DH-36 steel data at temperature of 800 K.

As displayed in Figs. 24 to 29, the fit to the data is now the result of a compromise between all the nine hardening functions. This implies the fact that the fit with the hardening functions in which at least one reference condition is present is less coherent than the one obtainable from the predictions of the EPS calibrated Johnson-Cook model. On the other hand, when the model fits the four hardening functions that do not refer to at least one reference condition, the errors become lower. Clearly, this is a consequence of having calculated the parameters C and m by considering experimental data from all the nine hardening functions.

Of course, the problem of having errors at the lower yield stresses is still present, since it is a consequence of the basic assumption of both the EPS and the OPTEPS strategies. Following Table 13 reports a comparison between the OPTEPS calibrated Johnson-Cook model predictions of the lower yield stresses and their experimental counterparts.

	Experimental Values	OPTEPS JC Values
0.001 s^{-1}, 77 K	915.555 MPa	915.555 MPa
0.1 s^{-1}, 77 K	974.565 MPa	911.718 MPa
3000 s^{-1}, 77 K	1150.46 MPa	903.129 MPa
0.001 s^{-1}, 296 K	282.455 MPa	606.076 MPa
0.1 s^{-1}, 296 K	305.455 MPa	603.536 MPa
3000 s^{-1}, 296 K	630.137 MPa	597.851 MPa
0.001 s^{-1}, 800 K	190.345 MPa	332.813 MPa
0.1 s^{-1}, 800 K	200.213 MPa	331.418 MPa
3000 s^{-1}, 800 K	305.345 MPa	328.296 MPa

Table 13
Comparison between experimental lower yield stresses and correspondent predicted lower yield stresses from the Johnson-Cook model calibrated with the OPTEPS strategy.

Following Table 14 reports both the yield stress and the percentage yield stress root mean square errors for each of the nine considered hardening functions, together with their algebraic mean value, i.e. their sum divided by nine. Comparing to the EPS calibration strategy, the situation is slightly improved.

	$\bar{s}_{err}$	$\bar{s}_{\%err}$
0.001 s^{-1}, 77 K	19.5893 MPa	1.784%
0.1 s^{-1}, 77 K	71.965 MPa	5.628%
3000 s^{-1}, 77 K	187.663 MPa	16.63%
0.001 s^{-1}, 296 K	167.537 MPa	35.08%
0.1 s^{-1}, 296 K	131.085 MPa	27.84%
3000 s^{-1}, 296 K	83.2915 MPa	9.424%
0.001 s^{-1}, 800 K	74.8550 MPa	17.20%
0.1 s^{-1}, 800 K	120.916 MPa	23.43%
3000 s^{-1}, 800 K	168.337 MPa	26.90%
Average	*113.915 MPa*	*18.21%*

Table 14
Yield stress (central column) and percentage yield stress (right column) root mean square errors for the OPTEPS calibrated Johnson-Cook model yield stress predictions.

2.2.1.1.5. GOPTEPS Calibration Strategy

The GOPTEPS (Global OPTimization Equivalent Plastic Strain) calibration strategy aims at further improving the OPTEPS calibration strategy by considering a simultaneous optimization of 7 of the 8 parameters of the Johnson-Cook model, i.e. all the parameters except for the melting temperature. All the experimental data are

used, trying to obtain values of the 7 parameters capable to provide the actual best fit for all the hardening functions made available, throughout the equivalent plastic strain, equivalent plastic strain rate and temperature ranges involved.

This optimization is carried-out by solving an overdetermined system of nonlinear equations and seven unknowns, namely the quasi-static parameters A, B and n, the strain rate parameter C, the temperature parameter m and the two reference parameters, i.e. the reference equivalent plastic strain rate $\dot{\bar{\varepsilon}}_0$ and the reference temperature T_0. Such nonlinear system uses all the available experimental data, intended in terms of couples of yield stress and corresponding equivalent plastic strain, as done for the OPTEPS calibration strategy, but this time in seven unknowns. The obtained values for these seven parameters simultaneously minimize the square errors for the nonlinear equations of the system, through a multi-objective nonlinear optimization. Some authors have investigated such calibration strategy, by introducing in the optimization more or less of the 8 Johnson-Cook parameters, including the melting temperature. In this regard, see, e.g., Langrand et al., 1999, Milani et al., 2008, and Scapin et al., 2012.

In the present work, the melting temperature, a parameter of clear physical meaning, is excluded from the multi-objective optimization. Assuming the melting temperature to be an optimization variable may lead to setting-up melting values totally different from the real value. This approach may make the Johnson-Cook model completely useless in FEM simulations in which it is not possible to know a priori the temperature field, and in particular whether the real melting temperature is reached or not. As a result, phase changes from solid to liquid, and consequent setting of a null yield stress, may be completely missed. This is a dangerous and unwanted consequence. Therefore, the present choice arises of not taking the melting temperature as an optimization variable.

It is also worthwhile to point-out a consideration about the reference equivalent plastic strain rate and temperature. In the four previous calibration strategies, such reference values were taken by choosing among the values of one of the available experimental hardening function, which was then labeled as the hardening function under reference conditions. The quasi-static parameters A, B and n were then determined through a regression of experimental data in such conditions, thanks to the vanishing of the strain rate and temperature terms. In such calibration strategies, the reference equivalent plastic strain rate and temperature have a value that must be equal to those of one of the hardening functions. In the GOPT calibration strategy, these reference values can be different from those of one of the experimental hardening functions, since they are considered as optimization variables. Anyway, their values identify the Johnson-Cook quasi-static conditions,

although these conditions are now unknown. This fact should allow for a better fitting of the experimental data.

Regarding the determination of the considered 7 Johnson-Cook parameters, the procedure is similar to that of the OPTEPS calibration strategy, although more complex. In order to introduce all the yield stress data provided by all the available hardening functions, the Johnson-Cook strength model, Eq. (28), is recalled a number of times equal to the number of available experimental observations, intended in terms of couples of yield stress and corresponding equivalent plastic strain values, throughout the equivalent plastic strain ranges experimentally investigated.

This approach leads to the construction of a large overdetermined system of nonlinear equations, in which the unknowns are the 7 parameters and the number of equations is equal to the number of available couples of yield stress and corresponding equivalent plastic strain values, which depend on the number of experimental hardening functions made available and on the sampling frequency adopted for reading the experimental measurements. In order to avoid to set-up too large systems, it is obviously possible to consider data at a sampling inferior than the one used for the experimental measurements, as said for the OPTEPS calibration strategy. The nonlinear system that arises is identical to that reported in Eq. (46), although this time the optimization variables are not composed by the parameters C and m only but rather by the previously stated seven parameters. In order to solve this system, an important point is relative to the enforcement of appropriate conditions on the seven optimization variables, making the process a multi-objective nonlinear optimization subjected to bounds. More in detail, the reference equivalent plastic strain rate is forced to be a positive number, since it cannot be a negative number, because natural logarithms of negative numbers cannot be calculated. Furthermore, the reference temperature is forced to be lower than or equal to the lowest temperature tested during the experimental campaign, since it is necessary to avoid calculations of negative homologous temperatures, in order to prevent computations of negative numbers raised to a possible non integer number, as previously said. The reference temperature is also forced to be greater than zero. Although the calculation of negative reference temperatures is not a problem from the mathematical point of view, it is considered reasonable to keep this parameter greater than zero, since temperatures lower than zero K are not physically admissible. No bounds are imposed to the other optimization variables.

The created system is fairly more complex than the one introduced in the OPTEPS calibration strategy, due to the enlargement of the optimization variables from 2 to 7. It can still be solved through a nonlinear least square method. If there are convergence problems, it is possible to enforce some further bounds on the objective variables, in order to restrict their existence domains and favor the

convergence of the system. The solution values for the considered 7 Johnson-Cook parameters are those characterized by minimizing the square errors of the Johnson-Cook model predictions against experimental data at each couple of yield stress and corresponding equivalent plastic strain values.

Regarding the experimental data necessary in order to carry-out the GOPTEPS calibration strategy, these are exactly the same as those required for the OPTLYS and OPTEPS strategies. In the following, the GOPTEPS calibration strategy is again applied to the data taken from Nemat-Nasser and Guo, 2003.

The overdetermined system of nonlinear equations and seven unknowns is set-up by taking couples of yield stress and equivalent plastic strain values with the same sampling of the experimental ones, i.e. for each digitalized couple of yield stress and corresponding equivalent plastic strain, as previously done for the OPTEPS calibration strategy. Following this approach, a large overdetermined system of 740 nonlinear equations and seven unknowns is created. It has been numerically solved with a nonlinear least squares trust-region-reflective algorithm with MathWorks MatLab 2010b, as previously done for the OPTLYS and OPTEPS calibration strategy, with a tolerance of 10^{-8}. Some convergence problems have been solved by setting the reference temperature equal to 77 K, since all the iterations showed that this parameter tended to such value. The seven Johnson-Cook parameters obtained through the GOPTEPS calibration strategy are summarized in following Table 15, together with the value of the melting temperature, which is taken as fixed.

A	747.412 MPa	m	0.5779
B	654.104 MPa	$\dot{\varepsilon}_0$	$8.79832 \cdot 10^{-4}$ s^{-1}
n	0.27334	T_0	77 K
C	0.00226	T_m	1773 K

Table 15
Johnson-Cook parameters for the DH-36 structural steel calculated through the GOPTEPS calibration strategy.

Following Figs. 30 to 32 show the hardening functions predicted by the Johnson-Cook model calibrated with the GOPTEPS strategy. The curves of the GOPTEPS calibrated Johnson-Cook model follow in the best possible way the experimental hardening curves throughout the equivalent plastic strain ranges. As previously said, this target is partially hindered by the fact that the material does not strictly respect the natural logarithm dependence of the yield stress on the dimensionless equivalent plastic strain rate and the power dependence on the homologous temperature.

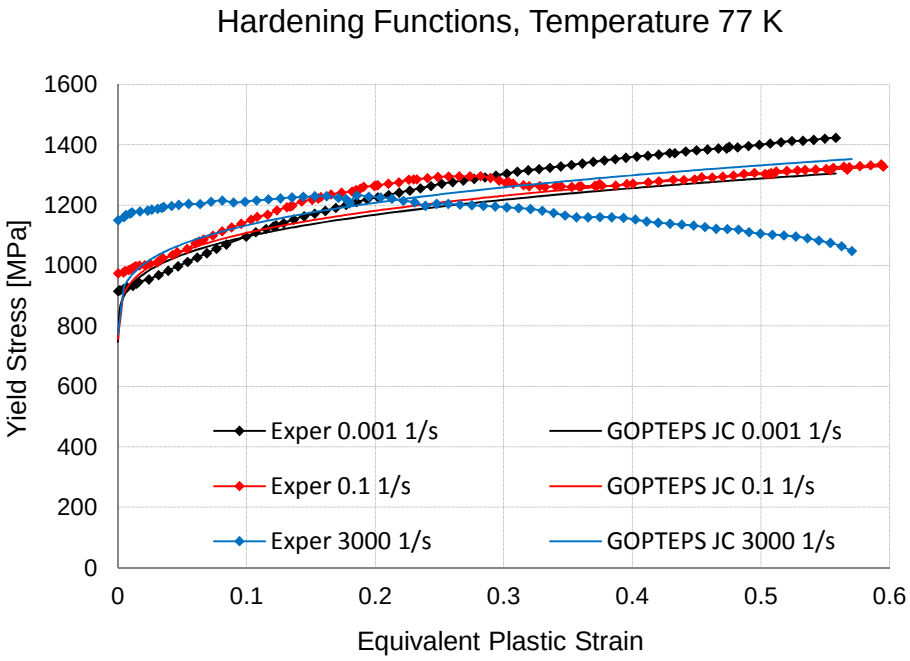

Figure 30. GOPTEPS calibrated Johnson-Cook fitting to DH-36 structural steel data at temperature of 77 K and at three different equivalent plastic strain rates.

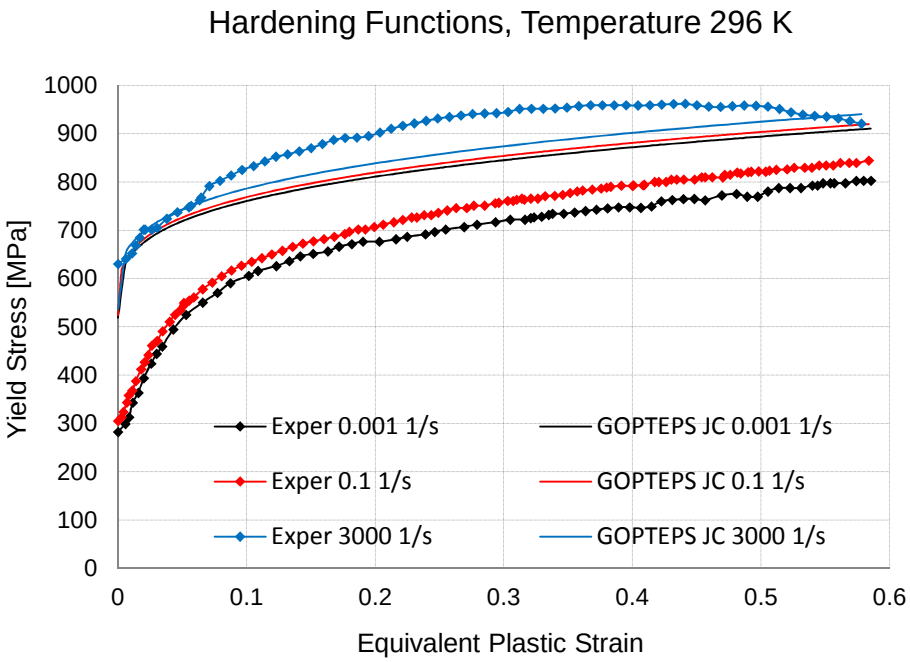

Figure 31. GOPTEPS calibrated Johnson-Cook fitting to DH-36 structural steel data at temperature of 296 K and at three different equivalent plastic strain rates.

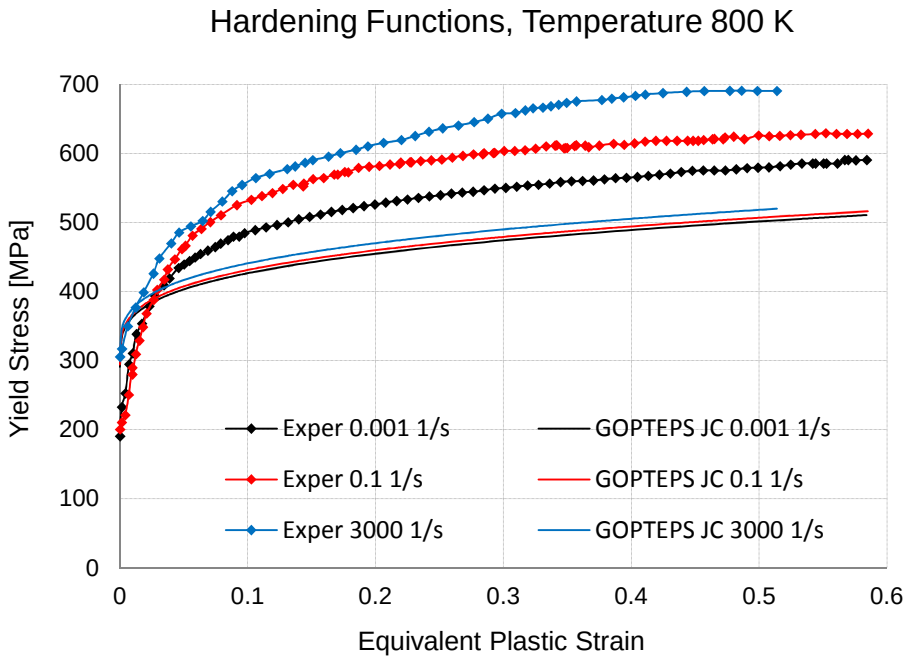

Figure 32. GOPTEPS calibrated Johnson-Cook fitting to DH-36 structural steel data at temperature of 800 K and three different equivalent plastic strain rates.

Following Figs. 33 to 35 further show the GOPTEPS results by surface plots.

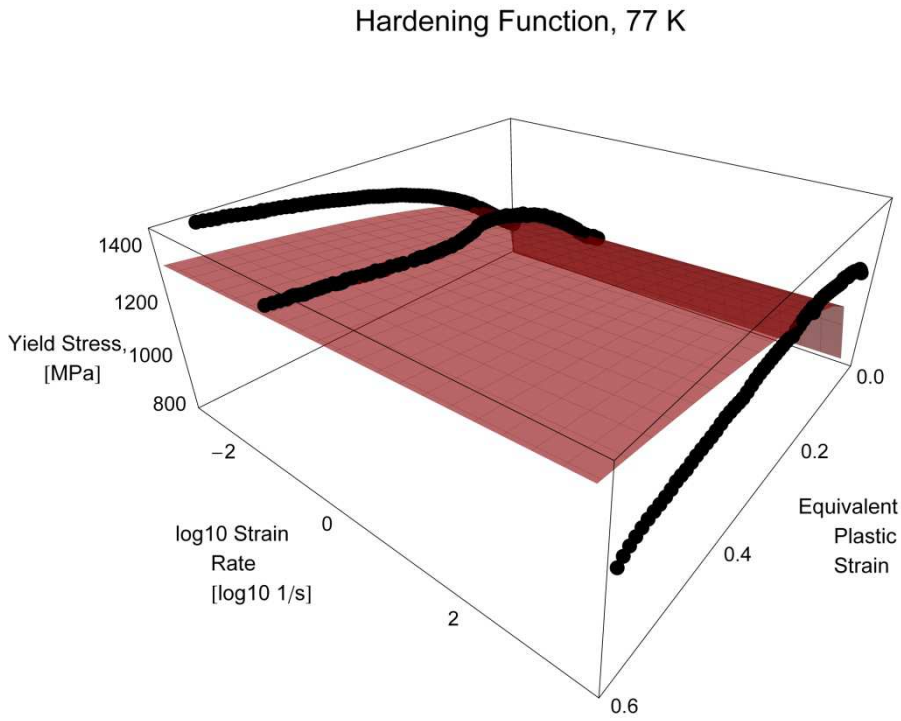

Figure 33. GOPTEPS calibrated JC model fitting to DH-36 steel data at temperature of 77 K.

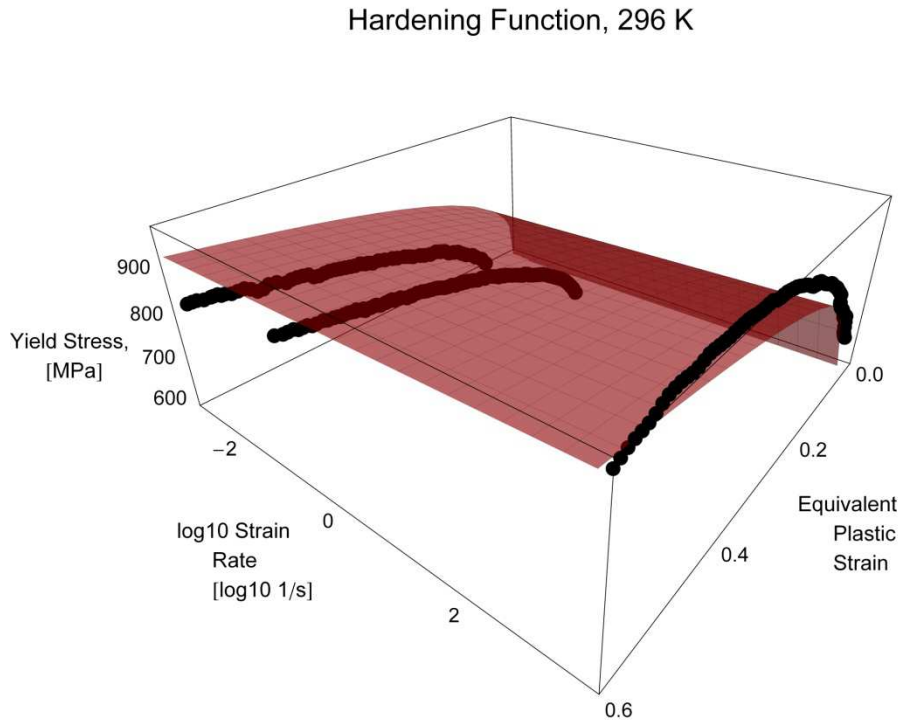

Figure 34. GOPTEPS calibrated JC model fitting to DH-36 steel data at temperature of 296 K.

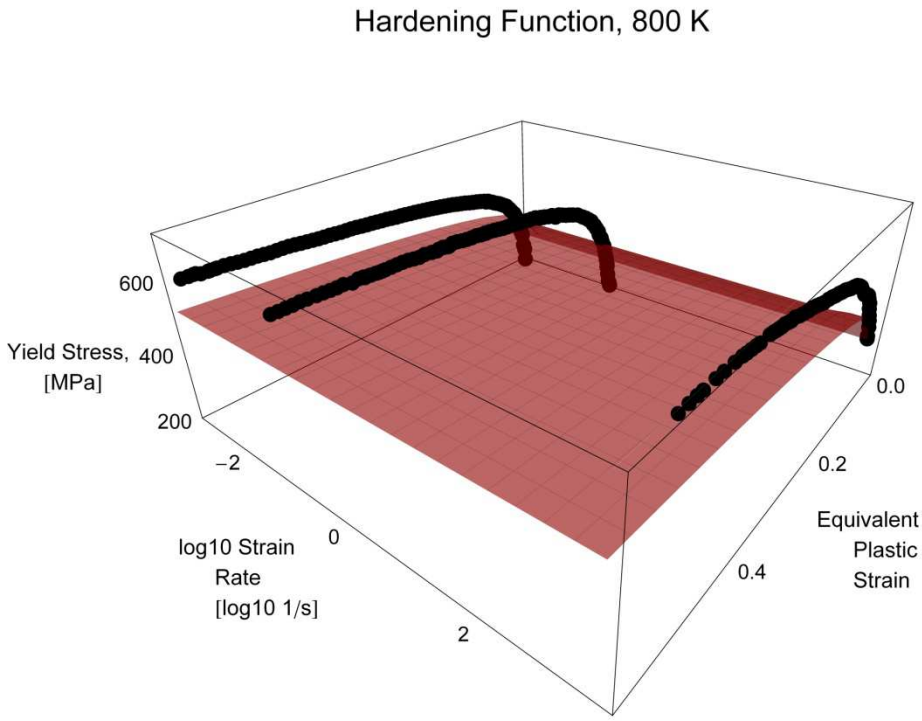

Figure 35. GOPTEPS calibrated JC model fitting to DH-36 steel data at temperature of 800 K.

As shown in Figs. 30 to 35, the hardening functions fitting throughout the equivalent plastic strain ranges appears to be improved, by comparing to the predictions of the EPS and OPTEPS calibrated Johnson-Cook models. This is mainly due to the fact of having optimized all together not only the parameters C and m but also other 5 parameters, with particular reference to the parameters B and n.

Of course, the problem of having errors at the lower yield stress is still present, since this is a consequence of the basic assumption of the EPS, OPTEPS and GOPTEPS strategies. Following Table 16 reports a comparison between the GOPTEPS calibrated Johnson-Cook model predictions of the lower yield stresses and their experimental counterparts.

	Experimental Values	GOPTEPS JC Values
0.001 s^{-1}, 77 K	915.555 MPa	747.628 MPa
0.1 s^{-1}, 77 K	974.565 MPa	755.407 MPa
3000 s^{-1}, 77 K	1150.46 MPa	772.820 MPa
0.001 s^{-1}, 296 K	282.455 MPa	518.571 MPa
0.1 s^{-1}, 296 K	305.455 MPa	523.967 MPa
3000 s^{-1}, 296 K	630.137 MPa	536.045 MPa
0.001 s^{-1}, 800 K	190.345 MPa	290.859 MPa
0.1 s^{-1}, 800 K	200.213 MPa	331.418 MPa
3000 s^{-1}, 800 K	305.345 MPa	300.660 MPa

Table 16
Comparison between experimental lower yield stresses and corresponding predicted lower yield stresses from the Johnson-Cook model calibrated with the GOPTEPS strategy.

Following Table 17 reports both the yield stress and the percentage yield stress root mean square errors for each one of the nine considered hardening functions, together with their algebraic mean value, i.e. their sum divided by nine. Comparing to the OPTEPS calibration strategy, the situation is further improved.

	$\bar{s}_{err}$	$\bar{s}_{\%err}$
0.001 s^{-1}, 77 K	79.6277 MPa	6.163%
0.1 s^{-1}, 77 K	49.7374 MPa	4.289%
3000 s^{-1}, 77 K	153.934 MPa	13.61%
0.001 s^{-1}, 296 K	158.594 MPa	34.26%
0.1 s^{-1}, 296 K	137.140 MPa	29.10%
3000 s^{-1}, 296 K	49.9562 MPa	5.573%
0.001 s^{-1}, 800 K	69.8119 MPa	15.23%
0.1 s^{-1}, 800 K	110.280 MPa	21.54%
3000 s^{-1}, 800 K	140.315 MPa	21.97%
Average	*105.488 MPa*	*16.86%*

Table 17
Yield stress (central column) and percentage yield stress (right column) root mean square errors for the GOPTEPS calibrated Johnson-Cook model yield stress predictions.

2.2.1.1.6. Calibration Strategies Comparison and Assessment

Following Figs. 36 to 44 allow to compare all together the results from the five calibration strategies presented above, by considering their application to the nine experimental hardening functions taken from Nemat-Nasser and Guo, 2003.

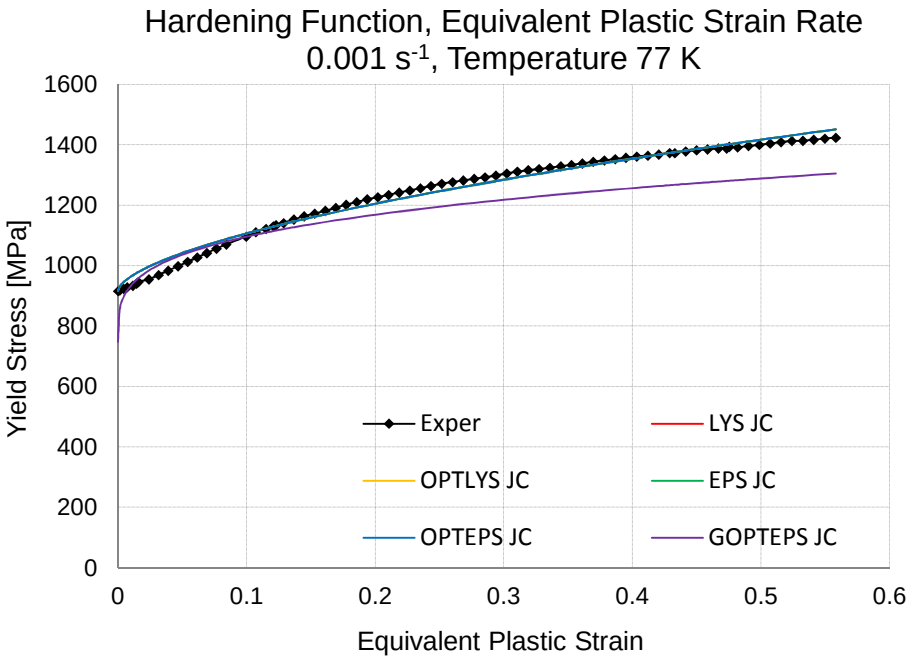

Figure 36. Five calibrations of JC model with different strategies and DH-36 steel data at temperature of 77 K and at equivalent plastic strain rate of 0.001 s^{-1}.

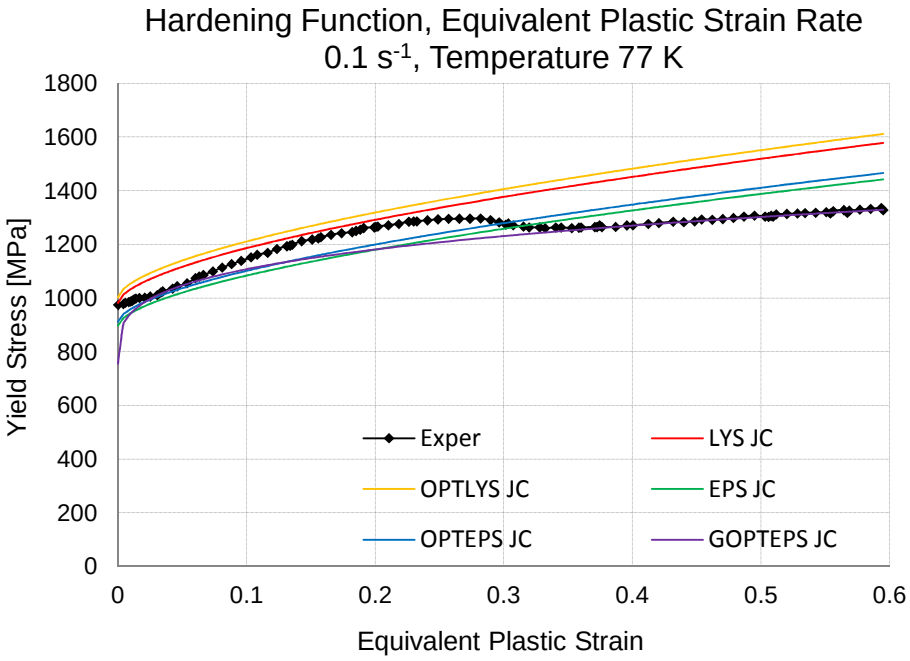

Figure 37. Five calibrations of JC model with different strategies and DH-36 steel data at temperature of 77 K and at equivalent plastic strain rate of 0.1 s^{-1}.

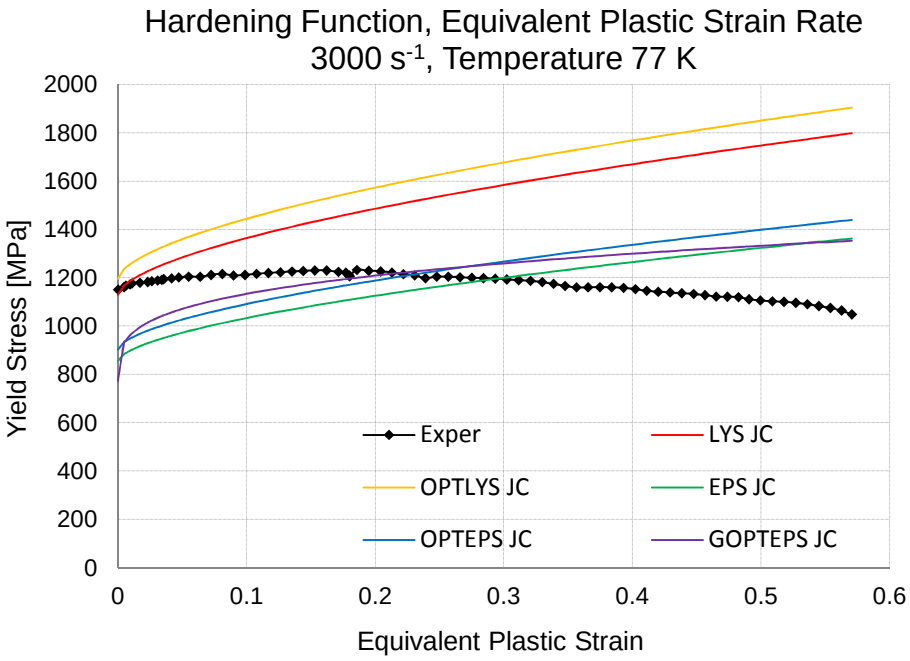

Figure 38. Five calibrations of JC model with different strategies and DH-36 steel data at temperature of 77 K and at equivalent plastic strain rate of 3000 s^{-1}.

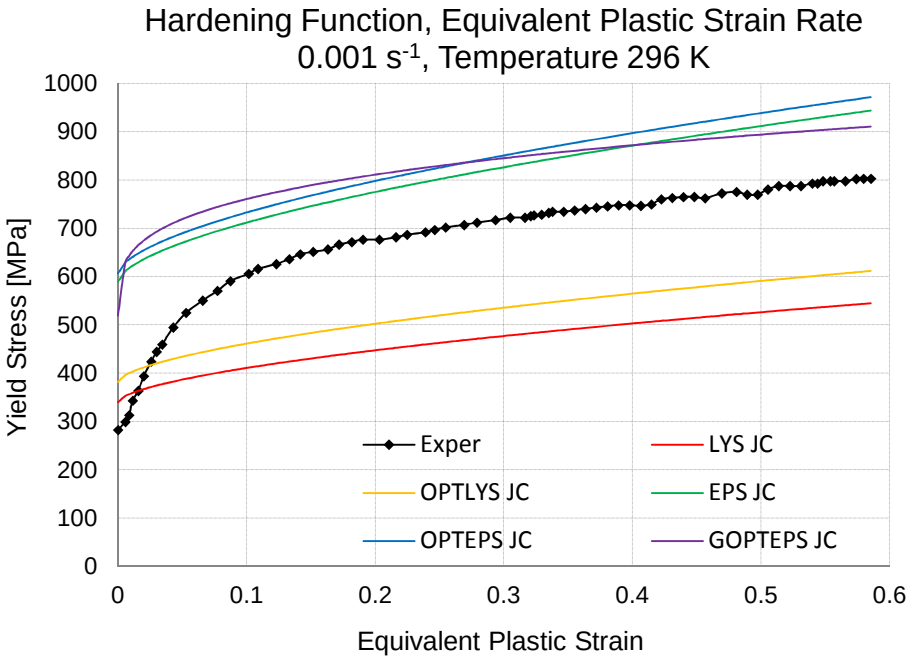

Figure 39. Five calibrations of JC model with different strategies and DH-36 steel data at temperature of 296 K and at equivalent plastic strain rate of 0.001 s^{-1}.

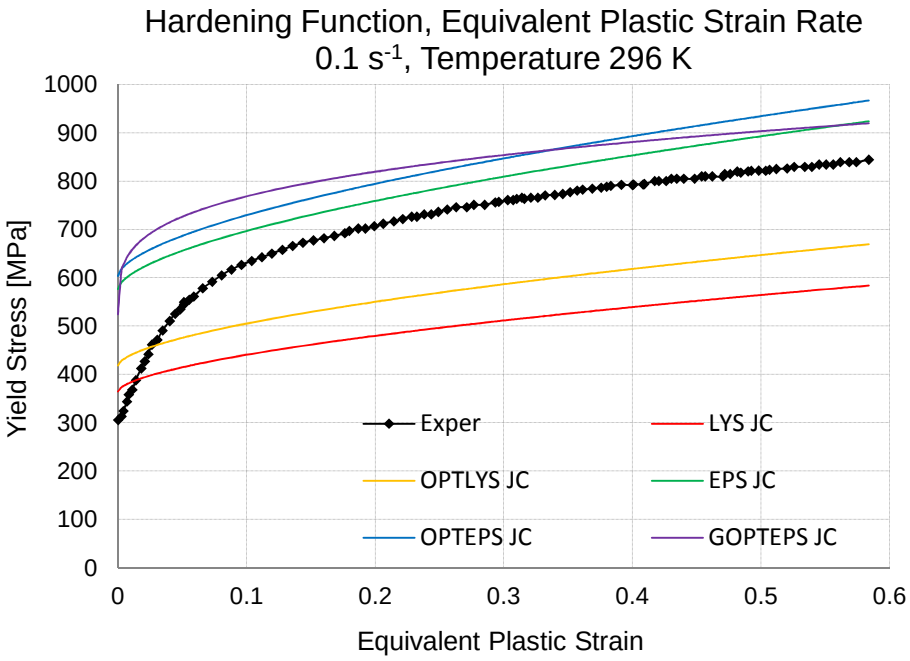

Figure 40. Five calibrations of JC model with different strategies and DH-36 steel data at temperature of 296 K and at equivalent plastic strain rate of 0.1 s^{-1}.

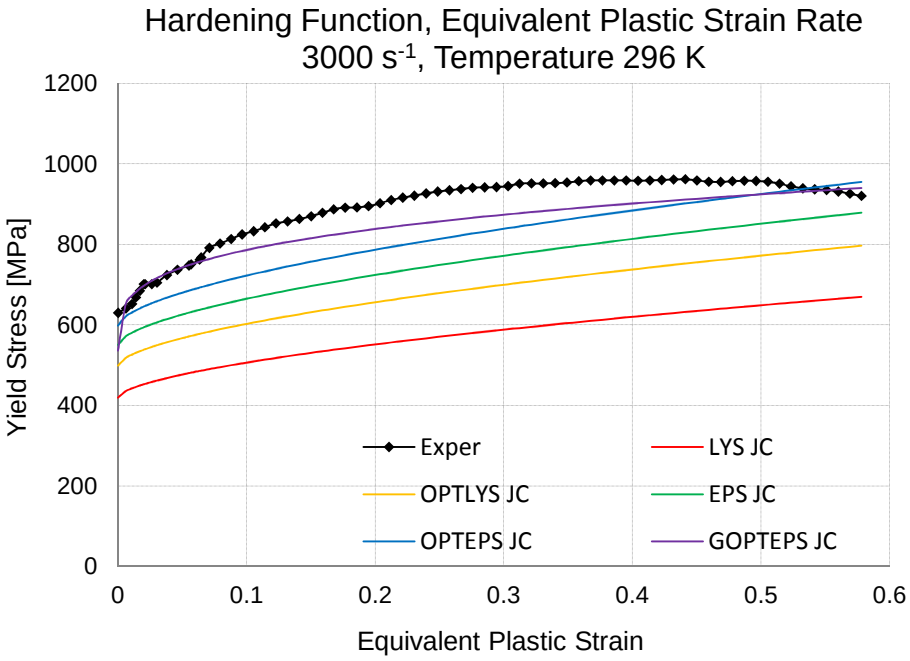

Figure 41. Five calibrations of JC model with different strategies and DH-36 steel data at temperature of 296 K and at equivalent plastic strain rate of 3000 s^{-1}.

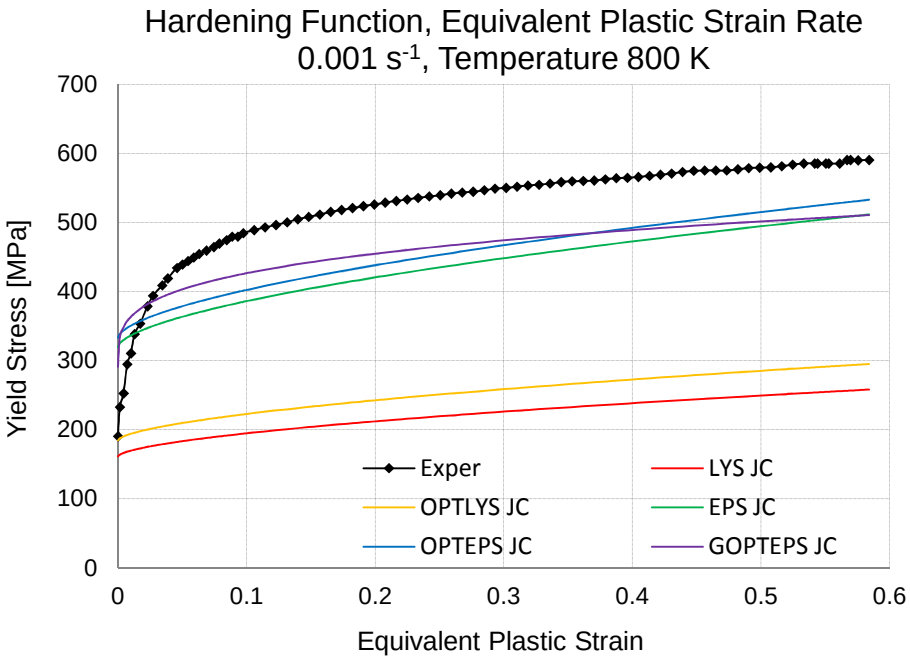

Figure 42. Five calibrations of JC model with different strategies and DH-36 steel data at temperature of 800 K and at equivalent plastic strain rate of 0.001 s^{-1}.

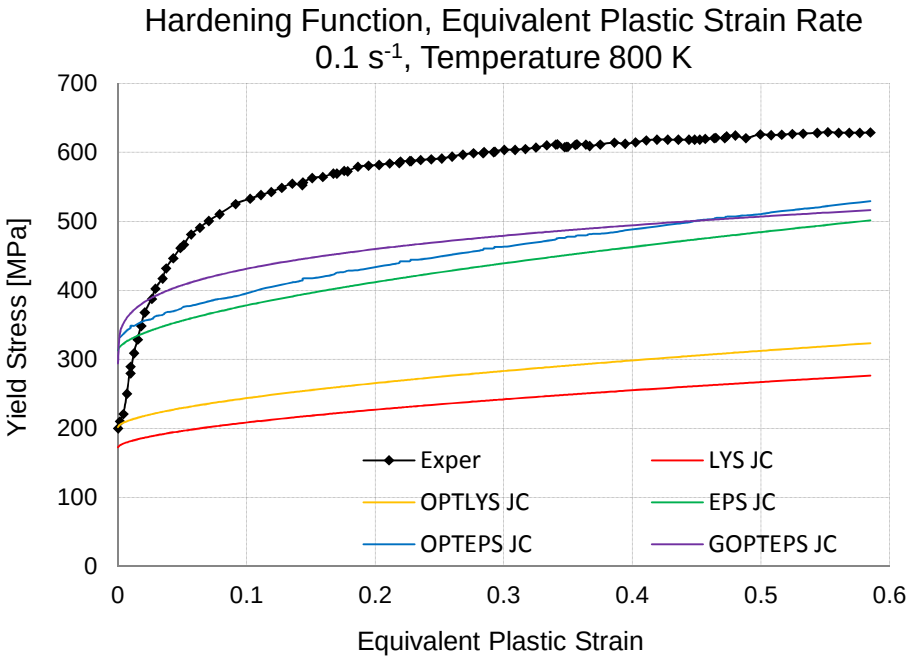

Figure 43. Five calibrations of JC model with different strategies and DH-36 steel data at temperature of 800 K and at equivalent plastic strain rate of 0.1 s^{-1}.

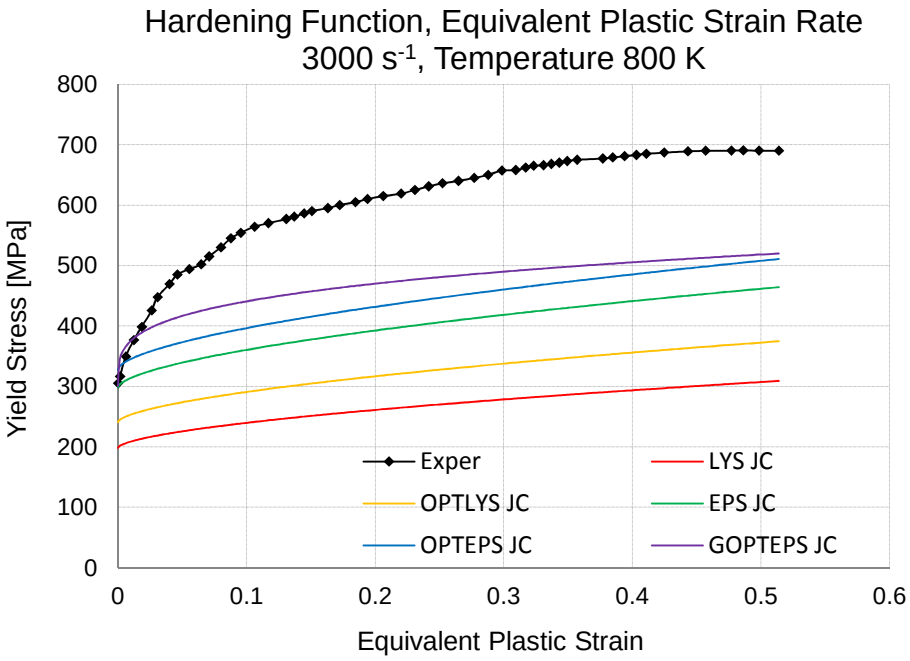

Figure 44. Five calibrations of JC model with different strategies and DH-36 steel data at temperature of 800 K and at equivalent plastic strain rate of 3000 s^{-1}.

Figs. 36 to 44 show in better detail what previously presented for each Johnson-Cook calibration strategy. The reported trends confirm the considerations previously stated regarding the strengths and weaknesses of each calibration strategy. Following Table 18 reports a comparison between the 5 calibrated Johnson-Cook model predictions of the lower yield stresses and their experimental counterparts.

	0.001 s^{-1}, 77 K	**0.1 s^{-1}, 77 K**	**3000 s^{-1}, 77 K**
Experimental Values	*915.555 MPa*	*974.565 MPa*	*1150.46 MPa*
LYS JC Values	915.555 MPa	981.323 MPa	1128.545 MPa
OPTLYS JC Values	915.555 MPa	1001.95 MPa	1195.34 MPa
EPS JC Values	915.555 MPa	896.883 MPa	855.085 MPa
OPTEPS JC Values	915.555 MPa	911.718 MPa	903.129 MPa
GOPTEPS JC Values	747.628 MPa	755.407 MPa	772.820 MPa
	0.001 s^{-1}, 296 K	**0.1 s^{-1}, 296 K**	**3000 s^{-1}, 296 K**
Experimental Values	*282.455 MPa*	*305.455 MPa*	*630.137 MPa*
LYS JC Values	340.015 MPa	364.439 MPa	419.115 MPa
OPTLYS JC Values	381.868 MPa	417.901 MPa	498.563 MPa
EPS JC Values	588.755 MPa	576.748 MPa	549.869 MPa
OPTEPS JC Values	606.076 MPa	603.536 MPa	597.851 MPa
GOPTEPS JC Values	518.571 MPa	523.967 MPa	536.045 MPa
	0.001 s^{-1}, 800 K	**0.1 s^{-1}, 800 K**	**3000 s^{-1}, 800 K**
Experimental Values	*190.345 MPa*	*200.213 MPa*	*305.345 MPa*
LYS JC Values	160.967 MPa	172.533 MPa	198.417 MPa
OPTLYS JC Values	184.331 MPa	201.724 MPa	240.660 MPa
EPS JC Values	319.443 MPa	312.928 MPa	298.344 MPa
OPTEPS JC Values	332.813 MPa	331.418 MPa	328.296 MPa
GOPTEPS JC Values	290.859 MPa	331.418 MPa	300.660 MPa

Table 18

Comparison between experimental lower yield stresses and corresponding predicted lower yield stresses from the Johnson-Cook model calibrated with five different calibration strategies.

Following Table 19 reports both the yield stress and the percentage yield stress root mean square average errors for each of the five considered Johnson-Cook calibration strategies.

	$\bar{s}_{err}$	$\bar{s}_{\%err}$
LYS Calibrated JC	253.860 MPa	34.85%
OPTLYS Calibrated JC	226.289 MPa	30.31%
EPS Calibrated JC	121.784 MPa	19.23%
OPTEPS Calibrated JC	113.915 MPa	18.21%
GOPTEPS Calibrated JC	105.488 MPa	16.86%

Table 2

Yield stress (central column) and percentage yield stress (right column) root mean square average errors for the yield stress predictions of the Johnson-Cook model calibrated with five different calibration strategies.

Some considerations are reported in the following, in order to better understand the consequences of choosing a particular calibration strategy or another.

The LYS calibration strategy allows to model quite coherently the lower yield stresses, by considering data provided only by those hardening functions which refer to at least one reference condition, whether it is the reference equivalent plastic strain rate or the reference temperature. As a result, the lower yield stresses are better modeled for these hardening functions, while errors may be introduced in the modeling of the other hardening functions. The OPTLYS calibration strategy extends the LYS calibration strategy by considering all experimental data. As a result, the fit to the lower yield stress is a compromise between the lower yield stresses of all the made available hardening functions. Both the LYS and the OPTLYS calibration strategies present the problem of possibly incoherently model the plastic flows, namely the yield stresses trends on the equivalent plastic strains. This aspect is strictly related to how much the best fit for the parameters B and n vary in the considered equivalent plastic strain rate and temperature ranges, i.e. how different are the power forms of the considered hardening functions. As a matter of fact, the LYS and OPTLYS approaches calibrate the parameters B and n only by considering the form of the experimental hardening function obtained by testing the material at the reference conditions. For the case under examination, this hardening function is the one at the equivalent plastic strain rate of 0.001 s^{-1} and at the temperature of 77 K. In fact, the LYS and OPTLYS fittings of the plastic flow are very good for these conditions, but then become worse for the other hardening functions. The more the plastic flow at a given equivalent plastic strain rate and at a given temperature deviates from its form at the reference conditions, the more modeling errors are introduced. The LYS and OPTLYS trends reported in Figs. 36 to 44 confirm these considerations, by proving also that the plastic flow prediction errors may actually be heavy.

The EPS calibration strategy allows for minimizing the modeling errors throughout the equivalent plastic strain ranges, by considering data provided only by those hardening functions which refer to at least one reference condition, whether it is the reference equivalent plastic strain rate or the reference temperature. As a result, the plastic flows are better modeled for these hardening functions, while errors may be introduced in the modeling of the other hardening functions. The OPTEPS calibration strategy extended the EPS calibration strategy by considering all experimental data. As a result, the fit to the plastic flows is a compromise between the plastic flows of all the made available hardening functions. The GOPTEPS calibration strategy further generalizes the OPTEPS calibration strategy by allowing 7 out of the 8 Johnson-Cook parameters to be optimized. As a result, its trends provide the best overall fit for all the experimental made available hardening functions. The GOPTEPS calibration strategy capacity to

better model the plastic flows throughout the equivalent plastic strain rate and temperature ranges is partially due to the fact of avoiding to calculate the parameters B and n by relying on the plastic flow at the reference conditions only, but rather by considering how to best fit all the experimental made available plastic flows, through a power form. This is the reason why the GOPTEPS calibration strategy provides the worst fit for the plastic flow at the reference conditions (0.001 s^{-1} and 77 K) but it is also one of the reasons why it provides the best overall fit to the plastic flows in the other conditions. However, since the parameters B and n are constant, i.e. they are not functions of the equivalent plastic strain rate and the temperature, the more the plastic flows trends at various equivalent plastic strain rates and temperatures are different, the more modeling errors are inevitably introduced.

The EPS, OPTEPS and GOPTEPS calibration strategies present the problem of possibly incoherently model the lower yield stresses, since all these calibration strategies do not assign a privileged role to the lower yield stresses (as the LYS and OPTLYS calibration strategies do), but they are considered as any other value in the plastic flow. The EPS, OPTEPS and GOPTEPS trends in Figs. 36 to 44 confirm these considerations, by proving also that the lower yield stress prediction errors may be heavy. The fact of incoherently model the first yielding implies the relevant problem of introducing an unwanted error in the determination of the transition from the elastic phase to the plastic phase, an aspect that can imply heavy errors in the strain computations. In particular, large errors in the evaluation of the plastic strain may cause heavy problems in the computation of damage and failure, at least for those damage models which mainly rely on the equivalent plastic strain, like, e.g., the Johnson-Cook damage and failure model. On the other hand, even if the lower yield stresses are predicted with bad coherency, if the hardening functions are capable to quickly improve their fitting and get near to the experimental trends, then the error in the transition from the elastic to the plastic phase may be not too harmful. In general, it is always necessary to carefully check the errors in the lower yield stress predictions when the calibration strategy adopted is either the EPS, the OPTEPS or the GOPTEPS, in order to be aware of the presence of possible errors of heavy magnitude.

Another important consideration regards the easiness of calibration, i.e. the number of calculations that each procedure needs in order to get the Johnson-Cook parameters and also the possible necessity of experimental data treatment. In this regard, the simplest calibration strategy is certainly the LYS, which requires only a regression (for determining B and n) together with the simple calculations involved in the determination of the parameters C and m. The OPTLYS calibration strategy involves heavier calculations, due to the fact that an overdetermined nonlinear system is required to be solved. However, this system has only 2 unknowns

(parameters C and m) and refers only to the single points at the lower yield stresses and therefore it does not involve a lot of equations. The great advantage of the LYS and OPTLYS calibration strategies is the fact that inverse analyses of the experimental hardening functions are not necessary, since these approaches utilize only experimental data at the lower yield stresses, for which structural effects can actually be considered as irrelevant.

The procedure necessary to carry-out the EPS calibration strategy is a little heavier, due to the fact that more regressions need to be considered in order to determine the parameters C and m. No overdetermined nonlinear systems need to be solved. Anyway, the main burden here is the fact that the experimental hardening functions need to be treated through inverse analyses, in order to purify results from structural and thermal effects, which are not negligible if data throughout the tested equivalent plastic strain ranges are considered. This aspect implies the necessity to use FEM codes. The OPTEPS calibration strategy further increases the number of calculations to be performed, since it also requires the solving of an overdetermined system of nonlinear equations. This system has only two unknowns (parameters C and m) but involves almost all the made available experimental data, intended in terms of couples of yield stress and corresponding equivalent plastic strain values, or at least a part of them, if it is deemed that considering only a part of this data is enough to properly represent the material behavior. Finally, the GOPTEPS calibration strategy further complicates things by increasing the number of experimental data to be considered and by raising from two to seven the number of unknowns in the overdetermined system, resulting in a problem that is more difficult to solve. All these aspects relative to the different requirements for the calibration of each strategy have contributed in making some calibration strategies more popular than the others. More in detail, the LYS calibration strategy appears to be the most popular, by far, due to its readiness of execution. The OPTLYS calibration strategy seems to be almost unused, while the EPS approach appears to be more known. Seemingly, the OPTEPS calibration strategy is almost unknown, while the GOPTEPS calibration strategy appears to have an average popularity.

Another important aspect pertinent to the choice of which calibration strategy shall be adopted is relative to the quantity of experimental data that are made available. As instance, if the plastic flows are not accessible or if the only known plastic flow is that referring to quasi-static conditions, and only lower yield stresses data are available, only the LYS and OPTLYS calibration strategies are adoptable. On the other hand, if plastic flows data are available, it is possible to choose between the five calibration strategies. In this regard, the following considerations appear to be of utter importance. In order to thoroughly investigate the material behavior, it is necessary to carry-out experimental tests, i.e., to obtain hardening

functions, at several different equivalent plastic strain rates and temperatures, with the aim of covering all the ranges of interest with enough resolution. This is the only way that allows to understand the real material behavior in such ranges, and the more the equivalent plastic strain rate and temperature ranges involved are wide, the more this aspect appears to be relevant. It is quite common to see calibrations of the Johnson-Cook model which rely on very few experimental data, and in particular by considering hardening functions only at two different equivalent plastic strain rates and at two different temperatures. Of course, in such cases the Johnson-Cook model provides very good fitting to experimental data, and this is due to the fact that the strain rate and temperature terms of the model can exactly fit two points in the equivalent plastic strain rate and temperature ranges. But however, the real material behavior outside of the ranges near the two points remains undetermined and may be quite different from the Johnson-Cook model predictions, as just shown in this chapter. Furthermore, it is quite common to fix a priori the values of the reference equivalent plastic strain rate and the reference temperature and then carry-out experimental tests which always refer to at least one reference condition, since this approach allows to calibrate the model through the LYS or the EPS calibration strategies, which are the most popular ones. However, such approach does not involve investigations of the material under conditions in which both the equivalent plastic strain rate and the temperature are different from their reference values. On the basis of the results and considerations pointed-out in this chapter, skipping this investigation may not be optimal, as the real material behavior in such conditions may be quite different from the prediction of a Johnson-Cook model calibrated through the LYS or EPS strategies, as clearly shown in Figs. 36 to 44. As a matter of fact, complicated dependencies of the material behavior on the equivalent plastic strain rate and on the temperature may not be revealed. Further experimental investigations of a material may indeed reveal behaviors of such kind. As instance, the experimental data considered for applying the calibrations introduced in the present chapter, i.e. the data taken from Nemat-Nasser and Guo, 2003, present a more complicated material dependence on the equivalent plastic strain rate and on the temperature. In fact, if data at 500 K are introduced in the analysis, the yield stress does not strictly increase with the equivalent plastic strain rate. Therefore, the more experimental data are considered, the more the material behavior is known but also the more the Johnson-Cook model may present difficulties in fitting complicated material behaviors.

Regarding the obtainment of experimental data, some considerations about the possibility of using Taylor test data to calibrate the Johnson-Cook model are made in the following. Taylor tests can be carried-out with the aim of obtaining data at various equivalent plastic strain rates. However, the experimental data obtainable

from the Taylor test may be biased by important structural effects. As stated above, the calibration of the Johnson-Cook parameters relies on the use of experimental data intended in terms of hardening functions, i.e. curves that relate the yield stress to the equivalent plastic strain. An inverse analysis is necessary in order to obtain a hardening function from Taylor test impact data. However, comparing to Hopkinson bar data, Taylor test results appear to be less prone to be treated with FEM inverse analysis. This aspect is related to the fact that Hopkinson bars, either compressive or tensile, produce more homogeneous equivalent plastic strain, equivalent plastic strain rate and stress fields in the specimen. Furthermore, the temperature control during a Taylor test may present difficulties. A specimen may be heated before being fired against the rigid target, but this process may be difficult to be realized in practice and however does not allow to control the specimen temperature immediately before the impact. In addition, Taylor test data may not be indicative of the material behavior up to fracture, as it is impossible to determine a fracture point in such a test.

All these aspects increase the structural complications involved in the analysis of Taylor test experimental data. Despite these problematics, some authors proposed a procedure to determine the Johnson-Cook parameters from such kind of tests. Among others, references that consider this topic are Johnson and Holmquist, 1988, Johnson and Holmquist, 1991, Allen et al., 1997, and Rule, 1997. The approaches presented in these references rely on the use of some structural data accessible from Taylor test impact results, like the specimen change in diameter and length, or the nature of the whole deformed shape. Anyway, it is worthwhile to point-out that these approaches should be performed with particular attention, due to possible mistakes introduced when trying to relate structural data to pure material behavior.

In this view, the present work relies on the procedure stated above, i.e. high strain rate data are assumed to be Hopkinson bar data. However, if there are Taylor test data available, these data could be used as a structural test of an already calibrated Johnson-Cook model. More in detail, the point here is that of carrying-out FEM simulations on the available Taylor impact data and see how coherently the Johnson-Cook model may fit the data, thus providing a validation of an already calibrated model. Assessments of such kind have been presented in many references, e.g. Johnson and Cook, 1983, Johnson and Holmquist, 1988, and Holmquist and Johnson, 1988, 1991. However, comparisons between FEM and experimental Taylor test results are usually done by comparing structural quantities, such as the specimen diameter or length changes. The FEM computation of these structural parameters depends on many aspects, among which the Johnson-Cook predicted hardening functions. Furthermore, it may be that most of the Taylor test specimen could be subjected to equivalent plastic strain rates and temperatures for

which the Johnson-Cook model provides quite coherent results, therefore producing good FEM simulations of the Taylor test, but this result does not ensure the calibrated Johnson-Cook model to be capable of providing good predictions throughout the equivalent plastic strain rate and temperature ranges of interest. Therefore, even if the calibrated Johnson-Cook model under consideration is capable to provide good results in fitting Taylor test data, its validity should be further checked. In particular, it appears that the only procedure capable to clearly identify the coherency of the model is that of comparing the Johnson-Cook predicted hardening functions against the available experimental hardening functions, as done in Figs. 36 to 44, since this comparison considers exactly what the Johnson-Cook model predicts, i.e. hardening functions.

A last aspect to be considered for choosing which calibration strategy shall be adopted regards whether the particular application in which the model is used is characterized by deformations during which the material undergoes large equivalent plastic strain or not. In the latter case, the adoption of the LYS or OPTLYS calibration strategies shall be favored, while in the former the EPS, OPTEPS or GOPTEPS calibration strategies should be favored. It may then be said that there does not exist a best calibration strategy in absolute terms, but rather that the best choice depends on many aspects relative to each specific case. Basically, it is possible to choose where to accept errors, but not really to avoid them. Only in very lucky cases the material behavior is actually well fit by the Johnson-Cook hardening function, namely cases in which the natural logarithm and the power dependences of the yield stress on the dimensionless equivalent plastic strain rate and on the homologous temperature are respected, together with the fact of having the parameters B and n independent from the equivalent plastic strain rate and the temperature.

In cases in which the Johnson-Cook model fits very poorly the experimental data, it may be worthwhile to consider a replacement of either the strain rate term or the temperature term, or both, in order to alleviate the Johnson-Cook first issue. Beyond this aspect, following Chapter 3 introduces a generalization of the Johnson-Cook model that appears to be capable of providing always better results, thanks to a mitigation of the second Johnson-Cook issue.

2.2.2. Zerilli-Armstrong Model

The wording Zerilli-Armstrong strength model refers to the hardening function proposed in Zerilli and Armstrong, 1987. The authors aimed at an improvement of the Johnson-Cook strength model, Eq. (28), by formulating a more sophisticated hardening function. As for the Johnson-Cook model, particular attention was paid to the necessity of maintaining a good predisposition to FEM codes and hydrocodes

implementations, and also keeping the capabilities to fit material data over wide ranges of equivalent plastic strain rates and temperatures. The authors proposed a critical review of the Johnson-Cook hardening function. In particular, considerations relative to incoherencies due to the total empirical nature of the model were pointed-out.

The framework of the Zerilli-Armstrong model consists in the classic elastoplastic model already used for the Johnson-Cook model. However, the strength model proposed in Zerilli and Armstrong, 1987, relied on some micromechanical considerations. The authors proposed a form for the evaluation of the yield stress as a function of the equivalent plastic strain, the equivalent plastic strain rate and the temperature, as for the Johnson-Cook model, but it was also stated that the atomic structure of the material does have an effect on the determination of the hardening laws. Indeed, the presented strength model was based on considerations stemming from dislocation mechanics. Following this statement, the two authors presented a model in which some microstructural parameters found place. More in detail, a hardening function suitable for face centered cubic metals and another hardening function suitable for body centered cubic metals were introduced. They are respectively reported in the following equations

$$\bar{s} = C_0 + C_2 \cdot \sqrt{\bar{\varepsilon}_p} \cdot e^{-C_3 \cdot T + C_4 \cdot T \cdot \ln \dot{\bar{\varepsilon}}_p} + k \cdot \sqrt{L}\,, \tag{47}$$

$$\bar{s} = C_0 + C_1 \cdot e^{-C_3 \cdot T + C_4 \cdot T \cdot \ln \dot{\bar{\varepsilon}}_p} + C_5 \cdot \bar{\varepsilon}_p^{\,n} + k \cdot \sqrt{L}\,. \tag{48}$$

In these equations, the material parameters are represented by C_0, C_1, C_2, C_3, C_4, C_5, k, L and n. More in detail, k indicates the so-called microstructural stress intensity, while L denotes the material average grain diameter. The remaining 6 parameters are to be determined from experimental investigations. Reviewing the procedure necessary to calibrate these parameters is not an aim of the present work.

As shown in Eqs. (47) and (48), the two hardening functions introduce different dependences on the equivalent plastic strain. In particular, the hardening function for face centered cubic metals implies a square root dependence, while the hardening function for body centered cubic metals implies a more general exponential dependence. Moreover, the yield stress dependence on the equivalent plastic strain rate and on the temperature is combined in an exponential fashion. The microstructural parameters, i.e. the microstructural stress intensity and the

material average grain diameter, are considered to act in the same manner for both hardening functions.

Zerilli and Armstrong, 1987, proposed a calibration of the new model on the same experimental data used and presented in Johnson and Cook, 1983, in particular by relying on two of the materials tested therein, i.e. OFHC copper and Armco iron. The model parameters for these two materials were presented as well. The Zerilli-Armstrong model was also implemented into the FEM code EPIC-2. The obtained results showed a good fitting to experimental data, better than that determined by the Johnson-Cook hardening function.

An assessment of the results provided by the Johnson-Cook and the Zerilli-Armstrong models is reported also in Holmquist and Johnson, 1988, in the context of the computational simulations of Taylor tests. The Zerilli-Armstrong model showed a better agreement with experimental measurements. Holmquist and Johnson, 1991, extended this analysis by introducing in the study the Holmquist and Johnson modification of the original Johnson-Cook model, namely Eq. (29). This last model did not determine conspicuous differences, comparing to the results obtained with the other considered strength models. Samantaray et al., 2009, provided a comparison of the outcomes from the Johnson-Cook model, a so-called modified Zerilli-Armstrong model and another strength model, with the aim to predict elevated temperature flow behaviour in a modified 9Cr-1Mo steel. It was shown that the Zerilli-Armstrong model provides better results comparing to the Johnson-Cook model, throughout the equivalent plastic strain, the equivalent plastic strain rate and the temperature tested ranges. Lin and Chen, 2010, presented an application of the Johnson-Cook model and the Zerilli-Armstrong model to an high-strength steel, by considering the temperature range between 850 K and 1150 K and equivalent plastic strain rates ranging from 1 s^{-1} to 50 s^{-1}. Both strength model predictions showed deviations from the experimental data. In this context, a combined Johnson-Cook and Zerilli-Armstrong model was presented. The model was capable to provide somehow better results. Gupta et al., 2013, presented a comparison between the Johnson-Cook model, the Zerilli-Armstrong model and other strength models, showing that the Johnson-Cook model provided the worst fit to some available experimental data.

This very brief review indicates only some of the many applications of the Zerilli-Armstrong strength model that can be found in the literature. However, based on it, it may be said that the Zerilli-Armstrong model appears to be capable to provide improvements on the modeling coherency, when comparing to the Johnson-Cook model. On the other hand, the parameters of the model require the availability of more information on the considered material. In particular, the determination of the micromechanical related parameters may not be straightforward in some cases.

Further considerations and developments on the Zerilli-Armstrong model may be found in Meyers et al., 2002.

2.2.3. Steinberg-Cochran-Guinan and Steinberg-Lund Models

The wordings Steinberg-Cochran-Guinan model and Steinberg-Lund model refer to the two strength models proposed in Steinberg et al., 1980, and Steinberg and Lund, 1988, respectively. The Steinberg-Lund model is a generalization of the Steinberg-Cochran-Guinan model. A brief review of the Steinberg-Cochran-Guinan model is proposed below, followed by a review of the Steinberg-Lund model.

The Steinberg-Cochran-Guinan model was developed with the aim of fitting the behavior of metals subjected to very high strain rates. In particular, the model was conceived with the target to fit experimental data at equivalent plastic strain rates equal or greater than 10^5 s^{-1}, approximately. At these conditions, the equivalent plastic strain rate influence on the yield stress appears to be constant, i.e. the yield stress does not change anymore if higher equivalent plastic strain rates are involved. The point here is that, although the yield stress increases with the equivalent plastic strain rate, it does not appear reasonable to expect it to do so without any limit. In particular, based on shock wave experimental results presented by the same authors (Steinberg et al., 1980), it was assumed that when the equivalent plastic strain rate value of 10^5 s^{-1} is reached, the material behavior can effectively be considered as rate-independent. The authors related the aspect of having a rapid decrease of rate dependent effects with increasing equivalent plastic strain rate to the fact that this kind of phenomena implies also a strong temperature increase, which may actually melt the material. As a matter of fact, rate dependent effects in liquids appear to decrease exponentially with temperature. A similar strong temperature dependence was hypothesized for shocked solids. It is worthwhile to note that other references pointed-out this same consideration. As instance, Wilkins and Guinan, 1973, presented experimental data that showed the manifestation of a critical equivalent plastic strain rate beyond which the material behavior appears to be rate-independent. This statement was sustained also by some computational simulations of high speed Taylor tests.

Comparing to the Johnson-Cook and the Zerilli-Armstrong models, the Steinberg-Cochran-Guinan model introduces more assumptions in order to coherently model such very high strain rate behaviors, then resulting in a more complicated framework. The main aspect considered in Steinberg et al., 1980, was the fact that both the shear modulus and the yield stress are functions of the pressure and the temperature, and in particular they increase with increasing pressure and decrease with increasing temperature. More in detail, the model does not consider the shear modulus G as constant with the pressure, the temperature

and the equivalent plastic strain rate, but rather it considers G as a function of such variables. The same assumption is made for the yield stress. The forms of these two functions were created based on experimental observations. Regarding the shear modulus, the authors were capable to collect an extensive amount of data. These measurements showed the pressure and temperature variation of the shear modulus, thus allowing to write down a relation between these parameters. The relation for the shear modulus is reported in the following equation

$$G = G_0\left(1+\frac{1}{G_0}\cdot\left.\frac{\partial G}{\partial p}\right|_0\cdot\frac{p}{\sqrt[3]{\eta}}+\frac{1}{G_0}\cdot\left.\frac{\partial G}{\partial T}\right|_0\cdot\left(T-300\right)\right). \tag{49}$$

In this equation, all the variables with the subscript 0 are intended at the reference condition, which is defined as the state with temperature of 300 K, null pressure and null equivalent plastic strain. Pressure and temperature are denoted by p and T, respectively. Partial derivatives of the shear modulus with respect to the pressure and the temperature, evaluated at the reference state, are required. The symbol η denotes the so-called compression, defined as the initial specific volume v_0 divided by the current specific volume v, as indicated in the following equation

$$\eta = \frac{v_0}{v}. \tag{50}$$

Eq. (49) has been conceived with the aim of following both experimental and theoretical observations. In particular, at low pressures, say lower than 2 GPa, the shear modulus G varies linearly with pressure. At ultrahigh pressures, the Thomas-Fermi theory (see, e.g., Lieb and Simon, 1977, for a description of such theory) states that the shear modulus is proportional to the parameter η raised to the power 4/3. Steinberg et al., 1980, presented considerations about the fact that Eq. (49) is actually capable to respect both conditions with good accuracy, showing how this equation owns appropriate limiting behavior at both low and high pressures.

Furthermore, Steinberg et al., 1980, stated that, for many important engineering materials, the shear modulus G decreases nearly linearly with temperature. This linear dependence may not be true anymore when the melting temperature is approached. However, Eq. (49) can be used with the adoption of a linear shear modulus dependence on temperature, up to the melting limit, thus allowing to evaluate the shear modulus derivative with respect to the temperature as a constant. This aspect was considered acceptable by the authors considering that Eq. (49) shear modulus temperature dependent term is deemed to be typically the

10% of the pressure dependent term, and therefore the precision of its determination is not absolutely critical.

The Steinberg-Cochran-Guinan model introduced also a hardening function. As done for the shear modulus, the effects of the pressure and of the temperature were considered, together with a dependence on the equivalent plastic strain. The proposed hardening function is reported in the following equation

$$\bar{s} = \bar{s}_0 \left(1+\beta \cdot \left(\bar{\varepsilon}_p + \bar{\varepsilon}_{pi}\right)\right)^n \cdot \left(1+\frac{1}{\bar{s}_0}\cdot\left.\frac{\partial \bar{s}}{\partial p}\right|_0 \cdot \frac{p}{\sqrt[3]{\eta}} + \frac{1}{G_0}\cdot\left.\frac{\partial G}{\partial T}\right|_0 \cdot (T-300)\right). \qquad (51)$$

The proposed hardening function is based on a power dependence on the equivalent plastic strain, reported in the first round parentheses. The parameter $\bar{s}_0$ represents the lower yield stress at the reference conditions, while β and n are hardening parameters used to fit the experimental data. If necessary, an initial equivalent plastic strain can be introduced, denoted by $\bar{\varepsilon}_{pi}$. This option may be useful to account for plastic deformations that the material might have undergone, like rolling or machining, although usually this parameter is considered to be null. The power form was adopted since it appeared as the one capable to best fit the metals tested in Steinberg et al., 1980. Furthermore, the authors highlighted its consistency with the indications pointed-out in Wilkins and Guinan, 1973, in which Taylor tests capable to reach equivalent plastic strain rates equal to 10^5 s^{-1} were presented, by considering several metals.

The second round parentheses include the terms that regulate the yield stress dependence on the pressure and on the temperature. It is conceived in a form very similar to the one adopted for the dependence of the shear modulus on these same two variables. This last aspect stems from some assumptions due to the lack of definitive data relatively to the yield stress dependence on the pressure and the temperature. More in detail, the temperature dependence of the yield stress is assumed to be equal to the temperature dependence of the shear modulus. This point justifies the presence in Eq. (51) of the partial derivatives of the shear modulus with respect to the temperature, evaluated at the reference state. The pressure dependence of the yield stress is instead modeled through the partial derivative of the yield stress with respect to the pressure itself, calculated at the reference state.

In order to further enhance the strength model, Steinberg et al., 1980, coupled Eqs. (49) and (51) with a simply melting model. This aspect allowed for accounting for the solid-liquid phase transition of shocked solid materials. The same reference presented some interesting computer simulations of shock wave experiments, in which the model appears to predict very well the experimental data. Further

computational applications of the model may be found in Steinberg, 1987, together with a discussion of some of its deficiencies. Further considerations about the model can be also found in Steinberg and Sharp Jr., 1988.

Following Steinberg et al., 1980, it is also possible to modify Eqs. (49) and (51) by replacing the temperature with the internal energy, in order to make these equations more suitable for implementations in FEM codes or hydrocodes that operate with energy rather than temperature. The link between the temperature and the energy can be set by defining the temperature as the difference between the total energy E and the energy along the zero Kelvin isotherm, E_c, divided by the specific heat C, as reported in the following equation

$$T = \frac{E - E_c}{C}. \tag{52}$$

Further information about the quantity E_c and the thermodynamic considerations on which it is based may be found in Guinan and Steinberg, 1974, and in Steinberg et al., 1980.

Steinberg and Lund, 1988, presented a hardening function that aimed at replacing Eq. (51). The point was that of extending the Steinberg-Cochran-Guinan hardening function in order to fit also mid and low equivalent plastic strain rates regimes. In particular, the target was that of extending the validity of the Steinberg-Cochran-Guinan model to fit experimental data over an equivalent plastic strain rate range spanning from 10^{-4} s^{-1} to 10^{6} s^{-1}. The Steinberg-Lund model is reported in the following equation

$$\bar{s} = \left(\bar{s}_T \left\{ \dot{\bar{\varepsilon}}_p, T \right\} + \bar{s}_H \left\{ \bar{\varepsilon}_p \right\} \cdot \bar{s}_A \right) \cdot \frac{1}{G_0} \cdot \left. \frac{\partial G}{\partial T} \right|_0 . \tag{53}$$

In this equation, $\bar{s}_H\{\bar{\varepsilon}_p\}$ represents a hardening term that is intended to be an undetermined function of the equivalent plastic strain. For instance, it may be conceived in the same power fashion adopted in the Steinberg-Cochran-Guinan model. The symbol $\bar{s}_A$ denotes a not better specified athermal part of the strength model. The symbol $\bar{s}_T\left\{\dot{\bar{\varepsilon}}_p, T\right\}$ denotes a so-called thermal part of the strength model. Following Hoge and Mukherjee, 1977, Steinberg and Lund, 1988, related this term to the following expression of the equivalent plastic strain rate

$$\dot{\bar{\varepsilon}}_p = \frac{2}{\rho \cdot L \cdot a \cdot b^2 \cdot \nu \cdot \omega^2} \cdot e^{\frac{2 \cdot U_k}{k \cdot T}\left(1 - \frac{\bar{s}_T}{Y_p}\right)^2} + \frac{D}{\rho \cdot b^2 \cdot \bar{s}_T}. \qquad (54)$$

In this equation, ρ represents the dislocation density, a the distance between Peierls valleys, b the Burgers vector, ν the Debye frequency, ω the width of a kink loop, $2 \cdot U_k$ the energy necessary to form a pair of kinks in a dislocation segment of length L, k the Boltzmann constant, D the drag coefficient and Y_p the Peierls stress. As usual, temperature is denoted by T. Eq. (54) is conceived together with the assumption that the thermal part of the stress is limited to be lower than the Peierls stress.

In Steinberg and Lund, 1988, the model was utilized in a series of computational simulations that showed a good coherence of the computed results with experimental data, even at low strain rates. Beyond these results, Zocher et al., 2000, presented a comparison of the results provided by the Johnson-Cook model, the Steinberg-Cochran-Guinan model and another strength model in the context of computational simulations of Taylor tests, carried-out with the FEM code CHAD (Computational Hydrodynamics for Advanced Design). The outcomes proved that the Johnson-Cook model provides the worst fit to experimental data, while the Steinberg-Cochran-Guinan model is actually capable to fit the data with very good coherency.

As a conclusion, it may be said that the Steinberg-Cochran-Guinan and the Steinberg-Lund strength models are capable to provide good modeling capabilities when very high strain rates, pressures and temperatures are involved, resulting in more coherent results when comparing to the other strength models considered in this work, namely the Johnson-Cook and the Zerilli-Armstrong models. On the other hand, these advanced models require the knowledge of a number of parameters that may be difficult to be determined in practice, in particular for the Steinberg-Lund model. To this end, a significant reference is Steinberg, 1996, in which the Steinberg-Cochran-Guinan model parameters are provided for a considerable number of materials.

2.3. Equations of State

Following Lemons and Lund, 1999, Equations Of State (EOS) characterize specific systems. This statement means that an equation of state is a function that involves two or more variables representative of the state of a material. As example, the ideal gas equation of state is used to model behavior of gases at low densities, by relating variables such as the relative volume, the pressure and the temperature.

While EOS for low density gases are usually similar, EOS for solids do exhibit a great variety of forms. This aspect is related to the fact that molecular lattices of solid matter may exist in numerous different forms, resulting in several classes of materials, like, e.g., metals, ceramics, composites and so on. For these reasons, EOS for gases are much more known than EOS for solids. Equations of state for solids can be effectively represented through analytical forms. In the present work, equations of state for solids are of specific interest. In particular, such EOS are intended here as functions capable to represent the volumetric material behavior of solid materials.

An equation of state for solids may involve several parameters, such as some measures of the volumetric strain, the temperature, the specific heat and possibly other thermodynamic parameters representative of the material behavior. As stated in Zukas, 2004, the parameters of EOS for solids are usually calibrated through flyer plate impact experiments. As a matter of fact, practical restrictions limit both the mass and the velocity of flyer plates. This aspect leads to the existence of a technological upper limit for pressures experimentally investigable in solid matter. This pressure value may be identified as in the neighborhood of 600 GPa, although technological improvements keep on enlarging the capabilities of experimentally investigating material responses. However, this limiting value is very large. It actually exceeds the pressure conditions within the center of the Earth. Following Asay and Shahinpoor, 1993, the use of plate impact experimental procedures begun after 1955, both in USA and URSS scientific laboratories. Pressure responses of virtually hundreds of condensed materials have been studied, including elements, compounds, alloys, rocks and minerals, polymers, fluids and porous media. The experimental procedures have required the use of both conventional and nuclear explosives, or impactors launched with speeds exceeding 10 km/s.

The present thesis aims at briefly introducing two of the most popular equations of state used for the modeling of high pressure behavior of metallic materials, i.e. the Mie-Grüneisen (Mie, 1903, and Grüneisen, 1912) and the Tillotson (Tillotson, 1962) equations of state. Moreover, a concise introduction to the Jones-Wilkins-Lee EOS (Jones and Miller, 1948, Wilkins et al., 1965, and Lee et al., 1968) is presented, in order to introduce an EOS capable of modeling the volumetric behavior of detonation products of explosives. The treatment provided here does not involve considerations on thermodynamic aspects and shock wave phenomena, but aims simply at exposing the way in which the considered equations of state model the pressure response of the materials.

Beyond the very concise introduction presented here, extensive treatments on equations of state for condensed matter may be found, e.g., in Asay and

Shahinpoor, 1993, Meyers, 1994, Fortov et al., 2004, and Zukas, 2004. A specific treatment on equations of state for metals is provided in Rose et al., 1984.

2.3.1. Mie-Grüneisen Equation of State

The wording Mie-Grüneisen equation of state is used to refer to a relation which considers the pressure of a solid material as a linear function of its internal energy. This equation of state is usually related to the work presented by Mie, 1903, and Grüneisen, 1912, although it may be linked to older references. Mendoza, 1982, provided a review of the history of the Mie-Grüneisen equation of state, presenting the more important developments that led to the final form of the model, tracking back to references published in the year 1843. Regardless of its history, the popularity and importance of this equation of state has grown throughout the years and nowadays it is widely used for the modeling of solids, under compressive pressures up to a few hundreds of GPa, say without exceeding 1000 GPa. Furthermore, it is sometimes used to model liquids, in particular when high compressive pressures are involved, even though it was originally conceived with the aim to model solid state matter. The Mie-Grüneisen equation of state is reported in the following relation

$$p = p_{ref} + \gamma \cdot \rho \cdot \left(E - E_{ref} \right). \tag{55}$$

In this equation, p_{ref} and E_{ref} denote respectively the pressure and the internal energy evaluated in the same reference state, while p and E represent respectively the pressure and the internal energy at a generic state. The material density is denoted by ρ and γ denotes the so-called Grüneisen parameter, defined by the following equation

$$\gamma = -\frac{\partial \ln(\xi)}{\partial \ln(v)}. \tag{56}$$

In this equation, ξ and v denote the atomic vibration frequency and the specific volume, respectively. In general, a solid material possesses more than one atomic vibration frequency. Grüneisen, 1912, simplified the treatment by assuming these frequencies to display the same value, denoted by ξ. This assumption allows to define a single Grüneisen parameter, as defined in Eq. (56). Otherwise, further Grüneisen parameters would be needed. For a general treatment on this aspect, see, e.g., Meyers, 1994, in which it is also possible to find a derivation of the

Grüneisen parameters starting from statistical assumptions on the atomic state of solid matter.

As shown in Steinberg, 1981, the Grüneisen parameter can be assumed to be constant with temperature, at least up to a substantial fraction of the melting temperature. It can then be assumed to be a function of the sole specific volume. Following Heuzé, 2012, it is possible to express the Grüneisen parameter by using other thermodynamic variables, such as the temperature. Moreover, Zukas, 2004, presented a further expression of the Grüneisen parameter, whose importance relies on the fact that it involves thermodynamic parameters that are usually known, such as the bulk modulus, denoted by K, the specific heat, denoted by C, and the thermal expansion coefficient, denoted by α. This relation is exposed as follows

$$\gamma = \frac{3 \cdot K \cdot \alpha}{\rho \cdot C}. \tag{57}$$

It is recalled that, under the assumption of isotropic behavior, the bulk modulus K is linked to the Young modulus E and the Poisson's ratio ν through the following classic relation

$$K = \frac{E}{3 \cdot (1 - 2 \cdot \nu)}. \tag{58}$$

The Mie-Grüneisen equation of state is sometimes said to be an incomplete equation of state, due to the fact that it is expressed in such a way that the pressure becomes a function of a volumetric strain measure and of the internal energy. Therefore, it does not allow to access neither temperature nor entropy. In order to make it a complete or general EOS, two other forms need to be specified, i.e. a form in which the temperature is a function of the volumetric strain and the internal energy and a form in which the entropy is a function of these same two variables. Details on how to get these two further forms of the Mie-Grüneisen equation of state and about their thermodynamic consistency can be found in Heuzé, 2012, and in Menikoff, 2012.

The Mie-Grüneisen equation of state is extensively used in FEM codes and hydrocodes. In these contexts, the EOS is elaborated in a structure more suitable to be used within such codes, which involves two forms that separately compute the pressure under compression and under tension. As exposed in Steinberg, 1996, the following form is usually adopted for the description of compressive volumetric behavior

$$p = \frac{\rho_0 \cdot C^2 \cdot \mu \cdot \left(1 + \left(1 - \frac{\gamma_0}{2}\right) \cdot \mu - \frac{a}{2} \cdot \mu^2\right)}{\left(1 - (S_1 - 1)\mu - S_2 \cdot \frac{\mu^2}{\mu + 1} - S_3 \cdot \frac{\mu^3}{(\mu + 1)^2}\right)^2} + (\gamma_0 + a \cdot \mu) \cdot \rho \cdot E. \quad (59)$$

Several additional parameters appear in this equation. The parameters γ_0 and ρ_0 denote the Grüneisen parameter and the density at a reference state, respectively. The so-called first order volume correction to the Grüneisen parameter is denoted by a. The non-dimensional parameters S_1, S_2 and S_3 characterize the volumetric material behavior and are obtained from plate impact experiments. The parameter μ describes the volumetric strain of the material in the form defined by the following equation

$$\mu = \frac{\rho}{\rho_0} - 1, \quad (60)$$

where ρ denotes the current density. The parameter C denotes the bulk sound speed, which is a function of the longitudinal and transversal sound speeds in the material, denoted by C_l and C_s respectively, as indicated by the following equation

$$C = \sqrt{C_l^2 - \frac{4}{3} C_s^2}. \quad (61)$$

When tensile volumetric behavior is involved, the equation of state assumes the following form

$$p = \rho_0 \cdot C^2 \cdot \mu + \gamma_0 \cdot \rho \cdot E. \quad (62)$$

Further information on the Mie-Grüneisen equation of state can be found in many references. Among others, applications of the Mie-Grüneisen EOS to the modeling of water are provided in Steinberg, 1987. A treatment on the thermodynamic stability of the Mie-Grüneisen equation of state can be found in Segletes, 1991, together with some considerations on its implementation in FEM codes and hydrocodes. Meyers, 1994, provided a discussion on the topic, including also some considerations about the use of the Mie-Grüneisen equation of state for the modeling of predicting the shock response of porous materials. Parameters of the Mie-Grüneisen equation of state for several materials can be found in

Steinberg, 1996. Interesting considerations are provided in Lemons and Lund, 1999, in which the use of the Mie-Grüneisen EOS for condensed matter at high temperatures is discussed. Further information can be found in Zukas, 2004, and in the extensive treatment provided by Nagayama, 2011.

2.3.2. Tillotson Equation of State

Tillotson, 1962, introduced an equation of state conceived with the aim of modeling metals subjected to ultra-high pressures and phase changes, such as melting or vaporization.

The followed strategy was that of considering more equations of state, in order to coherently model the material behavior under quite different pressure loadings. More in detail, it was pointed-out that the Mie-Grüneisen equation of state is capable to model with enough coherency compressive material behavior up to pressures of 500-1000 GPa. However, it was also pointed-out that the assumption of considering the Mie-Grüneisen coefficient as a function of the sole specific volume (see Eq. (56)) may no longer be justified, in particular at increasing internal energy. As a consequence, beyond pressure values of 500-1000 GPa, other models were assumed to be more coherent, with particular reference to the Thomas-Fermi statistical theory of atoms (see, e.g., Lieb and Simon, 1977). It was recognized that such theory provides poor results in the modeling of solid materials subjected to pressures lower than 1000 GPa, but it was also pointed-out how this theory, and its modifications, are actually capable to properly model the observed material behavior under compressive pressures higher than 1000 GPa.

As a matter of fact, Tillotson, 1962, considered extreme loading conditions, in terms of compressive pressures. For instance, it was pointed-out how the impact of tungsten projectiles against tungsten targets, up to impact velocities of 100 km/s, can result in enormous peak pressures of 90000 GPa, i.e. 900 Mbar. In this context, the developed model aimed at achieving the capability to coherently model such hypervelocity impacts, considering a range of compressive pressures that goes beyond the modeling capacity of the Mie-Grüneisen equation of state. Following these considerations, the author classified the compressive pressures in two ranges, the first one (called “low pressures”) lower than 1000 GPa and the second one (called “high pressures”) exceeding this value.

The proposed equations of state considered basically two regimes. The first one deals with material not yet melted nor vaporized. It considers the following form

$$p = \left(a + \frac{b}{\frac{E}{E_0 \cdot (1+\mu)^2} + 1} \right) \cdot E \cdot \rho + A \cdot \mu + B \cdot \mu^2 \,. \tag{63}$$

In this equation, a, b, A, B and E_0 are material parameters to be determined from experimental data, while p, E, ρ and μ have the same meaning previously assigned to the description of the Mie-Grüneisen EOS. This equation of state is conceived with the aim to model both positive (expansive) and negative (compressive) volumetric behavior of metallic solid materials.

The modeling of metallic materials in which a phase change has occurred was assumed to be described by another equation of state, which considered the solid material as being transformed into a gas. The following form was proposed

$$p = a \cdot E \cdot \rho + \left(\frac{b \cdot E \cdot \rho}{\frac{E}{E_0 \cdot (1+\mu)^2} + 1} + A \cdot \mu \cdot e^{-\beta \cdot \left(\frac{v - v_0}{v_0} \right)} \right) \cdot e^{-\alpha \cdot \left(\frac{v - v_0}{v_0} \right)^2} \,. \tag{64}$$

In this equation, two additional material parameters are introduced, denoted by α and β. These two variables control the rate of convergence of Eq. (64) to the ideal gas equation of state. See Tillotson, 1962, for further information on this aspect.

The equations of state defined by Eqs. (63) and (64) provide a compromise between the Mie-Grüneisen equation of state, at low pressures, and the Thomas-Fermi theory, at high pressures. Tillotson, 1962, declared this approach to be capable to provide results accurate to within 3% to 5%, below 500 GPa, and within 10% for all other pressures.

Beyond the few considerations presented in this brief overview, further information on the Tillotson equation of state can be found in Tillotson, 1962, in which thermodynamic motivations are presented, together with material parameters relative to nine different metals and a relevant amount of experimental data. Further considerations may also be found in Zukas, 2004.

2.3.3. Jones-Wilkins-Lee Equation of State

The Jones-Wilkins-Lee equation of state (also referred to as JWL equation of state) is an empirical model used to describe the volumetric behavior of detonation

products of explosives. Its development derives from the treatments proposed by Jones, 1947, Jones and Miller, 1948, Wilkins et al., 1965, and Lee et al., 1968.

The JWL equation of state lies on empirical bases. Basically, it provides a relation that allows to calculate the pressure of the gaseous products resulting from the detonation of explosive materials. Jones and Miller, 1948, proposed the following form for evaluating such pressure

$$p = A \cdot e^{-R \cdot v} - B + C \cdot T . \tag{65}$$

In this equation, v represents the relative volume, defined by the ratio of the current volume and the initial volume, while p and T represent the pressure and the temperature, as usually done. The parameters A, B, C and R need to be determined from experimental measurements.

Wilkins et al., 1965, provided experimental investigations and theoretical considerations. In particular, the equations of state of the high explosives PBX 9404 and LX04-01 were experimentally derived, by means of experiments conducted with spheres of explosive materials. On the basis of the obtained measurements, the authors proposed the following equation of state, which aims at describing the pressure of the detonation products

$$p = \frac{a \cdot (Q-1)}{v^{Q} \cdot (Q-1-\omega)} + B \cdot \left(1 - \frac{\omega}{R \cdot v}\right) \cdot e^{-R \cdot v} + \frac{\omega \cdot E}{v} . \tag{66}$$

In this equation, v and E denote again the relative volume and the internal energy. The other parameters, i.e. a, Q, ω, B and R, are to be determined from experimental observations.

Lee et al., 1968, gathered the information provided by Jones and Miller, 1948, and Wilkins et al., 1965, and further developed the treatment by extending the experimental investigations and by enriching the model. The authors pointed-out the capability of the model proposed in Wilkins et al., 1965, to accurately predict expansions of detonation products, in particular during the early stages of such processes. On this basis, the experimental investigations carried-out by Wilkins et al., 1965, were extended by considering so-called cylindrical metal expansion experiments, in order to further develop the model and in particular to make it capable to coherently model large expansions of the detonation products, i.e. to describe explosive processes throughout their evolution, even their latter stages. Lee et al., 1968, proposed the following equation of state and referred to it as Jones-Wilkins-Lee EOS

$$p = A \cdot \left(1 - \frac{\omega}{R_1 \cdot v}\right) \cdot e^{-R_1 \cdot v} + B \cdot \left(1 - \frac{\omega}{R_2 \cdot v}\right) \cdot e^{-R_2 \cdot v} + \frac{\omega \cdot E}{v}. \quad (67)$$

In this equation, v and E denote again the relative volume and the internal energy. The parameters A, B, R_1, R_2 and ω need to be determined from experiments. The form of the Jones-Wilkins-Lee equation of state allows to impose two important thermodynamic limitations at large expansions. First, this equation is capable to keep a fix total available energy, thus avoiding unrealistic divergences. Such total energy value is determined by assuming consistency with the chemical energy made available by a specific explosive, which may be experimentally determined through detonation calorimetry. Second, the Jones-Wilkins-Lee equation of state implies the detonation process at large values of relative volumes to be ruled basically by the value of the parameter ω. Following experimental observations, the authors limited this parameter to be greater than 0.2 and smaller than 0.4, in order to avoid unrealistic modeling of explosions when large expansions of the detonation products are involved. The authors claimed that the respect of these thermodynamic criteria implies the fact that Eq. (67) should not only be useful for engineering purposes but also serve as a description of the thermodynamic behavior of expanding gases resulting from explosive detonations. Lee et al., 1968, provided also the JWL parameters for ten explosives, together with a complete tabulation of the obtained experimental results.

Beyond the very brief introduction presented here and the three main related references, further information on the Jones-Wilkins-Lee equation of state can be found in Baudin and Serradeill, 2010, in which a description of the equation of state and its thermodynamic properties is presented, together with the proposal of a new derivation of the EOS. Anyway, it is necessary to say that, in order to fully describe the Jones-Wilkins-Lee equation of state from a thermodynamic point of view, the Chapman-Jouguet theory needs to be introduced. This is not an aim of this brief review. In this regard, pertinent treatments can be found in Chapman, 1899, Sternberg, 1970, Cooper, 1996, Chéret, 1999, and Fickett and Davis, 2000.

2.4. Damage and Failure Models

Damage and failure models aim at extending the description of material behavior by introducing criteria capable to account for the damage that the material has undergone, up to a failure level. Such models are usually conceived by creating a function of appropriate variables, like e.g. the equivalent plastic strain, whose values determine the level of undergone damage, through a so-called damage variable. Furthermore, limiting values on such variables can be set, with the aim of

triggering material failure. Simple damage and failure models do not imply that the damage variable may affect the value of some material parameters, such as its elastic or elastoplastic stiffness. The target is only that of providing a variable capable of indicating the amount of damage that the material has undergone, together with a cut-off value which determines whether the material has failed or not. More complicated models are instead capable to account for the variation of material properties (such as stiffness) due to the accumulated damage.

In the context of high strain rate phenomena, several damage and failure models have been proposed and developed. The present chapter aims at briefly introducing some considerations regarding damage and failure models used in this work. In this view, a short introduction to the so-called Johnson-Cook damage and failure model is provided, together with some considerations about the so-called spall phenomena.

It is recognized that the damage models introduced here are quite simple and more elaborated models may actually be introduced within the realm of continuum damage mechanics. In this regard, some considerations may be found in Carol et al., 1994 and 2001. Furthermore, an interesting contribution is provided in Carol et al., 2002, in which a damage model based on a volumetric and deviatoric decomposition is presented. This formulation may fit well in the context considered in the present work, i.e. a division of the constitutive model into its deviatoric and volumetric parts, through strength models and equations of state, respectively. Moreover, aspects relative to strain localization and localized damage are not addressed in this work. In this regard, information may be found, e.g., in Bigoni and Hueckel, 1991, Bigoni and Zaccaria, 1993, Loret et al., 1995, Rizzi, 1995, and Rizzi et al., 1996.

2.4.1. Johnson-Cook Damage and Failure Model

Johnson and Cook, 1985, proposed a cumulative damage and fracture model suitable for materials subjected to large strains, over a possible wide range of strain rates, temperatures and stress triaxialities. As for the Johnson-Cook hardening function, the willing was that of keeping the formulation well suitable for implementations in FEM codes. Three different metals, i.e. OFHC copper, Armco iron and 4340 steel, were analyzed through a high number of experimental tests, which aimed at revealing the fracture strain, over certain ranges of equivalent plastic strain rates, temperatures and stress triaxialities. Both tensile and torsion tests were considered, together with investigations carried-out through a Hopkinson bar. In order to explore high temperature behavior, ovens capable to properly heat the specimens were used.

Johnson and Cook, 1985, proposed to relate the cumulated damage to the value of equivalent plastic strain occurred in the material. A cumulative scalar damage parameter, denoted by D, was introduced. Assuming to divide the time of the material evolution in timesteps, the increment of the damage parameter is then calculated in each timestep. The cumulative damage is evaluated as the sum of the ratios between the increment of the equivalent plastic strain, denoted by $\Delta\bar{\varepsilon}_{p_i}$, and a so-called equivalent plastic strain to fracture, denoted by $\bar{\varepsilon}^{f}_{p_i}$, in each timestep i, for a total number of n timesteps. Therefore, the following relation is established

$$D = \sum_{i=1}^{n} \frac{\Delta\bar{\varepsilon}_{p_i}}{\bar{\varepsilon}^{f}_{p_i}}. \tag{68}$$

The damage parameter D is defined in such a way that when its value is zero there is no damage. On the other hand, when its value increases, the material damage increases accordingly. When D reaches the value of 1 the material is assumed to be completely damaged, thus triggering material fracture due to damage.

The equivalent plastic strain to fracture is assumed to be the equivalent plastic strain value at which the material has reached complete damage, i.e. when it fractures. This value varies in each timestep, since it is assumed to be a function of the current conditions of equivalent plastic strain rate, temperature and stress triaxiality. Indeed, the key point of this model is the definition of such equivalent plastic strain to fracture. On the basis of the obtained experimental results, Johnson and Cook, 1985, pointed-out that the equivalent plastic strain to fracture exhibited an exponential dependence on the stress triaxiality, a natural logarithmic dependence on the dimensionless equivalent plastic strain rate, Eq. (26), and a linear dependence on the homologous temperature, Eq. (27). According to these observations, the authors proposed the following formulation

$$\bar{\varepsilon}^{f}_{p} = \left(D_1 + D_2 \cdot e^{D_3 \cdot x}\right) \cdot \left(1 + D_4 \cdot \ln\frac{\dot{\bar{\varepsilon}}}{\dot{\bar{\varepsilon}}_0}\right) \cdot \left(1 + D_5 \cdot \left(\frac{T - T_0}{T_m - T_0}\right)\right). \tag{69}$$

In this equation, x represents the current stress triaxiality, referred to the Cauchy stress. The five parameters denoted by D_1, D_2, D_3, D_4 and D_5 are material parameters to be calibrated through appropriate experimental tests. An important point is the fact that Eq. (69) is assumed to be valid for stress triaxiality values lower than or equal to 1.5. When the stress triaxiality exceeds this value, Eq. (69) may not coherently predict the equivalent plastic strain to failure, due to the presence of

large tensile pressures which may trigger fracturing mechanisms not considered by such equation (e.g., spall fracture). Johnson and Cook, 1985, proposed a very simple method to overcome this problem. When the stress triaxiality exceeds 1.5, the equivalent plastic strain to fracture is no longer calculated with Eq. (69) but rather it is evaluated by linearly interpolating through the value calculated by inserting a stress triaxiality of 1.5 in this equation and a so-called minimum equivalent plastic strain to fracture, to be determined experimentally. Further details on this aspect can be found in Johnson and Cook, 1985. However, this approach was recognized to be too simplifying and possibly capable to produce incoherent results. Hence, when stress triaxialities higher than 1.5 are involved, another damage and failure model should be considered, either by replacing the Johnson and Cook model or adding to it.

Similarly to the Johnson-Cook strength model, the Johnson-Cook damage and failure model is conceived in a multiplicative fashion. The three terms contained in the three outer round brackets interact, with the aim of determining the value of the equivalent plastic strain to fracture.

The first multiplicative term introduces the dependence of the equivalent plastic strain to fracture on the stress triaxiality. Basically, this term enforces the equivalent plastic strain to fracture to decrease as the pressure goes towards positive values, since term D_3 is usually negative. Actually, the stress triaxiality appears to play a quite important role when high strain rates damage and failure need to be assessed. In this regard, further considerations on the role of stress triaxiality on the determination of the strain to fracture can be found, e.g., in Bao and Wierzbicki, 2004 and 2005.

The second multiplicative term introduces a natural logarithmic dependence of the equivalent plastic strain to fracture on the dimensionless equivalent plastic strain rate. It is worthwhile to note that this term is formally equal to the strain rate term of the Johnson-Cook hardening function, Eq. (28). This term is conceived in such a way that when the current equivalent plastic strain rate is equal to the reference equivalent plastic strain rate it becomes equal to one and therefore there are no strain rate effects on the computation of the current equivalent plastic strain to fracture. Beyond this aspect, this term determines an increase of the equivalent plastic strain to failure when the equivalent plastic strain rate increases.

The third and last multiplicative term introduces a linear dependence of the equivalent plastic strain to fracture on the homologous temperature. It is quite similar to the temperature term of the Johnson-Cook hardening function, Eq. (28). This term is conceived in such a way that when the current temperature is equal to the reference temperature it becomes equal to one and therefore there are no temperature effects on the computation of the current equivalent plastic strain to failure.

The procedure necessary for the calibration of the five parameters that appear in the Johnson-Cook damage model is somehow similar to the one presented for the determination of the parameters of the Johnson-Cook strength model. A review of such procedure is not an aim of the present work. In this regard, further considerations can be found in Johnson and Cook, 1985.

The authors evaluated their model by comparing its outcomes to independent series of Taylor tests and biaxial tests. The obtained results proved that the fracture occurs earlier comparing to the prediction of the model, thus proving some modeling coherency problematics. However, as stated by its authors, the Johnson-Cook damage and failure model should provide a coherency improvement comparing to other fracture models based only on the value of the equivalent plastic strain. Besides, the proposed model presents good capability to fit into computational frameworks, since it utilizes variables that are usually readily available in FEM codes, such as the equivalent plastic strain, the equivalent plastic strain rate, the temperature and the stress triaxiality. The latter variable can be evaluated after having computed the current pressure and the von Mises stress. Moreover, it involves only one simple scalar damage variable.

Further considerations on the Johnson-Cook damage and failure model can be found, e.g., in Xue and Wierzbicki, 2006. More sophisticated models may be considered, such as, e.g., the model proposed in Abu Al-Rub and Voyiadjis, 2006, and Voyiadjis and Abu Al-Rub, 2006. Evaluations on several damage and fracture models can be found in Teng, 2004, Wierzbicki et al., 2005, and Teng and Wierzbicki, 2006.

2.4.2. Spall Damage and Failure Models

Spall damage and fracture are phenomena due to the presence in the material of positive pressure, i.e. tensile pressure. Rinehart, 1951, and Rinehart, 1952, provided some of the first scientific analyses of such phenomena. Spall was referred to as scabbing. In particular, spall phenomena were studied in relation to the stresses produced in a body by exploding charges. Following Davison et al., 1996, solids fracture when subjected to a tensile pressure of sufficient magnitude. A typical manifestation of such conditions is due to the interaction of shock waves in solids subjected to fast dynamic loadings. These conditions may lead to tensile pressures of large magnitude and short duration, which causes the formation of microcracks or voids in the interior of a material body, eventually determining total fracture. Following Fig. 45 reports a component in which spall has occurred.

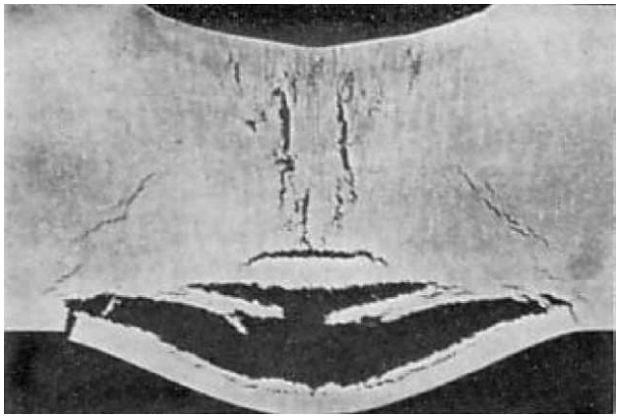

Figure 45. Spall fracture in a three inches mild steel plate subject to explosive loading (source Rinehart, 1952).

Spall damage and failure can be experimentally investigated in different ways. Most popular methods consist in plate impact and explosive loading experiments. Davison et al., 1996, provided extensive information on these procedures and how to experimentally produce spall fracture. However, spall strength may not be straightforward to be identified and it usually does not generally correlate well to the shear modulus or the yield strength, as stated in Cochran and Banner, 1977. Despite these issues, several spall damage and failure models can be found in the literature.

The simplest model consists only in setting-up a limiting tensile pressure and enforcing the material not to exceed this value. This approach does not introduce neither damage nor failure, but at least it is capable to limit the positive pressure in the material, in order to contain the tensile hydrostatic resistance of the material.

A more coherent spall damage and failure model was introduced in Cochran and Banner, 1977, resulting in one of the most popular models for describing such phenomena. The authors conducted experimental studies on spall in uranium and in few other metals, by carrying-out tests with a flyer plate fired by a light-gas gun against a target plate, which forms the tested material. When a stricken specimen spalls, stresses and displacements signals are produced, resulting in an acceleration of the specimen free surface. It is then possible to obtain information on the spalling properties of the material by measuring free-surface velocities of tested specimens. The experimental tests were carried-out by using flyer plate travelling at velocities of about 0.1 km/s, since this impact velocity is enough to produce spall phenomena in uranium and in the other tested materials.

The authors proposed a simple model for coherently introducing the spall phenomena in the simulations. The proposed model introduces a spall damage variable denoted by D and defined as the ratio between the volume of microcracks

V_c and the area A in a given representative volume element, as reported in the following relation

$$D = \frac{V_c}{A}. \tag{70}$$

Clearly, the representative volume element must be large compared to that of microcracks. Together with the introduction of such spall damage variable, the authors considered the existence of a spall strength, which is defined as the stress at which the material begins to spall. It can be measured through experimental tests. After the material has reached such value, spall damage is considered to be triggered. A simplifying approximation was introduced here. The spall damage variable is calculated by assuming that all the volumetric expansion (i.e. positive volumetric strain) that occurs after the spall strength has been reached actually becomes microcracks volume. Therefore, the spall damage variable is directly computed as a function of the volumetric expansion that the spalled material undergoes. Furthermore, a critical spall damage value is introduced, in order to regulate the maximum spall damage that the material can sustain before total fracture occurs. On these bases, the Cochran-Banner model introduces only 2 material parameters, i.e. the spall strength and the maximum spall damage.

Cochran and Banner, 1977, tested such spall damage and failure model on their experimental results, referring to uranium. The obtained experimental results were presented, together with an accurate description of the experimental procedures adopted for their achievement. A comparison between model predictions and experimental data was carried-out. Excellent agreement between model predictions and observed data was obtained, for different testing conditions.

Other spall damage and fracture models have been proposed by several authors. Among others, Al-Hassani et al., 1997, proposed a model based on a non-local view of spall damage and fracture, applicable to both ductile and brittle materials, obtaining good agreement with experimental data. Clayton, 2003, proposed a much more complicated spall model, considering a tungsten heavy alloy. Cohesive failure models were employed, in order to represent intergranular fracture at grain and phase boundaries. Chen et al., 2005, proposed a modification of the Cochran-Banner spall model, by introducing some further considerations in the model. The authors considered the same 2 material parameters introduced in the original Cochran-Banner model, namely the spall strength and the maximum spall damage.

Beyond this short review, further information on spall damage and failure can be found in pertinent references. Among others, Schmidt et al., 1978, studied spall damage and failure in the context of vulnerability of aerospace components,

providing also relevant results on the temperature dependence of spall strength of four metal alloys. Meyers and Aimone, 1983, provided a treatment on spalling of metals which includes a discussion on several metallurgical aspects. Furthermore, Cortes and Elices, 1995, provided experimental studies in aluminum, presenting also numerical modeling of spall fracture, showing good agreement between model predictions and experimental data. An extensive treatment on spall can be found in Antoun et al., 2003. Other information can be found in Zukas, 2004, and Kedrinskii, 2005.

3. PROPOSAL OF A NEW STRENGTH MODEL. SPLIT JOHNSON-COOK MODEL

In this chapter, a new strength model is introduced. This model is inspired by the Johnson-Cook model (Johnson and Cook, 1983) and it is conceived in the same framework. Namely, it consists in a hardening function that fits in the classic elastoplastic context (see, e.g., Hill, 1950, Kachanov, 1971, Lubliner, 2006, and Bigoni, 2012). It is referred to here as Split Johnson-Cook model, or also SJC model. The aims are those of elaborating the original Johnson-Cook hardening function in order to solve or mitigate the negative consequences due to the fact that the equivalent plastic strain, the equivalent plastic strain rate and the temperature effects on the yield stress are totally independent from each other. This aspect has been described in Chapter 2, Section 2.2.1, and referred to as the second issue of the Johnson-Cook model. Furthermore, the new model aims at maintaining the positive features of the original Johnson-Cook model, i.e. simplicity and high predisposition to computational implementations. In the following, the motivation for the introduction of the new strength model are further debated. The Split Johnson-Cook model is then exposed and described, together with a discussion on its calibration strategies, similar to those already presented in Chapter 2. Afterwards, the new model is applied to a real case of material behavior, i.e. to the same structural steel analyzed for the Johnson-Cook model in Chapter 2. Results are then compared to those of the original Johnson-Cook model as exposed in Chapter 2.

3.1. Motivation for the Introduction of the Split Johnson-Cook Model

As described in Chapter 2, the Johnson-Cook model does present some drawbacks. In particular, two major flaws have been identified and discussed (Section 2.2.1), and have been referred to as first and second Johnson-Cook issues. They are briefly recalled here.

The first issue consists in the fact that the natural logarithmic dependence of the yield stress on the dimensionless equivalent plastic strain rate may not be suitable to coherently fit the strain rate behavior of some materials. Analogously, the power dependence of the yield stress on the homologous temperature may present the same issue. The second problem consists in the fact that the equivalent plastic strain, the equivalent plastic strain rate and the temperature effects on the yield stress are totally independent from each other, which is a direct consequence of the choice of adopting a hardening function conceived in a multiplicative fashion.

As exposed in Chapter 2, these problematics may cause heavy modeling errors, and this may hold for a wide number of engineering materials. As previously stated, the first Johnson-Cook issue may be partially solved or mitigated by substituting either or both the original strain rate and temperature terms with some other forms, which may enhance the coherency of the model. A review of some of these substitutive terms is provided in Chapter 2, Section 2.2.1. On the other hand, the second Johnson-Cook issue appears to be less prone to be mitigated. In fact, the main aim of the new model is that of partially solving or alleviating such problem. More in detail, the new model aims at relieving the problem of having to choose between coherently model either the lower yield stresses, through the LYS or OPTLYS calibration strategies, or the plastic flows, through the EPS, OPTEPS or GOPTEPS calibration strategies.

Since the new model derives from the Johnson-Cook model, it maintains a total empiric nature. Actually, this aspect is central in order to properly frame the context in which the new model lies. Comparing to the Johnson-Cook model, it is understood that there exist some strength models capable to provide more physically-founded descriptions of the hardening behavior of materials, such as, e.g., the Zerilli-Armstrong model (Zerilli and Armstrong, 1987). In this regard, see also the physically-based model exposed in Nemat-Nasser and Isaacs, 1997, and Nemat-Nasser et al., 1999. However, the target here is that of providing a total empiric model that does not involve material parameters that may be difficult to determine, possibly related to micromechanical considerations. The target is that of allowing to set-up a strength model that requires only the experimental data already available, i.e. a set of hardening functions at different equivalent plastic strain rates and temperatures, as assumed for the original Johnson-Cook model. On these bases, the new model must be capable to better reproduce the experimental data, by providing an improvement of the fitting capabilities. As already mentioned, the Split Johnson-Cook model must also strive to maintain the same computational appeal of the original Johnson-Cook model, i.e. it shall operate by requiring information only from the equivalent plastic strain, the equivalent plastic strain rate and the temperature, thus allowing to perfectly fit in the same computational framework of the original Johnson-Cook model.

3.2. Formulation of the Split Johnson-Cook Model

The present Split Johnson-Cook model defines a hardening function which takes the additively split following form

$$\bar{s} = A \cdot \left(1 + C_1 \cdot \ln \frac{\dot{\bar{\varepsilon}}_p}{\dot{\bar{\varepsilon}}^0_{p_1}}\right) \cdot \left(1 - \left(\frac{T - T_{0_1}}{T_m - T_{0_1}}\right)^{m_1}\right) + B \cdot \bar{\varepsilon}_p^n \cdot \left(1 + C_2 \cdot \ln \frac{\dot{\bar{\varepsilon}}_p}{\dot{\bar{\varepsilon}}^0_{p_2}}\right) \cdot \left(1 - \left(\frac{T - T_{0_2}}{T_m - T_{0_2}}\right)^{m_2}\right). \quad (71)$$

The 12 parameters denoted by A, C_1, $\dot{\bar{\varepsilon}}^0_{p_1}$, m_1, T_{0_1}, B, n, C_2, $\dot{\bar{\varepsilon}}^0_{p_2}$, m_2, T_{0_2} and T_m are the parameters of the Split Johnson-Cook strength model. They need to be calibrated through appropriate experimental tests. Following Table 19 reports their dimensions and possible units.

A	Stress, e.g. [MPa]	n	Non-dimensional
C_1	Non-dimensional	C_2	Non-dimensional
m_1	Non-dimensional	m_2	Non-dimensional
$\dot{\bar{\varepsilon}}^0_{p_1}$	Strain rate, e.g. [s^{-1}]	$\dot{\bar{\varepsilon}}^0_{p_2}$	Strain rate, e.g. [s^{-1}]
T_{0_1}	Temperature, e.g. [K]	T_{0_2}	Temperature, e.g. [K]
B	Stress, e.g. [MPa]	T_m	Temperature, e.g. [K]

Table 19
Dimensions and possible units for the Split Johnson-Cook parameters.

The proposed hardening function is conceived in the same multiplicative fashion as for the original Johnson-Cook model, with the same strain rate and temperature terms, but the equivalent plastic strain rate and temperature effects are now separated for the lower yield stress, described by the parameter A, and the plastic flow, described by the parameters B and n. The name Split Johnson-Cook model actually refers to this aspect. Thus, the parameter A is called lower yield stress parameter and the parameters B and n are called plastic flow parameters. Regarding the yield stress dependence on the equivalent plastic strain, the same power form already used in the original Johnson-Cook model is maintained. The parameters C, m and the reference values for the equivalent plastic strain rate and the temperature are doubled, yielding to a total number of 12 parameters, i.e. 4 parameters more than the original Johnson-Cook model.

The Split Johnson-Cook model is a generalization of the original Johnson-Cook model, which in fact is recovered if the parameters C_1 and C_2 are equal, if the parameters m_1 and m_2 are equal and if the reference values of the equivalent plastic strain rate and of the temperature are equal. On the other hand, when these parameters are different from each other, the Split Johnson-Cook model allows to

independently model strain rate and temperature effects on the lower yield stress and on the plastic flow. In general, the parameters C_1 and C_2 and the parameters m_1 and m_2 become equal only in very particular cases, i.e. cases in which the material presents the same exact lower yield stress and plastic flow dependencies on the equivalent plastic strain rate and on the temperature. More in general, the parameters C_1 and C_2 may be quite different, as for the parameters m_1 and m_2. Beyond the splitting of the equivalent plastic strain rate and temperature effects on the lower yield stress and on the plastic flow, the way in which these effects are introduced in the hardening function is exactly the same as that in the original Johnson-Cook model.

The first additive term of the hardening function describes the lower yield stress throughout the equivalent plastic strain rate and temperature ranges. It is then called lower yield stress term. The two multiplicative terms that act on such lower yield stress term act together to determine the lower yield stress. The first one is called lower yield stress strain rate term and introduces a natural logarithmic dependence on the so-called lower yield stress dimensionless equivalent plastic strain rate $\dot{\bar{\varepsilon}}^{*}_{p_1}$, which is reported in the following equation

$$\dot{\bar{\varepsilon}}^{*}_{p_1} = \frac{\dot{\bar{\varepsilon}}_{p}}{\dot{\bar{\varepsilon}}^{0}_{p_1}}, \tag{72}$$

where $\dot{\bar{\varepsilon}}^{0}_{p_1}$ represents the so-called lower yield stress reference equivalent plastic strain rate. The lower yield stress strain rate term is conceived in such a way that when the current equivalent plastic strain rate is equal to the lower yield stress reference equivalent plastic strain rate it becomes equal to 1 and therefore there are no strain rate effects on the computation of the lower yield stress. Otherwise, the effect of the strain rate is determined by the current value of the equivalent plastic strain rate and ruled by the lower yield stress reference equivalent plastic strain rate and by the parameter C_1.

The second multiplicative term that acts on the first additive term is called lower yield stress temperature term and introduces a power dependence on the so-called lower yield stress homologous temperature T_1*, which is reported in the following equation

$$T_1^{*} = \frac{T - T_{0_1}}{T_m - T_{0_1}}, \tag{73}$$

where T_m represents the melting temperature and T_{0_1} represents the so-called lower yield stress reference temperature. The lower yield stress temperature term is conceived in such a way that when the current temperature is equal to the lower yield stress reference temperature it becomes equal to 1 and therefore there are no temperature effects on the computation of the lower yield stress. Otherwise, the effect of the temperature on the lower yield stress is determined by the current value of the temperature and ruled by the reference lower yield stress temperature, by the melting temperature and by the parameter m_1.

The second additive term of the hardening function describes the plastic flow throughout the equivalent plastic strain rate and temperature ranges. It is then called plastic flow term. These two multiplicative terms act together to determine the plastic flow. The first one is called plastic flow strain rate term and introduces a natural logarithmic dependence on the so-called plastic flow dimensionless equivalent plastic strain rate $\dot{\bar{\varepsilon}}^*_{p_2}$, which is reported as follows

$$\dot{\bar{\varepsilon}}^*_{p_2} = \frac{\dot{\bar{\varepsilon}}_p}{\dot{\bar{\varepsilon}}^0_{p_2}}, \tag{74}$$

where $\dot{\bar{\varepsilon}}^0_{p_2}$ represents the so-called plastic flow reference equivalent plastic strain rate. The plastic flow strain rate term is conceived in such a way that when the current equivalent plastic strain rate is equal to the plastic flow reference equivalent plastic strain rate it becomes equal to 1 and therefore there are no strain rate effects on the computation of the plastic flow. Otherwise, the effect of the strain rate is determined by the current value of the equivalent plastic strain rate and ruled by the plastic flow reference equivalent plastic strain rate and the parameter C_2.

The second multiplicative term that acts on the second additive term is called plastic flow temperature term and introduces a power dependence on the so-called plastic flow homologous temperature T_2*, which is reported in the following

$$T_2^* = \frac{T - T_{0_2}}{T_m - T_{0_2}}, \tag{75}$$

where T_m represents the melting temperature and T_{0_2} represents the so-called plastic flow reference temperature. The plastic flow temperature term is conceived in such a way that when the current temperature is equal to the plastic flow reference temperature it becomes equal to 1 and therefore there are no

temperature effects on the computation of the plastic flow. Otherwise, the effect of the temperature on the plastic flow is determined by the current value of the temperature and ruled by the reference plastic flow temperature, the melting temperature and the parameter m_2.

In general, the lower yield stress and plastic flow reference equivalent plastic strain rates and temperatures are not forced to be equal. As a matter of fact, the Split Johnson-Cook model provides better fitting capabilities if these parameters may be different in general. On the other hand, the melting temperature is maintained equal for both the lower yield stress and the plastic flow additive terms, and in fact it refers to the real melting temperature of the material. It is worthwhile to note that when the current temperature reaches the melting temperature, both the lower yield stress and the plastic flow additive terms become equal to zero and thus the yield stress is null and the material is assumed to offer no deviatoric resistance. Temperatures higher than the melting temperature are allowed to occur but then the yield stress is no longer computed with the Split Johnson-Cook model, which would lead to the computation of a negative yield stress. In such cases, the yield stress is just set to zero, as done for the original Johnson-Cook model.

The proposed form of the Split Johnson-Cook model strives to favor as much as possible the maintaining of characteristics similar to those of the original Johnson-Cook model but, at the same time, it aims at providing an improvement of the modeling capabilities. In this regard, many possible forms have been set-up and investigated, like, e.g., generalizing the value of the plastic flow parameters B and n, by considering them not as constants but rather as functions of the equivalent plastic strain rate and the temperature. However, the proposed form is believed to constitute the best compromise between the willing of improving the model coherency and that of maintaining a simple form, possibly similar to that of the original Johnson-Cook model. More complex hardening functions have been elaborated and investigated, but they are always afflicted by the introduction of unwanted complexities into the model, in particular by needing a much larger number of material parameters. The fact of presenting a form very similar to that of the original Johnson-Cook model allows for some interesting options, such as the possibility to substitute one or more of the Split Johnson-Cook model lower yield stress and plastic flow strain rate and temperature terms with some of the proposed substitutive terms, previously reviewed in Chapter 2, Section 2.2.1. Furthermore, having a form very similar to that of the original Johnson-Cook model allows to partially reuse some of the material parameters of the original Johnson-Cook model, that may be already known from previous calibrations.

3.3. Split Johnson-Cook Model Calibration Strategies

The calibration of the Split Johnson-Cook model requires a certain amount of experimental data. Actually, it is possible to define various calibration strategies, as for the original Johnson-Cook model. The main approaches are described in the following. In order to clarify the exposition, all the calibration strategies introduced are illustrated by applications to the same practical case considered in Chapter 2, i.e. the experimental data provided by Nemat-Nasser and Guo, 2003. Data at three different equivalent plastic strain rates and at three different temperatures are considered, i.e. the nine hardening functions already used in Chapter 2. The considered equivalent plastic strain rates are 0.001 s^{-1}, 0.1 s^{-1} and 3000 s^{-1}, while the considered temperatures are 77 K, 296 K and 800 K.

In the following, three different calibration strategies are proposed, described and applied to the considered experimental data. These approaches appear to be the most intuitive, although it is recognized that they are not the only ones possible and other calibration strategies may be defined. Due to the similarity of the Split Johnson-Cook model with the original Johnson-Cook model, these approaches are actually quite similar to those previously proposed for the calibration of the original Johnson-Cook model. In order to ease the identification of such calibration strategies, a name is defined here and associated to each of them. Considerations about how to choose which experimental tests are necessary to carry-out each procedure are presented as well. As for the calibration of the original Johnson-Cook model, experimental data are always meant in terms of hardening functions.

3.3.1. STA Calibration Strategy

The STA (STAndard) calibration strategy is the simplest approach capable to determine the 12 parameters of the Split Johnson-Cook model. This calibration strategy has the same role played by the LYS and EPS approaches for the original Johnson-Cook model, since it follows similar considerations, in order to determine the values of the Split Johnson-Cook model parameters.

The very first parameter to be determined is the melting temperature of the material. This phase is straightforward, provided that melting data are available. The next phase of the calibration strategy consists in the determination of the lower yield stress term parameters. Clearly, the parameters relative to the lower yield stress term are determined by considering experimental data at zero equivalent plastic strain, i.e. with a vanishing plastic flow additive term. In these conditions, the Split Johnson-Cook model reduces to the following form

$$\bar{s} = A \cdot \left(1 + C_1 \cdot \ln \frac{\dot{\bar{\varepsilon}}_p}{\dot{\bar{\varepsilon}}_{p_1}^0} \right) \cdot \left(1 - \left(\frac{T - T_{0_1}}{T_m - T_{0_1}} \right)^{m_1} \right). \tag{76}$$

The form of this equation is totally analogous to that of the original Johnson-Cook model in the case in which the equivalent plastic strain is zero. As a first step, it is necessary to identify the equivalent plastic strain rates and temperatures at which it is possible to test the considered material. For what it concerns the determination of the lower yield stress reference equivalent plastic strain rate and temperature, the same considerations previously made for the original Johnson-Cook model LYS calibration strategy are valid here. Hence, the lower yield stress reference equivalent plastic strain rate is chosen as one of the equivalent plastic strain rate at which the material is tested, and the lower yield stress reference temperature is chosen as the lowest temperature at which the material is tested, in order to avoid the computation of negative lower yield stress homologous temperature, since this term is then raised to the power parameter m_1, that may be a non integer number, and therefore, in such cases, the calculation of this power may not be possible.

The next phase consists in the determination of the lower yield stress parameter A, which is simply equal to the lower yield stress of the experimental hardening function referring to the test conducted at the lower yield stress reference equivalent plastic strain rate and temperature. In fact, when such reference conditions are considered, the lower yield stress strain rate and temperature terms become equal to 1 and the Split Johnson-Cook model further reduces to the following form

$$\bar{s} = A. \tag{77}$$

The data used for the determination of the parameter A need not to be purified from structural effects through an inverse analysis, because the only point considered is that at the lower yield stress, for which the structural effects are considered to be irrelevant.

The next step is relative to the determination of the lower yield stress strain rate parameter, i.e. the parameter C_1. This step is totally equivalent to the step necessary to determine the parameter C of the original Johnson-Cook model when the LYS calibration strategy is adopted. Indeed, the value of the parameter C_1 can be obtained by considering experimental data at the lower yield stress reference temperature. This fact implies the vanishing of the lower yield stress temperature term. The parameter C_1 can then be determined through the following equation

$$C_1 = \frac{\frac{\bar{s}}{A} - 1}{\ln \frac{\dot{\bar{\varepsilon}}_p}{\dot{\bar{\varepsilon}}_{p_1}^0}}. \tag{78}$$

At this point, the same issue already discussed for the original Johnson-Cook LYS calibration strategy arises, i.e. it is possible to compute different values of the parameter C_1, by considering all the available hardening functions which refer to the lower yield stress reference temperature and to the various tested equivalent plastic strain rates which differ from the lower yield stress reference equivalent plastic strain rates. Once again, if the material respects the natural logarithmic dependence of the lower yield stress on the lower yield stress dimensionless equivalent plastic strain rate, the same value of C_1 must be recovered for all the available experimental data that cover the various tested equivalent plastic strain rates. This may not be the case. In such a case, the value of C_1 is taken as an average value of all the available values. Considerations similar to those already stated for the determination of the parameter C through the original Johnson-Cook LYS calibration strategy hold true.

The next step aims at the determination of the lower yield stress temperature parameter, i.e. the parameter m_1. This step is totally equivalent to the step necessary to determine the parameter m of the original Johnson-Cook model when the LYS calibration strategy is adopted. Indeed, the value of the parameter m_1 can be obtained by considering experimental data at the lower yield stress reference equivalent plastic strain rate. This fact implies the vanishing of the lower yield stress equivalent plastic strain rate term. The parameter m_1 can then be determined through the following equation

$$m_1 = \frac{\ln\left(1 - \frac{\bar{s}}{A}\right)}{\ln\left(\frac{T - T_{0_1}}{T_m - T_{0_1}}\right)}. \tag{79}$$

At this point, the same issue already outlined for the original Johnson-Cook LYS calibration strategy arises, i.e. it is possible to compute different values of the parameter m_1, by considering all the available hardening functions referring to the lower yield stress reference equivalent plastic strain rate and to the various tested temperatures differing from the lower yield stress reference temperatures. Once again, if the material respects the power dependence of the lower yield stress on

the lower yield stress homologous temperature, the same value of m_1 must be recovered for all the available experimental data that cover the various tested temperatures. This may not be the case. In such a case, the value of m_1 is taken as an average value of all the available values. Considerations similar to those already stated for the determination of the parameter m through the original Johnson-Cook LYS calibration strategy hold true.

The next step regards the determination of the plastic flow reference equivalent plastic strain rate and temperature, together with the plastic flow parameters B and n. The plastic flow reference equivalent plastic strain rate is chosen as one of the equivalent plastic strain rates at which the material is tested, and the plastic flow reference temperature is chosen as the lowest temperature at which the material is tested, in order to avoid the computation of negative plastic flow homologous temperatures and thus the problematics related to impossibility to calculate such power. Hence, this calibration strategy prescribes the plastic flow reference temperature to be equal to the lower yield stress reference temperature, and the two reference equivalent plastic strain rates may actually be equal as well.

The parameters B and n are to be determined next. This point makes use of data obtained at the plastic flow reference equivalent plastic strain rate and temperature. These data must be purified from structural effects through an inverse analysis of the experimental tests, to be carried-out with FEM codes, since data throughout the tested equivalent plastic strain range are considered. The fact that the test is carried-out at the plastic flow equivalent plastic strain rate and temperature reference values implies that the Split Johnson-Cook strength model assumes the following form

$$\bar{s} = A \cdot \left(1 + C_1 \cdot \ln \frac{\dot{\bar{\varepsilon}}_p}{\dot{\bar{\varepsilon}}^0_{p_1}} \right) \cdot \left(1 - \left(\frac{T - T_{0_1}}{T_m - T_{0_1}} \right)^{m_1} \right) + B \cdot \bar{\varepsilon}_p^n \,. \tag{80}$$

As a matter of fact, the lower yield stress strain rate and temperature terms may vanish too if the lower yield stress and the plastic flow reference equivalent plastic strain rates and temperatures are equal. It is possible to determine the parameters B and n by fitting the experimental points of the hardening function at the reference plastic flow equivalent plastic strain rate and temperature with the function shown in Eq. (80). A good strategy here is that of adopting a code that provides nonlinear regression capabilities.

The next point is relative to the determination of the plastic flow strain rate parameter C_2. This step involves experimental tests conducted at the plastic flow reference temperature and at equivalent plastic strain rates different from the plastic

flow reference equivalent plastic strain, from the lowest one tested up to the highest one. The value of the parameter C_2 can be obtained by noting that the plastic flow temperature term becomes equal to 1 and the Split Johnson-Cook model assumes the following form

$$\bar{s} = A \cdot \left(1 + C_1 \cdot \ln \frac{\dot{\bar{\varepsilon}}_p}{\dot{\bar{\varepsilon}}^0_{p_1}} \right) \cdot \left(1 - \left(\frac{T - T_{0_1}}{T_m - T_{0_1}} \right)^{m_1} \right) + B \cdot \bar{\varepsilon}_p^n \cdot \left(1 + C_2 \cdot \ln \frac{\dot{\bar{\varepsilon}}_p}{\dot{\bar{\varepsilon}}^0_{p_2}} \right). \qquad (81)$$

As a matter of fact, the lower yield stress temperature term may become equal to 1 too if the lower yield stress and the plastic flow reference temperatures are equal. It is then possible to determine the parameter C_2 through a regression of the hardening function data at a given equivalent plastic strain rate, of course different from the plastic flow reference equivalent plastic strain rate, by considering the Johnson-Cook form presented in Eq. (81), i.e. a regression in which the only parameter to be determined is C_2. The same considerations previously stated about the necessity to carry-out an inverse analysis of the experimental data hold true.

The procedure above allows for determining the value of the parameter C_2 at a given tested equivalent plastic strain rate. The same procedure must be followed for the other tested equivalent plastic strain rates, by considering the correspondent hardening functions. At this point, if the material follows the natural logarithmic dependence of the plastic flow on the plastic flow dimensionless equivalent plastic strain rate, as assumed in the Split Johnson-Cook model, the same value of C_2 must be recovered for all the available experimental data that cover the various tested equivalent plastic strain rate. This may not be the case. In such a case, the value of C_2 is taken as an average value of all the available values. Considerations similar to those already stated for the determination of the parameter C through the original Johnson-Cook EPS calibration strategy hold true.

The next point is relative to the determination of the plastic flow temperature parameter m_2. This step involves experimental tests conducted at the plastic flow reference equivalent plastic strain and at temperatures different from the plastic flow reference temperature, from the lowest one tested up to the highest one. The value of the parameter m_2 can be obtained by noting that the plastic flow equivalent plastic strain term becomes equal to 1 and the Split Johnson-Cook model assumes the following form

$$\bar{s} = A \cdot \left(1 + C_1 \cdot \ln \frac{\dot{\bar{\varepsilon}}_p}{\dot{\bar{\varepsilon}}^0_{p_1}} \right) \cdot \left(1 - \left(\frac{T - T_{0_1}}{T_m - T_{0_1}} \right)^{m_1} \right) + B \cdot \bar{\varepsilon}_p^n \cdot \left(1 - \left(\frac{T - T_{0_2}}{T_m - T_{0_2}} \right)^{m_2} \right). \qquad (82)$$

As a matter of fact, the lower yield stress strain rate term may become equal to 1 too if the lower yield stress and the plastic flow reference equivalent plastic strain rates are equal. It is then possible to determine the parameter C_2 through a regression of the hardening function data at a given temperature, of course different from the plastic flow reference temperature, by considering the Johnson-Cook form presented in Eq. (82), i.e. a regression in which the only parameter to be determined is m_2. The same considerations previously stated about the necessity to carry-out an inverse analysis of the experimental data hold true.

The procedure above allows for determining the value of the parameter m_2 for a given tested temperature. The same procedure must be followed for the other tested temperatures, by considering the corresponding hardening functions. At this stage, if the material follows the power dependence of the plastic flow on the plastic flow homologous temperature, as assumed in the Split Johnson-Cook model, the same value of m_2 must be recovered for all the available experimental data that cover the various tested temperatures. This may not be the case. In such a case, the value of m_2 is taken as an average value of all the available values. Considerations similar to those already stated for the determination of the parameter m through the original Johnson-Cook EPS calibration strategy hold true.

It is worthwhile to note that the STA calibration strategy of the Split Johnson-Cook model can be carried-out by using the same experimental data necessary to calibrate the original Johnson-Cook model with the LYS or EPS calibration strategies. In the following, the STA calibration strategy is applied to the nine experimental hardening functions extracted from Nemat-Nasser and Guo, 2003.

The melting temperature is taken equal to 1773 K. The lower yield stress reference equivalent plastic strain rate is chosen as the lowest tested equivalent plastic strain rate, i.e. 0.001 s^{-1}. The lower yield stress reference temperature is chosen as the lowest tested temperature, i.e. 77 K. The parameter A is then equal to 915.555 MPa. Regarding the parameter C_1, it is obtained by using Eq. (78) with data from the two equivalent plastic strain rates different from the lower yield stress reference equivalent plastic strain rates, i.e. 0.1 s^{-1} and 3000 s^{-1}, at the reference temperature of 77 K. The computed values of C_1 are equal to 0.01399 and 0.01720, for the equivalent plastic strain rates of 0.1 s^{-1} and 3000 s^{-1}, respectively. Following the procedure described above, the parameter C_1 is then set equal to their average value, namely 0.01560. This step is totally equivalent to that previously made for the determination of the parameter C for the original Johnson-Cook LYS calibration strategy. In fact, the same value is recovered. Regarding the parameter m_1, it is obtained by using Eq. (79) with data from the two temperatures different from the lower yield stress reference temperature, i.e. 296 K and 800 K, at the reference equivalent plastic strain rate of 0.001 s^{-1}. The computed values are equal to 0.18022 and 0.27336, for the temperatures of 296 K and 800 K, respectively.

Following the procedure described above, the parameter m_1 is then set equal to their average value, namely 0.22679. This step is totally equal to that previously made for the determination of the parameter m for the original Johnson-Cook LYS calibration strategy. Thus, the same value is calculated.

The plastic flow reference equivalent plastic strain rate and temperature are taken as equal to the lower yield stress reference values, i.e. 0.001 s^{-1} and 77 K. The parameters B and n are obtained by evaluating the experimental hardening function at these reference values, through a fitting carried-out within Wolfram Mathematica 7, by considering Eq. (80). The obtained parameters B and n become equal to 760.782 MPa and 0.60101, respectively. This step is equivalent to the one relative to the determination of the quasi-static parameters A, B and n in the original Johnson-Cook LYS, OPTLYS, EPS and OPTEPS calibration strategies, with the only difference that the parameter A in this case has already been determined. Indeed, the same values are recovered. Among other things, this fact is due to having chosen the plastic flow reference parameters equal to the lower yield stress reference parameters.

The parameter C_2 is determined next. It is obtained by carrying-out a regression of experimental data through Eq. (81). Both hardening functions that refer to the two equivalent plastic strain rates different from the plastic flow reference equivalent plastic strain rates, i.e. 0.1 s^{-1} and 3000 s^{-1}, at the reference temperature of 77 K, are considered. The code Wolfram Mathematica 7 has been used to achieve such task. The computed values of C_2 are equal to -0.06181 and -0.06166, for the equivalent plastic strain rates of 0.1 s^{-1} and 3000 s^{-1}, respectively. The two obtained values are very similar, thus proving that the material follows quite well the natural logarithm dependence of the plastic flow on the plastic flow dimensionless equivalent plastic strain rate. Following the procedure described above, the parameter C_2 is set equal to their average value, namely -0.06174.

Regarding the parameter m_2, it is obtained by carrying-out a regression of the experimental data through Eq. (82). Both hardening functions that refer to the two temperatures different from the plastic flow reference temperature, i.e. 296 K and 800 K, at the reference equivalent plastic strain rate of 0.001 s^{-1}, are considered. The code Wolfram Mathematica 7 has been used to achieve such task. The computed values of m_2 are equal to 1.42221 and 4.25422, for the temperatures of 296 K and 800 K, respectively. The two obtained values are quite different, thus proving that the material does not respect quite well the power dependence of the plastic flow on the plastic flow homologous temperature. Following the procedure described above, the parameter m_2 is set equal to their average value, namely 2.83816.

The 12 Split Johnson-Cook parameters obtained through the STA calibration strategy are summarized in following Table 20.

A	915.555 MPa	n	0.60101
C_1	0.01560	C_2	-0.06174
m_1	0.22679	m_2	2.83816
$\dot{\varepsilon}^0_{p_1}$	0.001 s^{-1}	$\dot{\varepsilon}^0_{p_2}$	0.001 s^{-1}
T_{0_1}	77 K	T_{0_2}	77 K
B	760.782 MPa	T_m	1773 K

Table 20
Split Johnson-Cook parameters for the DH-36 structural steel calculated through the STA calibration strategy.

Following Figs. 46 to 48 show the hardening functions predicted by the Split Johnson-Cook model calibrated with the STA calibration strategy. As expected, the curves of the model follow in the best possible way the first yielding of the experimental hardening curves but this time their fittings throughout the equivalent plastic strain ranges are much improved by comparing to the original Johnson-Cook model calibrated with the LYS strategy.

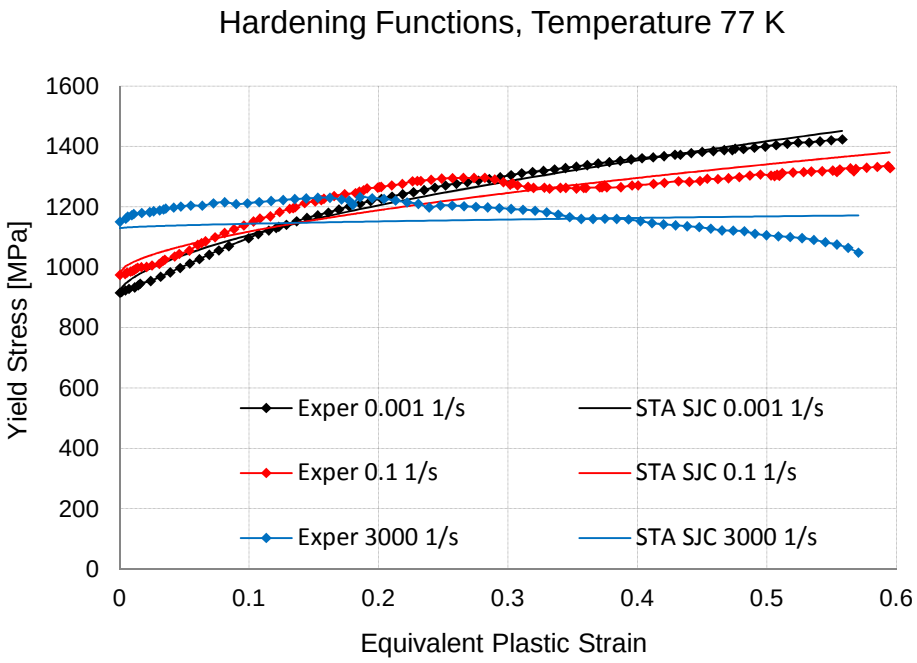

Figure 46. STA calibrated Split Johnson-Cook fitting to DH-36 structural steel data at temperature of 77 K and at three different equivalent plastic strain rates.

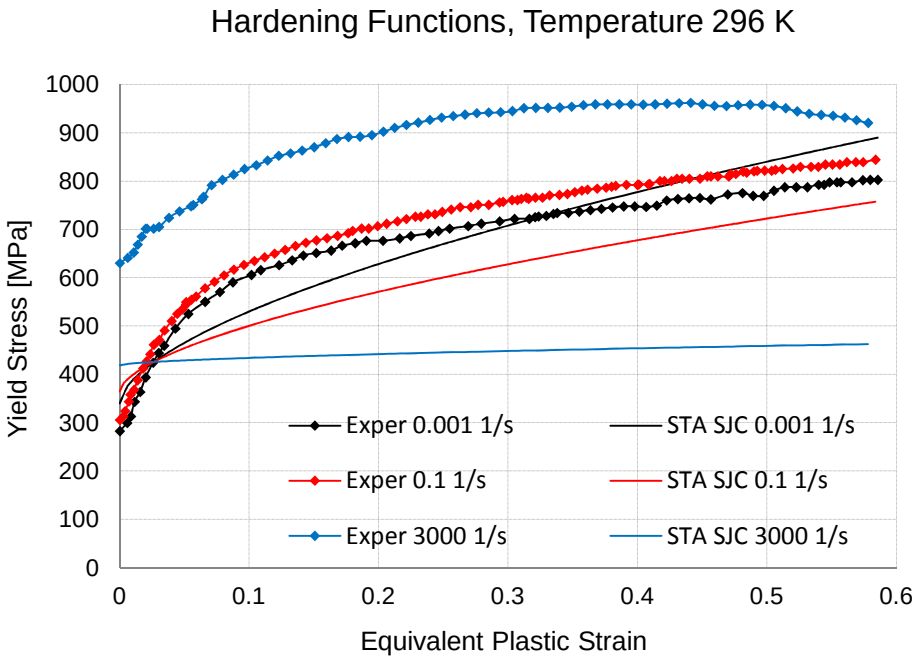

Figure 47. STA calibrated Split Johnson-Cook fitting to DH-36 structural steel data at temperature of 296 K and at three different equivalent plastic strain rates.

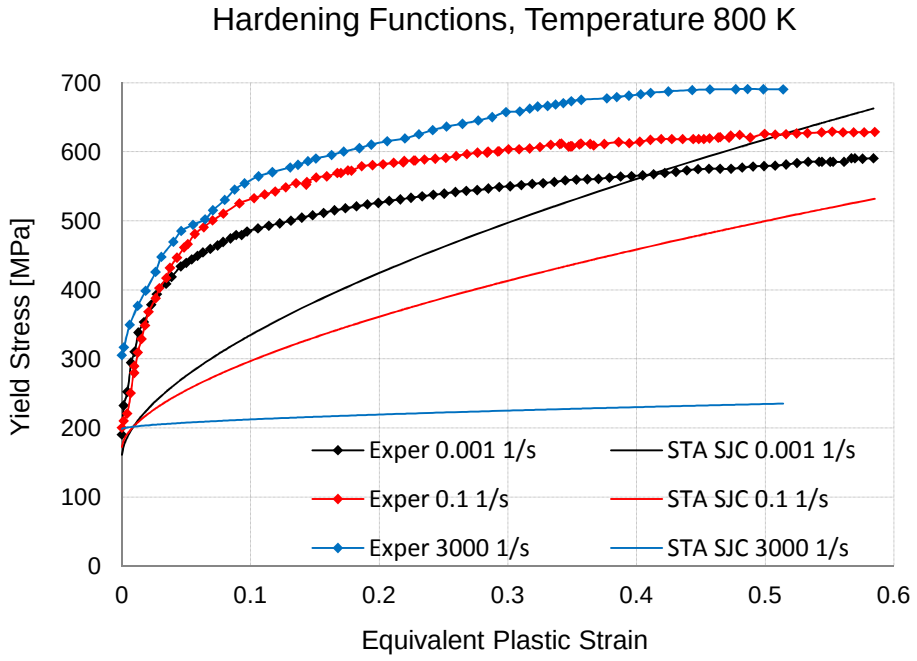

Figure 48. STA calibrated Split Johnson-Cook fitting to DH-36 structural steel data at temperature of 800 K and at three different equivalent plastic strain rates.

Following Figs. 49 to 51 show the same results but the yield stress is visualized by surface plots as a function of the equivalent plastic strain and the base 10 logarithm of the equivalent plastic strain rate. Experimental data are reported with black dots whilst the predictions of the Split Johnson-Cook model are presented with red surfaces.

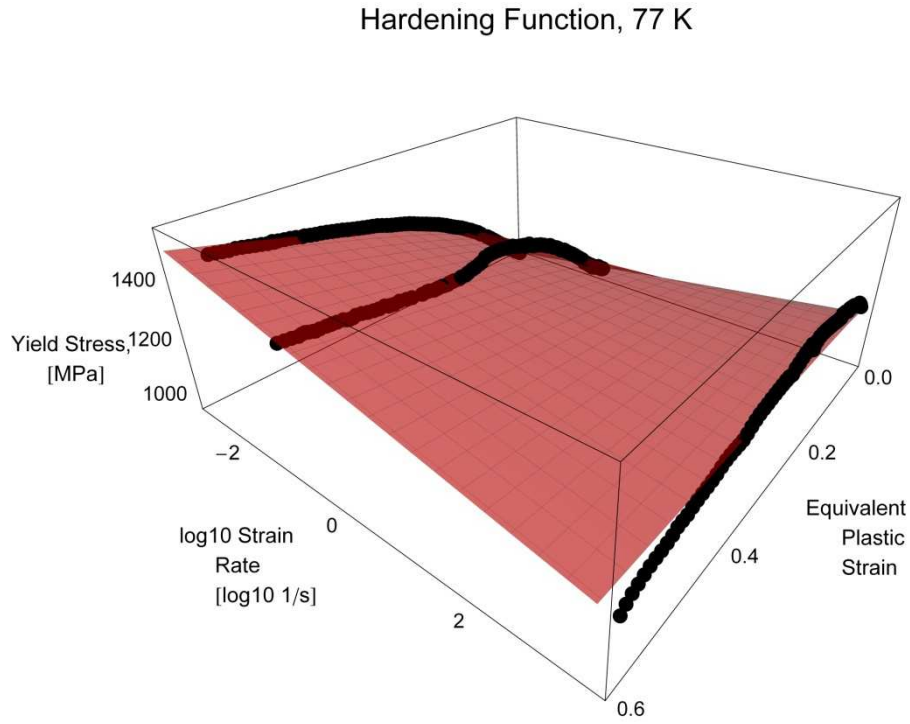

Figure 49. STA calibrated SJC model fitting to DH-36 steel data at temperature of 77 K.

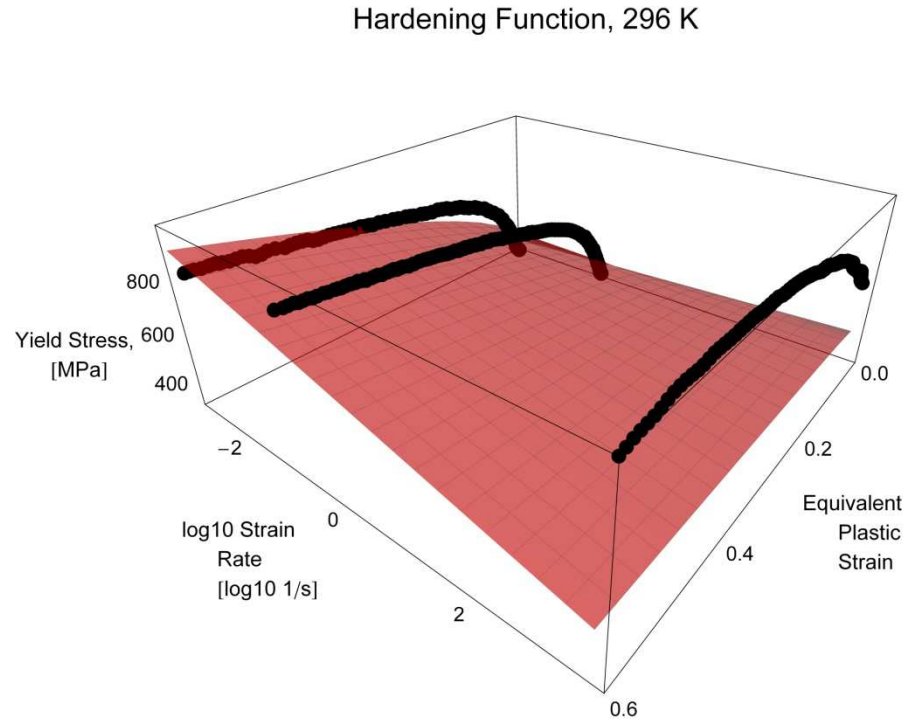

Figure 50. STA calibrated SJC model fitting to DH-36 steel data at temperature of 296 K.

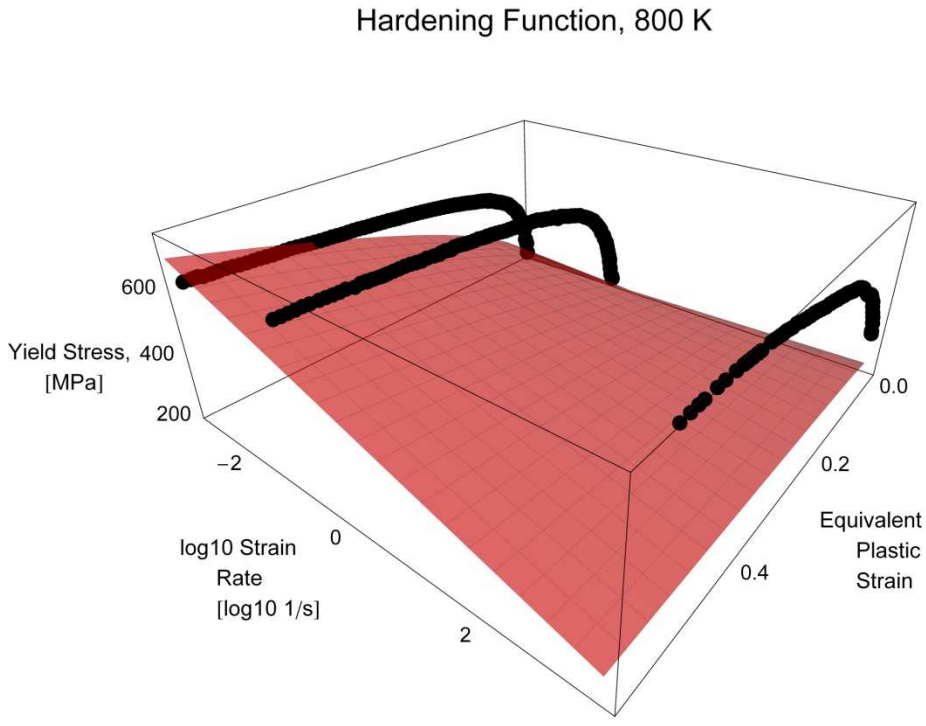

Figure 51. STA calibrated SJC model fitting to DH-36 steel data at temperature of 800 K.

As shown in Figs. 46 to 51, the fit to the lower yield stress is very good for the hardening functions in which at least one reference conditions is present, i.e. an equivalent plastic strain rate of 0.001 s^{-1} or a temperature of 77 K. Actually, this fitting is the same as that obtained with the original Johnson-Cook model calibrated with the LYS strategy. Following Table 21 reports a comparison between the STA calibrated Split Johnson-Cook model predictions of the lower yield stresses, which are equal to those of the LYS calibrated Johnson-Cook model, and their experimental counterparts.

	Experimental Values	**STA SJC Values**
0.001 s^{-1}, 77 K	915.555 MPa	915.555 MPa
0.1 s^{-1}, 77 K	974.565 MPa	981.323 MPa
3000 s^{-1}, 77 K	1150.46 MPa	1128.545 MPa
0.001 s^{-1}, 296 K	282.455 MPa	340.015 MPa
0.1 s^{-1}, 296 K	305.455 MPa	364.439 MPa
3000 s^{-1}, 296 K	630.137 MPa	419.115 MPa
0.001 s^{-1}, 800 K	190.345 MPa	160.967 MPa
0.1 s^{-1}, 800 K	200.213 MPa	172.533 MPa
3000 s^{-1}, 800 K	305.345 MPa	198.417 MPa

Table 21
Comparison between experimental lower yield stresses and correspondent predicted lower yield stresses from the Split Johnson-Cook model calibrated with the STA strategy.

Comparing to the LYS calibrated Johnson-Cook model, the fitting throughout the equivalent plastic strain ranges is significantly improved when the model fits data which refer to at least one reference condition. On the other hand, when the model fits the four hardening functions that do not refer to at least one reference condition, i.e. 0.1 s^{-1} and 296 K, 3000 s^{-1} and 296 K, 0.1 s^{-1} and 800 K, and 3000 s^{-1} and 800 K, large errors may be introduced, as clearly visible in Figs. 46 to 51. This fact is due to having calculated the parameters C_1, m_1, C_2 and m_2 by considering reference temperature and equivalent plastic strain rate conditions only. As a matter of fact, the four hardening functions that do not refer to at least one reference condition are never used when the STA calibration strategy is adopted, as for the LYS and EPS original Johnson-Cook calibration strategies. In particular, fitting incoherencies arise for the two hardening functions at 3000 s^{-1} and 296 K, and at 3000 s^{-1} and 800 K, due to the fact that the parameter C_2 is calibrated by considering only data at 77 K, which present a material softening for the case relative to the equivalent plastic strain rate of 3000 s^{-1}. Therefore, the calibration of the parameter C_2 tries to fit this softening trend, which is however completely

different for the two hardening functions at 3000 s^{-1} and 296 K, and at 3000 s^{-1} and 800 K. Hence, considerable mismatches arise in these cases.

These aspects are actually analogous to those that arose for the original Johnson-Cook LYS and EPS calibration strategies. As for those cases, assessing the model predictions only against the hardening functions which refer to at least one reference condition may lead to considerable discrepancies. Rather, the model should be checked even against hardening functions which do not refer to at least one reference condition, in order to assess the possible introduction of heavy calibration problematics. Following Table 22 reports both the yield stress and the percentage yield stress root mean square errors for each of the nine considered hardening functions, together with their algebraic mean value, i.e. their sum divided by 9. Important errors are introduced, most of all due to the fitting problematics of the two hardening functions at 3000 s^{-1} and 296 K, and at 3000 s^{-1} and 800 K, while the other cases are actually much more coherent.

	$\bar{s}_{err}$	$\bar{s}_{\%err}$
0.001 s^{-1}, 77 K	19.5893 MPa	1.784%
0.1 s^{-1}, 77 K	43.9967 MPa	3.530%
3000 s^{-1}, 77 K	57.9250 MPa	4.976%
0.001 s^{-1}, 296 K	51.7883 MPa	8.728%
0.1 s^{-1}, 296 K	111.359 MPa	15.74%
3000 s^{-1}, 296 K	440. 5960 MPa	49.01%
0.001 s^{-1}, 800 K	97.0358 MPa	21.55%
0.1 s^{-1}, 800 K	176.6159 MPa	32.44%
3000 s^{-1}, 800 K	383.025 MPa	62.07%
Average	*153.548 MPa*	*22.20%*

Table 22
Yield stress (central column) and percentage yield stress (right column) root mean square errors for the STA calibrated Split Johnson-Cook model yield stress predictions.

3.3.2. OPT Calibration Strategy

The OPT (OPTimized) calibration strategy aims at improving the STA calibration strategy by optimizing the value of the parameters C_1, C_2, m_1 and m_2. In order to achieve such target, this strategy introduces in the calibration procedure experimental data relative to the hardening functions which do not refer to at least one reference condition, trying to obtain values of the parameters C_1, C_2, m_1 and m_2 capable to provide the actual best fit for all the made available hardening functions. The optimized calibration strategy has the same role played by the OPTLYS and the OPTEPS original Johnson-Cook calibration strategies, i.e. it offers an

improvement of the STA calibration strategy by considering all the experimental data for the aim of determining the parameters C_1, C_2, m_1 and m_2.

For what it concerns the calibration of the melting temperature, the lower yield stress reference equivalent plastic strain rate and temperature, the lower yield stress parameter A, the plastic flow reference equivalent plastic strain rate and temperature and the parameters B and n, the procedure is exactly the same as what exposed for the STA calibration strategy. Differences arise just for the determination of the four parameters C_1, C_2, m_1 and m_2.

The first step regards the determination of the lower yield stress parameters C_1 and m_1. In order to introduce all the lower yield stress data provided by all the available hardening functions, the Split Johnson-Cook model, Eq. (71), is recalled a number of times equal to the number of available hardening functions which do not refer to lower yield stress reference conditions, for both the equivalent plastic strain rate and the temperature, i.e. all the available hardening functions except the one which refers to the lower yield stress reference conditions for both the equivalent plastic strain rate and the temperature. This approach leads to the construction of an overdetermined system of nonlinear equations, in which the unknowns are the parameters C_1 and m_1. Of course, the equivalent plastic strain is always set equal to zero, because only the lower yield stress is considered. Therefore, the plastic flow term vanishes. Such system is reported as follows

$$\bar{s}_i = A \cdot \left(1 + C_1 \cdot \ln \frac{\dot{\bar{\varepsilon}}_{p_i}}{\dot{\bar{\varepsilon}}^0_{p_1}} \right) \cdot \left(1 - \left(\frac{T_i - T_{0_1}}{T_m - T_{0_1}} \right)^{m_1} \right). \tag{83}$$

In these equations, the subscript i refers to the values relative to the i-th hardening function. This system is totally analogous to the one that arises for the calibration of the original Johnson-Cook model when the OPTLYS calibration strategy is adopted. As previously said, a system of this kind can be solved through a nonlinear least square method.

The second step regards the determination of the plastic flow parameters C_2 and m_2. In order to introduce all the data provided by all the available hardening functions, the Split Johnson-Cook model, Eq. (71), is recalled a number of times equal to the number of available experimental observations, intended in terms of couples of yield stress and corresponding equivalent plastic strain values, throughout the experimentally investigated equivalent plastic strain ranges. These data refer to all the available hardening functions which do not refer to plastic flow reference conditions for both the equivalent plastic strain rate and the temperature, i.e. all the available hardening functions except for the one which refers to plastic

flow reference conditions for both the equivalent plastic strain rate and the temperature. This approach leads to the construction of a large overdetermined system of nonlinear equations, in which the unknowns are the plastic flow parameters C_2 and m_2 and the number of equations is equal to the number of available couples of yield stress and corresponding equivalent plastic strain values, which depends on the number of made available experimental hardening functions and on the sampling frequency adopted for the experimental measurements. In order to avoid to set-up too large systems, it is possible to consider data at a sampling inferior than the one used for the experimental measurements, as previously said for the original Johnson-Cook model OPTEPS calibration strategy. Such system is reported as follows

$$\bar{s}_i = A \cdot \left(1 + C_1 \cdot \ln \frac{\dot{\bar{\varepsilon}}_{p_i}}{\dot{\bar{\varepsilon}}^0_{p_1}} \right) \cdot \left(1 - \left(\frac{T_i - T_{0_1}}{T_m - T_{0_1}} \right)^{m_1} \right) + B \cdot \bar{\varepsilon}_{p_i}^n \cdot \left(1 + C_2 \cdot \ln \frac{\dot{\bar{\varepsilon}}_{p_i}}{\dot{\bar{\varepsilon}}^0_{p_2}} \right) \cdot \left(1 - \left(\frac{T_i - T_{0_2}}{T_m - T_{0_2}} \right)^{m_2} \right). \quad (84)$$

In these equations, the subscript i refers to the i-th couple of yield stress and corresponding equivalent plastic strain values, at a given equivalent plastic strain rate and temperature. As said for some of the original Johnson-Cook calibration strategies, a system of this kind can be solved through a nonlinear least square method.

Regarding the experimental data necessary in order to carry-out the optimized calibration strategy, these are exactly the same required for the original Johnson-Cook OPTLYS or OPTEPS calibration strategies. In the following, the optimized calibration strategy is applied to the nine experimental hardening functions extracted from Nemat-Nasser and Guo, 2003.

Regarding the lower yield stress parameters, a system of 8 nonlinear equations in 2 unknowns is set-up. It has been numerically solved with a nonlinear least squares trust-region-reflective algorithm within MathWorks MatLab 2010b, with a tolerance of 10^{-8}. The obtained values for the parameters C_1 and m_1 are equal to 0.01906 and 0.67222, respectively, showing that the material does not respect very well the natural logarithm dependence of the lower yield stress on the lower yield stress reference equivalent plastic strain. For what it concerns the plastic flow parameters, C_2 and m_2, couples of yield stress and corresponding equivalent plastic strain values are taken with the same sampling of the experimental ones, i.e. for each digitalized couple of yield stress and corresponding equivalent plastic strain. Following this approach, a large overdetermined system of 664 nonlinear equations and 2 unknowns is created, and it has been numerically solved with the same MathWorks MatLab 2010b nonlinear least squares trust-region-reflective algorithm,

with a tolerance of 10^{-8}. The obtained values for the parameters C_2 and m_2 simultaneously minimize the square errors for the 664 nonlinear equations of the system, through a multi-objective nonlinear optimization. These optimized values are equal to -0.02582 and 3175.41, for the parameters C_2 and m_2, respectively. The 12 Split Johnson-Cook parameters obtained through the OPT calibration strategy are summarized in following Table 23.

A	915.555 MPa	n	0.60101
C_1	0.02049	C_2	-0.02582
m_1	0.26367	m_2	3175.41
$\dot{\bar{\varepsilon}}^0_{p_1}$	0.001 s^{-1}	$\dot{\bar{\varepsilon}}^0_{p_2}$	0.001 s^{-1}
T_{0_1}	77 K	T_{0_2}	77 K
B	760.782 MPa	T_m	1773 K

Table 23
Split Johnson-Cook parameters for the DH-36 structural steel calculated through the OPT calibration strategy.

Following Figs. 52 to 54 show the hardening functions predicted by the Split Johnson-Cook model calibrated with the OPT strategy.

The curves of the optimized calibrated Split Johnson-Cook model follow in the best possible way the experimental hardening curves throughout the equivalent plastic strain ranges, this time considering not only the hardening functions which have either the equivalent plastic strain or the temperature equal to the reference value, but all the nine hardening functions. As previously said, this target is partially hindered by the fact that the material does not strictly respect the natural logarithm dependence of the lower yield stress on the lower yield stress dimensionless equivalent plastic strain rate and the power dependence on the lower yield stress homologous temperature. The same aspect arises for the plastic flow dependence on the equivalent plastic strain rate and on the temperature. Another aspect that involves some problems in fitting the data is the fact that the hardening parameters B and n are actually chosen as the ones capable to best fit only hardening functions at the reference conditions.

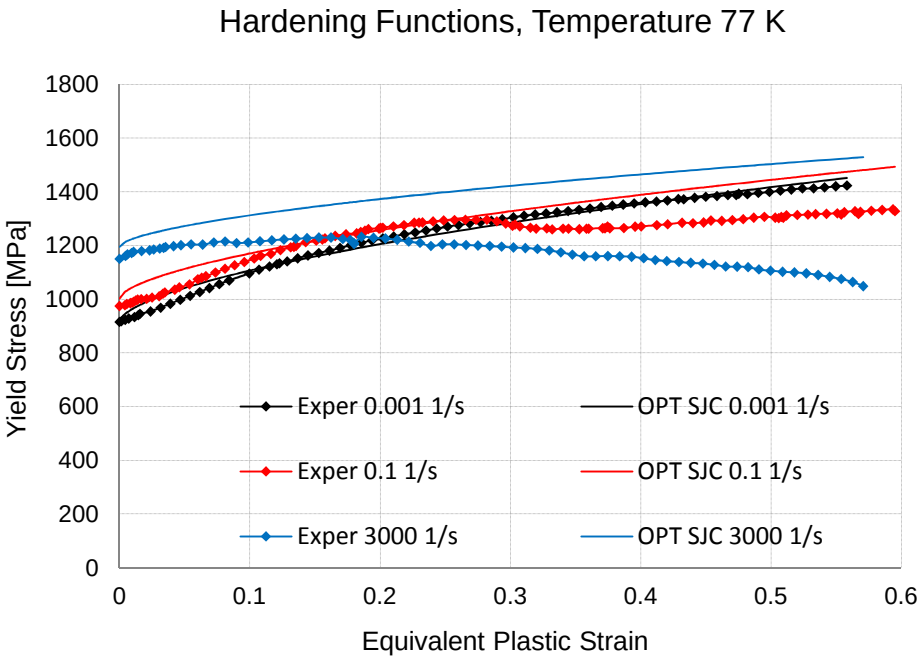

Figure 52. OPT calibrated Split Johnson-Cook fitting to DH-36 structural steel data at temperature of 77 K and at three different equivalent plastic strain rates.

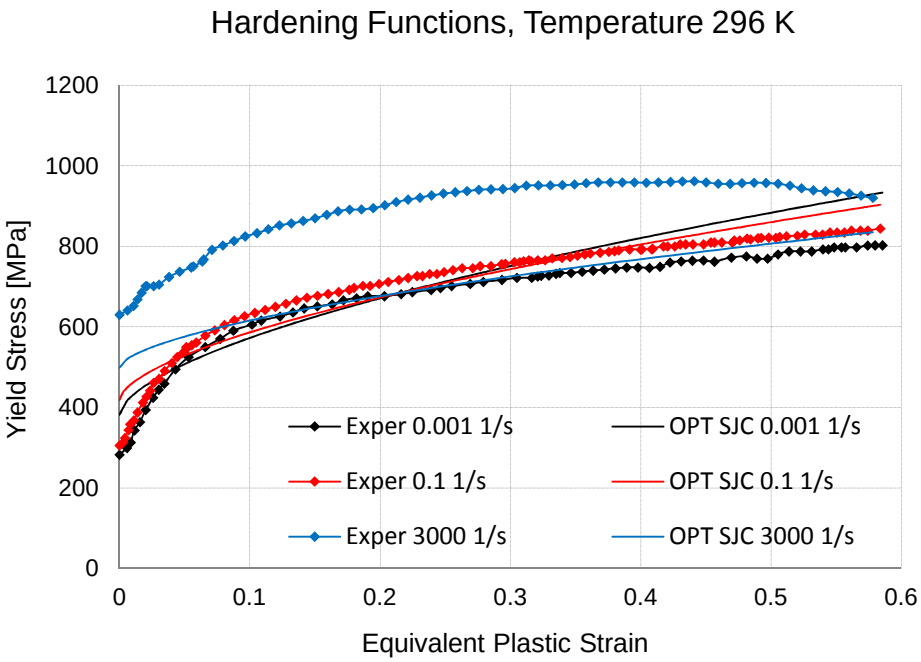

Figure 53. OPT calibrated Split Johnson-Cook fitting to DH-36 structural steel data at temperature of 296 K and at three different equivalent plastic strain rates.

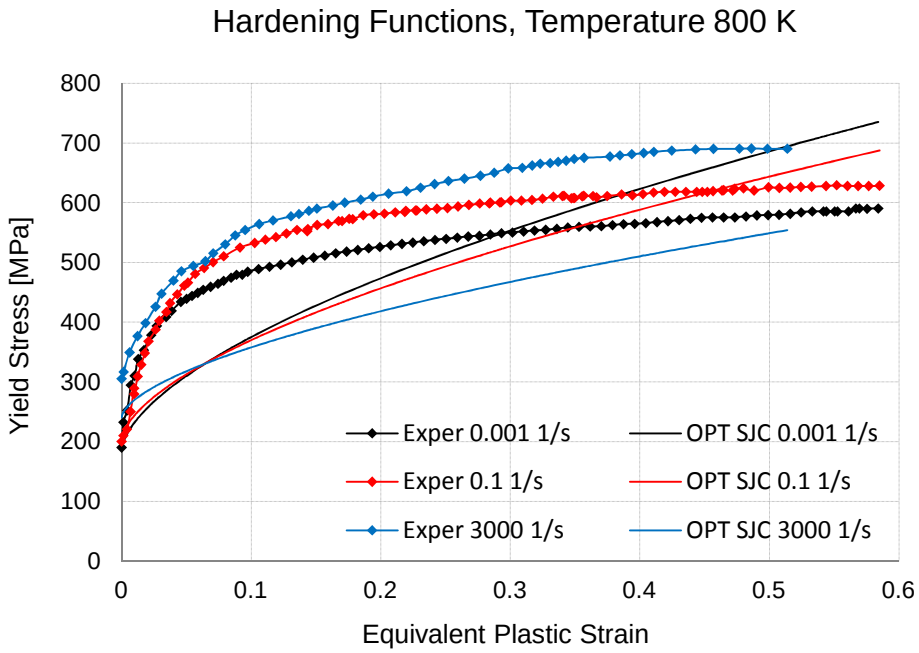

Figure 54. OPT calibrated Split Johnson-Cook fitting to DH-36 structural steel data at temperature of 800 K and at three different equivalent plastic strain rates.

Following Figs. 55 to 57 further show the OPT results by surface plots.

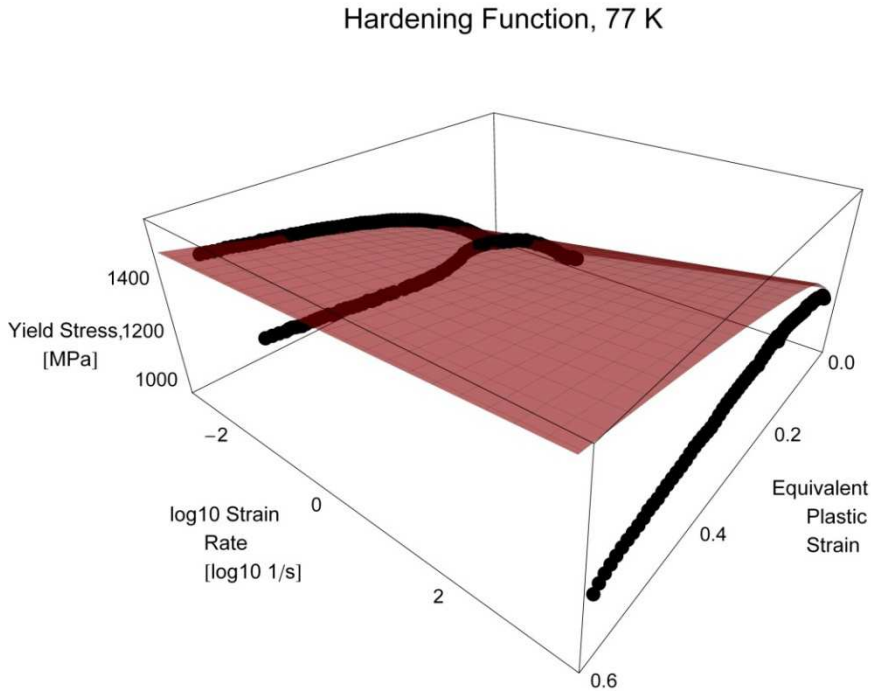

Figure 55. OPT calibrated SJC model fitting to DH-36 steel data at temperature of 77 K.

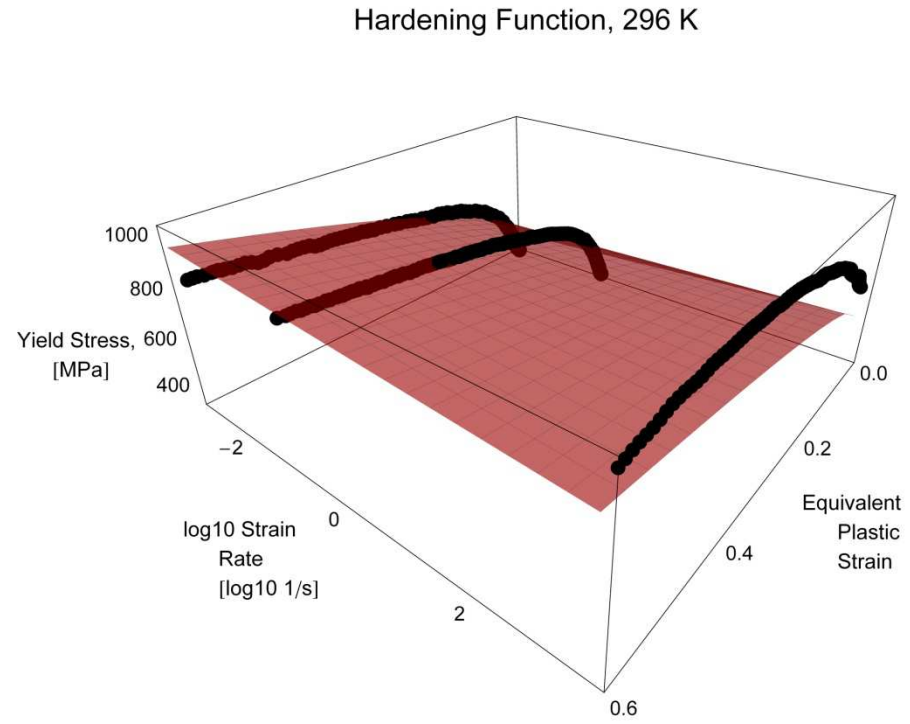

Figure 56. OPT calibrated SJC model fitting to DH-36 steel data at temperature of 296 K.

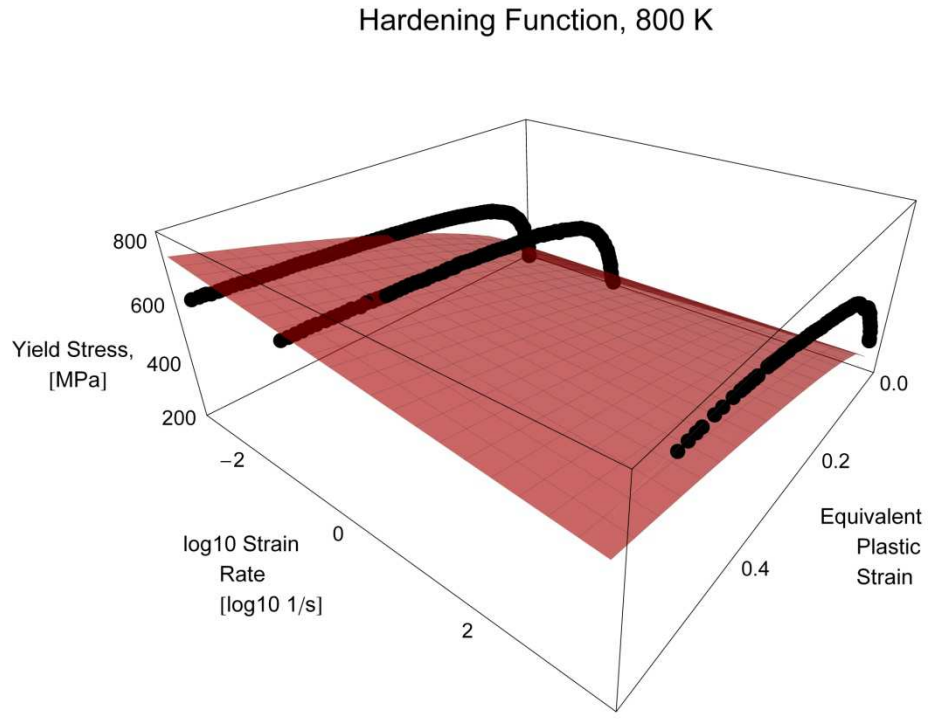

Figure 57. OPT calibrated SJC model fitting to DH-36 steel data at temperature of 800 K.

As displayed in Figs. 52 to 57, the fit to the data is now the result of a compromise between all the nine hardening functions. This point implies the fact that the fit with the hardening functions in which at least one reference conditions is present is less coherent than the one obtainable from the predictions of the STA calibrated Split Johnson-Cook model. On the other hand, when the model fits the four hardening functions that do not refer to at least one reference condition, the errors are lower, both for the lower yield stress and for the plastic flow. Clearly, this is a consequence of having calculated the parameters C_1, m_1, C_2 and m_2 by considering experimental data from all the nine hardening functions. In particular, the fittings for the two hardening functions at 3000 s^{-1} and 296 K, and at 3000 s^{-1} and 800 K have benefit a strong improvement when comparing to the STA calibrated Split Johnson-Cook model predictions. Following Table 24 reports a comparison between the OPT calibrated Split Johnson-Cook model predictions of the lower yield stresses, which are equal to those of the OPTLYS calibrated Johnson-Cook model, and their experimental counterparts.

	Experimental Values	**OPT SJC Values**
0.001 s^{-1}, 77 K	915.555 MPa	915.555 MPa
0.1 s^{-1}, 77 K	974.565 MPa	1001.95 MPa
3000 s^{-1}, 77 K	1150.46 MPa	1195.34 MPa
0.001 s^{-1}, 296 K	282.455 MPa	381.868 MPa
0.1 s^{-1}, 296 K	305.455 MPa	417.901 MPa
3000 s^{-1}, 296 K	630.137 MPa	498.563 MPa
0.001 s^{-1}, 800 K	190.345 MPa	184.331 MPa
0.1 s^{-1}, 800 K	200.213 MPa	201.724 MPa
3000 s^{-1}, 800 K	305.345 MPa	240.660 MPa

Table 24
Comparison between experimental lower yield stresses and corresponding predicted lower yield stresses from the Split Johnson-Cook model calibrated with the OPT strategy.

Following Table 25 reports both the yield stress and the percentage yield stress root mean square errors for each one of the nine considered hardening functions, together with their algebraic mean value, i.e. their sum divided by 9. The average errors are sensibly lower than those of the STA calibrated Split Johnson-Cook model, and are also lower than those of the best calibrated original Johnson-Cook model, i.e. the GOPTEPS calibrated model.

	$\bar{s}_{err}$	$\bar{s}_{\%err}$
0.001 s^{-1}, 77 K	19.5893 MPa	1.784%
0.1 s^{-1}, 77 K	89.6059 MPa	7.070%
3000 s^{-1}, 77 K	248.454 MPa	22.01%
0.001 s^{-1}, 296 K	72.7610 MPa	12.45%
0.1 s^{-1}, 296 K	41.4574 MPa	9.365%
3000 s^{-1}, 296 K	188.087 MPa	21.54%
0.001 s^{-1}, 800 K	90.1739 MPa	18.47%
0.1 s^{-1}, 800 K	93.1929 MPa	18.06%
3000 s^{-1}, 800 K	174.677 MPa	29.61%
Average	*113.1109 MPa*	*15.60%*

Table 25
Yield stress (central column) and percentage yield stress (right column) root mean square errors for the OPT calibrated Split Johnson-Cook model yield stress predictions.

3.3.3. GOPT Calibration Strategy

The GOPT (Global OPTimization) calibration strategy aims at obtaining the best set of parameters by considering a multi-objective optimization of 11 of the 12 parameters of the Split Johnson-Cook model, i.e. all the parameters except for the melting temperature. All the experimental data are used, trying to obtain all together values of the 11 parameters capable to provide the actual best fit for all the made available hardening functions, throughout the equivalent plastic strain ranges involved.

This optimization is carried-out by solving an overdetermined system of nonlinear equations and eleven unknowns. Such nonlinear system uses all the available experimental data, intended in terms of couples of yield stress and corresponding equivalent plastic strain, as done for the GOPTEPS original Johnson-Cook calibration strategy, but this time on eleven unknowns. The obtained values for these eleven parameters simultaneously minimize the square errors for the nonlinear equations of the system, through a multi-objective nonlinear optimization.

The melting temperature is excluded from the multi-objective optimization, for the same reasons previously stated for the GOPTEPS original Johnson-Cook calibration strategy. Indeed, assuming the melting temperature to be an optimization variable may lead to setting-up melting values that are totally different from the real phase change value. It is also worthwhile to point-out a consideration about the lower yield stress and plastic flow reference equivalent plastic strain rates and temperatures. As in the GOPTEPS original Johnson-Cook calibration strategy, these reference values can be different from those of one of the experimental

hardening functions, since they are left as optimization variables. Anyway, their values identify the Johnson-Cook lower yield stress and plastic flow quasi-static conditions, although they are now unknowns. This aspect should provide a better fitting of the experimental data.

Regarding the determination of the remaining 11 Split Johnson-Cook parameters, the procedure is analogous to that of the GOPTEPS original Johnson-Cook calibration strategy. In order to introduce all the yield stress data provided by all the available hardening functions, the Split Johnson-Cook strength model is recalled a number of times equal to the number of available experimental observations, intended in terms of couples of yield stress and corresponding equivalent plastic strain values, throughout the experimentally investigated equivalent plastic strain ranges, as done for the second phase of the OPT Split Johnson-Cook calibration strategy. However, this time the unknowns are not only C_2 and m_2 but all the 11 considered optimization variables. Furthermore, the number of equations increases up to 740, because data from all the nine hardening functions are now considered, including that at 0.001 s^{-1} and 77 K. In order to avoid to set-up too large systems, it is obviously possible to consider data at a sampling inferior than that used for the experimental measurements, as previously mentioned. In order to solve this system, an important point is relative to the enforcement of appropriate conditions on the eleven optimization variables, making the process a multi-objective nonlinear optimization subjected to bounds, similarly to what done for the original Johnson-Cook GOPTEPS calibration strategy. Therefore, the lower yield stress and plastic flow reference equivalent plastic strain rates are forced to be positive numbers, since they cannot be negative, because natural logarithms of negative numbers cannot be calculated. Furthermore, the lower yield stress and plastic flow reference temperatures are forced to be lower than or equal to the lowest temperature tested during the experimental campaign, since it is necessary to avoid calculations of negative lower yield stress or plastic flow homologous temperature, in order to prevent computations of negative numbers raised to a possible non integer negative number, as previously said. The lower yield stress and plastic flow reference temperatures are also forced to be greater than zero, as done for the original Johnson-Cook GOPTEPS calibration strategy. Although the calculation of negative reference temperatures is not a problem from the mathematical point of view, it is considered reasonable to keep these parameters greater than zero, since temperatures lower than 0 K are not physically admissible. No bounds are imposed on the other parameters.

The created system is quite complex, due to the presence of 11 objective variables. It can still be solved through a nonlinear least square method. If there are convergence problems, it is possible to enforce some further bounds on the objective variables, in order to restrict their existence domains and favor the

convergence of the system. The solution values for the 11 Split Johnson-Cook parameters are those characterized by being capable to minimize the square errors of the Split Johnson-Cook model predictions against experimental data at each couple of yield stress and correspondent equivalent plastic strain values.

Regarding the experimental data necessary to carry-out the GOPT calibration strategy, these are exactly the same required for the OPT Split Johnson-Cook calibration strategy, i.e. the same data required for the original Johnson-Cook OPTLYS and OPTEPS strategies. In the following, the GOPT calibration strategy is applied again to the nine experimental hardening functions extracted from Nemat-Nasser and Guo, 2003.

The overdetermined system of nonlinear equations and eleven unknowns has been numerically solved with a nonlinear least squares trust-region-reflective algorithm within MathWorks MatLab 2010b, as previously done for the other calibration strategies, with a tolerance of 10^{-8}. Some convergence problems have been solved by setting both the lower yield stress and the plastic flow reference temperatures equal to 77 K, since all the iterations showed that these parameters tended to such value. This point is similar to what happened for the calibration of the original Johnson-Cook model through the GOPTEPS calibrations strategy. The obtained values for the 11 Johnson-Cook parameters simultaneously minimize the square errors for the 740 nonlinear equations of the system, through a multi-objective nonlinear optimization subjected to bounds. The obtained 11 Johnson-Cook parameters are summarized in following Table 26, together with the value of the melting temperature, which is taken as fixed.

A	758.729 MPa	n	0.19036
C_1	-0.01524	C_2	0.03035
m_1	0.20964	m_2	2.80589
$\dot{\bar{\varepsilon}}^0_{p_1}$	0.04350 s^{-1}	$\dot{\bar{\varepsilon}}^0_{p_2}$	$3.94813 \cdot 10^{-6}$ s^{-1}
T_{0_1}	77 K	T_{0_2}	77 K
B	487.221 MPa	T_m	1773 K

Table 26
Split Johnson-Cook parameters for the DH-36 structural steel calculated through the GOPT calibration strategy.

Following Figs. 58 to 60 show the hardening functions predicted by the Split Johnson-Cook model calibrated with the GOPT strategy.

The curves of the GOPT calibrated Split Johnson-Cook model follow in the best possible way the nine experimental hardening curves throughout the equivalent plastic strain ranges. Comparing to the other two Split Johnson-Cook calibration strategies, the fittings are now significantly improved.

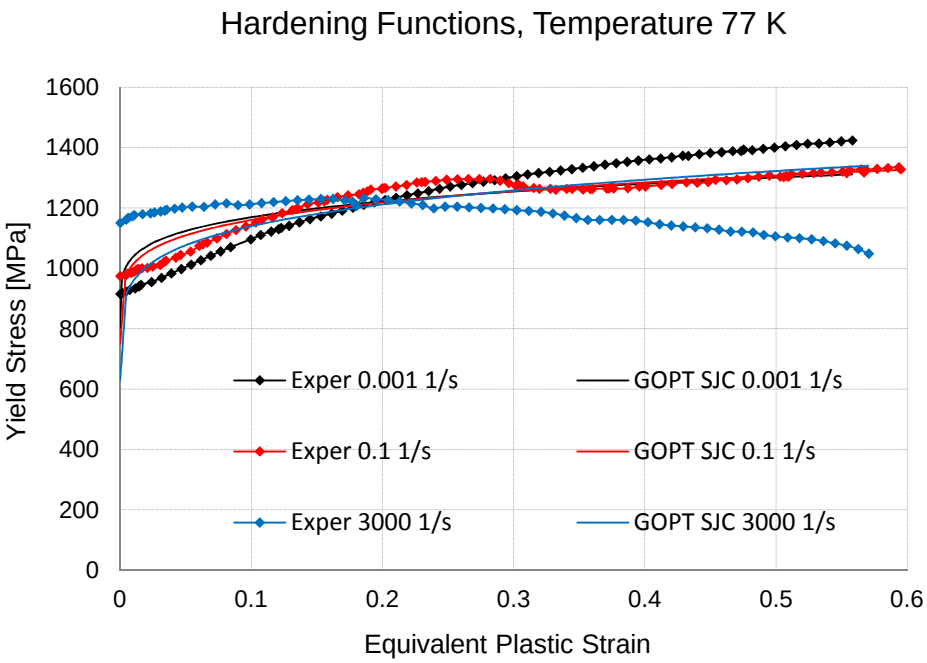

Figure 58. GOPT calibrated Split Johnson-Cook fitting to DH-36 structural steel data at temperature of 77 K and at three different equivalent plastic strain rates.

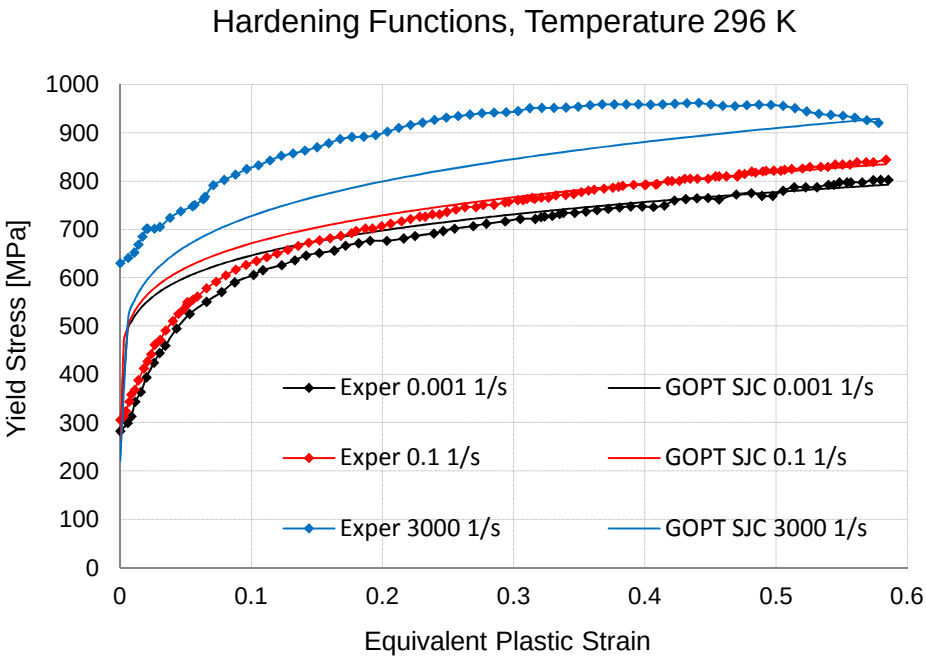

Figure 59. GOPT calibrated Split Johnson-Cook fitting to DH-36 structural steel data at temperature of 296 K and at three different equivalent plastic strain rates.

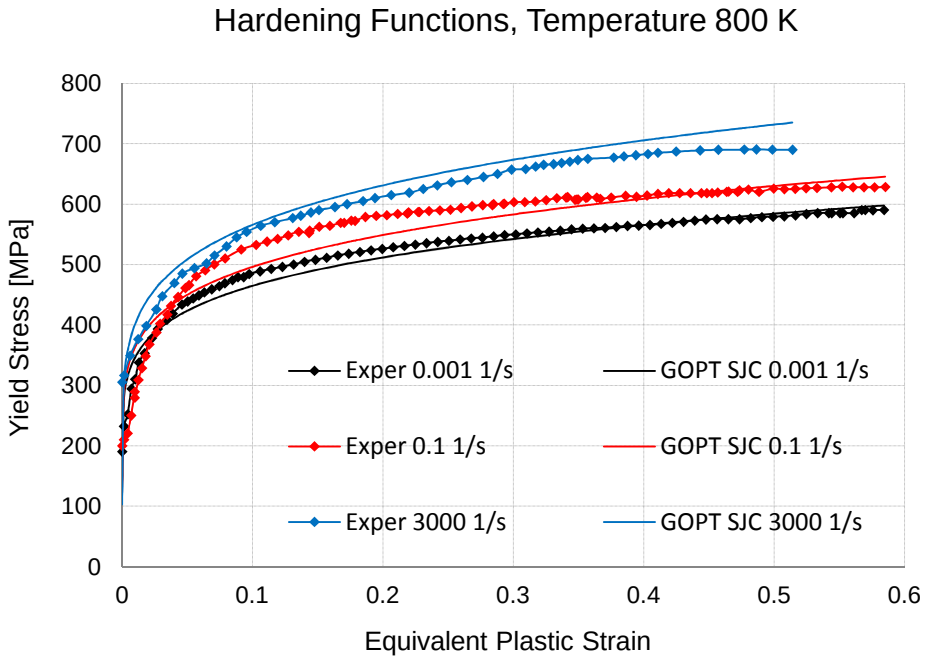

Figure 60. GOPT calibrated Split Johnson-Cook fitting to DH-36 structural steel data at temperature of 800 K and at three different equivalent plastic strain rates.

Following Figs. 61 to 63 further show the GOPT results by surface plots.

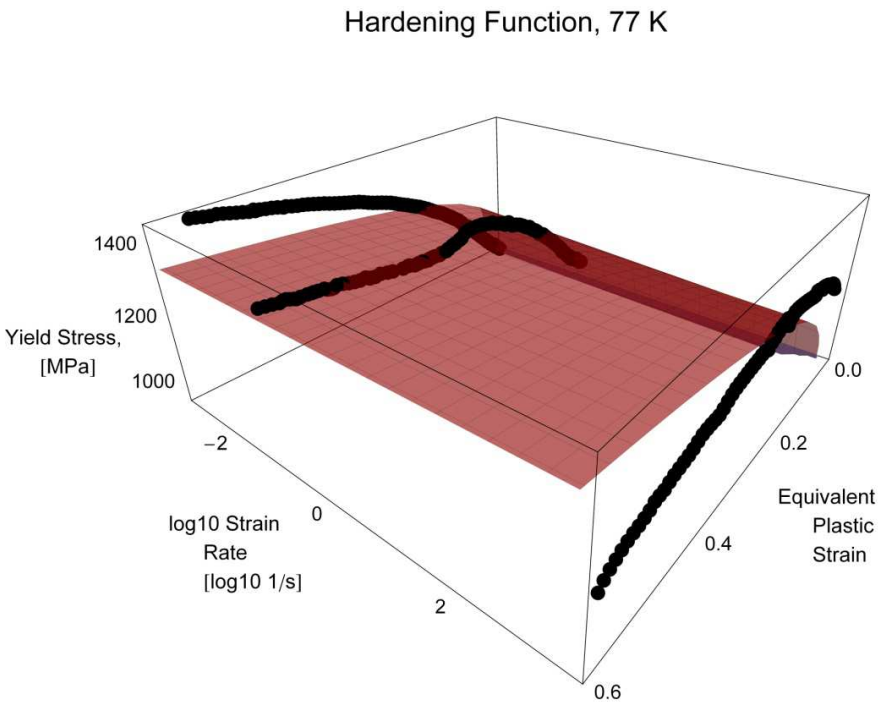

Figure 61. GOPT calibrated SJC model fitting to DH-36 steel data at temperature of 77 K.

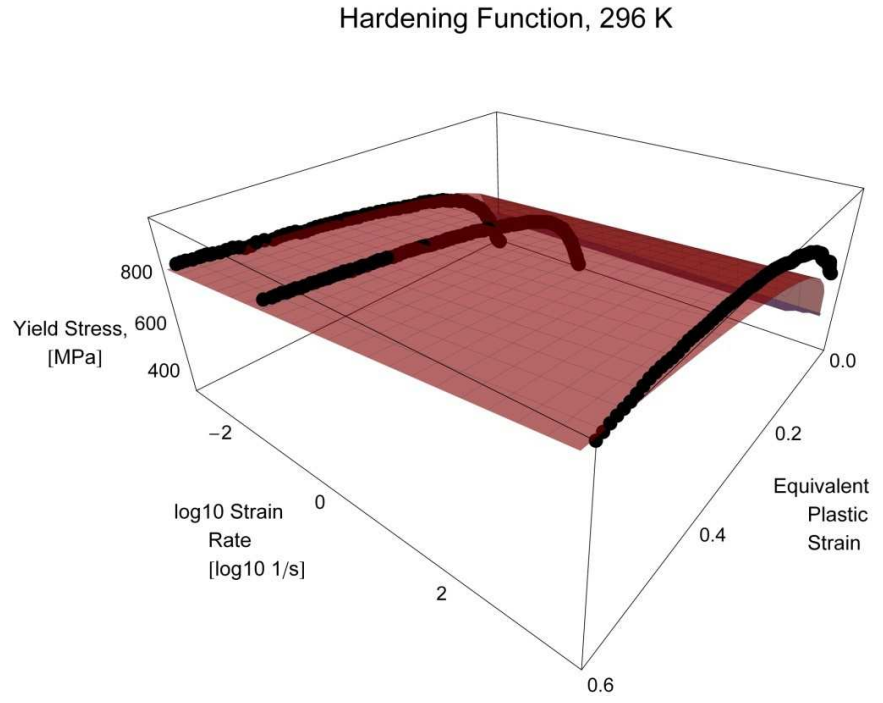

Figure 62. GOPT calibrated SJC model fitting to DH-36 steel data at temperature of 296 K.

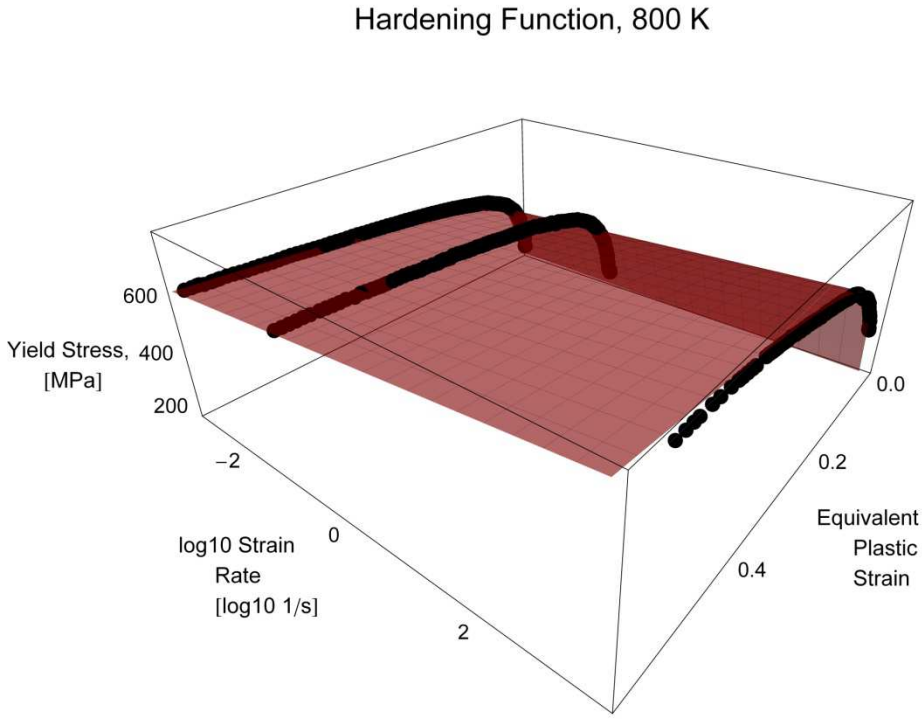

Figure 63. GOPT calibrated SJC model fitting to DH-36 steel data at temperature of 800 K.

Following Table 27 reports a comparison between the GOPT calibrated Split Johnson-Cook model predictions of the lower yield stresses and their experimental counterparts.

	Experimental Values	**OPTLYS JC Values**
0.001 s^{-1}, 77 K	915.555 MPa	802.362 MPa
0.1 s^{-1}, 77 K	974.565 MPa	749.101 MPa
3000 s^{-1}, 77 K	1150.46 MPa	629.872 MPa
0.001 s^{-1}, 296 K	282.455 MPa	279.957 MPa
0.1 s^{-1}, 296 K	305.455 MPa	261.373 MPa
3000 s^{-1}, 296 K	630.137 MPa	219.772 MPa
0.001 s^{-1}, 800 K	190.345 MPa	131.328 MPa
0.1 s^{-1}, 800 K	200.213 MPa	122.610 MPa
3000 s^{-1}, 800 K	305.345 MPa	103.095 MPa

Table 2
Comparison between experimental lower yield stresses and corresponding predicted lower yield stresses from the Split Johnson-Cook model calibrated with the GOPT strategy.

Following Table 28 reports both the yield stress and the percentage yield stress root mean square errors for each of the nine considered hardening functions, together with their algebraic mean value, i.e. their sum divided by 9. Comparing to the OPT calibrated Split Johnson-Cook model results, the average errors are further lowered.

	$\bar{s}_{err}$	$\bar{s}_{\%err}$
0.001 s^{-1}, 77 K	78.7608 MPa	6.833%
0.1 s^{-1}, 77 K	37.5824 MPa	3.481%
3000 s^{-1}, 77 K	155.248 MPa	13.70%
0.001 s^{-1}, 296 K	59.4984 MPa	16.13%
0.1 s^{-1}, 296 K	54.7770 MPa	13.63%
3000 s^{-1}, 296 K	98.8377 MPa	12.78%
0.001 s^{-1}, 800 K	16.6539 MPa	5.762%
0.1 s^{-1}, 800 K	31.1816 MPa	10.37%
3000 s^{-1}, 800 K	35.5619 MPa	9.895%
Average	*63.1224 MPa*	*10.29%*

Table 28
Yield stress (central column) and percentage yield stress (right column) root mean square errors for the GOPT calibrated Split Johnson-Cook model yield stress predictions.

3.3.4. Calibration Strategies Comparison and Assessment

Following Figs. 64 to 72 allow to compare the results from the three Split Johnson-Cook model calibration strategies presented above, by considering the nine experimental hardening functions from Nemat-Nasser and Guo, 2003. Moreover, the five different calibrated original Johnson-Cook predictions (Chapter 2) are presented as well, in order to favor a comparison of the two models. The original Johnson-Cook model predictions are presented with continuous lines, while those of the Split Johnson-Cook model are presented with dashed lines.

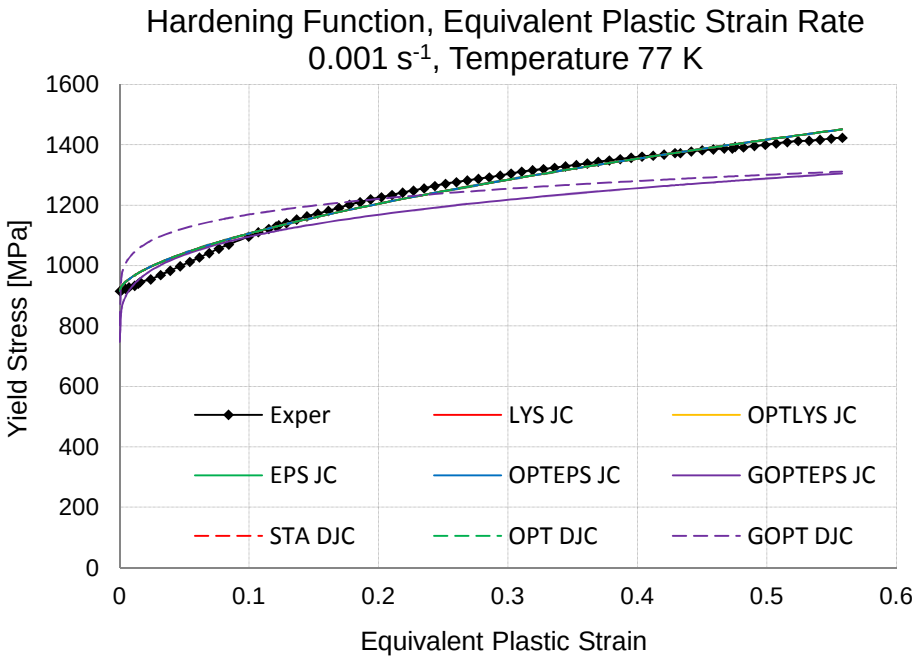

Figure 64. Fitting of original and Split Johnson-Cook models calibrated with different strategies to DH-36 steel data.

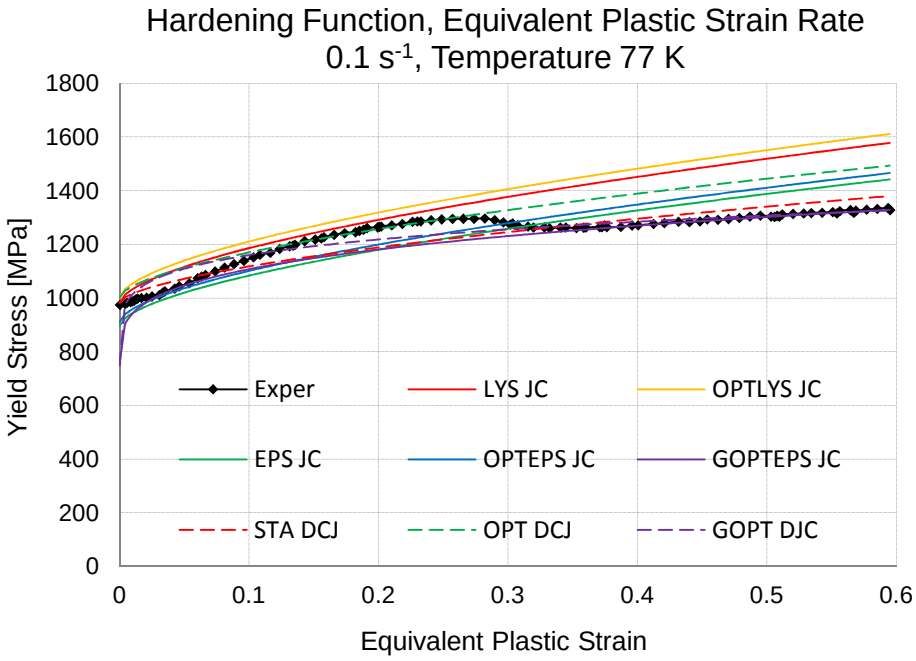

Figure 65. Fitting of original and Split Johnson-Cook models calibrated with different strategies to DH-36 steel data.

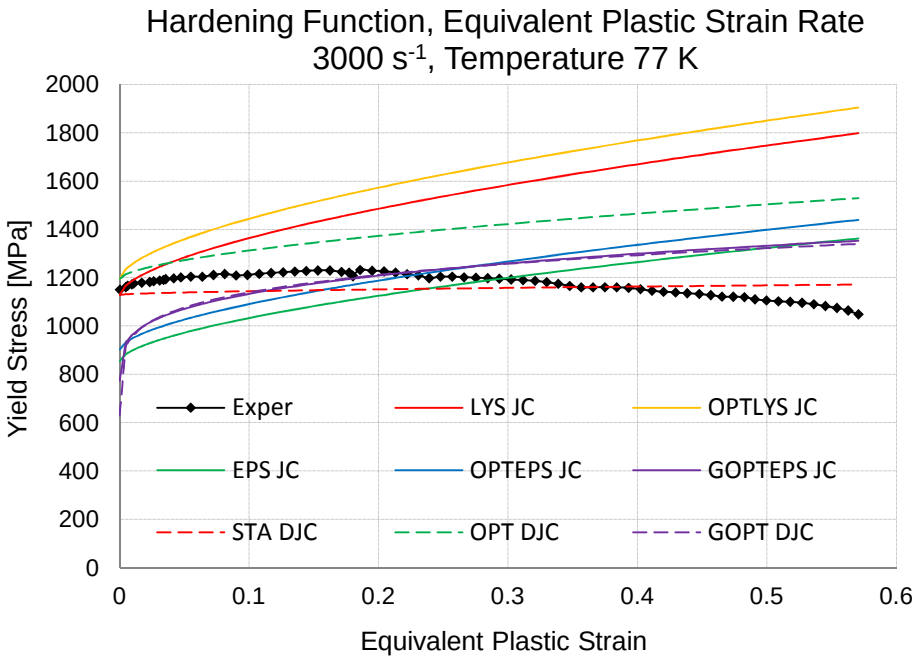

Figure 66. Fitting of original and Split Johnson-Cook models calibrated with different strategies to DH-36 steel data.

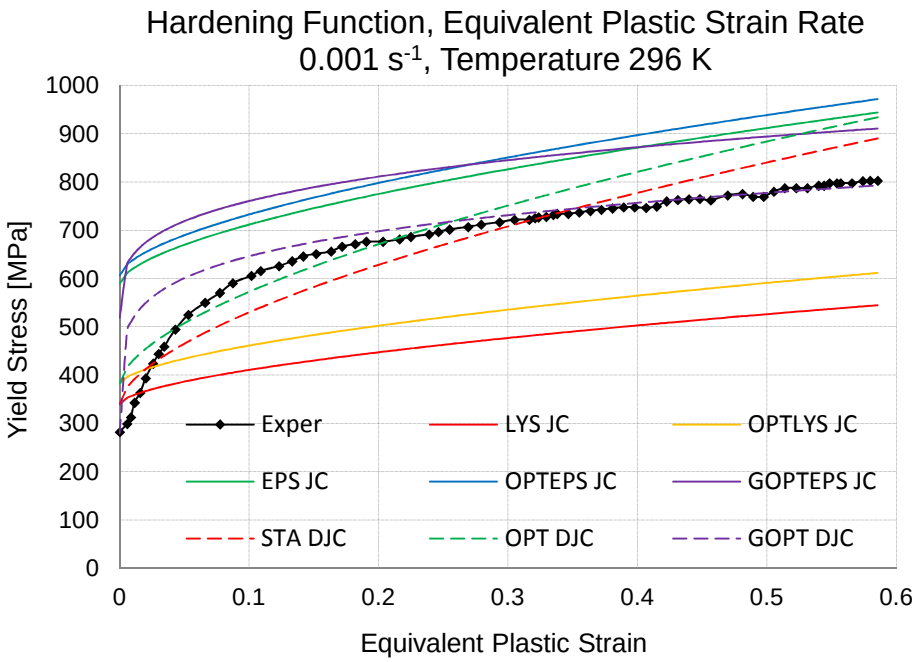

Figure 67. Fitting of original and Split Johnson-Cook models calibrated with different strategies to DH-36 steel data.

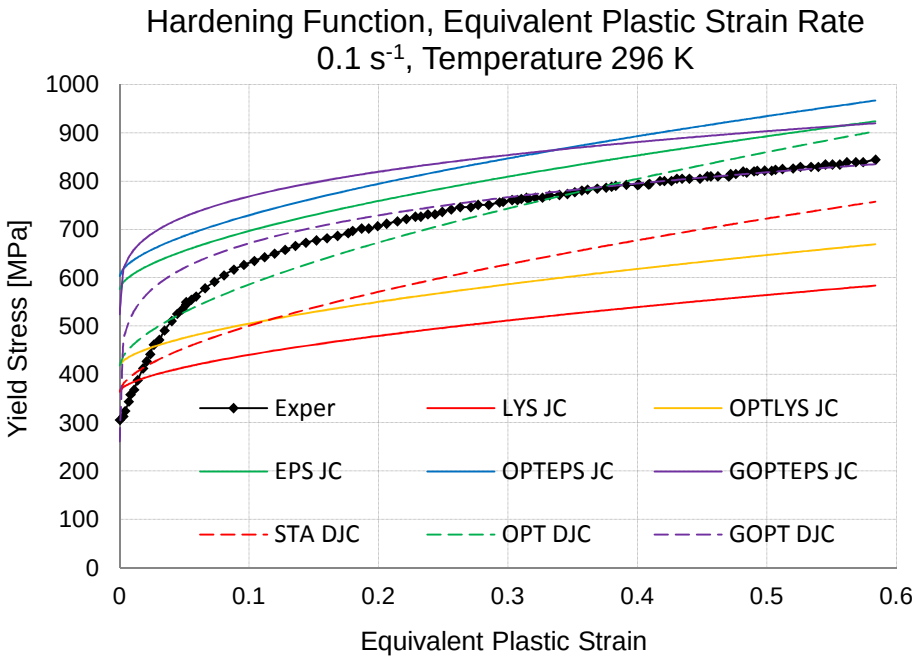

Figure 68. Fitting of original and Split Johnson-Cook models calibrated with different strategies to DH-36 steel data.

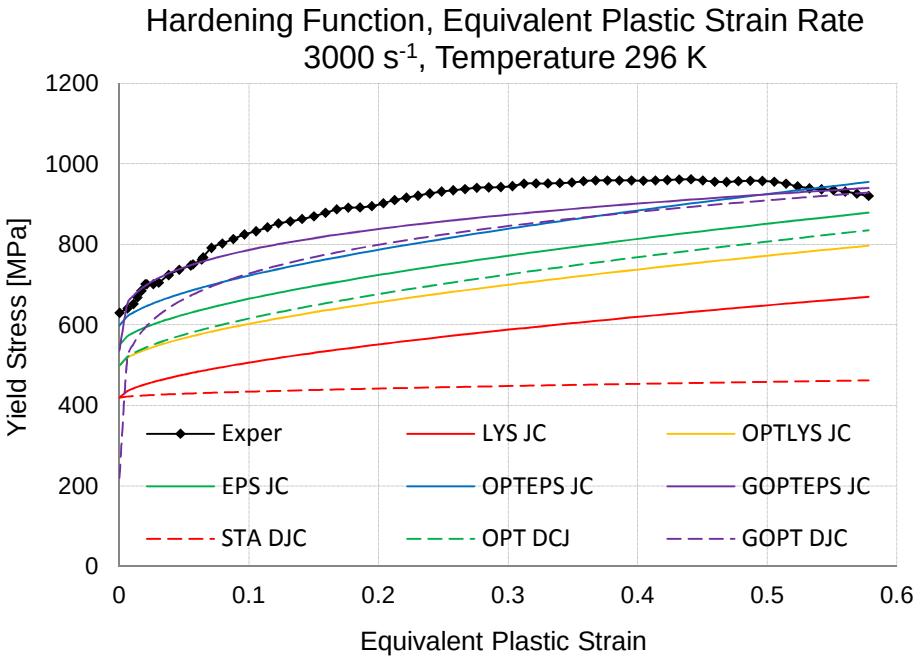

Figure 69. Fitting of original and Split Johnson-Cook models calibrated with different strategies to DH-36 steel data.

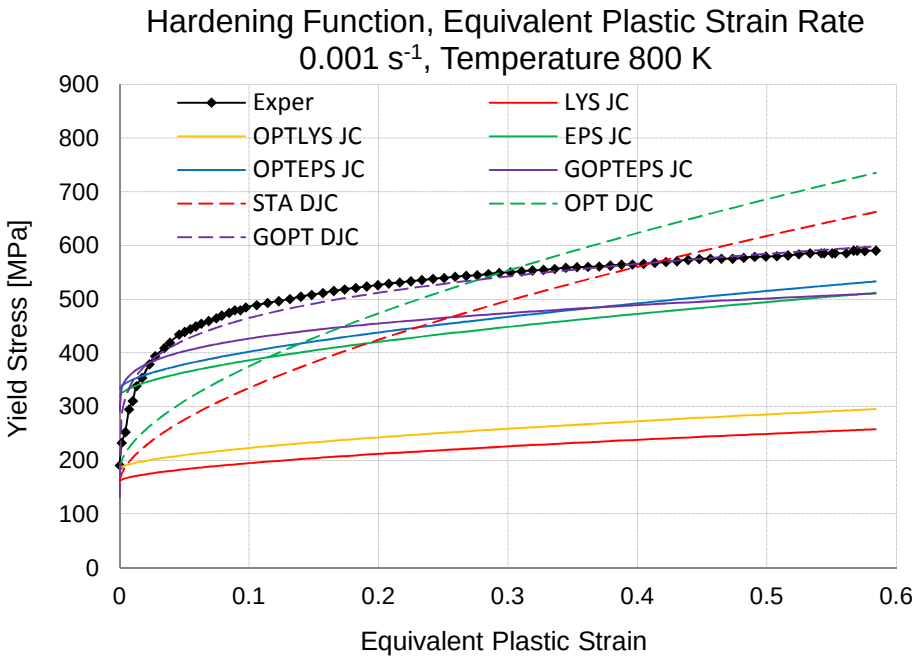

Figure 70. Fitting of original and Split Johnson-Cook models calibrated with different strategies to DH-36 steel data.

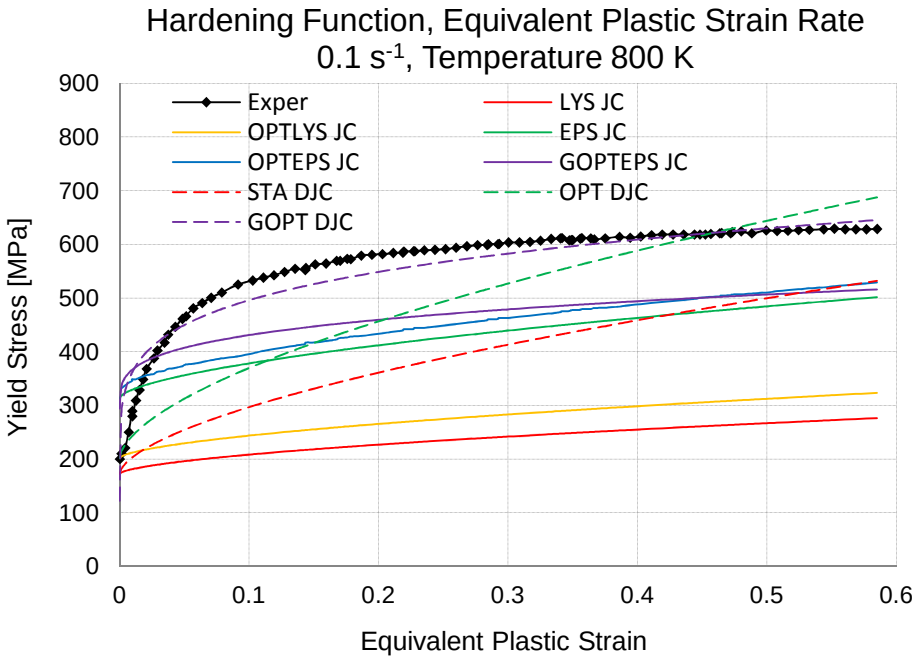

Figure 71. Fitting of original and Split Johnson-Cook models calibrated with different strategies to DH-36 steel data.

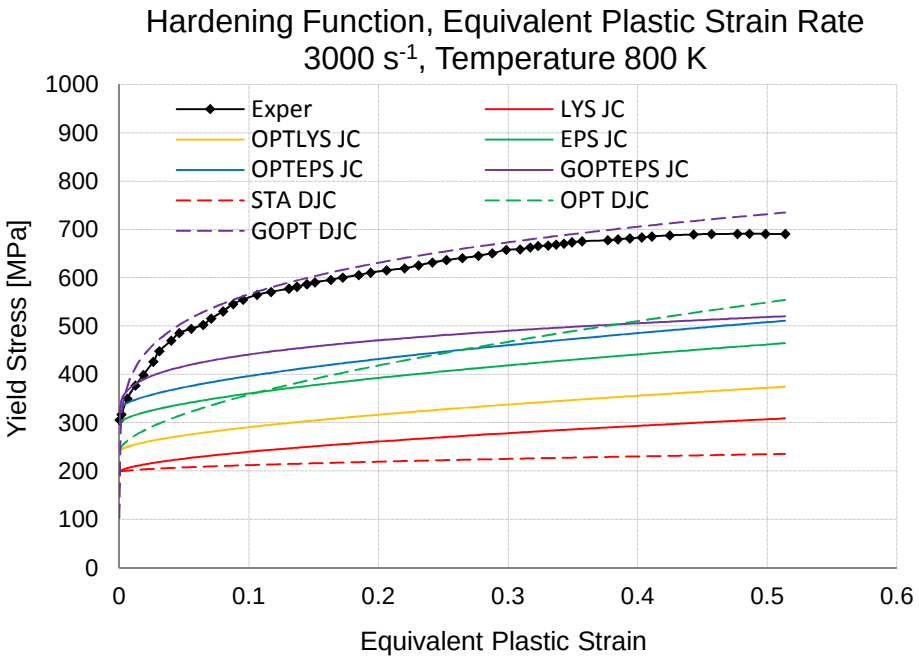

Figure 72. Fitting of original and Split Johnson-Cook models calibrated with different strategies to DH-36 steel data.

Figs. 64 to 72 show in better detail what previously presented for each original and Split Johnson-Cook calibration strategy. The reported trends confirm the considerations previously stated regarding the strengths and weaknesses of each calibration strategy. Following Table 29 shows a comparison between the five calibrated original Johnson-Cook models and the three calibrated Split Johnson-Cook models predictions of the lower yield stresses and their experimental counterparts.

	0.001 s^{-1}, 77 K	**0.1 s^{-1}, 77 K**	**3000 s^{-1}, 77 K**
Experimental Values	*915.555 MPa*	*974.565 MPa*	*1150.46 MPa*
LYS JC Values	915.555 MPa	981.323 MPa	1128.545 MPa
OPTLYS JC Values	915.555 MPa	1001.95 MPa	1195.34 MPa
EPS JC Values	915.555 MPa	896.883 MPa	855.085 MPa
OPTEPS JC Values	915.555 MPa	911.718 MPa	903.129 MPa
GOPTEPS JC Values	747.628 MPa	755.407 MPa	772.820 MPa
STA SJC Values	915.555 MPa	981.323 MPa	1128.55 MPa
OPT SJC Values	915.555 MPa	1001.95 MPa	1195.34 MPa
GOPT SJC Values	802.362 MPa	749.101 MPa	629.872 MPa
	0.001 s^{-1}, 296 K	**0.1 s^{-1}, 296 K**	**3000 s^{-1}, 296 K**
Experimental Values	*282.455 MPa*	*305.455 MPa*	*630.137 MPa*
LYS JC Values	340.015 MPa	364.439 MPa	419.115 MPa
OPTLYS JC Values	381.868 MPa	417.901 MPa	498.563 MPa
EPS JC Values	588.755 MPa	576.748 MPa	549.869 MPa
OPTEPS JC Values	606.076 MPa	603.536 MPa	597.851 MPa
GOPTEPS JC Values	518.571 MPa	523.967 MPa	536.045 MPa
STA SJC Values	340.015 MPa	364.439 MPa	419.115 MPa
OPT SJC Values	381.868 MPa	417.901 MPa	498.563 MPa
GOPT SJC Values	279.957 MPa	261.373 MPa	219.772 MPa
	0.001 s^{-1}, 800 K	**0.1 s^{-1}, 800 K**	**3000 s^{-1}, 800 K**
Experimental Values	*190.345 MPa*	*200.213 MPa*	*305.345 MPa*
LYS JC Values	160.967 MPa	172.533 MPa	198.417 MPa
OPTLYS JC Values	184.331 MPa	201.724 MPa	240.660 MPa
EPS JC Values	319.443 MPa	312.928 MPa	298.344 MPa
OPTEPS JC Values	332.813 MPa	331.418 MPa	328.296 MPa
GOPTEPS JC Values	290.859 MPa	331.418 MPa	300.660 MPa
STA SJC Values	160.967 MPa	172.533 MPa	198.417 MPa
OPT SJC Values	184.331 MPa	201.724 MPa	240.660 MPa
GOPT SJC Values	131.328 MPa	122.610 MPa	103.095 MPa

Table 29
Comparison between experimental lower yield stresses and corresponding predicted lower yield stresses from the original and Split Johnson-Cook models calibrated with different strategies.

Following Table 30 reports both the yield stress and the percentage yield stress root mean square average errors for each one of the five considered original Johnson-Cook calibration strategies and of the three considered Split Johnson-Cook calibration strategies.

	$\bar{s}_{err}$	$\bar{s}_{\%err}$
LYS Calibrated JC	253.860 MPa	34.85%
OPTLYS Calibrated JC	226.289 MPa	30.31%
EPS Calibrated JC	121.784 MPa	19.23%
OPTEPS Calibrated JC	113.915 MPa	18.21%
GOPTEPS Calibrated JC	105.488 MPa	16.86%
STA SJC Values	153.548 MPa	22.20%
OPT SJC Values	113.111 MPa	15.60%
GOPT SJC Values	63.1224 MPa	10.29%

Table 30
Yield stress (central column) and percentage yield stress (right column) root mean square average errors for the yield stress predictions of the original and Split Johnson-Cook models calibrated with different strategies.

Some considerations are reported in the following, in order to better understand the consequences of choosing a particular calibration strategy or the other.

The STA calibration strategy allows to model quite coherently both the lower yield stress and the plastic flow, by considering data provided only by those hardening functions which refer to at least one reference condition, whether it is the reference equivalent plastic strain rate or the reference temperature. This aspect is true for both the lower yield stress and the plastic flow terms. As a result, the lower yield stress and the plastic flow are better modeled for these hardening functions, in particular for the hardening function referring to the reference conditions for both the lower yield stress and the plastic flow, i.e. the hardening function at the equivalent plastic strain rate of 0.001 s^{-1} and at the temperature of 77 K. This is due to the fact that the parameters A, B and n are determined by fitting this hardening function only. On the other hand, errors may be introduced for the predictions of the other hardening functions. Such errors may actually become considerable, as clearly visible in Figs. 69 and 72. Therefore, this strategy should be avoided if experimental data which do not refer to at least one reference condition are available, both for the lower yield stress and for the plastic flow. The OPT and GOPT calibration strategies should be preferred. Anyway, it is recognized that the DH-36 data appear as quite an unlucky case for the use of the Split Johnson-Cook STA calibration strategy, as its effectiveness is heavily hindered by the fact that the hardening function at 3000 s^{-1} and 77 K, which plays an important role for the determination of the material parameters, presents a very different behavior compared to those at the same equivalent plastic strain rate but at different temperatures. In other cases, the STA calibration strategy may actually provide better results than those obtained for the considered DH-36 steel case. However,

the OPT and GOPT calibration strategies are capable to overcome unlucky cases of such kind.

The OPT calibration strategy extends the capabilities of the STA calibration strategy by considering all the experimental data. As a result, the fit of the lower yield stress and of the plastic flow is a compromise between the lower yield stresses and plastic flows of all the made available hardening functions. The GOPT calibration strategy further improves the calibration by allowing 11 out of the 12 Split Johnson-Cook parameters to be optimized. As a result, its trends provide the best overall fit for all the made available experimental hardening functions. The GOPT calibration strategy capacity to better model the plastic flows throughout the equivalent plastic strain rate and temperature ranges is partially due to the fact of avoiding to calculate the parameters B and n, by relying on the plastic flow at the plastic flow reference conditions only, but rather by considering how to best fit all the made available experimental plastic flows, through a power form. This is the reason why the GOPT calibration strategy provides the worst fit for the plastic flow at the conditions which act as reference for the other calibration strategies (i.e., 0.001 s^{-1} and 77 K) but it is also one of the reasons why it provides the best overall fit to the plastic flows in other conditions. However, since the parameters B and n are constants and thus not functions of the equivalent plastic strain rate and the temperature, the more the plastic flow trends at diverse equivalent plastic strain rates and temperatures are different, the more modeling errors are introduced, even when this calibration strategy is adopted. Clearly, this aspect is similar to what arises for the original Johnson-Cook GOPTEPS calibration strategy.

It is worthwhile to point-out some considerations regarding the easiness of calibration of each strategy, i.e. the number of calculations that each procedure needs in order to get the Split Johnson-Cook parameters and the possible necessity of experimental data treatment. In this regard, the STA calibration strategy is the simplest, since it requires a regression (for determining the parameters B and n) together with the simple calculations involved in the determination of the parameters C_1 and m_1 and some other nonlinear regression necessary in order to determine the values of the parameters C_2 and m_2. The STA calibration strategy requires to carry-out inverse analyses of all the considered hardening functions, i.e. all those which refer to at least one reference condition, since they are thoroughly used for the determination of the plastic flow parameters C_2 and m_2.

The OPT calibration strategy involves heavier calculations, due to the fact that two overdetermined nonlinear systems are required to be solved. Furthermore, all the experimental hardening functions need to be treated through inverse analyses, in order to purify results from structural effects. Finally, the GOPT calibration

strategy further complicates things by introducing 11 unknowns in the overdetermined system, resulting in a problem that is more difficult to solve.

All three Split Johnson-Cook model calibration strategies require experimental data in terms of entire hardening functions, i.e. not only lower yield stress data. For the Split Johnson-Cook model, the more experimental data are made available, the better for the aim of calibrating the model. As previously said for the original Johnson-Cook model, the only way that allows to understand the real material behavior is that of carrying-out experimental tests, i.e., to obtain hardening functions, at several different equivalent plastic strain rates and temperatures, with the aim of covering the ranges of interest with enough resolution. All the available data can fruitfully be introduced in the calibration procedures of the Split Johnson-Cook model. Moreover, the modeling of cases in which the lower yield stress and the plastic flow present quite different dependencies on the equivalent plastic strain rate and temperature are no longer a problem, differently from what happens for the original Johnson-Cook model. Rather, such cases can be successfully reproduced thanks to the features of the new model.

The Split Johnson-Cook model appears to be capable to provide a significant improvement comparing to the original Johnson-Cook model. This statement relies on the yield stress average errors reported in Table 30. Considering the same experimental data (Nemat-Nasser and Guo, 2003), the original Johnson-Cook model calibrated with the strategy that appears to be the most popular, i.e. the LYS calibration strategy, provides a yield stress percentage average error equal to 34.85%, while the same model calibrated with the most refined approach, i.e. the GOPTEPS strategy, presents an error equal to 16.86%. The Split Johnson-Cook model calibrated with the less fine strategy, i.e. the STA approach, provides an error equal to 22.20%. As already mentioned, the considered DH-36 steel case appears to be an unlucky case for the application of such calibration strategy, which may instead provide better results for other cases, in particular for those materials which do not present heavy differences on the hardening behavior when passing from conditions in which at least one reference condition is satisfied, to those in which both reference conditions are not satisfied, both for the lower yield stress and the plastic flow terms. The Split Johnson-Cook model calibrated with the two best calibration approaches, i.e. the OPT and the GOPT strategies, provides an error equal to 15.60% and 10.29%, respectively. This means passing from an yield stress average error of 105.488 MPa (original Johnson-Cook best calibration strategy, i.e. GOPTEPS) to an average error of 63.1224 MPa (Split Johnson-Cook best calibration strategy, i.e. GOPT). As a matter of fact, the proposed model appears to be capable to almost halve the fitting errors. This positive consequence is due to the fact of having split the equivalent plastic strain rate and temperature effects on

the lower yield stress and on the plastic flow, hence avoiding possibly large modeling errors of one case or the other.

The calibration of the proposed model requires the same experimental data needed for the calibration of the original Johnson-Cook model, although the model parameters are increased from 8 to 12. The enlargement of material parameters does not appear to be a problematic issue. Indeed, the calibration procedures for the original and for the Split Johnson-Cook models require basically the same effort in terms of data processing and calculations. Furthermore, when the STA and OPT calibration strategies are adopted, the Split Johnson-Cook model can rely on some parameters already calculated for the original Johnson-Cook model. More in detail, the STA calibration strategy uses the same 8 parameters used for the original Johnson-Cook LYS strategy, and the only parameters to be determined are the 4 parameters C_2, m_2, $\dot{\varepsilon}_{p_2}^{0}$ and T_{0_2}. Regarding the OPT Split Johnson-Cook calibration strategy, the same 8 parameters used for the original Johnson-Cook OPTLYS calibration strategy are used. Again, the parameters that need to be determined are the 4 parameters C_2, m_2, $\dot{\varepsilon}_{p_2}^{0}$ and T_{0_2} only. For what it concerns the Split Johnson-Cook GOPT calibration strategy, the only reusable parameter is the melting temperature.

As said for the original Johnson-Cook model, the procedure adopted to calibrate the parameters of the Split Johnson-Cook model has great importance relatively to the aim of setting-up a strength model capable to display a good coherency throughout the equivalent plastic strain, equivalent plastic strain rate and temperature ranges of interest. Even though the Split Johnson-Cook model is capable to diminish some of the original Johnson-Cook modeling errors, these incoherencies cannot be totally eliminated when it is an aim to maintain a very simple modeling framework. As for the original Johnson-Cook model, the choice of the calibration strategy allows to redistribute these errors according to different criteria. Such choice should be made by considering all the aspects exposed and explained in the present chapter, being aware of the nature and of the consequences of each calibration strategy. In cases in which the Split Johnson-Cook model fits very poorly the experimental data, it may be worthwhile to consider a replacement of some of the lower yield stress or plastic flow strain rate or temperature terms, or of all of them.

The Split Johnson-Cook model maintains the same computational appeal of the original Johnson-Cook model towards computational implementations, with particular reference to applications in FEM codes. In fact, the model uses the same variables used by the original Johnson-Cook model, i.e. the equivalent plastic strain, the equivalent plastic strain rate and the temperature. These variables are usually already available in most FEM codes and hydrocodes. In fact, it is common

use to insert these variables among the information provided in each timestep. Regarding the computational heaviness of the implementation, the only point that differs from the original Johnson-Cook model consists in the fact that the Split model implies a slight increase of the number of operations necessary to compute the current yield limit, since the proposed model contains two Split additive terms, rather than a single one. Comparing to the computational requirements necessary to run an analysis with the original Johnson-Cook model, this aspect does not appear to be crucial in further burden the computational requirements necessary for carrying-out the FEM analysis.

A last consideration is reported in the following. If the material behavior that needs to be fitted appears to present complicated dependencies of the yield stress on the equivalent plastic strain rate and on the temperature, other strength models may be adopted, with the target to provide a better experimental data interpolation. This aspect is particularly true for materials that do not respect the natural logarithmic and the power dependencies on the lower yield stress and plastic flow dimensionless equivalent plastic strain rate and on the lower yield stress and plastic flow homologous temperatures, respectively. Moreover, materials that present a heavy dependence of the plastic flow parameters B and n on the equivalent plastic strain rate and on the temperature may further worsen this aspect. In such cases, one idea may be that of adopting a strength model which considers the same power dependence of the Johnson-Cook model on the equivalent plastic strain, but also considers the lower yield stress parameter A and the plastic flow parameter B and n to be functions of the equivalent plastic strain rate and of the temperature, as reported in the following equation

$$\bar{s} = A\left\{\dot{\bar{\varepsilon}}, T\right\} + B\left\{\dot{\bar{\varepsilon}}, T\right\} \cdot \bar{\varepsilon}^{n\left\{\dot{\bar{\varepsilon}}, T\right\}} . \tag{85}$$

This approach imposes a power function between the yield stress and the equivalent plastic strain, and this function is fitted to different equivalent plastic strain rate and temperature data through the introduction of an appropriate modeling of the two parameters that characterize the function. The three functions that define the trends for the parameters A, B and n throughout the tested equivalent plastic strain rates and temperatures can be shaped accordingly to the available experimental data and can be enriched in the case in which more material information is available. As instance, these functions may be multi-variables polynomials or piecewise functions. Considering the structural steel analyzed in this work, simple linear trends shall not be capable to fit the material behavior with enough coherency. Clearly, this approach leads to a serious complication of the model, due to the strong increase in the number of parameters necessary in order to coherently represent the three involved functions. Therefore, this aspect involves

a loss of simplicity which shall probably be the main positive aspect of the original and Split Johnson-Cook models.

4. APPLICATION TO AN INDUSTRIAL CASE: PERFORATING GUN DEVICES

The aim of this chapter is that of producing a campaign of FEM simulations of a perforating gun device of specific interest of the industrial partner co-supporting the present research project. In order to reach qualitative and possibly quantitative results, some of the models exposed in the previous chapters will be used all together. The first step of this chapter consists in a brief description of perforating gun devices. After that, FEM simulations will be exposed, together with an assessment of the obtained results.

4.1. Brief Description of Perforating Gun Devices

Perforating guns are devices widely used for the perforation of oil and gas wells. As a matter of fact, one of the most critical phases of oil and gas extraction processes is that consisting in the radial perforation of an already completed well. Usually, hydrocarbons deposits are found as fluid masses trapped inside porous rocks or soils. When an hydrocarbon reserve is located, one or more wells are accomplished through the ground, down to a level deep enough to reach the reservoirs. After this phase, the completed wells need to be radially perforated in order to create multiple perforations in the rocks or soils in which the hydrocarbons are contained. The resulting holes do favor the subsequent hydrocarbon flow pumping towards the upper surface, and are then necessary in order to achieve a good extraction capacity, therefore determining a good productive well. Since decades ago, oil companies have been focusing on the achievement of a better execution of this phase, because this is recognized as one of the best ways to ensure a superior performance of an extraction well. After World War II, the quest for the best radial perforation technique has been a leading research theme for major oil companies. The first solutions adopted consisted in perforation strategies related to mechanical perforation or firing of solid projectiles. Later on, a specific radial perforation technique emerged above the others. This technique involved the use of so-called shaped charges, i.e. explosive charges specifically shaped with the aim to concentrate the explosive energy on a specific metallic target. The enormous pressure unleashed by the explosive detonation acts on this metallic target, that is specifically designed to become a fluid jet travelling at very high velocity, possibly supersonic. This projectile displays then a high penetration capacity, that allows the perforation of the well and of the surrounding media, i.e. rocks and soils. The shaped charge perforation technology prevailed over others due to rapidity of use

and in particular due to better penetration capacity and overall quality of the resulting holes. Perforating devices that adopted this technology were called perforating guns or oil-well perforators. The introduction of perforating guns implied a dramatic increase of oil wells extraction performances. However, researches for improving oil well perforation capacities still go on, and solutions different from that of using shaped charges have recently been proposed. An example of that sort is provided, e.g., in Fugelso et al., 2004. Nonetheless, technologies related to the use of shaped charges do appear to be the most used techniques for radially perforating oil wells.

In this work, the wording perforating gun device refers to a system composed by all the components that are somehow involved in the firing of the perforating gun. In particular, six major components are identified, i.e. the shaped charges, the carrier, the casing, the concrete coating, the ambient fluid and the soil. As mentioned above, the shaped charges are the components appointed for delivering the blast, which will then be responsible for the creation of the subsequent metallic perforating jets. The carrier is a sealed pipe usually made of steel whose main function is that of carrying the shaped charges and their detonation system at a specific deepness in the well, in order to perform the radial perforation. The casing is a steel pipe inserted in the well in order to give it stability and avoid wall collapses. The concrete coating is a concrete cover of the part of the well directly in contact with soil and rocks, and is delimited in its inner side by the casing. The ambient fluid fills the space between the carrier and the casing, i.e. it is the fluid naturally present inside the well. Finally, the soil is the ultimate target of the metallic perforating jets, namely the medium in which hydrocarbons are embedded. Here it is called soil but in general this may mean soil, rock or both. In the context of the present work, the wording perforating gun device refers to the six components just introduced, as previously mentioned, and the wording perforating gun refers to the shaped charges and the carrier only.

Following Fig. 73 illustrates the firing of a perforating gun inserted in a well. It is possible to see the six just defined major components. In this figure, the firing of a perforating gun is analyzed through a subdivision in three subsequent phases, represented from left to right.

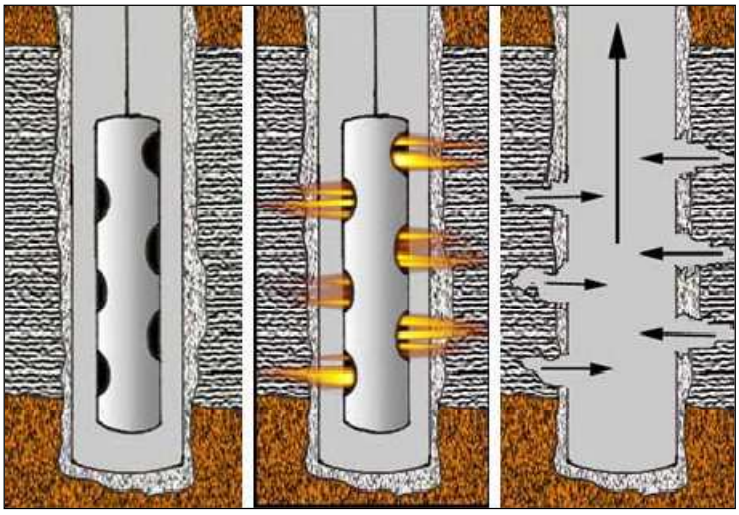

Figure 73. Firing of a perforating gun (source www.usoilandgas.net).

In the first phase (left image in Fig. 73), the carrier is introduced into the well and dropped at the desired deepness. The second phase (central image in Fig. 73) consists in the detonation of the shaped charges explosives and in the subsequent creation of metallic perforating jets, which pierce the carrier and, after travelling in the ambient fluid, the casing, the concrete coating and then terminate their travel as far as possible in the soil. In the third phase (right image in Fig. 73), the perforating gun is taken back to the surface. Afterwards, the hydrocarbons are pumped-out of the soil up to the surface through a proper hydraulic system, by taking advantage of the performed holes.

For their role in the firing process, two out of the six components of a perforating gun device take the most importance. These components are the shaped charges and the carrier. In the following, a brief description of them is presented.

4.1.1. Shaped Charges

Shaped charges are the core of a perforating gun device. A shaped charge may be defined as a system made by a certain quantity of explosive and delimited by two distinct solid parts. One of this two solid parts is a container that delimits the explosive on one end and on the sides, and it is technically called case. The other solid part is a piece conveniently shaped for enclosing the other end of the explosive material. It is technically called liner.

The case can be made of a number of different materials, such as steel or zinc, and may be shaped in several different geometries. Its main function is to resist as much as possible to the high pressure caused by the explosive detonation, then redirecting the energy of the explosive towards the liner.

The explosive is usually composed by two parts, i.e. a main explosive, which has the function to transfer a great amount of energy to the liner through pressure and temperature, and a small adjunct explosive, called primer or booster, whose only function is that of initiating the detonation of the main explosive. More specifically, a detonation system (e.g. a detonating cord) triggers the primer, which in turn initiates the main explosive. Pressed secondary explosives with a high detonation velocity, such as HMX and RDX, are usually chosen as main explosives.

The liner has the function to collapse on its axis, under the effect of the pressure and temperature of the detonated main explosive, thus creating a thin hyperfast jet of material which owns a high penetration capacity. The liner may be made with a number of different materials, such as metals, alloys, ceramics and even woods. The higher penetration capacities are obtained by using ductile and dense metals. Copper appears to be one of the most used materials for the realization of liners. The liner geometry may be chosen among a number of different options, although the most adopted geometries seem to be the cone and the hemisphere. The phenomenon of having a shaped explosive charge concentrating detonation energy on a specific target, resulting in powerful projectiles, is known as Munroe or Neumann effect. In this regard, some considerations can be found in Birkhoff et al., 1948. Following Fig. 74 gives a cross-section representation of a shaped charge with a conical liner.

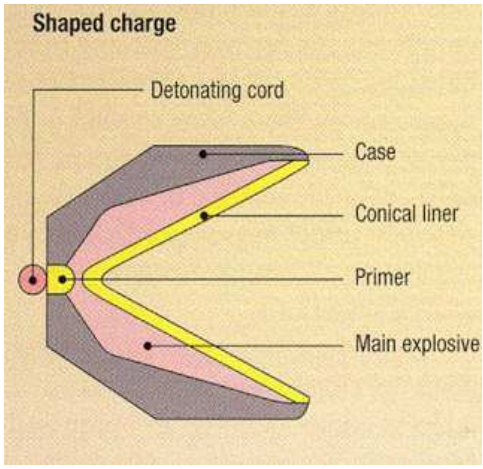

Figure 74. Cross section of a shaped charge (source www.slb.com).

Following Fig. 75 reports a picture that clearly shows the three main components of a shaped charge, i.e. the case, the explosive and the liner.

Figure 75. Components of a shaped charge (source www.slb.com).

It is worthwhile to report some other considerations regarding the evolution that the liner undergoes during the firing of a perforating gun device. After the detonation of the main explosive, the huge pressure and temperature force the solid liner to melt. Due to the liner shape, the melting process occurs in a way which implies the formation of a needle-shaped hyperfast jet. Experimental measurements reported in Ambrosi and Briganti, 2010, indicate that some specific melted liner may reach velocities near 8 km/s on their tip and lower velocities, near 2 km/s, on their tail. These values refer to the phase before the impact occurring between the melted liner and the inner surface of the carrier. Following Grove et al., 2006, about 40% of the total main explosive energy goes into kinetic energy of the case, about 30% goes into kinetic energy of the liner, about 25% remains in the detonation products and the remaining 5% goes into heating of the case and the liner.

The distance between a shaped charge and the carrier (or a generic target) is technically called standoff distance. This parameter is quite important when it comes to evaluating the penetration capacity of the liner. In particular, short standoffs imply that the liner does not have enough space to stretch out and gain the efficacious needle shape. On the other hand, long standoffs cause the liner to break into particles, which tend to drift off the axis of the shaped charge, resulting in wider but shorter perforations. Loss of velocity due to air drag is another issue when long standoffs are adopted.

Shaped charges were born and first used in military contexts. Nowadays, along with their success as perforating tools in the oil industry, they are widely used in the production of military weapons. Among others, a famous historical use of shaped charges with conical liner was in the anti-tank German weapon called *Panzerfaust*, widely used during World War II. Following Fig. 76 reports a picture which clearly shows the conical liner in the warhead of such weapon.

Figure 76. Shaped charge in a World War II German anti-tank weapon. The component on the left of the shaped charge is an aerodynamic cover (source defense-update.com).

Considerations about the opportunity of adopting analytical models in order to predict some key parameters of a shaped charge explosion, such as the jet velocity, can be found, e.g., in Birkhoff et al., 1948, Xi, 1995, and Novokshanov and Ockendon, 2006. Moreover, reviews on the history of shaped charges can be found, e.g., in Eather and Griffiths, 1984, and in Walters, 2008.

4.1.2. Carrier

Basically, the carrier consists in a pipe made of steel which contains the shaped charges, their support and their detonating system. The photograph reported in following Fig. 77 shows the shaped charges and their support and detonation systems while being inserted into the carrier.

Figure 77. Insertion of shaped charges and their support and detonation systems in a carrier (source exprogroup.com).

The shaped charges and their support and detonation systems need to be fixed into the carrier. After that, the carrier is sealed, in order to isolate the shaped charges from the outside. In fact, the ambient fluid (i.e. the fluid that fills the well, whether liquid or gas), may be potentially harmful to the shaped charges functionality.

Basically, a carrier has two main functions. First, it has to carry the shaped charges and their support and detonation systems at a specific deepness into the well, in order to allow the radial perforation to be accomplished. Second, it needs to resist at the relevant stresses at which it is submitted, due to the firing of the perforating gun device. Following Grove et al., 2006, and Ambrosi and Briganti, 2010, these stresses may be decomposed into three main parts. The first one consists in the piercing effect due to hypervelocity impacts with each liner produced from the shaped charges explosion, resulting in several perforations of the carrier, technically called exit holes. The second one consists in the blast effect due to the explosive detonation inside each shaped charge. The explosive material expands at high velocity and eventually hits the inner surface of the carrier. The third one consists in possible impacts between the carrier and high velocity fragments that detach from the fired shaped charges or their support and detonation systems.

In order to resist to these stresses, a carrier needs to fulfill two requirements that are somehow in conflict. On one side, it requires high resistance in order to limit the resulting deformation. This characteristic usually implies brittleness. On the other hand it requires a good ductility in order to avoid possible fragmentation due to the blast loading derived from the explosions. This conflict between material properties is partially mitigated by introducing ad hoc geometrical weaknesses in correspondence of the impact zone of each liner. This stratagem facilitates the penetration of the carrier by the jets and favors the preservation of energy and velocity in the travelling liners, which will then be useful to achieve maximum soil penetration. These designed weaknesses are technically called scallops. This solution favors the limitation of the fracture zones nearby each scallop. Scallops are also useful to avoid contacts between possible burrs that may develop on the perimeters of the exit holes and the walls of the well. This phenomenon would be harmful for the post-firing extraction of the perforating gun from the well. Following Fig. 78 reports a picture that clearly shows some scallops in a carrier of an unfired perforating gun.

Figure 78. Scallops in an unfired carrier (source www.justbeneaththesurfacewv.com).

The carrier is perhaps the most critical component of a perforating gun device. It needs to be easily pierced by the melted liners but at the same time it needs to avoid severe deformations and in particularly destructive fragmentation. Moreover, the carrier needs to resist and thus contain the blasts derived from the firing of the shaped charges, that may be potentially harmful to the well's walls, possibly resulting in unfixable structural damages that may compromise the well working capacity or even determine serious impairment of its functionality. These aspects may possibly lead to a breakdown of the well, with dramatic economic consequences, in particular for wells whose drilling have required months of highly expensive perforating operations. Avoiding such situations is of primary importance.

The structural resistance of the carrier is extremely important also for keeping a shape suitable for extracting the perforating gun from the well. As a matter of fact, failure on the perforating gun fishing may result in massive expenses due to the necessity of adopting ad-hoc systems for the recovering of the stuck device. This operation may be further aggravated by the presence of fragments detached from the fired device and obstructing the well. The situation gets even worse when the well is located in hardly reachable areas, such as for wells dug beneath the sea bed.

Considering what just exposed, it appears clear that the resistance of the carrier to the three main stressing effects previously introduced is of critical importance for achieving a successful use of the perforating gun device. Some further considerations regarding the deformations that usually appear in this component are made in the following.

While the perforating effect due to the liners seems to produce only very localized fractures (exit holes), the blasts effect appears to be the most dangerous

stressing factor. The detonation products reach the carrier when the liners have already pierced it. Thus, they act on an already damaged component, i.e. the carrier with the produced exit holes. Their action produces huge pressures and temperatures on the inner surface of the carrier, in correspondence of each pierced scallop. This effect may cause severe bulges in the surroundings of the scallops, technically called localized bulges. Moreover, the blast effect causes stresses in other zones of the carrier as well, due to quite complicated physical phenomena related to fast blast or impact loadings, such as spall fracture. Spall fracture is suspected to be responsible for very dangerous cracks that may potentially arise in different zones of the carrier, even distant from the scallops. This last phenomenon is technically called cracking. Finally, the possible impacts of fragments detached from the shaped charges (in particular from their cases and supporting system) that hit the inner surface of the carrier at a high velocity may cause further damage to the component.

The synergic interaction of these three main stressing factors may in general strengthen the global solicitation that acts on the carrier. Following Fig. 79 reports the photography of a fired carrier in which the phenomena of exit holes, localized bulges and cracking are identifiable.

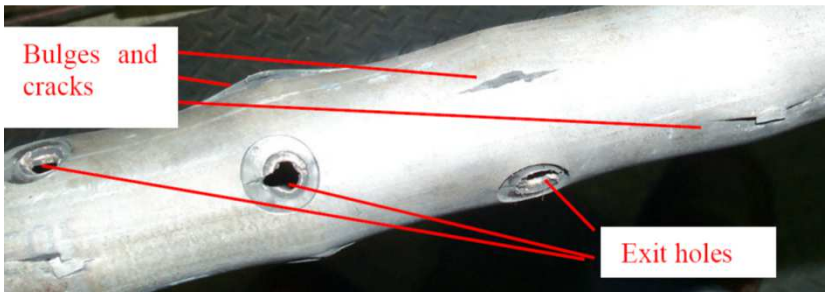

Figure 79. Localized bulges and cracking in the carrier of a fired perforating gun (source Grove et al., 2006).

Localized bulges are acceptable as long as they do not compromise the possibility of extracting the carrier from the well. They are no longer admissible if the resulting bulges jeopardize this prospect. Cracking is usually not admissible, as it does not hinder the detonation products from reaching the outside of the carrier and thus the well's wall, resulting in possible inadmissible damages. Anyway, small cracks may still be tolerated if they still prevent the detonation products from reaching the outside of the carrier, or strongly limit this effect.

Of course, extensive damages in the carrier are not admissible. In particular, if severe cracking appears, the resulting cracks may merge with the exit holes producing then extended longitudinal fracture patterns, which are technically called

splits. The photograph reported in following Fig. 80 shows a damaged carrier in which a split has occurred.

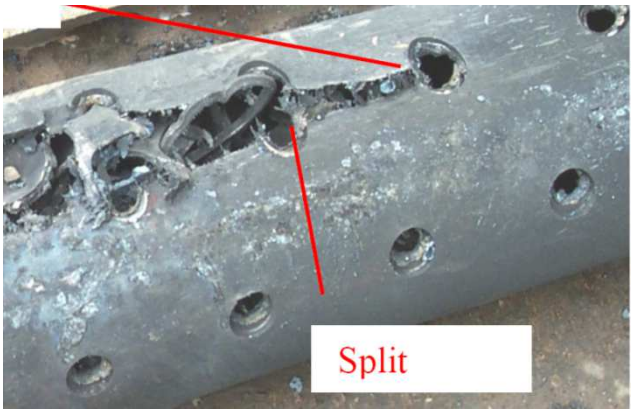

Figure 80. Manifestation of a split in the carrier of a fired perforating gun (source Grove et al., 2006).

In worst cases, splits may be much more severe than what shown in Fig. 80, leading to what may be called an “explosion” of the carrier. Such an example is shown in Fig. 81.

Figure 81. Total destruction of the carrier of a fired perforating gun (pictures provided by the industrial partner).

On the opposite, following Fig. 82 reports a photograph that shows a carrier that resisted the firing process particularly well, with an almost inexistent bulging, no cracking and the formation of very clear and localized exit holes.

Figure 82. Exit holes in a carrier that properly resisted to the shaped charge explosions (source www.justbeneaththesurfacewv.com).

Shaped charges may be dislocated inside the carrier in different ways. One of the most common consists in a helical layout, in which the shaped charges are spaced along a helix, or even a number of helixes. In such cases, helical layouts are further defined by the geometrical parameters of the helixes and the density of shaped charges along the helixes. Those parameters are chosen based on the characteristics of the well and on those of the soil to be perforated. Several solutions of such kind are made available by perforating gun producers. The diameter of the perforating gun used is typically determined by the presence of wellbore restrictions or limitations imposed by the surface equipment. Following Fig. 83 shows two examples of scallop geometrical disposals in a carrier, and therefore of the corresponding disposals of the shaped charges in their supporting system.

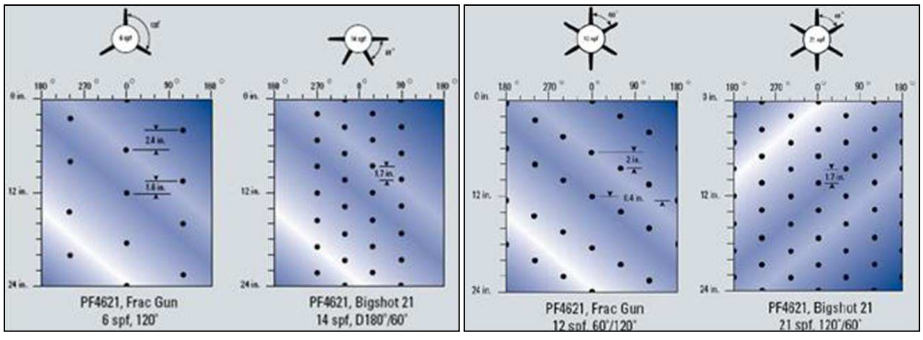

Figure 83. Examples of scallop configurations in perforating gun carriers (source www.slb.com).

4.2. Difficulties and Objectives of FEM Simulations of Perforating Gun Devices

The main target of the present chapter is that of exposing a campaign of computational FEM simulations of the firing of a specific perforating gun device proposed by the industrial partner of the present research project. These simulations aim at achieving as much coherence as possible, compatibly with the available experimental results and computational means. The FEM tool has been chosen for its good versatility and for the wide diffusion of the method, nowadays available through many commercial and research software packages.

The industrial partner manifested particular interest in the analysis of the resistance of the carrier component, in relation to the three stressing actions due to the firing of the perforating gun device. Their major concern referred to the possible manifestation of splits in the carrier, or even the total fracture (explosion) of the component. Such possibilities imply all the previously explained negative consequences. In this view, the main target of the proposed FEM simulations is that of exposing and understanding, as much as possible, the key physical phenomena that are involved in the firing of a perforating gun and in particular the effect of this process on the carrier resistance. The evaluation of the equivalent plastic strain and damage fields of the carrier are of primary importance. More in detail, the aim is that of obtaining computational results capable to improve the knowledge on what really happens to the carrier during the firing of the perforating gun, in order to better design such an important component.

It may be pointed-out that, beyond the investigation on the resistance of the carrier, further investigations on the functionality of the device may be made, potentially of high interest. An example of such investigations consists in the analysis of the liner penetration capacity. Such aspect can be related to, e.g., the radial length of soil that the liners can successfully perforate, together with the diameter and cleanness of the resulting holes. Moreover, a lot of sensitivity studies may be performed in order to better identify the role of the critical features of the components on the results obtained from the firing of the device. As instance, a sensitivity study on the effect of the geometry of the scallops may be carried-out. Similar sensitivity studies may be conducted on the explosive characteristics, on the shaped charge characteristics, on the standoff distance and so on. In this context, the target would be that of optimizing some of these parameters, in order to achieve maximum resistance of the carrier together with maximum penetration capacity of the liners. Of course, other aspects may be taken into consideration as well. Anyway, the main target of this chapter is that of assessing the carrier resistance, and therefore the main efforts are devoted to achieving the fulfillment of this objective. In particular, this choice is due to the fact that the FEM simulations under consideration do require relevant computational capacities and therefore it has

been necessary to limit their number, and therefore limit the carried-out investigations.

The industrial partner provided some data useful for carrying-out the proposed FEM simulations. Pertinent information is resumed in the following list.

- A reference carrier geometry has been provided. It considers a carrier with external diameter of 114 mm, internal diameter of 98 mm and thus a thickness of 8 mm. This is a configuration characterized by a medium scallops density, and therefore medium shaped charges density. The scallops are displaced along two helixes. The result is that two consequent shaped charges, and thus scallops, are separated by a longitudinal distance of 50.8 mm (2 inches) and along the helix by an angle of 60°. Supposing to unfold the cylindrical carrier pipe in order to form a plane, these geometrical features result in a pattern of 18 scallops per meter, and thus a pattern of 18 shaped charges per meter. The scallops are created by producing circular holes on the external surface of the carrier, whose axes correspond to the shaped charge axes. Those holes have diameters of 20 mm and deepness of 4 mm, thus decreasing the carrier thickness from 8 mm to 4 mm in the zones in which the scallops are located, i.e. a 50% diminution.

- Some experimental data regarding the steel used for the carrier have been provided. This steel is identified with the nomenclature SAE4130. The company conducted a preliminary analysis on two materials deemed as potentially suitable for the production of pipes used for the realization of carriers. These tests quite evidently displayed better characteristics for one of the materials over the other. The best material is considered throughout the work. The industrial partner provided some experimental measurements of the plastic flow of this material. Room temperature quasi-static tensile tests, considered at an equivalent plastic strain rate of 0.001 s^{-1}, and room temperature Hopkinson bar tensile and compressive tests, considered at an average equivalent plastic strain rate of 1100 s^{-1}, have both been provided. The steel density, Poisson's ratio, melting temperature and specific heat have been provided as well. Experimental measurements of the bulk sound speed of the carrier steel have been supplied. These data have been obtained through ultrasonic measurements. Unfortunately, no experimental data relative to the temperature dependence of the carrier steel plastic flow have been made available. All the provided experimental data will be actually used for the calibration of the adopted constitutive models. Moreover, the company has provided some other information through the reference compiled by Bonora et al., 2010.

- The ambient fluid is assumed to be air. This assumption is due to the belief of the industrial partner that this condition may be one of the worst possible for the carrier, according to their field experience. Therefore, the work will follow this suggestion, by analyzing only perforating gun devices that fire on air. It is also assumed that the air pressure is equal to 1 atmosphere, i.e. 101325 Pa.

- The shaped charge liners are made by copper. However, none material properties have been specified.

Unfortunately, no other data have been provided by the industrial partner, neither geometrical nor regarding material properties. Therefore, important parameters such as the properties of the shaped charges, their standoff distance or the properties of the casing, the concrete coating or the soil are missing. Moreover, no high pressure volumetric behavior, neither damage nor fracture data regarding the carrier steel have been provided. The missing information will be recovered from the literature, trying to consider materials and applications as near as possible to the one under analysis.

The company provided also a work compiled by Ambrosi and Briganti, 2010, which presented a previous work conducted on the same topic, i.e. the analysis of the resistance of a perforating gun carrier. Anyway, this publication considered a carrier steel different from that adopted here, although the geometrical properties of the carrier are the same. Some considerations about a comparison of the results obtained here and the results exposed in this former contribution are presented in the Conclusions.

In order to overcome the problems due to missing data, the following assumptions are adopted, with the aim of completing the information necessary for carrying-out the FEM simulations of the case of interest.

- The geometric characteristics of the shaped charges usually adopted for the considered carrier have been taken from Ambrosi et. al., 2010. They are reported in following Fig. 84. Some dimensions are missing and are then hypothesized.

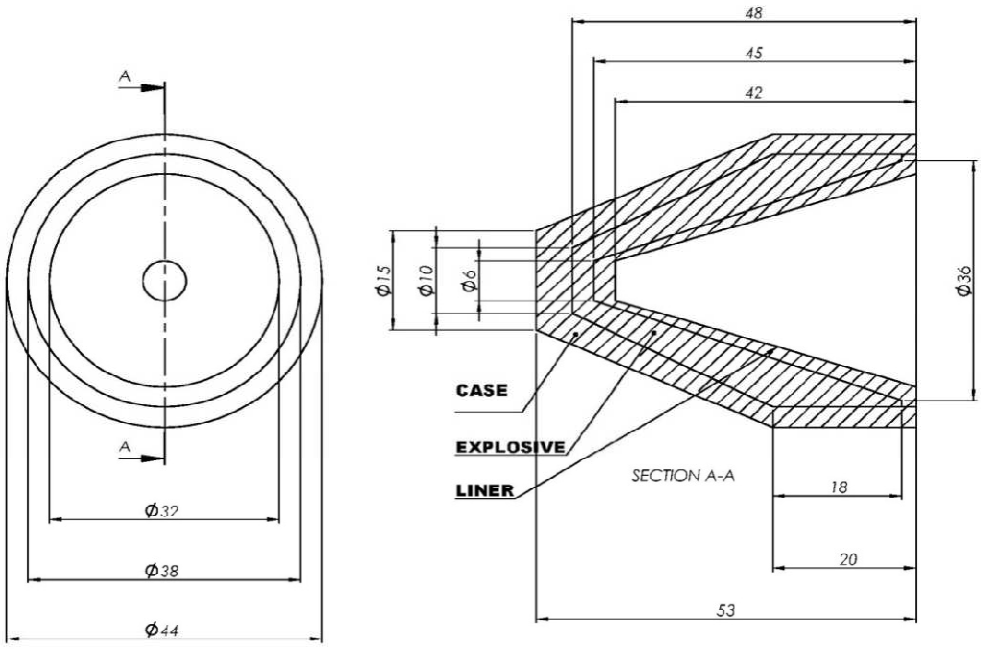

Figure 84. Technical draft of the shaped charge considered for the analysis of the considered perforating gun. Dimensions in millimeters.

- The case material is assumed to be a generic high resistance steel.
- Following company communications and other references, such as Lee, 2002, and Ambrosi and Briganti, 2010, the main explosive is assumed to be RDX.
- Following Jin et al., 2002, in which a perforating gun device has been analyzed, the standoff distance is assumed to be equal to 10 mm.
- The casing is assumed to be a pipe made of 4340 steel, a material for which data is widely available. Its internal and external diameters are assumed to be equal to 124 mm and 144 mm, respectively, hence resulting in a thickness of 10 mm. As a consequence, the distance between the inner surface of the casing and the external surface of the carrier is equal to 5 mm.
- The concrete coating internal and external diameters are assumed to be equal to 144 mm and 164 mm, respectively, therefore resulting in a thickness of 10 mm. As a consequence, the inner surface of the concrete coating is assumed to be in contact with the external surface of the casing.
- The soil is assumed to be directly in contact with the external surface of the concrete coating and extended for a length of 260 mm.

Some considerations about the strategy followed for the realization of the FEM simulations are outlined in the following.

Carriers of the kind proposed by the industrial partner may reach total lengths of meters. For the stated objective of this work, i.e. the analysis of the stressing effects on the carrier and its resistance, it is considered sufficient to carry-out two simulations, namely a single scallop simulation and a three scallop simulation. The former considers only what happens in the proximity of a single scallop, whilst the latter considers what happens in the proximity of three subsequent scallops. In a first phase, single scallop simulations will be considered, with the aim of understanding as better as possible what happens on a sole scallop during the firing process. One of the major objectives of these first simulations consists in the evaluation of the effect of two of the three stressing actions on the carrier, i.e. the piercing liner and the blast effect. Of particular interest is the possible synergic interaction of these actions, together with the investigation of the formation of the exit hole and of a possible localized bulge.

In a second phase, three scallop simulations are considered. The main objective of these simulations is that of evaluating the possible synergy due to the simultaneous explosions of three subsequent shaped charges. Beyond the effects of the piercing liners and of the blast loadings, impacts with fragments detaching from the shaped charges and their support and detonation systems may be considered as well. Possibilities like cracking and splits can be further investigated through this second kind of simulations.

The physical phenomena to model go far beyond the standard applications of FEM simulations. The firing of a perforating gun device involves large strains, extremely high strain rates, very high temperatures, together with damage and fracture of the adopted materials. The constitutive modeling of all the involved materials is a critical point. Appropriate choices need to be made for each component of the perforating gun device. The simulation of the detonations of the high potential explosive placed inside each shaped charge is one of the most challenging and important step of the work. This process determines the velocity and temperature fields of the detonation products and of the melted liners, that are of utter importance in order to coherently model the stressing factors that act on the carrier. The melting of the liners and the subsequent formation of hyperfast fluid jets is another crucial phase of the simulations. The modeling of phase changes is a non standard procedure in typical FEM simulations, therefore it requires specific attention. Furthermore, supersonic impacts between the liners and the targets may arise, resulting in an even more complex general framework. All these aspects must be introduced and handled in computational codes, together with other complicated issues, such as large strain elastoplastic modeling, implementations of strength models and equations of state and so on. Treatments on the analysis of similar phenomena in FEM contexts can be found, e.g., in Wilkins, 1963, Wilkins et al., 1974, Benson, 1991, and Zukas, 2004. Specific considerations on the FEM

simulation of ballistic penetration of targets are provided, e.g., in Wilkins, 1978, Camacho and Ortiz, 1997, Scheffler and Zukas, 2000, Zukas and Scheffler, 2000, Rodríguez-Martínez et al., 2010, and Worsham et al., 2010. Analyses on the effects of explosives on solid bodies are provided, e.g., by Rinehart, 1951, and Pearson and Rinehart, 1952. Considerations on the FEM modeling of the effects of explosions on structural elements are provided, e.g., in Lu and Wang, 2006.

First, an attempt with Lagrangian FEM is considered. However, problems due to the nature of this spatial integration method are expected to strongly limit the possibility of obtaining a fruitful accomplishment of FEM simulations of this kind. Anyway, this is a first step towards the achievement of the objectives of this work. After that, the possibility of a simulation with non-Lagrangian techniques is analyzed. Methods such as Smoothed Particle Hydrodynamics (SPH from now on) and Eulerian FEM are of interest here.

It is understood that the required simulations need a FEM code that offers powerful tools in aiding the input file preparation, that presents a choice on the spatial integration method, in particular by offering non-Lagrangian methodologies, and also capable of modeling different materials with good versatility. In particular, the code is required to make available constitutive models suitable for describing the behavior of the considered materials under large strains, in a wide range of temperatures, included very high temperatures, and subjected to high and very high strain rate and pressures.

In this context, a preliminary phase of the work has been conducted with the aim of identifying the FEM code that may better serve for the scopes of the present study. The commercial FEM code LS-DYNA has been chosen (see, e.g., Livermore Software Technology Corporation (LSTC), 2006, and 2012). Since its birth, one of the major target of this code has been that of simulating complex transient dynamical phenomena, ranging from medium strain rate situations, such as automotive crash tests, up to very high strain rate cases, like those frequently recurring in military applications. This code offers all the required capabilities, probably more than other evaluated FEM codes. Thus, its choice has arisen. In particular, beyond the classical Lagrangian spatial integration technique, it offers both SPH and Eulerian spatial integrations methodologies. A series of preliminary simulations has been conducted in order to identify which of these two methodologies would actually be capable to offer better simulation capacities for the case under examination in the present work. These tests showed a superior capacity of the Eulerian methodology over the SPH. This is due mainly to the fact that the Eulerian analyses run much faster that the SPH ones and to the fact that explosive detonations appear to be better modeled when Eulerian capabilities are adopted. Therefore, beyond Lagrangian FEM simulations, the achievement of the targets of this chapter relies on the use of Eulerian FEM methodologies.

In order to better assess the possibility of using Eulerian FEM approaches, preliminary investigations with the 2-dimensional research FEM code RAVEN (Benson, 2000) have been conducted. All the obtained results proved that Eulerian FEM simulations may be successfully carried-out. Furthermore, a considerable part of the carried-out work has dealt with the possibility of implementations of user materials and user equations of state in the code LS-DYNA. In this regard, some considerations on the implementation of strength models in LS-DYNA can be found in Moraes and Nicholson, 2000, Unosson and Buzaud, 2000, and Ehrart, 2011.

Investigations on FEM analyses of the explosion of shaped charges are provided in Kucher and Harrison, 1977, Molinari, 2002, Liu et al., 2003, and Hussain et al., 2009. Studies on numerical simulations of perforating gun devices can be found in Regalbuto and Gill, 1997, Lee, 2002, Grove et al., 2006, Zhang et al., 2008, Ambrosi and Briganti, 2010, and Jin et al., 2010. In particular, relevant comparison between 2-dimensional Eulerian FEM simulations and experimental data are provided in Lee, 2002, with particular reference to the analysis of the modeling of the shape of the liner produced from the shaped charge explosion.

The obtained FEM results are presented in the following. Lagrangian FEM simulations are exposed first and Eulerian FEM simulations are exposed second. All the LS-DYNA FEM simulations presented here have been set-up by using millimeters as length unit, seconds as time unit, tons as mass unit and then Newton as force unit, megaPascal as stress unit and milliJoules as energy unit. This system forms a consistent set of units.

4.3. Lagrangian FEM Simulations

The Lagrangian FEM technique is the basic approach for structural analysis in commercial FEM codes. LS-DYNA offers wide capabilities in this field. Only tridimensional analyses are considered. Preliminary two-dimensional analyses have been carried-out as well. However, one of the main points here is that of modeling the possible synergic interaction of the explosions of more shaped charges, which are not in the same plane and therefore compulsorily require a tridimensional analysis.

Among all the components of a perforating gun device, the Lagrangian FEM simulation will consider only the liner and the carrier. This is due to the fact that the simulation of the explosive detonation and of fluid materials is not suitable with a Lagrangian spatial discretization, due to the very large strains that characterize these phenomena. Preliminary simulations have confirmed these limitations. To overcome these problems, the following strong hypotheses are made, following the same approach adopted in Ambrosi and Briganti, 2010. The detonation process in the shaped charge is not modeled and the liner is assumed to be a projectile made

of a rigid material, i.e. a material that cannot undergo strains. The rigid material assumption becomes necessary because the adoption of a non-rigid constitutive model results in the production of very large strains during the impact of the liner against the carrier, which are not acceptable within the context of a Lagrangian FEM simulation. Strains of such entity eventually lead to a premature end of the simulations, due to topological problems in the mesh. Computation of negative volumes and complex sound speeds in some finite elements are the major involved problems. The description of these problems is not a target of the present work. Reference is made to, e.g., Hughes, 1987, Simo and Hughes, 1998, Belytschko et al., 2000, Fish and Belytschko, 2007, and De Souza Neto et al., 2008. Clearly, this approach implies the problem of determining the rigid liner velocity. Following communications provided by the industrial partner, an initial speed of 4 km/s is hypothesized, since this is considered to be approximately the mean value of the velocity field in liners arising from shaped charges similar to those considered here.

Furthermore, the carrier is considered as the only target on the liner path. The casing, the concrete coating and the soil are not modeled in the Lagrangian simulations. As a matter of fact, the hypothesis of a rigid liner makes useless the modeling of these components, considering that the evaluation of the structural response of the carrier is the main target of such simulations. This is due to the fact that the liner effect on the carrier is assumed to be independent from the impacts of the rigid liner with the targets located beyond the carrier. Indeed, the rigid liner keeps on travelling by piercing through the targets placed after the carrier but, being a rigid body, it never deforms. On the other hand, a fluid liner that hits the targets positioned beyond the carrier may undergo severe deformations due to these further impacts, that may then have also a role in partially determining the shape of the fluid liner, possibly involving the zone of impact of the rear liner with the carrier, thus resulting in conditioning the carrier resistance itself. Therefore, the assumption of a rigid liner involves this incoherence that adds on to the other previously made approximations.

The impossibility to model explosives and fluids strongly limits the usefulness of the Lagrangian approach. In general, this kind of Lagrangian FEM simulations allows to evaluate the effect of only one of the three stressing actions on the carrier, i.e. the piercing effect of the liner. The effects due to blast loading of the explosives and to possible impacts between the carrier and fragments of the exploded shaped charges or their supporting system are totally unconsidered. Furthermore, the only effect considered, i.e. the impact with the liner, may be negatively biased by the previously stated strong hypotheses, in particular due to the rigid behavior of the impacting liner, which may overestimates the impact consequences on the carrier and incorrectly model the shape of the liner.

Only a reduced portion of the carrier will be considered, limited both in the circumferential and longitudinal directions. More in detail, a portion determined by a circumferential angle of 54° and a height of 63 mm has been considered. These dimensions are considered to be sufficient for the aim of analyzing what happens to a single scallop portion of the carrier during the perforating gun firing process. These dimensions are the same as those considered in Ambrosi and Briganti, 2010. The fact of limiting the part of the carrier that needs to be modeled allows to diminish the number of adopted finite elements. This aspect favors the diminution of the computational time required to complete the analysis.

The liner is assumed to be, in the initial conditions, placed at a distance of 0.2 mm from the carrier. This value is different from the assumed standoff distance of 10 mm. However, the value of this distance is totally irrelevant for the purposes of the simulation. In fact, the liner undergoes no modifications of its velocity during the travel preceding the impact with the carrier. Hence, the distance between the two impacting bodies is kept very low in order to speed up the computational calculation, by minimizing the travel in the void of the liner. The initial temperature field of the liner and the carrier are assumed to be uniform and equal to 293 K.

According to the hypotheses made, the initial configuration of the single scallop simulation is reported in following Fig. 85.

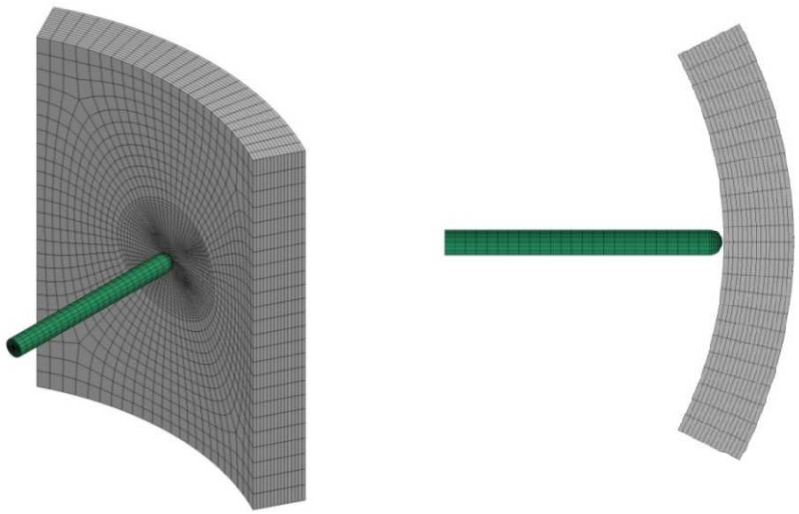

Figure 85. Initial configuration for the single scallop Lagrangian FEM simulation. The cylindrical rigid liner is represented in green while the carrier in grey.

Following Fig. 86 reports a detailed view of the scallop zone meshing.

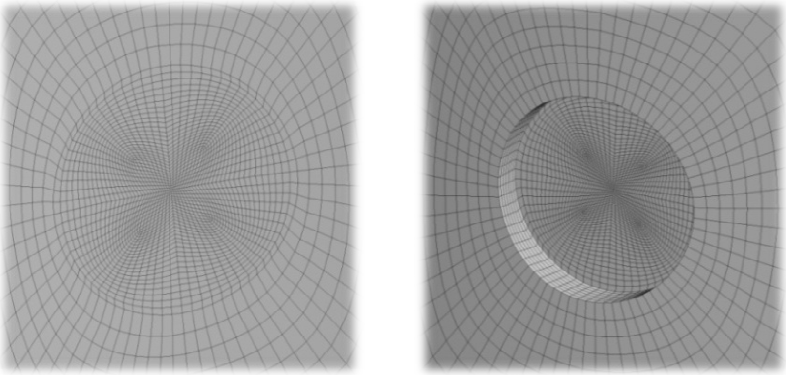

Figure 86. Detailed view of the inner (left figure) and outer (right figure) mesh of the scallop zone for the single scallop Lagrangian FEM simulation.

Both the carrier and the rigid liner are modeled with hexahedral finite elements. The carrier is composed by 28188 finite elements, with 15 elements through the thickness. The liner is composed of 4000 finite elements. The mesh is made finer in correspondence to the impact zone, i.e. the scallop zone (see Fig. 86). Boundary conditions are defined by imposing null displacements on the four edges of the carrier portion. This last assumption has been chosen following Ambrosi and Briganti, 2010, in which FEM tests on the same geometry have been conducted, proving that, in such a case, the nature of the boundary conditions on the four edges is almost irrelevant concerning the final computed results.

The liner has been dimensioned with apposite criteria. First of all, the tip shape is assumed to be spherical. Other shapes such as conical, ogival and flat have been considered as well. The spherical geometry is considered to be the best one in order to reproduce the shape of the jet created by a shaped charge, thus its choice. Following communications from the industrial partner and Ambrosi and Briganti, 2010, the melted liner of the considered shaped charge (Fig. 84) can be assumed to have a diameter of 3 mm and a mass of about 2 g. By assuming a density for the copper, it is possible to determine the dimensions of the liner. To this purpose, the reference density value of copper is used, i.e. 8940 kg/m^3. These assumptions result in a liner volume of 216.65 mm^3 and therefore a total length of 32.1 mm.

The analysis is assumed to be structural, i.e. an uncoupled structural and thermal analysis. This choice basically addresses the need of diminishing the required computational time. Heat transfer is not introduced in the analysis, which is then considered adiabatic. However, this assumption appears to be coherent with the fact that the firing of a perforating gun happens in a very short time, which is way smaller than the characteristic times of heat transfer. Its validity has been

successfully assessed in Ambrosi and Briganti, 2010, in the context of FEM simulations very similar to the ones considered here. Adiabatic behavior is then enforced. However, a material point can undergo temperature increments due to the part of plastic work that transforms to thermal energy and therefore in a temperature increment. More in detail, temperature fields are calculated by computing the increment of temperature in each timestep with the following assumption

$$\Delta T = \frac{\chi \cdot \sum_{i=1}^{3} \sum_{j=1}^{3} \sigma_{ij} \cdot \dot{\varepsilon}_{ij}^{p}}{\rho \cdot C_P}. \tag{86}$$

In this equation, the double contraction of the adopted stress measure with the adopted strain measure indicates the plastic work produced in the material. The parameter χ represents the amount of plastic work converted into heat, usually assumed to be equal to 0.9. The material density is indicated by the symbol ρ, while C_p represents the specific heat at constant pressure. This approach actually allows for accounting for adiabatic thermal behavior of the material.

Due to the hyperfast nature of the phenomenon under consideration, an explicit time integration method is adopted. The output is saved at intervals of 10^{-8} s. Preliminary tests assured that this frequency is fine enough for achieving results capable to provide a good time resolution of the phenomenon. The contact is handled through the penalty stiffness formulation implemented in LS-DYNA. In this regard, information can be found in Livermore Software Technology Corporation (LSTC), 2006, and 2012. Regarding the modeling of friction effects between the liner and the carrier, a dynamic friction coefficient of 0.15 and a static friction coefficient of 0.53 are adopted, following Ambrosi and Briganti, 2010. Appropriate controls on hourglass finite element modes are activated. Particular attention has been paid to the timestep scale factor. A long series of preliminary tests has been conducted in order to identify the value necessary to get convergence of the results when such hyperfast phenomena are involved. This value has then been adopted throughout the analysis.

The three scallop simulations are set-up by adopting all the above stated assumptions for the single scallop simulation. The only different aspect is the geometrical setting, which now considers three subsequent scallops. A height of 150 mm has been considered. This dimension is a little reduced comparing to the ones considered in Ambrosi and Briganti, 2010. This reduction is considered to be as non influent on the final results and allows to speed-up the computational analyses. In fact, the dimensions of the studied zone are considered to be sufficient

for the aim of analyzing what happens to a three scallop portion of the carrier during the perforating gun firing process. Following Fig. 87 reports the initial configuration of the three scallop simulation.

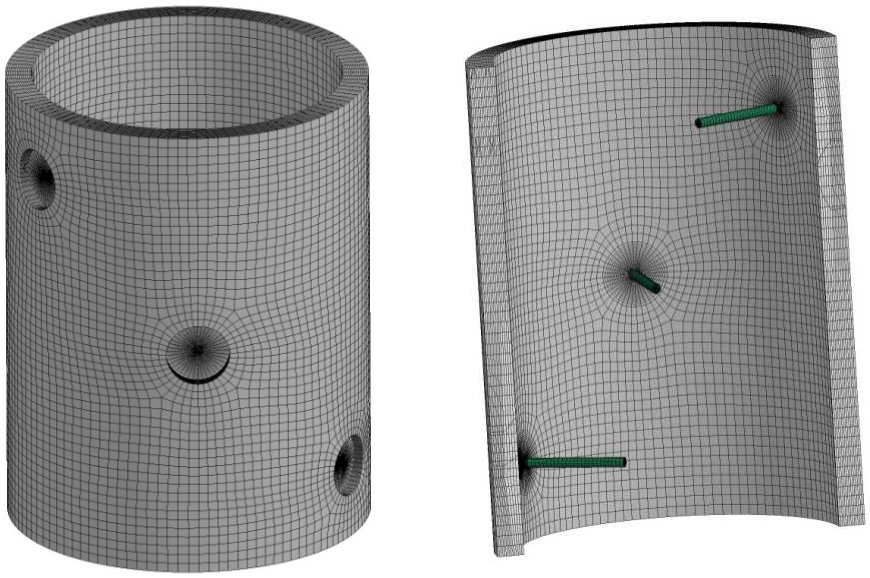

Figure 87. Initial configuration for the three scallop Lagrangian FEM simulation. The cylindrical rigid liners are represented in green while the carrier in grey.

The mesh is topologically very similar to the single scallop mesh. It is made a little coarser in order to limit the computational time, that can reach vary long values due to the very low timestep adopted during the calculation. The carrier is composed of 99585 hexahedral finite elements, again with 15 elements on the thickness. Each of the three liners is composed of 4000 hexahedral finite elements.

Following Fig. 88 reports a detail of the scallop zone meshing, a bit less refined than that in Fig. 86 for single scallop simulations.

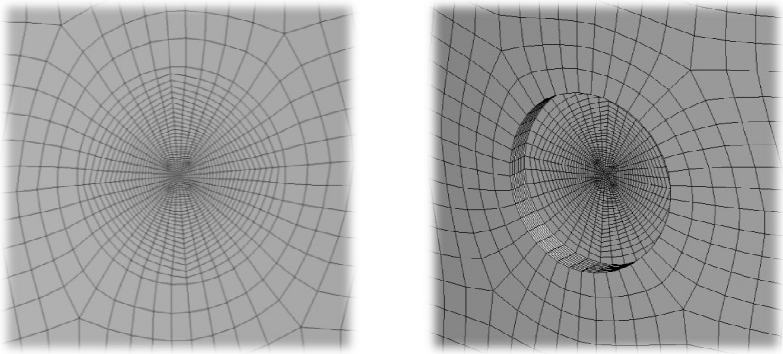

Figure 88. Detailed view of the inner (left figure) and outer (right figure) mesh of the scallop zone for the three scallop Lagrangian FEM simulation.

4.3.1. Constitutive Modeling

According to what stated above, the only two components of the perforating gun that are modeled in the Lagrangian simulations are the liner and the carrier. Proper constitutive modeling needs to be chosen for both components.

Being a rigid body, the model for the liner is straightforward. It requires the specification of the density, set equal to that of solid copper, i.e. 8940 kg/m^3. Moreover, isotropic elastic parameters are required, since they are used by the penalty stiffness algorithm. The adopted values are 120000 MPa for the Young modulus, 48000 MPa for the shear modulus and 0.34 for the Poisson's ratio. These are typical values for copper, easily recoverable from the literature.

For what it concerns the strength model of the carrier, it appears clear that the need here is that of having a model capable to account for the plastic flow dependence on both the strain rate and the temperature. Moreover, the strain rate and the temperature fields are expected to vary strongly in the carrier, thus the chosen model needs to keep its coherence over a pretty wide range of strain rates and temperatures. With these considerations in mind, the original Johnson-Cook strength model, Eq. (28), is chosen. This choice is mainly due to the fact that the available experimental data provided by the industrial partner are very limited and the choice of more complicated models, such as the Steinberg-Cochran-Guinan model, would have led to the total impossibility of calibration of any parameter of the model. The adoption of the Johnson-Cook model has allowed at least for calibrating some parameter by using the available company steel experimental data. The Johnson-Cook model is calibrated with the LYS strategy, because the prediction of the lower yield stress is considered capable of playing a more important role comparing to that played by the prediction of the subsequent plastic flow. This aspect is due to the fact that the carrier tipically develops very high temperatures during and after the impact with the liner, likely higher than the melting temperature. Therefore, the deviatoric resistance may be quickly set equal to zero or at least strongly lowered by the temperature effect. In this context, it may be better to get a good result for the lower yield stresses rather than a description of the whole plastic flow, since the lower yield stress values determine the separation of the elastic and plastic phases, i.e. the beginning of the phase in which the Johnson-Cook model starts to operate, that corresponds to the phase from which the deviatoric resistance may actually be set equal to zero.

Following the LYS calibration strategy (Chapter 2, Section 2.2.1.1.1), the parameters A, B, n and C have been determined, together with the reference equivalent plastic strain rate and temperature. However, it was impossible to calibrate the parameter m, due to complete unavailability of temperature data. The parameter m has then been recovered from available literature data. In particular,

Johnson and Cook, 1983, provided values of the parameter m for several steels. On this basis, the value 1 has been chosen, which corresponds to enforcing a linear dependence of the yield stress on the homologous temperature. The assumed Johnson-Cook hardening parameters are reported in following Table 31.

A	1170 MPa	m	1
B	471 MPa	$\dot{\bar{\varepsilon}}_0$	0.001 s^{-1}
n	0.4	T_0	293 K
C	0.041	T_m	1800 K

Table 31
Johnson-Cook strength model parameters for the steel carrier.

The heavy lack of experimental data makes it practically useless to implement and use the Split Johnson-Cook model proposed in Chapter 3, since its calibration would rely on only two hardening functions, therefore strongly limiting the possible enhancements related to this model. In such a case, the absence of experimental measurements implies the fact of producing results very similar to the ones provided by the original Johnson-Cook model.

For what it concerns the volumetric behavior of the carrier, a Mie-Grüneisen equation of state, Eq. (55), is adopted. In consideration of what stated in Chapter 2, such equation of state is capable to predict with good coherence the volumetric behavior of metals under the high pressure involved in the considered application. Regarding the EOS calibration, the industrial partner provided the bulk sound speed. No other experimental data have been made available for the purpose of determining the other parameters of the equation of state, i.e. S_1, S_2, S_3 and γ_0. Values of these parameters for a high resistance steel have been kindly provided by prof. David J. Benson at the University of California at San Diego, and these values have been adopted for the modeling of the steel of the carrier. Such values are reported in following Table 32.

C_0 [m/s]	S_1	S_2	S_3	γ_0
4640	1.33	0	0	1.52

Table 32
Mie-Grüneisen parameters for the steel carrier.

Values very similar to these are also indicated in Steinberg, 1996, for 4340 steel. It is worthwhile to highlight the fact that in the case in which the materials reach or get over the melting temperature, the Johnson-Cook model prescribes a null yield stress and thus provides no deviatoric resistance. Its behavior is then volumetric

only and it is ruled by the considered Mie-Grüneisen equation of state. Approximately, this EOS may be assumed to be acceptable in order to model high pressure metal fluid flow with volumetric behavior only. Therefore, the adopted constitutive modeling accounts for the description of a possible phase change from a solid to a high pressure volumetric fluid only, even if in a simplified way. It is also worthwhile to note that the material can exceed the melting temperature, resulting in a heated material with no deviatoric behavior.

Regarding the modeling of damage and failure, the Johnson-Cook damage model, Eq. (69), is adopted. The damage variable regulates the removal of failed finite elements. The total lack of experimental data on the steel carrier fracture strain implies the total impossibility to calibrate the five parameters of the Johnson-Cook damage model. The industrial partner proposed the adoption of the same parameters used in Ambrosi and Briganti, 2010. The values of these parameters derived from literature investigations carried-out by the company and by the authors. These parameters are then adopted, with the only difference consisting in the fact of assuming a different value for the parameter D_5. This parameter was assumed to be equal to zero in Ambrosi and Briganti, 2010. However, this assumption implies the temperature to have no effect on the fracture strain. This condition does not appear to be coherent and therefore the parameter D_5 has been set equal to 0.61, by considering the D_5 value for the high resistance 4340 steel reported in Johnson and Cook, 1985. The 5 Johnson-Cook adopted damage parameters are reported in following Table 33.

D_1	D_2	D_3	D_4	D_5
0.0705	1.732	-0.540	0.015	0.610

Table 33
Johnson-Cook damage and failure parameters for the steel carrier.

The values provided by the company have been used for some other required parameters, i.e. the steel density, assumed equal to 7850 kg/m^3, the Poisson's ratio, assumed equal to 0.3, and the specific heat, assumed equal to 452 J/kg·K. Temperature increments are computed through Eq. (86), by assuming adiabatic conditions. Thermal expansion has been considered as well, through the introduction of an isotropic volumetric thermal expansion coefficient, equal to 0.000012 K^{-1}, a value relative to a generic steel and easily recoverable in the literature. This value has been considered as independent from the temperature, since pertinent experimental data were missing.

A very simple model for considering spall fracture phenomena has been activated as well. This model imposes a cut-off value on the tensile pressure, i.e. expansive pressure (which is denoted by negative values in LS-DYNA conventions,

because the code considers compressive pressure as positive), that the material cannot exceed. If tensile pressures higher than this value are computed, then the pressure is reset to the imposed cut-off value. Basically, this model delimits the tensile pressure in order to simulate the maximum material capacity to tolerate this kind of pressures, which indeed is the cause of spall fracture phenomena. It is worthwhile to note that this model does not imply finite element removals. The industrial partner did not provide data relative to the spall behavior of the adopted steel. A cut-off pressure value for a generic steel has been recovered from Davison et al., 1996, i.e. 13000 MPa, intended as maximum tensile pressure sustainable by the material. This value has been adopted for the spall modeling of the carrier, even though there is uncertainty about whether this value may coherently apply to the considered steel or not. Future experimental investigations may clarify this aspect.

Before proceeding with the exposition of the FEM simulations of the perforating gun firing phenomenon, several preliminary FEM analyses have been carried-out, with the aim to test the sensitivity of some of the parameters of the adopted models. All the carried-out investigations produced consistent results.

4.3.2. Simulation Results

Lagrangian FEM simulation results are presented, first for single scallop simulations and then for three scallop simulations. All the carried-out simulations satisfy energy balance requirements, i.e. the ratio between the total energy and the initial energy is practically equal to 1, considering all the energy forms involved in the analysis. The simulations have been extended in time until no noticeable variations in the stress and strain fields of the carrier appeared. This led to a total simulation time of 10^{-5} s, i.e. 10 μs. For single scallop simulations, following Figs. 89 to 94 report the configurations at 0.12 μs, 0.5 μs, 1 μs, 1.5 μs, 2 μs, 4 μs, 6.5 μs and 10 μs (final configuration), seen both from the inner and outer sides of the carrier.

The temperature fields are actually temperature increment fields, from the Johnson-Cook reference temperature imposed, i.e. 293 K, hence they are called temperature increment fields. Therefore, in order to retrieve the absolute temperature, the value 293 K must be added to the presented values.

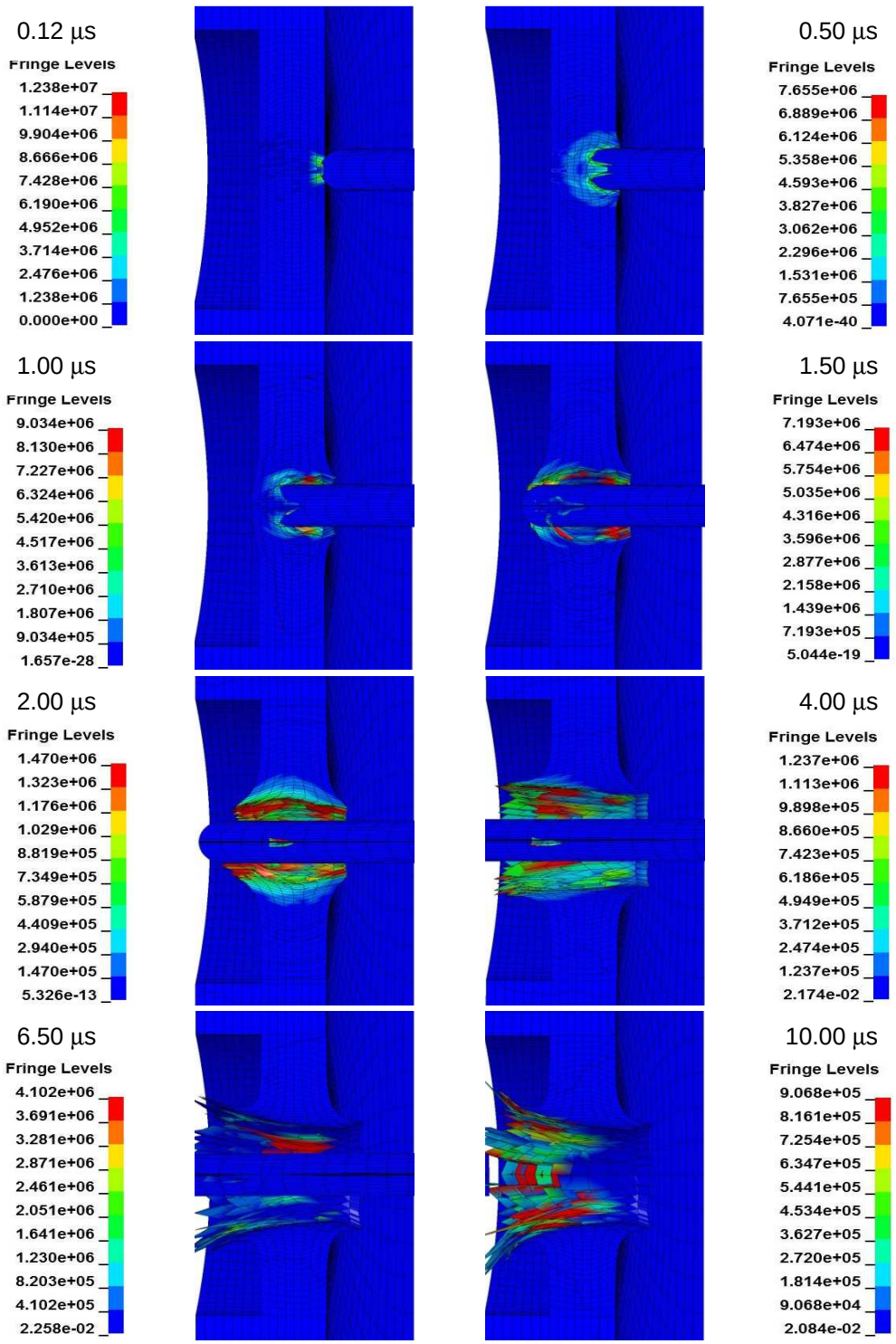

Figure 89. Equivalent plastic strain rate field [s^{-1}] in the scallop zone of the carrier.

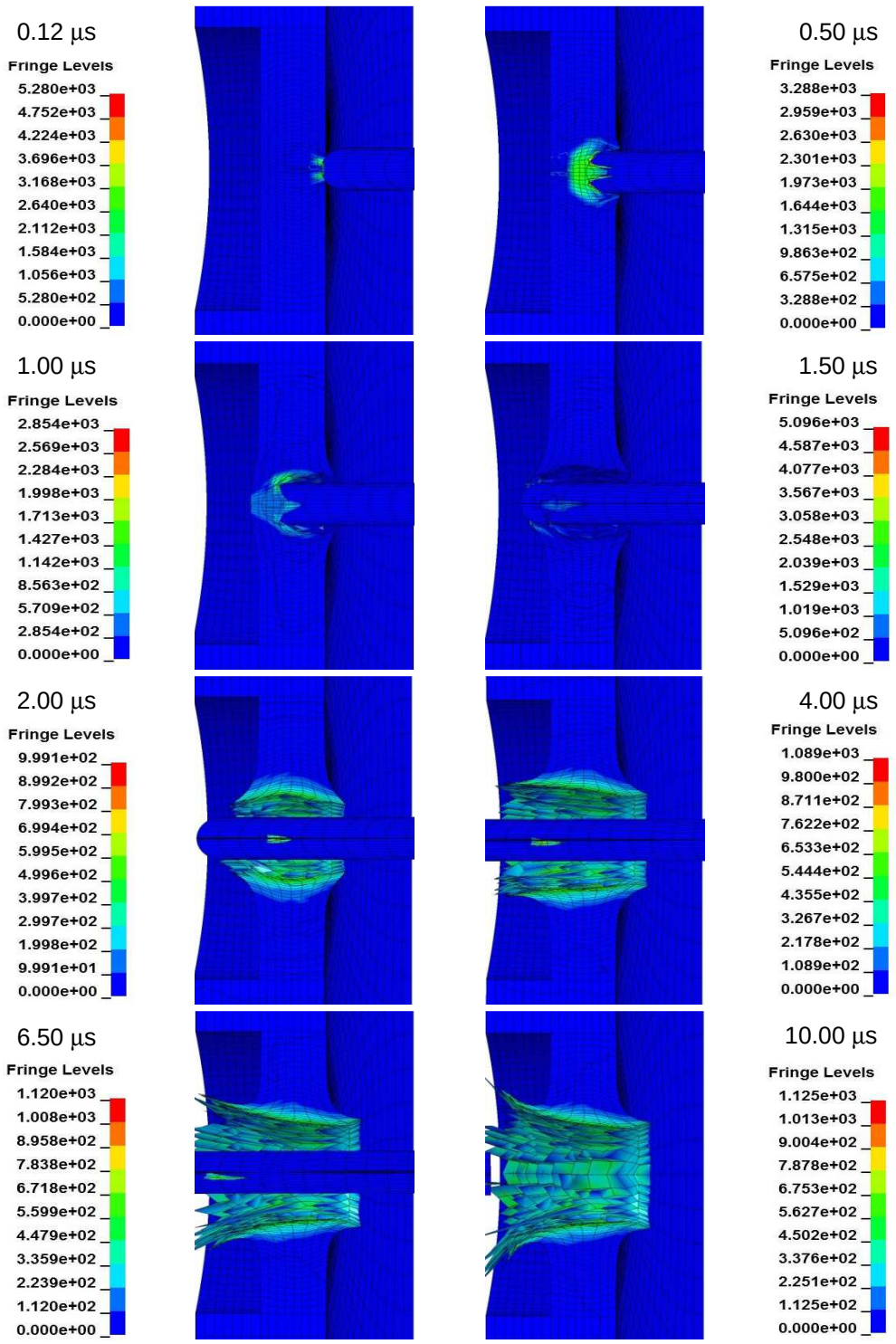

Figure 90. Temperature increment field [K] in the scallop zone of the carrier.

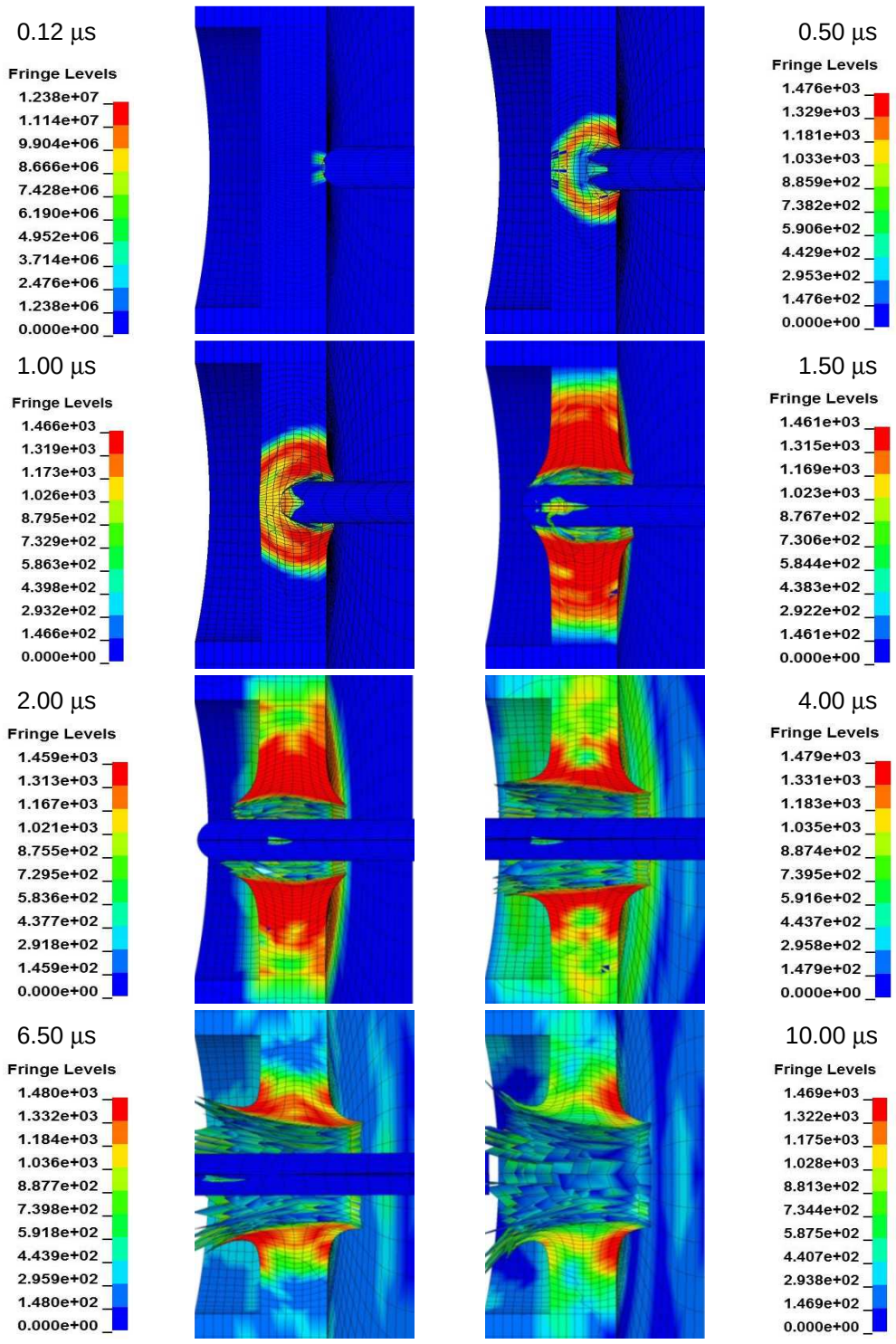

Figure 91. von Mises stress field [MPa] in the scallop zone of the carrier.

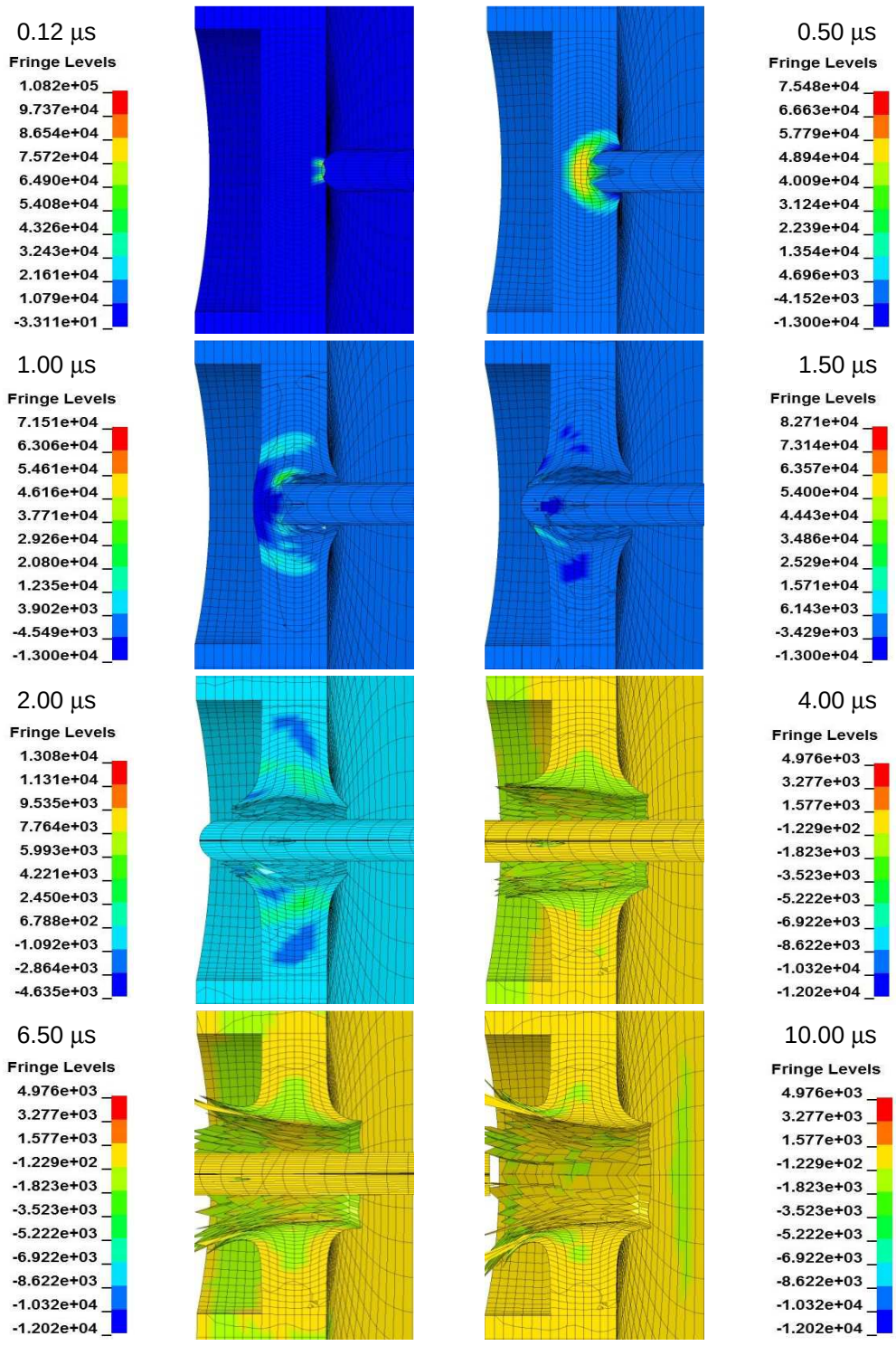

Figure 92. Pressure field [MPa] in the scallop zone of the carrier.

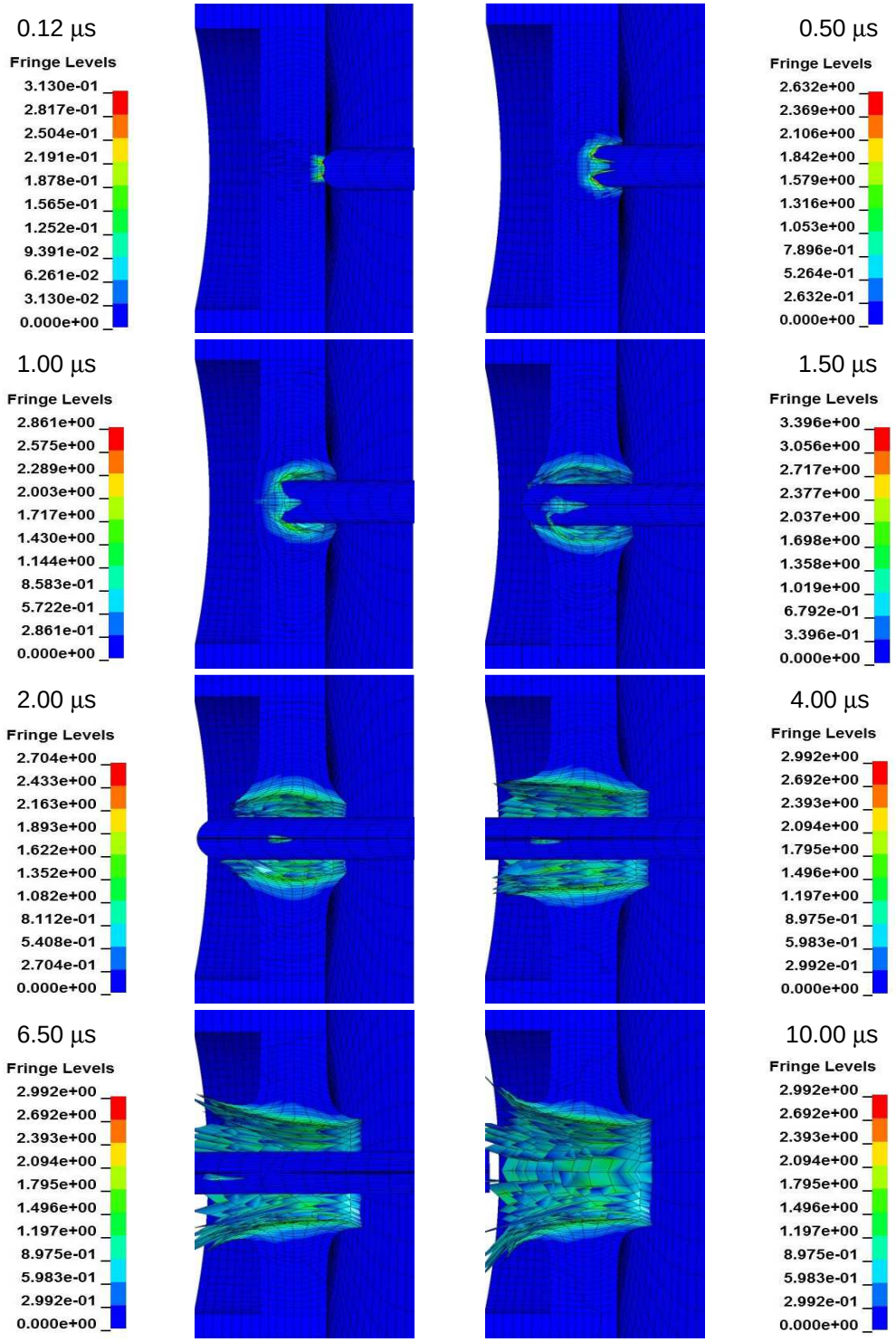

Figure 93. Equivalent plastic strain field in the scallop zone of the carrier.

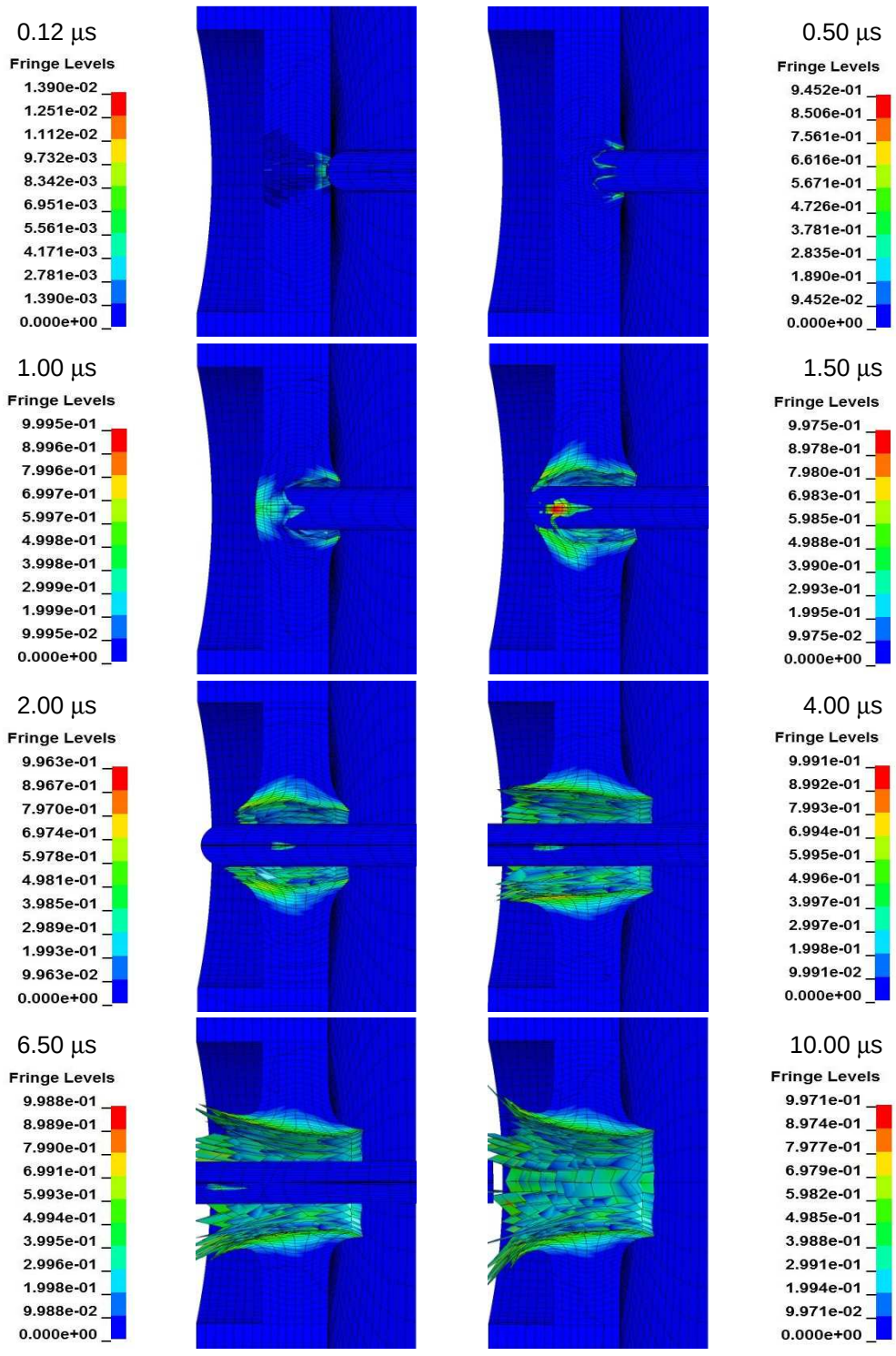

Figure 94. Johnson-Cook damage field in the scallop zone of the carrier.

In order to better assess the simulation results, the maximum and minimum values reached throughout the FEM analysis by the six considered variables are reported in following Table 34.

	MIN	MAX
Equivalent plastic strain rate [s^{-1}]	0	$1.920 \cdot 10^{7}$
Temperature increment [K]	0	12940
von Mises stress [MPa]	0	1487
Pressure [MPa]	-13000	263800
Equivalent plastic strain	0	4.573
Johnson-Cook damage	0	0.999

Table 34
Maximum and minimum values for the six considered variables. It is recalled that in LS-DYNA positive pressures are intended as compressive and negative pressures as tensile.

Some considerations regarding the single scallop simulation results are made in the following, with particular reference to the carrier and to the only stressing factor that is considered in this simulation, i.e. the piercing effect of the liner.

First of all, it is interesting to note the huge maximum values reached by the equivalent plastic strain rate. As soon as the rigid liner impacts against the carrier, values over $1 \cdot 10^{7}$ s^{-1} are involved. Furthermore, extremely high equivalent plastic strain rate values are maintained throughout the piercing phase. Approximately, it may be said that this perforating phase happens at an equivalent plastic strain rate average value of about $1 \cdot 10^{7}$ s^{-1}. This very high values are confined within a thin zone near the rigid liner piercing trajectory. Outside this zone, the equivalent plastic strain rate values appear to be some orders of magnitude lower, ranging from $1 \cdot 10^{4}$ s^{-1} to $5 \cdot 10^{5}$ s^{-1}, approximately.

For what it concerns the temperature, considerably high values are reached, with the maximum of 13233 K, obtained by summing the reference temperature of 293 K to the maximum temperature increment, i.e. 12940 K. This value far exceeds the melting temperature of the material. In these conditions, the steel carrier is basically an overheated fluid, since its deviatoric resistance is set equal to zero, as previously explained. The material behavior is then solely volumetric and it is ruled by the Mie-Grüneisen equation of state. As for the equivalent plastic strain rate, it is also interesting to see that this high temperature zone is confined in a very narrow zone near the rigid liner trajectory. Outside this zone the temperature appears to never exceed 1000 K and therefore the deviatoric behavior is always present, although the material strength is strongly diminished by the high temperatures present.

For what it concerns the von Mises stress, it is clear that the values here are heavily influenced by the equivalent plastic strain rate and the temperature, as ruled by the Johnson-Cook hardening function. On one side, the huge equivalent plastic strain rate values tend to increase the yield stress, but on the other side the elevated temperature values tend to diminish it. The value of the resulting yield stress is a consequence of these two conflicting aspects. The von Mises stress field appears to present high values in a wider zone comparing to the very localized zone in which the highest equivalent plastic strain rates and temperatures are reached. Clearly, the zones in which the temperature has exceeded the melting value present a zero von Mises stress.

Regarding the pressure, very high compressive values are involved, up to 263 GPa and over. It is necessary to say that these values are much higher comparing to generic experimental observations referring to shaped charges similar to that in consideration. In fact, maximum compressive pressure on the carrier are expected to be around 20 GPa, as communicated by the industrial partner and further stated in Ambrosi and Briganti, 2010. Moreover, Novokshanov and Ockendon, 2006, provided further confirmation of this value. It is also worthwhile to note that, due to the adoption of the Johnson-Cook damage and fracture model, these pressure values act directly in the computation of the damage, through the term in which the stress triaxiality is involved, and thus their correct computation appears to be quite important. The Mie-Grüneisen equation of state should provide a coherent modeling of the volumetric material behavior when such high compressive pressures are involved. In fact, it is considered to provide a good modeling up to some hundreds of GPa, as stated in Chapter 2. The highest compressive pressure values are reached in the first microseconds after the rigid liner impact with the carrier. After that, the compressive pressure appears to relax down to lower values. Similarly to what happens for the equivalent plastic strain rate and the temperature, the highest compressive pressure values are confined in a tiny zone near the rigid liner trajectory. Outside this zone, the compressive pressure values appear to lie between 5 GPa and 10 GPa, which however are still quite high values.

It is also very interesting to analyze the tensile pressure in the carrier. In particular, the steel spalls some microseconds before than the scallop zone is definitely pierced by the liner. This effect is highlighted in following Fig. 95, in which the pressure field is plotted by imposing a maximum value of 0 MPa and a minimum value of -13000MPa, i.e. the spall limit.

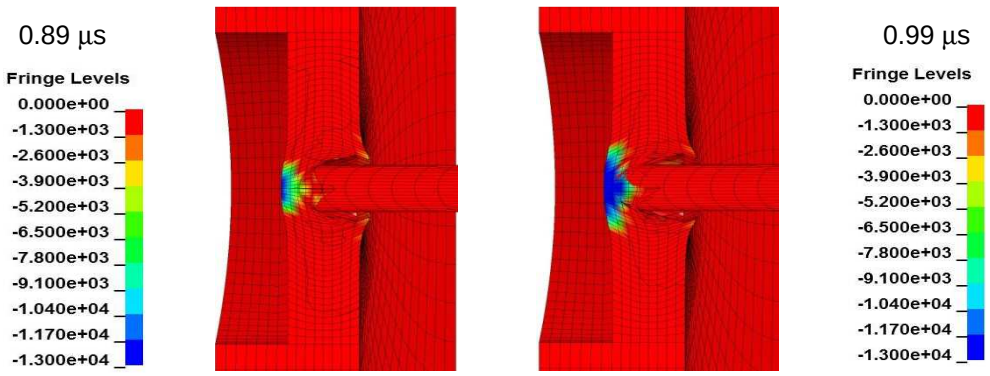

Figure 95. Pressure field [MPa] in the scallop zone of the carrier. Tensile pressure limitation due to spall modeling is highlighted.

Regarding the equivalent plastic strain and the Johnson-Cook damage variable, it can be noted that their results are very similar. This is expected due to the fact that the Johnson-Cook damage parameter is evaluated on the basis of the equivalent plastic strain, as previously described in Chapter 2. The results of these two variables indicate that the piercing effect of the rigid liner causes very localized effects. Indeed, the equivalent plastic strain and the damage parameter are pretty limited outside of the piercing zone, i.e. moving away from the rigid liner trajectory. As a matter of fact, this aspect is further confirmed by the final configuration of the carrier, in which deformations are strongly limited to the pierced zone, i.e. the central zone of the scallop. It is also necessary to note that high positive stress triaxialities are involved in some limited zones of the carrier, in particular in the zone in which the spall limit pressure is reached. Stress triaxialities up to about 10 are involved. It is recalled that the Johnson-Cook damage and failure model is not conceived to model damage and failure for stress triaxialities that exceed the value 1.5. However, the zones with stress triaxiality over 1.5. are quite limited in extension.

More in general, it can be said that the piercing effect of the liner influences a very thin zone of the carrier, resulting in a very localized effect that takes place in a narrow band in the scallop zone. Indeed, the equivalent plastic strain and the Johnson-Cook damage parameter are almost null outside this zone. It is worthwhile to point-out that these conclusions apply only for the assessment of the first of the three mentioned stressing factors of the carrier, namely the liner perforating effect. Furthermore, these results may be more or less flawed by the heavy simplifying assumptions that have been made, in particular by the assumption of imposing a rigid liner.

Regarding the three scallop simulations, the most important point appears that of investigating the possible manifestation of synergic interactions between the stressing effects provided by the three rigid liners. As expected, no such effects

have been revealed. As a matter of fact, the obtained FEM results are very similar, if not equal, to the outcomes of the single scallop simulations, resulting in a very localized effect of each of the three piercing rigid liners. Therefore, these simulations do not contemplate potential synergic interactions between the simultaneous impact of several liners, totally excluding possibilities like cracking. Once again, it is worthwhile to recall the fact that these simulations consider only one of the three stressing factors of the carrier and furthermore there may be some incoherencies due to heavy hypotheses that characterize these simulations. Following Figs. 96 to 101 show some exemplificative results from the three scallop simulations. Configurations at 3 μs and 10 μs (final configuration) are presented.

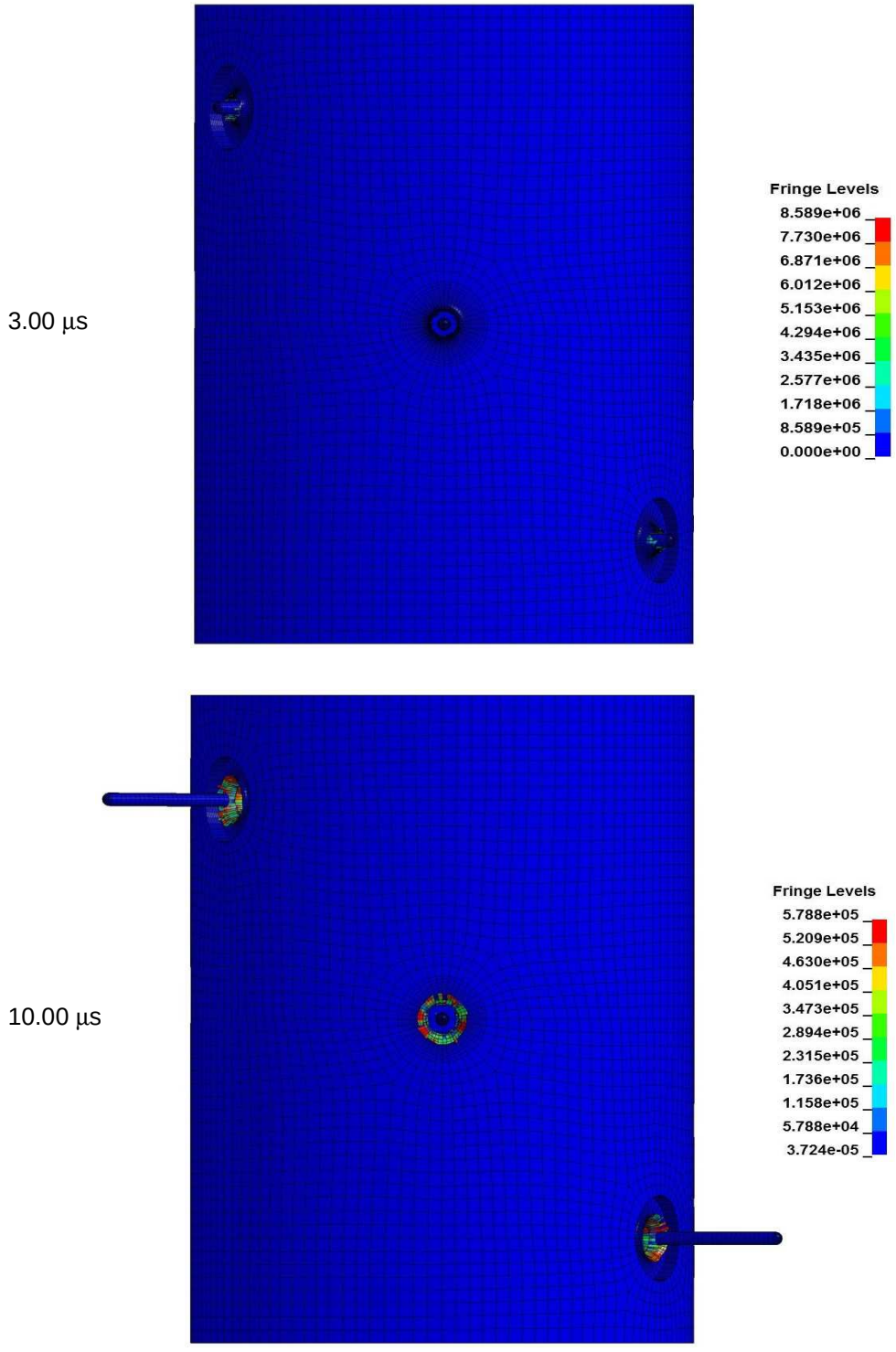

Figure 96. Equivalent plastic strain rate field [s^{-1}] in the carrier.

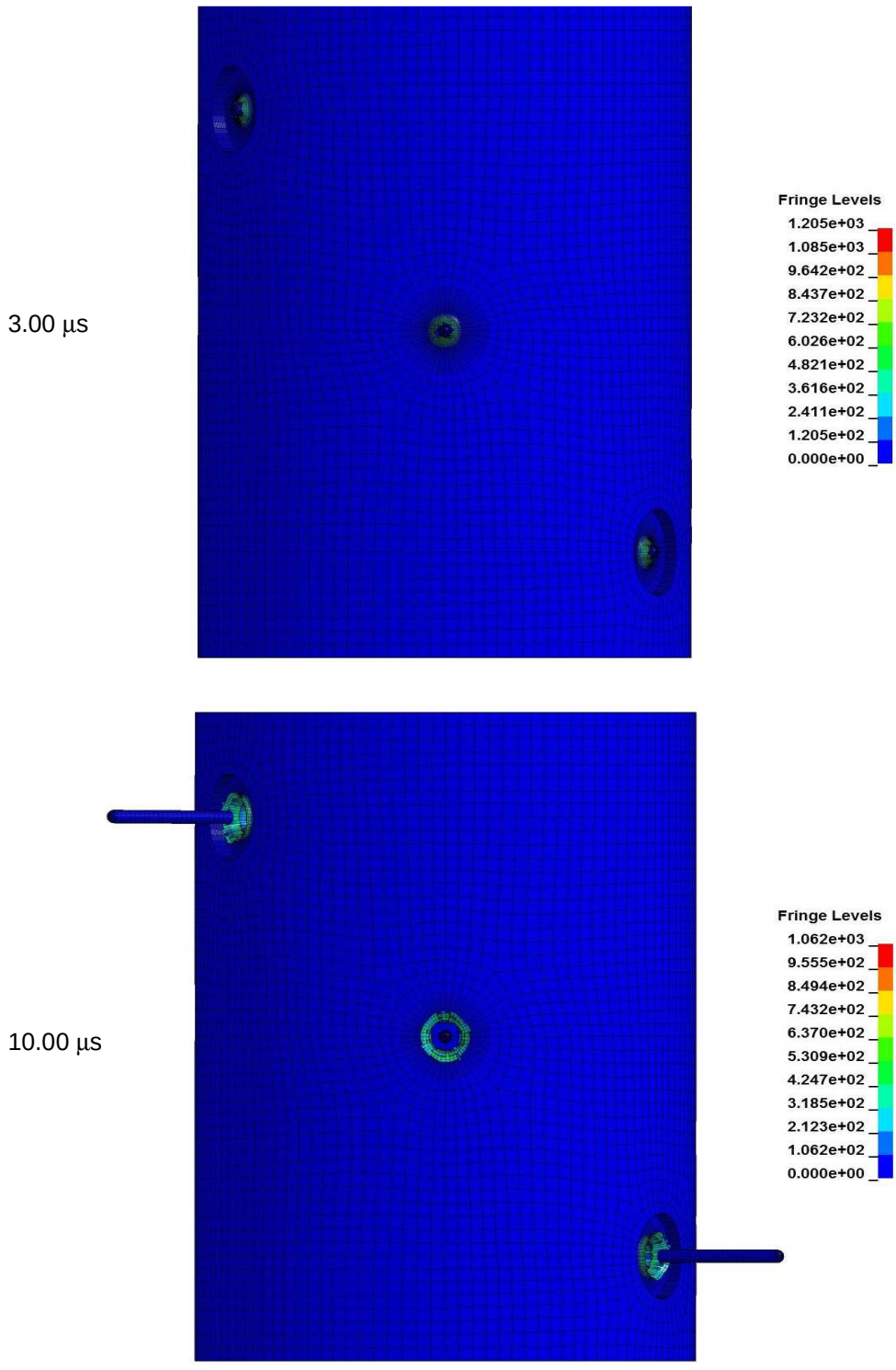

Figure 97. Temperature increment field [K] in the carrier.

3.00 µs

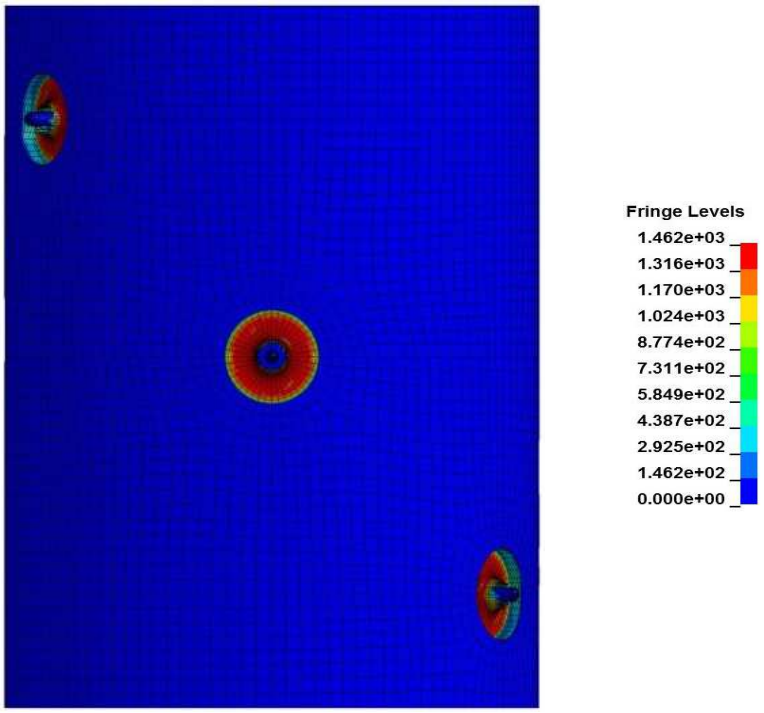

10.00 µs

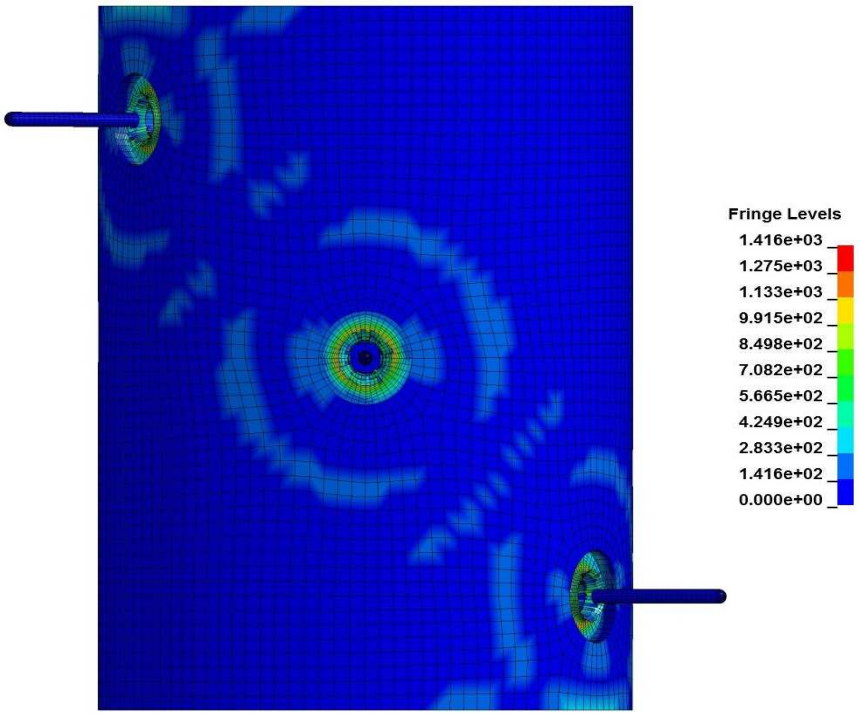

Figure 98. von Mises stress field [MPa] in the carrier.

3.00 µs

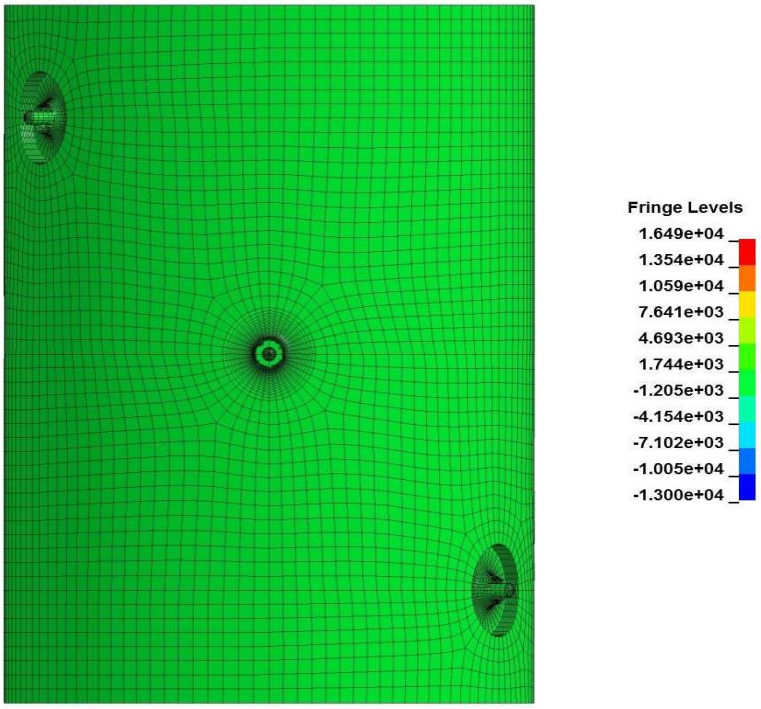

10.00 µs

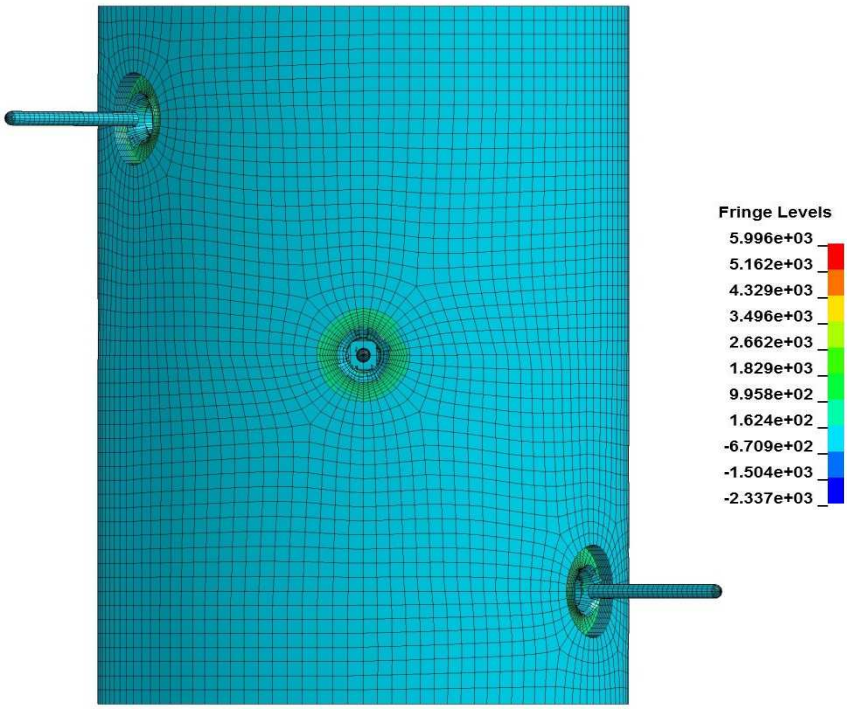

Figure 99. Pressure field [MPa] in the carrier.

3.00 μs

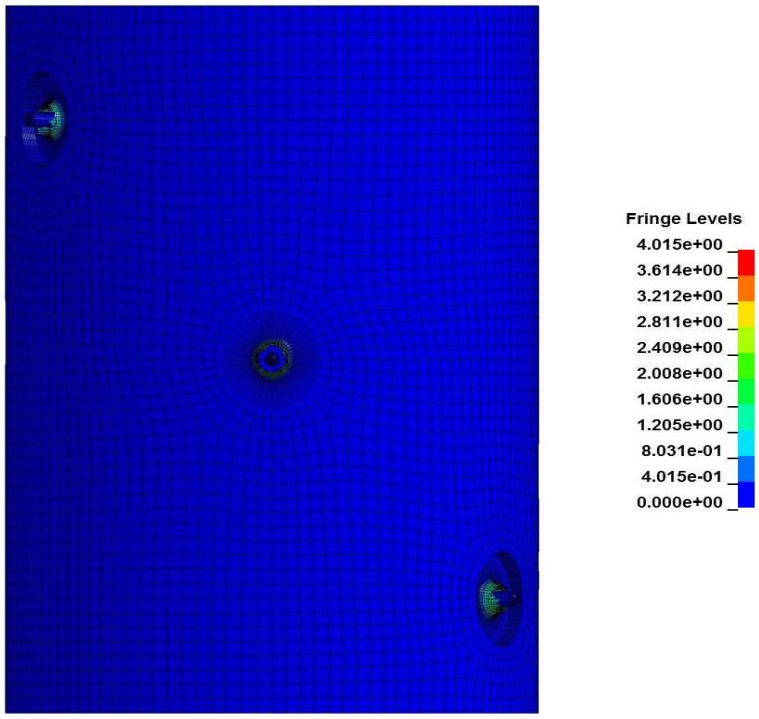

10.00 μs

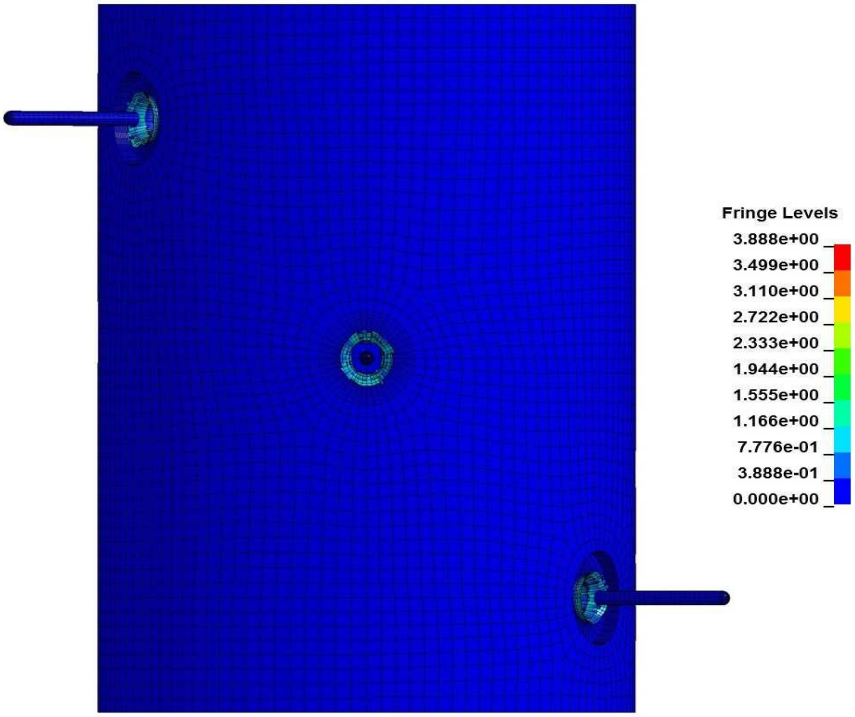

Figure 100. Equivalent plastic strain field in the carrier.

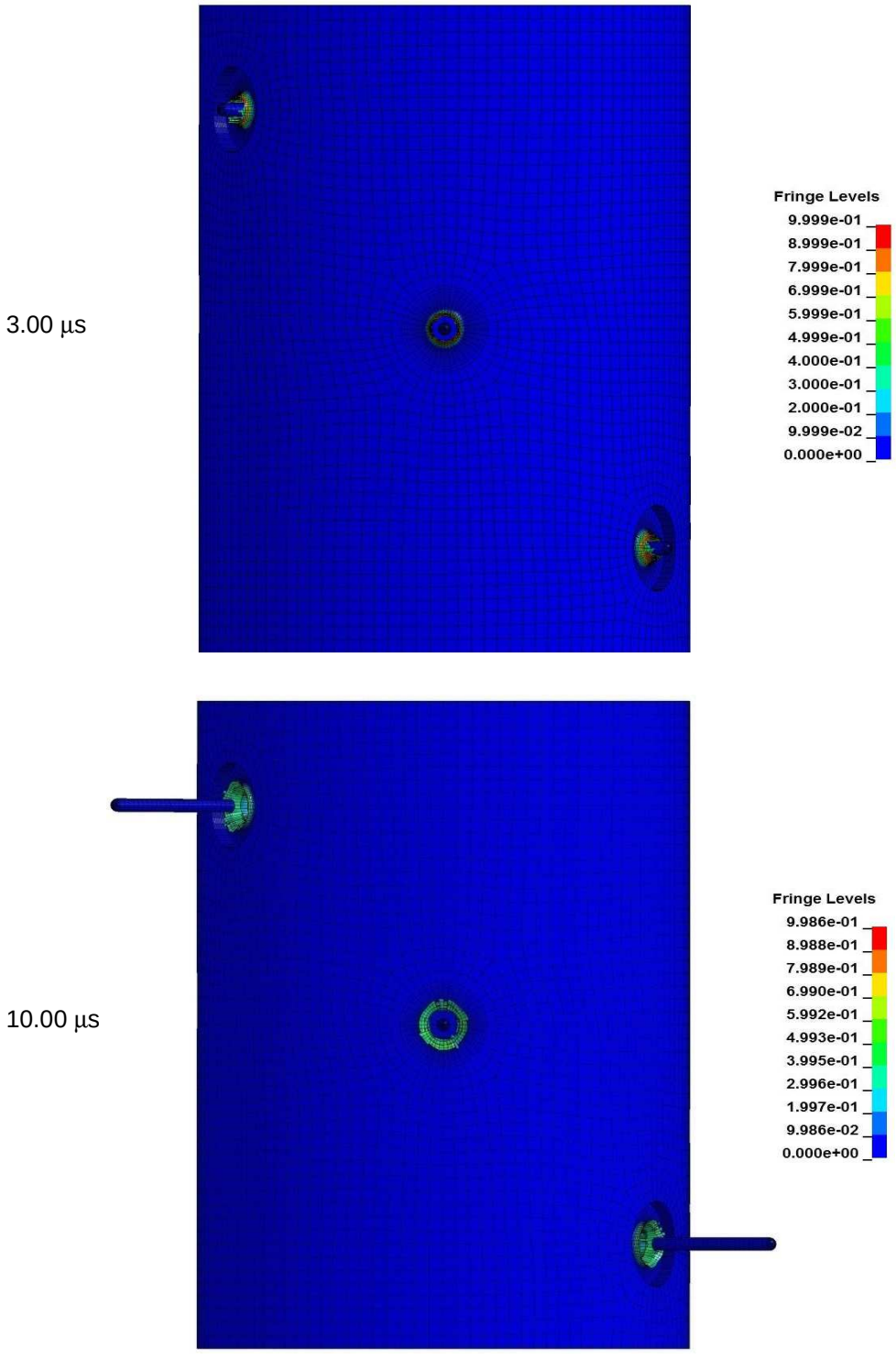

Figure 101. Johnson-Cook damage field in the carrier.

4.4. Eulerian FEM Simulations

The adopted FEM code LS-DYNA offers good potentialities in terms of Eulerian FEM capabilities. In particular, the implemented spatial integration method belongs to formulations usually referred to as Arbitrary Lagrangian-Eulerian (also called with the acronym ALE). This method offers a wide versatility for modeling general large strain phenomena, by allowing to perform full Eulerian analyses. Thanks to this approach, the difficulties due to finite element distortions are no longer problematic. The description of the ALE methodology is not a target of this work. Reference is made, e.g., to Hirt et al., 1974, Benson, 1991, Casadei and Halleux, 1995, Benson et al., 1997, Benson, 2000, Benson and Stainier, 2000, and Casadei et al., 2001. Further considerations on the specific use of ALE capabilities within LS-DYNA can be found, e.g., in Souli et al., 2002, Schwer, 2004, Aquelet and Souli, 2008, Van Dorsselaer and Lapoujade, 2008, Day, 2009, and Lapoujade et al., 2010.

The adoption of a full Eulerian solving approach requires the meshing of the space of the analysis through ad-hoc finite elements which allow the material to flow through them. It is possible to introduce more than one material, resulting in multi-material finite elements which allow the flow of more than one material into a single finite element. Contacts, impacts, failure and mixture of the different materials are efficiently handled by the algorithm implemented in the FEM code. In this regard, see, e.g., Benson, 1995, Benson, 1996, Benson and Okazawa, 2004, and Vitali and Benson, 2011.

Thanks to the stated capabilities, the aim of the present Eulerian FEM simulations of the perforating gun device firing is that of expanding what done with the previous Lagrangian FEM simulations by simulating all the components of the perforating gun device, i.e. the shaped charges, the carrier, the ambient fluid, the casing, the concrete coating and the soil. These improvements may dramatically enhance the simulation coherence. As done for the Lagrangian FEM simulations, only tridimensional analyses are considered, in order to fulfill the same motivations previously exposed. However, preliminary two-dimensional analyses have been carried-out as well, as done for the Lagrangian FEM simulations.

The strongly limiting hypotheses introduced for the Lagrangian FEM simulations are removed, in particular by releasing the assumption of replacing the shaped charges with rigid liners and imposing a priori the liner initial velocity. Instead, the shaped charge detonation process is simulated thoroughly and the melted liner and its features, such as the velocity field, will now be a result of this modeling. An important point related to this latter aspect is the fact that the impact between the liners and the carrier can now be modeled with much more coherence. More in detail, the liner is not rigid anymore and can be modeled for having both deviatoric and volumetric resistances. Therefore, it can also change its shape, coherently with

the stress field to which it is subjected. As a consequence, the first of the three mentioned stressing factors which act on the carrier can now be modeled in a more appropriate fashion. Furthermore, the other two stressing actions that influence the carrier response are now introduced in the simulation. The fact of modeling the blast of the shaped charges allows for evaluating the evolution of the detonation products and investigate their possible action on the carrier. It is also possible to assess the possible impacts between the carrier and the fragments detaching from the shaped charges and their support and detonation systems, and hence evaluate possible related consequences.

The introduced enhancements make worthwhile the fact of extending the simulation to the modeling of the targets located over the carrier, i.e. the casing, the concrete coating and the soil. Therefore, the penetration capacity of the produced liner may also be assessed. Moreover, the presence of these bodies influences also the impact of the liner against the carrier. In fact, the final shape of the liner is determined also by the subsequent impacts between the liner itself and the casing, the concrete coating and the soil, due to the deformable nature of the liner itself.

All the spatial zones that in the initial conditions are not occupied by either the shaped charge, the carrier, the casing, the concrete coating or the soil, are not considered as void, i.e. without any material filling them, but rather they are filled with the ambient fluid. Following industrial partner communications, the ambient fluid is considered to be air at the atmospheric pressure, as previously stated. Therefore, the Eulerian space will be filled with eight different parts, i.e. the case, the explosive, the liner, the carrier steel, the casing steel, the concrete coating, the soil and finally the air.

The initial pressure fields are assumed to be all zero except within the air fluid, in which the atmospheric pressure is set, i.e. 101325 Pa. The initial temperature fields of all the parts involved are assumed as uniform and equal to 293 K, as done for the Lagrangian FEM simulations. The only other initial condition imposed is the presence of a detonation point located in the rear zone of the shaped charge. In fact, the explosive booster is not modeled but it is replaced by such detonation point, from which the explosive blast starts and spreads throughout the main explosive, which is the only introduced explosive material.

For a full Eulerian simulation, an Eulerian space needs to be defined and discretized with multi-material finite elements. The dimensions of this space are critical for the determination of the required computational time, considering also that multi-material finite elements are computationally much more expensive than standard Lagrangian finite elements. In view of this, the limitation of the Eulerian space to the minimum volume necessary to describe the phenomena of interest is of utter importance in order to avoid extremely long computational times. The made available computational resources during the execution of the present work were

barely sufficient to model the firing of one shaped charge, i.e. an Eulerian single scallop simulation. It has not been possible to carry-out Eulerian three scallop simulations. Therefore, as opposed to previous Lagrangian FEM simulations, only Eulerian single scallop simulations are presented here.

The Eulerian space is shaped in a doubly cylindrical fashion, which means that the considered space is defined by two cylinders with different radii and lengths. Both cylinders have axis coincident with the shaped charge axis. The first cylinder, with bigger radius and smaller length, includes the shaped charge, the carrier, the casing, the concrete coating and the very first part of the soil. The second cylinder, with smaller radius and longer length, includes the remaining part of the soil. Following Fig. 102 shows the adopted Eulerian space and the adopted mesh of multi material finite elements that compose it.

Figure 102. Single scallop Eulerian space composed of multi-material finite elements.

The Eulerian space is composed by a total of 1039760 multi-material finite elements. Preliminary tests have helped in the determination of the dimensions of these cylinders, i.e. the dimensions of the Eulerian space. The adopted configuration allows for capturing the evolution of all the aspects of interest and minimizing the dimensions of the space, that are very important due to the limited available computational resources. The multi-material finite elements of the Eulerian space have been created through the revolution of two planes with respect to the shaped charge axis. This strategy allows to deploy a higher number of multi-

material finite elements on the shaped charge axis, i.e. where the most important part of the perforating gun firing process takes place. This is principally due to the fact that the solid liner is expected to collapse on the shaped charge axis. This fact assumes even more relevance when considering that the resolution of the material filling of the Eulerian space multi-material finite elements is determined only by the dimensions of the multi-material finite elements themselves. Thus, having finer elements means having a better material filling. This has been a critical point for the initial filling of the multi-material finite elements, in particular for the aim of correctly following the geometrical characteristics of the shaped charge, where the case, the explosive and the liner are in contact and their geometry is characterized by having some severe direction changes. Considering these aspects, a wide series of preliminary tests has been carried-out with the aim of determining the best mesh topology for the Eulerian space. The best option appeared to be the adopted one, namely the double cylinder option. Typically, full Eulerian simulations are carried-out with multi-material finite elements that are all equal, i.e. with the same shape and dimensions. This assumption is not true anymore when the double cylinder option is enforced, because the multi-material finite elements in this case are generated through a revolution of two planes of two-dimensional elements, which leads to the creation of non uniform hexahedral elements. Preliminary tests have been conducted to verify the possible differences between the adopted double cylinder option and the all equal elements option, resulting in no noticeable differences, but a better resolution of the flowing materials for the double cylinder option. Therefore, its adoption.

One last point that needs to be highlighted is the fact that the support and detonation system of the shaped charge are not introduced in the modeling. This is due to the facts that there was total unavailability of information about the nature of this component for the considered perforating gun device. Its design can heavily vary as a function of several parameters, and even when one solution is identified, geometry and materials may strongly differ. Furthermore, the introduction in the Eulerian model of this component would have necessarily led to an extension of the model space, resulting in the requirement of more powerful computational means, not available during the execution of the present work.

According to the hypotheses made, the initial configuration of the single scallop simulation is reported in following Fig. 103.

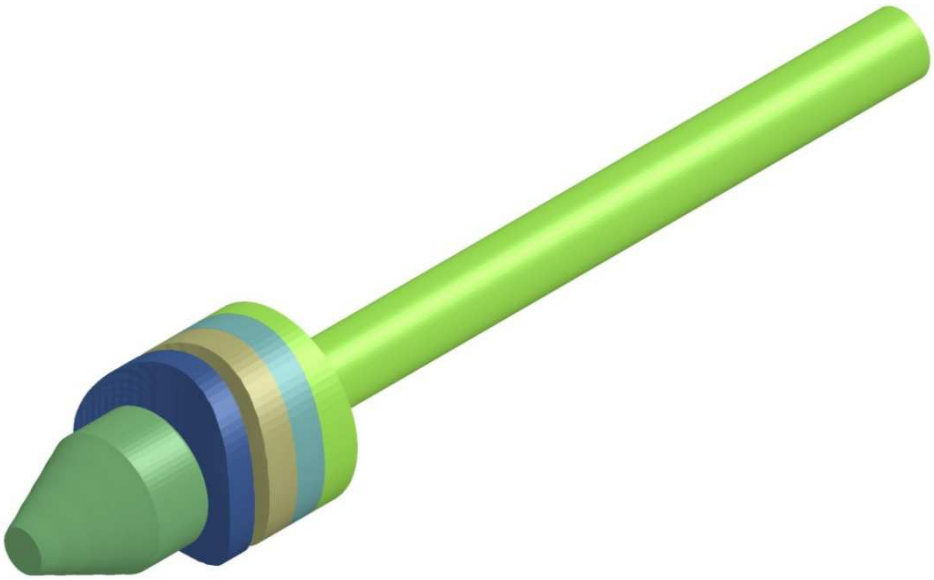

Figure 103. Initial configuration of the single scallop Eulerian FEM simulation. The shaped charge is represented in dark green, the carrier in blue, the casing in light brown, the concrete coating in sky blue and the soil in light green. Air is hidden in order to allow the other components to be seen.

Following Fig. 104 reports a longitudinal cross-sectional view of the initial configuration.

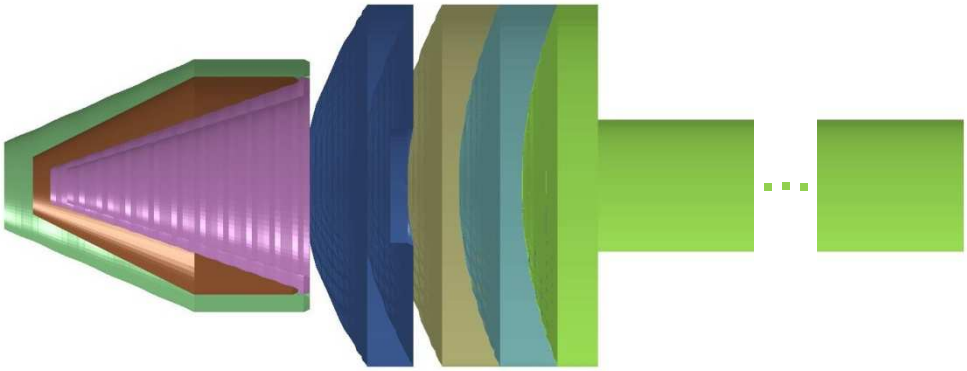

Figure 104. Cross section of the initial configuration of the single scallop Eulerian FEM simulation. It is possible to see the three components of the shaped charge. The case is represented in dark green, the explosive in brown and the liner in purple. It is also possible to see the scallop in the carrier. The soil is interrupted in order to allow an enlargement of the other components. Air is hidden in order to allow the other components to be seen.

Boundary conditions can be defined on the Eulerian space frontiers. Zero displacements on the external boundary of the carrier, the casing, the concrete coating and the soil are enforced, i.e. the parts of these components which are in direct contact with the external surface of the Eulerian space. This is done coherently with what assumed in the Lagrangian FEM simulations in order to avoid unwanted rigid longitudinal displacements of the considered components.

As done for the Lagrangian FEM simulations, an explicit time integration method is adopted. The output is enforced to be saved at intervals of $2.5 \cdot 10^{-7}$ s. Such frequency is looser than the one adopted for the Lagrangian FEM simulations. This is necessary in order to limit the weight of the output data, due to the available computational capacities. However, preliminary tests assured that this frequency is still enough to achieve a good time resolution of the underlying phenomenon.

The contact is handled through the LS-DYNA ALE contact algorithm, see Livermore Software Technology Corporation (LSTC), 2006, and 2012, for LS-DYNA contact algorithms. The timestep scale factor has been lowered to ad-hoc found values, comparing to the LS-DYNA default value. A long series of preliminary tests has been conducted, in order to correctly set-up the cited parameters and all the other ALE controls.

4.4.1. Constitutive Modeling

According to what stated above, it is necessary to properly define the constitutive modeling of eight parts.

The carrier is modeled in the same way previously outlined for the Lagrangian FEM simulations, i.e. the Johnson-Cook strength model, the Mie-Grüneisen equation of state and the Johnson-Cook damage and failure model, together with a cut-off on the tensile pressure to simulate material spall resistance. The same parameters previously introduced for the Lagrangian FEM simulations have been adopted. For Eulerian analyses, there is no removal of completely damaged material, i.e. material that gets a Johnson-Cook damage variable equal to 1, but rather this material is assumed to offer neither deviatoric nor volumetric resistance.

Regarding the shaped charge, three parts are identified, i.e. the case, the main explosive and the liner. For what it concerns the case, no data were made available. The hypothesis here is that the material is a high resistance steel. In this context, the same strength model, equation of state and damage and failure model of the carrier have been adopted, with the same parameters.

The constitutive model of the liner is a critical one. It needs to model both the solid behavior of copper and its high pressure fluid behavior, after the shaped charge detonation. In order to model this aspects, the Johnson-Cook strength model and the Mie-Grüneisen equation of state have been adopted again, together

with the Johnson-Cook damage and failure model and the cut-off on the tensile pressure for introducing a spall resistance. These choices are due to the fact that the Johnson-Cook strength model provides a strain rate and temperature modeling for the deviatoric behavior of the material, which vanishes when the melting temperature is reached or exceeded. The idea here is that when the solid copper undergoes the explosive blast, it may generate a large increment of temperature that may melt the copper, resulting in a null deviatoric behavior and a volumetric behavior only, ruled by the Mie-Grüneisen equation of state. As previously stated, this choice of constitutive modeling allows for accounting for a phase change, from solid to a high pressure volumetric fluid. Having no copper experimental data, its parameters have been derived from literature data. The 8 parameters of the Johnson-Cook hardening model have been taken from Johnson and Cook, 1983, referring to the OFHC (Oxygen-Free High Conductivity) copper data therein presented. Following Table 35 exposes such parameters.

A	90 MPa	m	1.09
B	292 MPa	$\dot{\bar{\varepsilon}}_0$	0.002 s^{-1}
n	0.31	T_0	293 K
C	0.025	T_m	1356 K

Table 35
Johnson-Cook strength model parameters for the copper liner.

The total lack of experimental data makes it impossible to implement and use the Split Johnson-Cook model proposed in Chapter 3. Johnson and Cook, 1983, provided also OFHC copper specific heat, which is equal to 383 J/(kg·K). Density and other necessary elastic parameters of a generic copper can be found in the literature. Density is taken equal to 8940 kg/m^3, Young modulus equal to 120000 MPa, shear modulus equal to 48000 MPa and Poisson's ratio equal to 0.34.

For what it concerns the copper liner Mie-Grüneisen equation of state, the parameters have been taken from Steinberg, 1996, referring to OFHC copper. Such parameters are reported in following Table 36.

C_0 [m/s]	S_1	S_2	S_3	γ_0
3940	1.489	0	0	2.02

Table 36
Mie-Grüneisen parameters for the copper liner.

The 5 parameters of the Johnson-Cook damage model have been taken from Johnson and Cook, 1985, which presents such parameters for OFHC copper. Following Table 37 reports their values.

D_1	D_2	D_3	D_4	D_5
0.54	4.89	-3.03	0.014	1.12

Table 37
Johnson-Cook damage and failure parameters for the copper liner.

Thermal expansion has been considered as well, through the introduction of an isotropic volumetric thermal expansion coefficient, equal to 0.000017 K^{-1}, a value relative to a generic copper and quoted in the literature. This value has been considered as independent from the temperature, as done for the coefficient of the steel carrier.

The cut-off tensile pressure value for the copper liner has been recovered from Davison et al., 1996, and assumed equal to 1360 MPa, intended as maximum tensile pressure. However, there is some uncertainty about the applicability of this value to the considered copper.

The last shaped charge component is represented by the explosive. Again, no data were made available. As previously said, the assumption here is that of adopting RDX as main explosive. This choice appears to be coherent with the kind of explosives usually adopted for the considered shaped charge. The detonation product of explosives with a high detonation velocity, such as RDX, can be fruitfully modeled through the Jones-Wilkins-Lee equation of state, Eq. (67), which has then been adopted. The JWL parameters for RDX have been taken from Coleburn, 1964, and Ambrosi and Briganti, 2010. They are reported in following Table 38.

A [MPa]	B [MPa]	R_1	R_2	ω
778370	7070	4.2	1	0.3

Table 38
Jones-Wilkins-Lee parameters for RDX explosive.

The Jones-Wilkins-Lee equation of state defines the pressure after the detonation. i.e. the pressure of the detonation products. The detonation point imposes the coordinates at which the first detonation appears. After that, the blast spreads throughout the explosive material. This phenomenon is ruled through a so-called burn fraction, denoted by F. This parameter is defined to be greater than 0 and lower than 1. It multiplies the pressure computed from the Jones-Wilkins-Lee equation of state, Eq. (67), with the aim to control the release of chemical energy

for better simulating detonations in finite element computations. The pressure is then calculated through the following equation

$$p = F\left(A\left(1 - \frac{\omega}{R_1 v} \right) e^{-R_1 v} + B\left(1 - \frac{\omega}{R_2 v} \right) e^{-R_2 v} + \frac{\omega E}{v} \right). \tag{87}$$

When an explosive material is introduced in a finite element simulation, its detonation needs to be triggered. Following Livermore Software Technology Corporation (LSTC), 2006, and 2012, this can be done in two ways. The first one deals with the definition of one or more detonation points. A specific detonation instant must then be defined for each detonation point. For each finite element of the mesh, it is then possible to define a so-called lightning time, denoted by t_l, which consists in the time necessary for the blast wave to reach the finite element in question and trigger the explosion in it. It is computed with the following equation

$$t_l = \frac{d}{D}, \tag{88}$$

where d denotes the distance from a considered detonation point to the center of the considered finite element, and D is a parameter of the explosive material, called detonation velocity or burn velocity. For a given finite element, the number of lightning times computed is equal to the number of detonation points introduced in the simulation. For each element, it is possible to compute the minimum lightning time. The finite element burn fraction is then taken equal to 0 if the simulation time is lower or equal to the minimum lightning time, i.e. when the burn front has not reached the element yet, while it is taken equal to the value specified by the following equation if the simulation time is greater than the minimum lightning time

$$F = \frac{2 \cdot \left(t - \min\left(t_l \right) \right) \cdot D \cdot A_{e_{max}}}{3 \cdot V_e}. \tag{89}$$

In this equation, t denotes the simulation time, $\min(t_l)$ denotes the computed minimum lightning time for the considered finite element, $A_{e_{max}}$ denotes the maximum area of the element faces and V_e denotes the finite element volume. If Eq. (89) returns a value of F greater than 1, it is reset to 1.

The second way used to trigger the detonation deals with compression of the explosive material. In this case, the hypothesis is that of considering compressive

deformations as capable to initiate detonations. The burn fraction is then calculated through the following equation

$$F = \frac{1 - v}{1 - v_{CJ}}. \tag{90}$$

In this equation, v_{CJ} denotes the so-called Chapman-Jouguet relative volume (see, e.g., Chapman, 1899, Sternberg, 1970, Cooper, 1996, Chéret, 1999, and Fickett and Davis, 2000). If both detonation triggering hypotheses are adopted, the burn fraction of a given finite element is calculated as the maximum between the values computed with Eqs. (89) and (90). It is also possible to define a deviatoric resistance for the explosive material, in order to model possible deformations that it may undergo before detonating.

For the case under consideration, namely the firing of a perforating gun device, only one detonation point is defined, on the rear part of the main explosive, where the booster is usually located. Specifically, the detonation point is placed on the shaped charge axes, 2 millimeters prior to the surface that delimits the main explosive from the shaped charge case. The detonation instant is set-up at the beginning of the simulation, i.e. at the beginning of the very first timestep. Then, deviatoric behavior for the explosive material is not considered, since such material does not undergo deformations before detonating.

Following Coleburn, 1964, and Ambrosi and Briganti, 2010, the RDX detonation velocity is taken equal to 8750 m/s. RDX density has been taken equal to 1891 kg/m^3 and the RDX Chapman-Jouguet pressure (see e.g., Chapman, 1899) has been taken equal to 33800 MPa. Furthermore, RDX thermal expansion has been considered as well, through the introduction of an isotropic volumetric thermal expansion coefficient, equal to 0.000065 K^{-1}, following Baytos, 1979, and Weese et al., 2005. This value has been considered to be independent from the temperature.

Several simulations have been carried-out in order to assess the coherency of the exposed model when high explosive detonations are introduced into the simulation. All the obtained results confirmed a good coherency for the adopted JWL and burn fraction models.

Beyond the carrier and the three shaped charge components, the remaining components that need to be modeled are the casing, the concrete coating, the soil and the ambient fluid, i.e. air.

For what it concerns the casing, no data have been provided from the industrial partner, as previously stated. As said, the material is considered to be a 4340 steel. This component is placed right behind the carrier. It will be pierced by the liner after the perforation of the carrier. Hence, the casing is subjected to very high strain rate phenomena similar to those that happen in the carrier, although the incoming liner

will have a little less velocity and energy comparing to the impact with the carrier. In this view, the same constitutive model hypotheses made for the carrier are considered to be valid for the casing as well. Therefore, the Johnson-Cook strength model, the Mie-Grüneisen equation of state and the Johnson-Cook damage and failure model are used again. Johnson-Cook hardening function parameters are taken from Johnson and Cook, 1983, in which 4340 steel data are made available. The adopted parameters are exposed in following Table 39.

A	792 MPa	m	1.03
B	510 MPa	$\dot{\bar{\varepsilon}}_0$	0.002 s^{-1}
n	0.26	T_0	293 K
C	0.014	T_m	1793 K

Table 39
Johnson-Cook strength model parameters for the steel casing.

As previously stated for the liner, the total lack of experimental data makes it impossible to implement and use the Split Johnson-Cook model proposed in Chapter 3. Johnson and Cook, 1983, provided also the 4340 steel specific heat, equal to 477 J/kg·K. Density and other necessary elastic parameters can be found in the literature, referring to 4340 steel. Density is equal to 7830 kg/m^3, Young modulus to 200000 MPa, shear modulus to 77000 MPa and Poisson's ratio to 0.29.

For what it concerns the casing Mie-Grüneisen equation of state, the parameters have been taken from Steinberg, 1996, for 4340 steel. They are reported in following Table 40.

C_0 [m/s]	S_1	S_2	S_3	γ_0
4578	1.33	0	0	1.67

Table 40
Mie-Grüneisen parameters for the steel casing.

The five parameters of the Johnson-Cook damage model have been taken from Johnson and Cook, 1985, which presents such parameters for 4340 steel. Following Table 41 reports their values.

D_1	D_2	D_3	D_4	D_5
0.05	3.44	-2.12	0.002	0.61

Table 41
Johnson-Cook damage and failure parameters for the steel casing.

Thermal expansion has been considered as well, in the same way previously done for the carrier, namely through the introduction of an isotropic volumetric thermal expansion coefficient, set equal to 0.000012 K^{-1}, once again considered as independent from temperature, as done for the steel carrier. Regarding spall fracture, the same simple model adopted for the carrier has been considered, with a cut-off pressure assumed equal to 13000 MPa.

For the concrete coating, the same considerations regarding the involvement of very high strain rates and high temperatures previously stated for the carrier and for the casing hold true. For low strain rates and room temperature behaviors, concrete response is usually described by non-associative elastoplastic models. Anyway, for the considered hyperfast dynamic and thermal conditions, the choice made here is that of modeling concrete with a classic associative elastoplastic strength model, coupled with a separate Mie-Grüneisen equation of state. A simple failure and finite element removal criterion completes the model. It imposes material failure and element erosion when a predetermined equivalent plastic strain value is reached. This strategy follows Jin et al., 2002, where concrete subjected to very high strain rate phenomena was modeled with this approach. Although this constitutive modeling may lack coherence, it favors simplicity and furthermore it does not require to define a long list of material parameters. This choice appears to be reasonable by considering also the total lack of material data for the specific case under target. The material parameters for such model are taken based on the values of a generic concrete, from the literature. They consist in a shear modulus of 2200 MPa, a compressive yield stress of 40 MPa, a density of 2300 kg/m^3 and a specific heat of 880 J/kg·K. Perfectly plastic behavior is assumed, thus defining a zero hardening modulus. Following Jin et al., 2002, the failure equivalent plastic strain has been set equal to 0.1. Data for the Mie-Grüneisen equation of state are taken from this same reference, except for the bulk sound speed which is taken equal to 3400 m/s, i.e. a generic value for concrete. The adopted EOS parameters are reported in following Table 42.

C_0 [m/s]	S_1	S_2	S_3	γ_0
3400	1.4	0	0	0

Table 42
Mie-Grüneisen parameters for the concrete coating.

Concrete thermal expansion has been considered as well, in the same way as previously done for the the other components, i.e. through the introduction of an isotropic volumetric thermal expansion coefficient, equal to 0.000012 K^{-1}, considered independent from temperature. More in general, considerations on the

adoption of more refined concrete models for fast dynamic loadings and their applications in FEM simulations can be found in Tu and Lu, 2008.

For what it concerns the soil, the constitutive model adopted is that presented in Krieg, 1972. This model is already implemented in LS-DYNA. It is a simple model that allows to describe soil elastoplastic behavior up to failure. As stated in Livermore Software Technology Corporation (LSTC), 2006, other constitutive models may actually provide a more coherent description of soil behavior. Anyway, this model is useful when material properties are not well characterized, since it requires less material parameters. The choice of this specific model is mainly due to this aspect. Following the exposition given in Krieg, 1972, the soil is considered to manifest an isotropic elastoplastic behavior, with a pressure dependent nonlinear Drucker-Prager yield function defined by the following equation

$$\phi = J_2 - \left(a_0 + a_1 p + a_2 p^2\right). \tag{91}$$

In this equation, a_0, a_1 and a_2 are soil parameters to be determined through experimental measurements, while J_2 is the second invariant of the stress deviator of the adopted stress measure.

The soil is considered to have perfectly plastic behavior, i.e. no hardening is considered. Volumetric behavior is introduced as well, by considering compressive resistance only. Therefore, no tensile pressure can be resisted by the soil. The compressive volumetric resistance is modeled through a nonlinear equation of state, defined by a function that relates the pressure and a volumetric strain measure defined as the natural logarithm of the relative volume. Unloading paths are defined through a linear function between the pressure and such volumetric strain measure. Hence, when the soil undergoes compressive unloading, it does not follow the loading nonlinear EOS but rather the linear unloading relation. Both the loading nonlinear equation of state and the slope of the linear unloading function, i.e. an unloading bulk modulus, need to be defined as input data for the code LS-DYNA.

No soil experimental data are made available. The material parameters for the described model are then taken from Bojanowski and Kulak, 2010. A shear modulus of 34.5 MPa is assumed, together with a density of 2350 kg/m^3. The yield parameters a_0 and a_1 are taken equal to zero, while the parameter a_2 is taken equal to 0.602. The unloading bulk modulus is set equal to 15 MPa. The nonlinear compressive loading function is plotted in following Fig. 105. It refers to hydrostatic soil experimental data exposed in Bojanowski and Kulak, 2010.

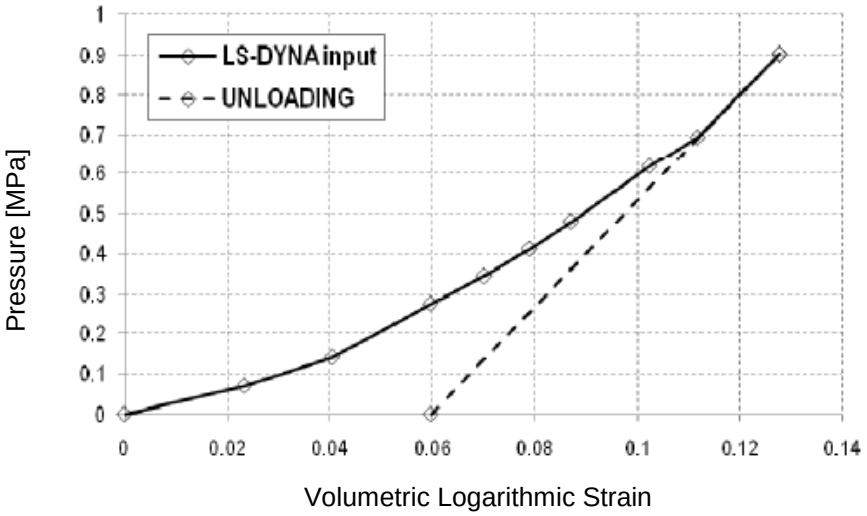

Figure 105. Volumetric behavior of the soil (source Bojanowski and Kulak, 2010).

Coordinates of the points indicated with diamonds in Fig. 105 are reported in following Table 43. These data are directly introduced into the LS-DYNA input.

ln(v)	0	0.08	0.15	0.28	0.35
p [MPa]	0	0.024	0.041	0.059	0.070
ln(v)	0.41	0.48	0.62	0.70	0.90
p [MPa]	0.078	0.088	0.103	0.112	0.128

Table 43
Tabular data for soil compressive volumetric behavior (source Bojanowski and Kulak, 2010).

Due to unavailability of data, the possibility of soil thermal expansion is not introduced in the model.

The last material to model is the ambient fluid, i.e. air at the atmospheric pressure. Air is assumed to be an ideal gas. Therefore, no deviatoric resistance is introduced. The volumetric behavior is modeled through an ideal gas equation of state, which computes the pressure through the following equation

$$p = (\gamma - 1) \cdot \frac{E}{v}, \tag{92}$$

where E denotes the internal energy, v denotes the relative volume and γ represents the ratio between the constant pressure and the constant volume specific heats. For air, γ is equal to 1.4. Furthermore, air is initiated to a pressure of

101325 Pa, in order to account for the atmospheric pressure. Air density is taken equal to 1.225 kg/m^3, i.e. the density for air at the atmospheric pressure. Air thermal expansion is not considered relevant and thus it is not introduced in the model.

4.4.2. Simulation Results

Following Figs. 106 to 117 show the outcomes of the single scallop Eulerian FEM simulations. As for the Lagrangian analyses, all the carried-out simulations satisfy energy balance requirements, i.e. the ratio between the total energy and the initial energy is practically equal to 1, considering all the energy forms involved in the analysis.

The simulations have been extended in time until no noticeable variations in the stress and strain fields of the carrier have appeared. This led to a total time of the simulation of $9.425 \cdot 10^{-5}$ s, i.e. 94.25 μs.

Figure 106. Eulerian FEM simulation at the initial instant.

Figure 107. Eulerian FEM simulation at 5 μs. The shaped charge begins to expand due to the pressure from the detonation products.

Figure 108. Eulerian FEM simulation at 10 µs. The needle-shaped liner is already created.

Figure 109. Eulerian FEM simulation at 15 µs. The liner has pierced the carrier.

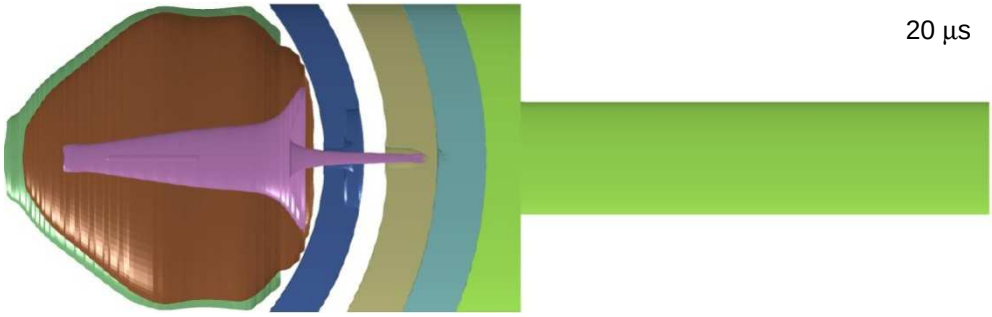

Figure 110. Eulerian FEM simulation at 20 µs. The liner is piercing the casing.

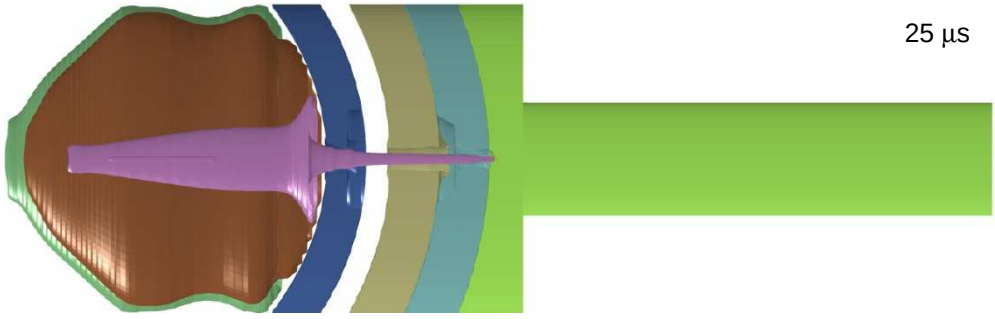

Figure 111. Eulerian FEM simulation at 25 µs. The liner has pierced the concrete coating.

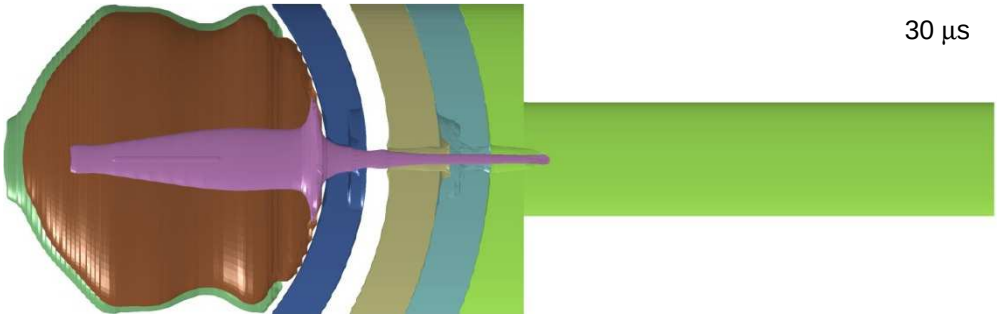

Figure 112. Eulerian FEM simulation at 30 µs. The liner is piercing the soil.

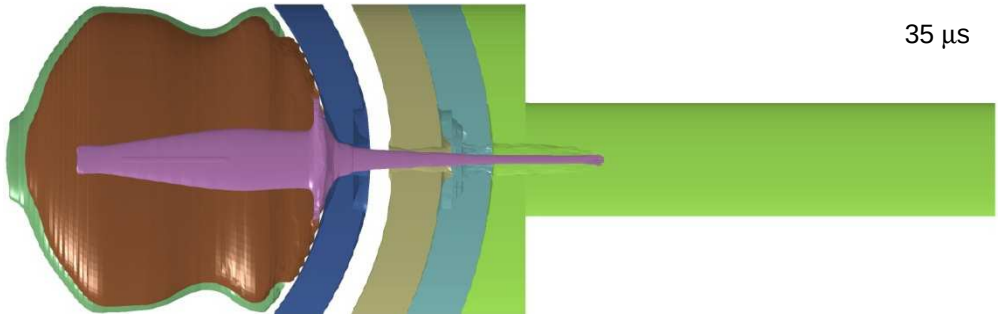

Figure 113. Eulerian FEM simulation at 35 µs. The rear part of the liner is pushing on the carrier.

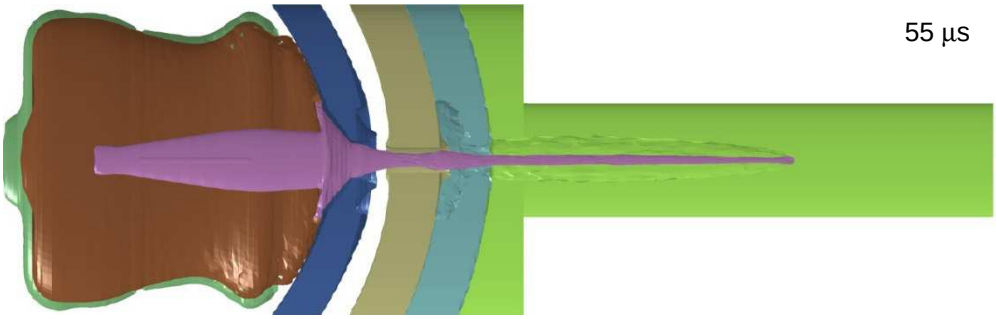

Figure 114. Eulerian FEM simulation at 55 µs. The front part of the liner is piercing the soil. The rear part has flared the carrier, which is also hit by the detonation products.

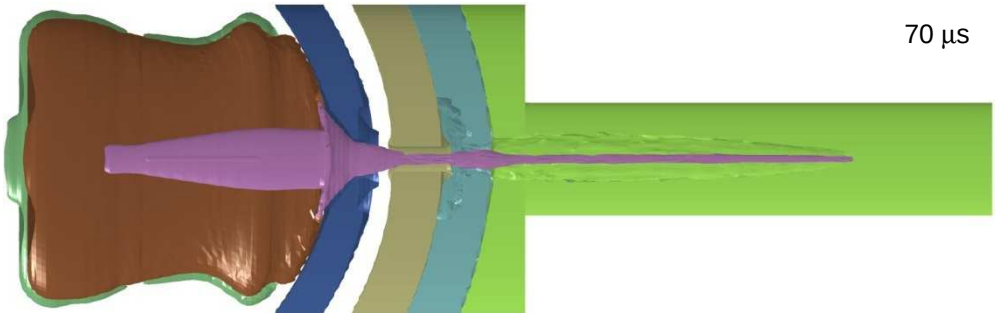

Figure 115. Eulerian FEM simulation at 70 µs. The liner keeps on piercing the soil. The rear part of the liner and the detonation products have further deformed the carrier.

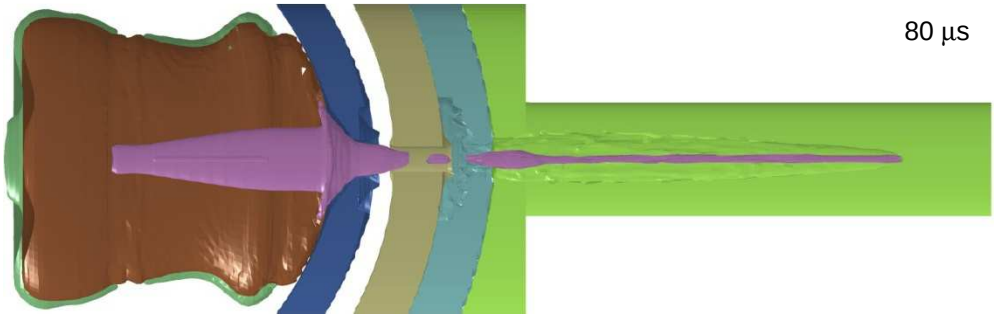

Figure 116. Eulerian FEM simulation at 80 µs. The middle part of the liner fractured while the front part keeps on piercing the soil. The carrier is further deformed.

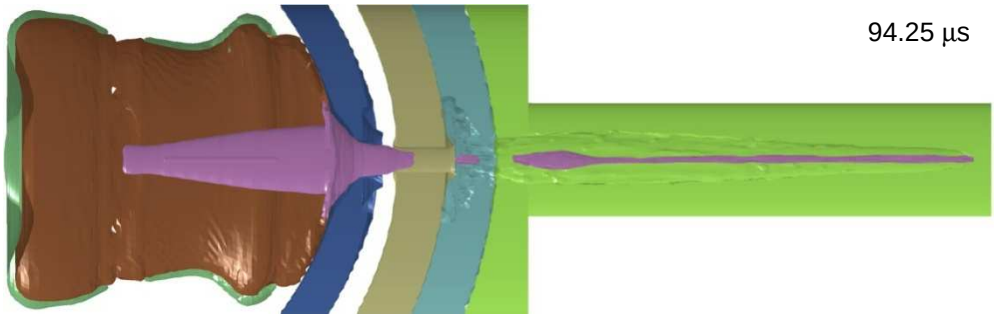

Figure 117. Eulerian FEM simulation at the final instant, 94.25 µs. The soil is further pierced. The carrier shows its final deformation.

Following Fig. 118 provides a tridimensional view of the final configuration, considering the shaped charge and the carrier only.

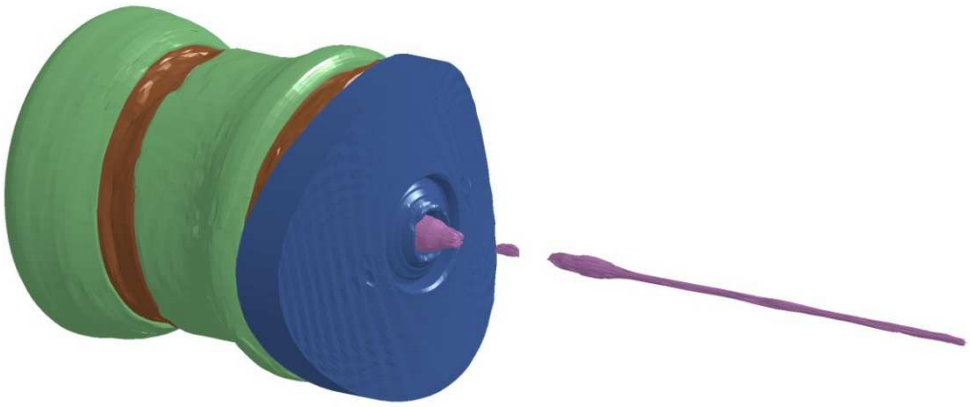

Figure 118. Eulerian FEM simulation at the final instant. 3D view of the shaped charge components and of the carrier.

Following Fig. 119 provides a tridimensional view of the final configuration of the carrier.

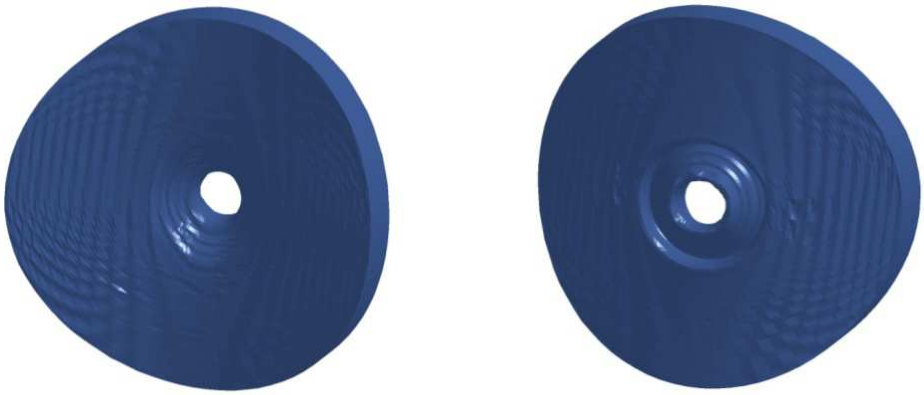

Figure 119. Eulerian FEM simulation at the final instant. 3D view of the inner (left figure) and outer (right figure) sides of the carrier. The exit hole is clearly visible. The inner side of the carrier presents a flaring due to the impact of the rear part of the liner. The carrier presents also a bulging.

Following Fig. 120 provides a more detailed view of the first phase of the shaped charge explosion, in order to better visualize the formation of the needle-shaped liner.

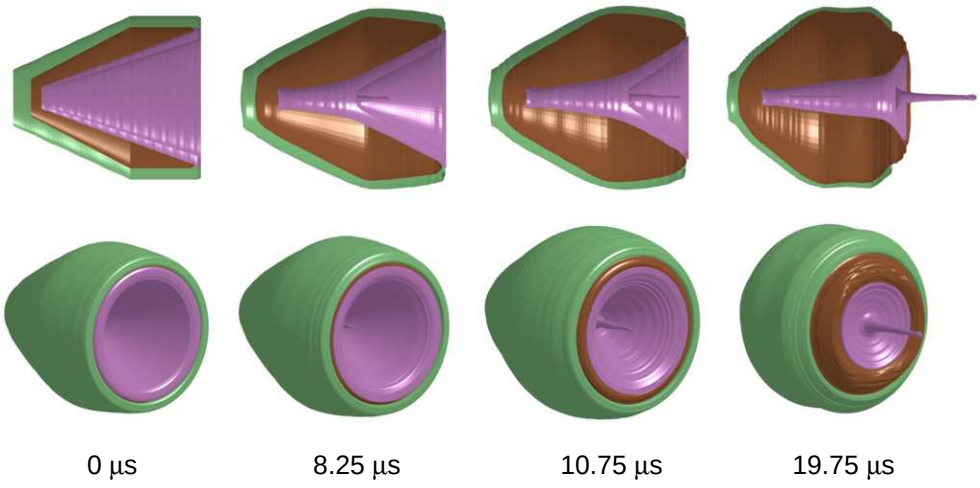

Figure 120. Evolution of the shaped charge explosion and consequent formation of the needle-shaped liner.

Following Fig. 121 allows for visualizing the pressure of the explosive after detonation. In order to better assess the phenomenon, only the explosive and the liner are shown, and the pressure field is evaluated for the explosive only. It is

possible to see the evolution of the pressure wave, which is computed with the burn fraction algorithm described previously.

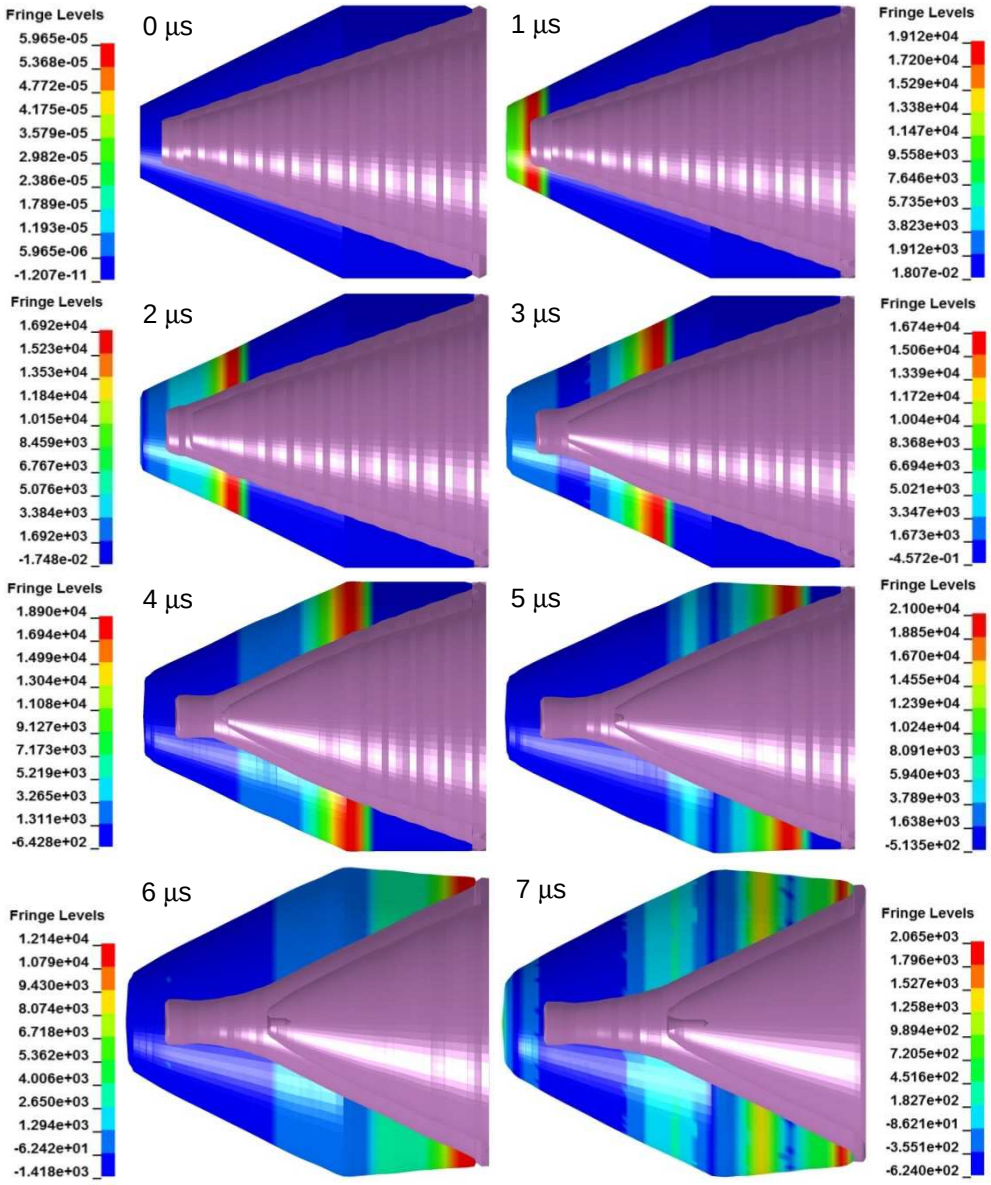

Figure 121. Pressure wave [MPa] in the main explosive. Pressures over 21 GPa are reached.

Following Fig. 122 shows the velocity modulus field in the shaped charge at the simulation time of 8.25 µs, i.e. the instant in which the liner reaches its maximum velocity.

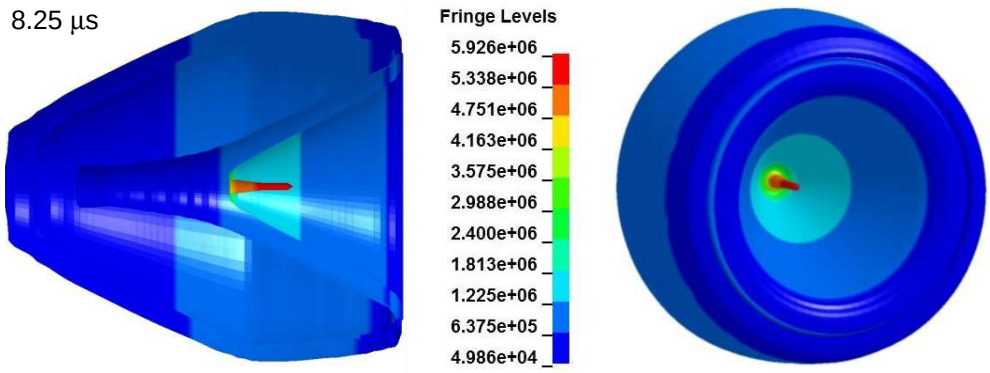

Figure 122. Velocity modulus field [mm/s] in the shaped charge 8.25 μs after the initial instant. The peak velocity of 5.926 km/s is reached.

Figure 122 shows a maximum liner velocity modulus near to 6 km/s. This value looks coherent with experimental observations discussed in Novokshanov and Ockendon, 2006, and also with some communications from the industrial partner, which are further pointed-out in Ambrosi and Briganti, 2010. After reaching this maximum value, the liner slightly slows down and impacts the carrier with a velocity modulus of 5.524 km/s.

Following Figs. 123 to 130 aim at showing in details the carrier response. Results are evaluated in terms of the equivalent plastic strain rate field, the von Mises stress field, the pressure field and the equivalent plastic strain field. In order to better assess the phenomenological output, only the shaped charge and the carrier are shown. Furthermore, the considered fields are plotted only for the carrier.

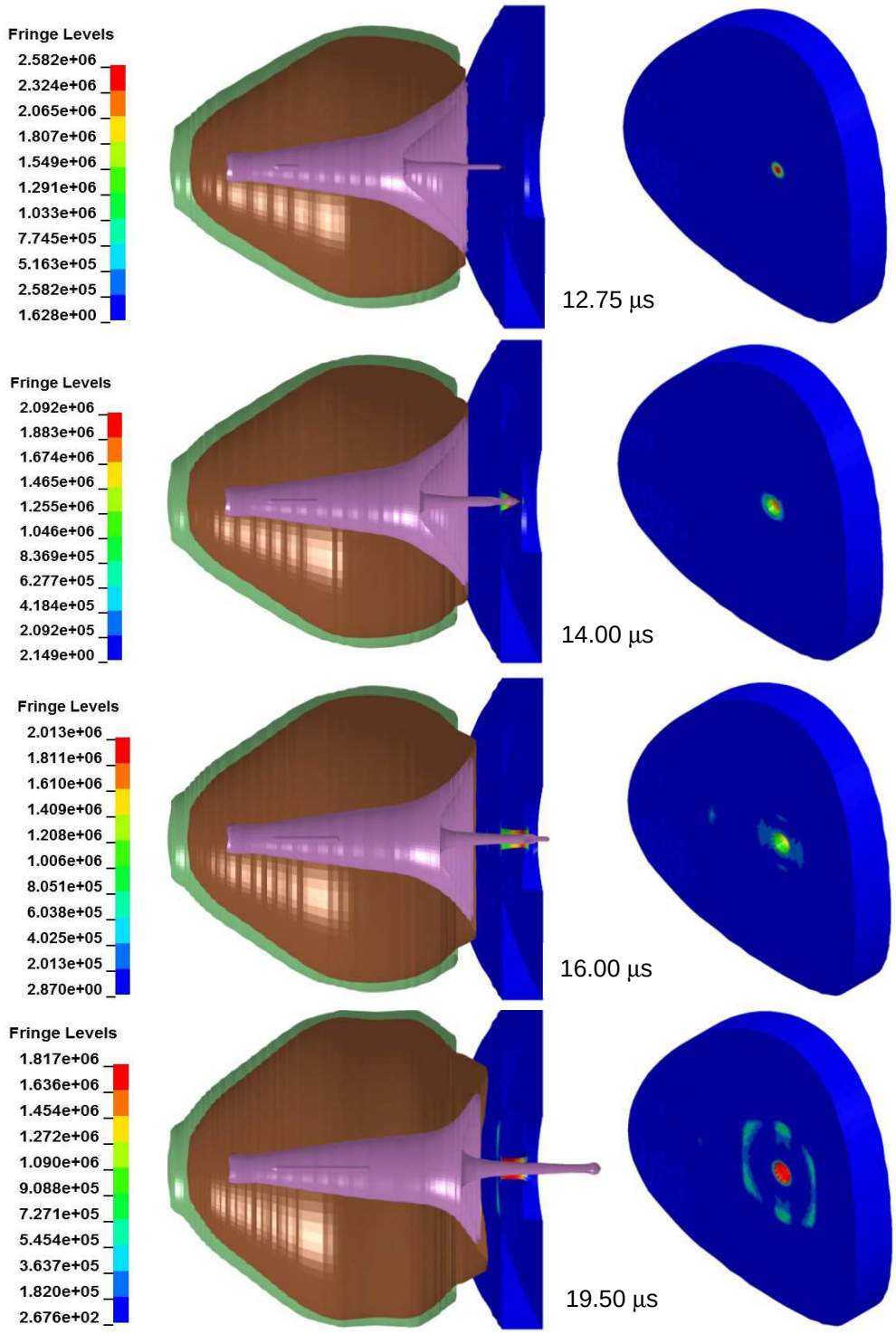

Figure 123. Equivalent plastic strain rate field [s^{-1}] in the carrier at four different simulation times.

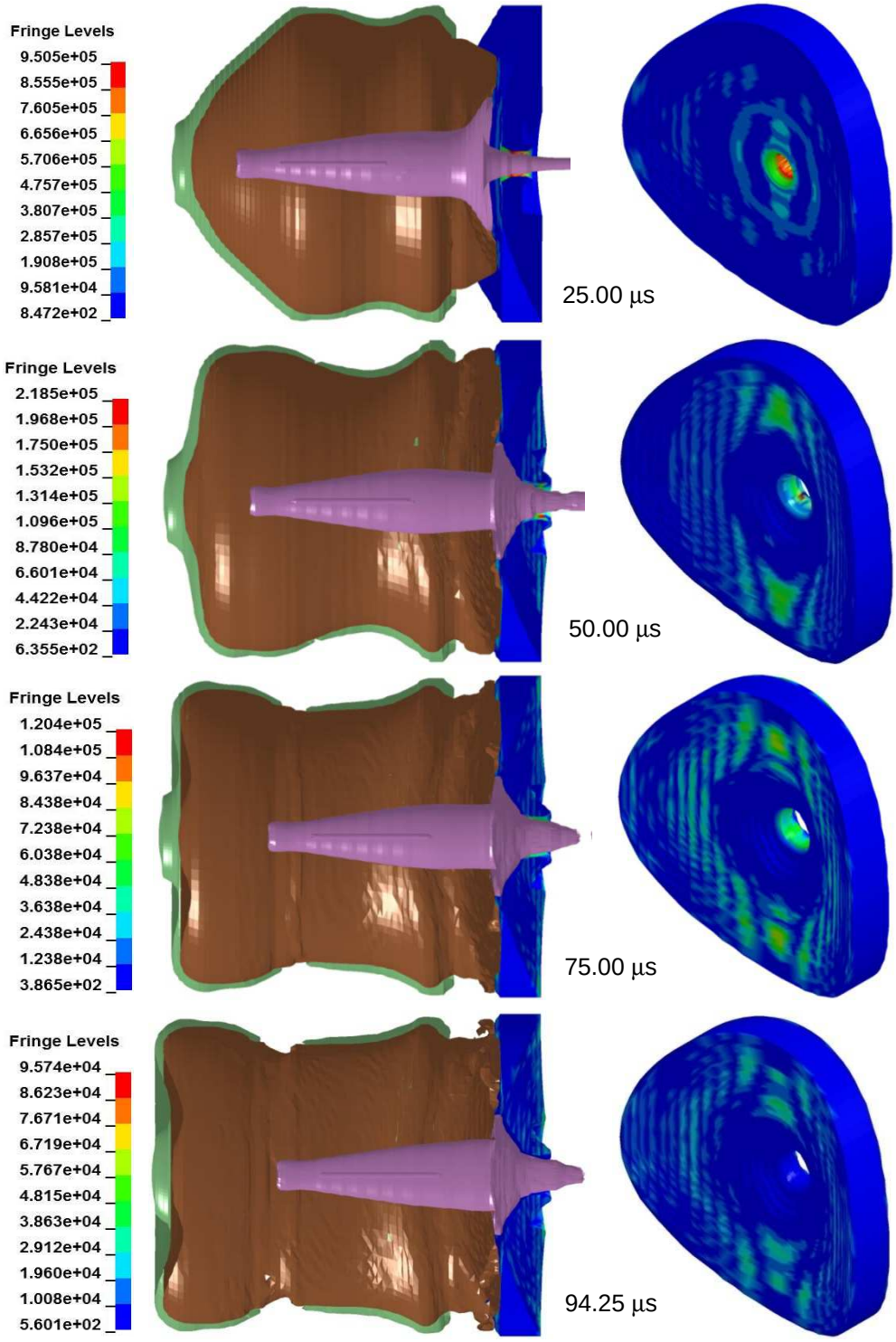

Figure 124. Equivalent plastic strain rate field [s^{-1}] in the carrier at four different simulation times.

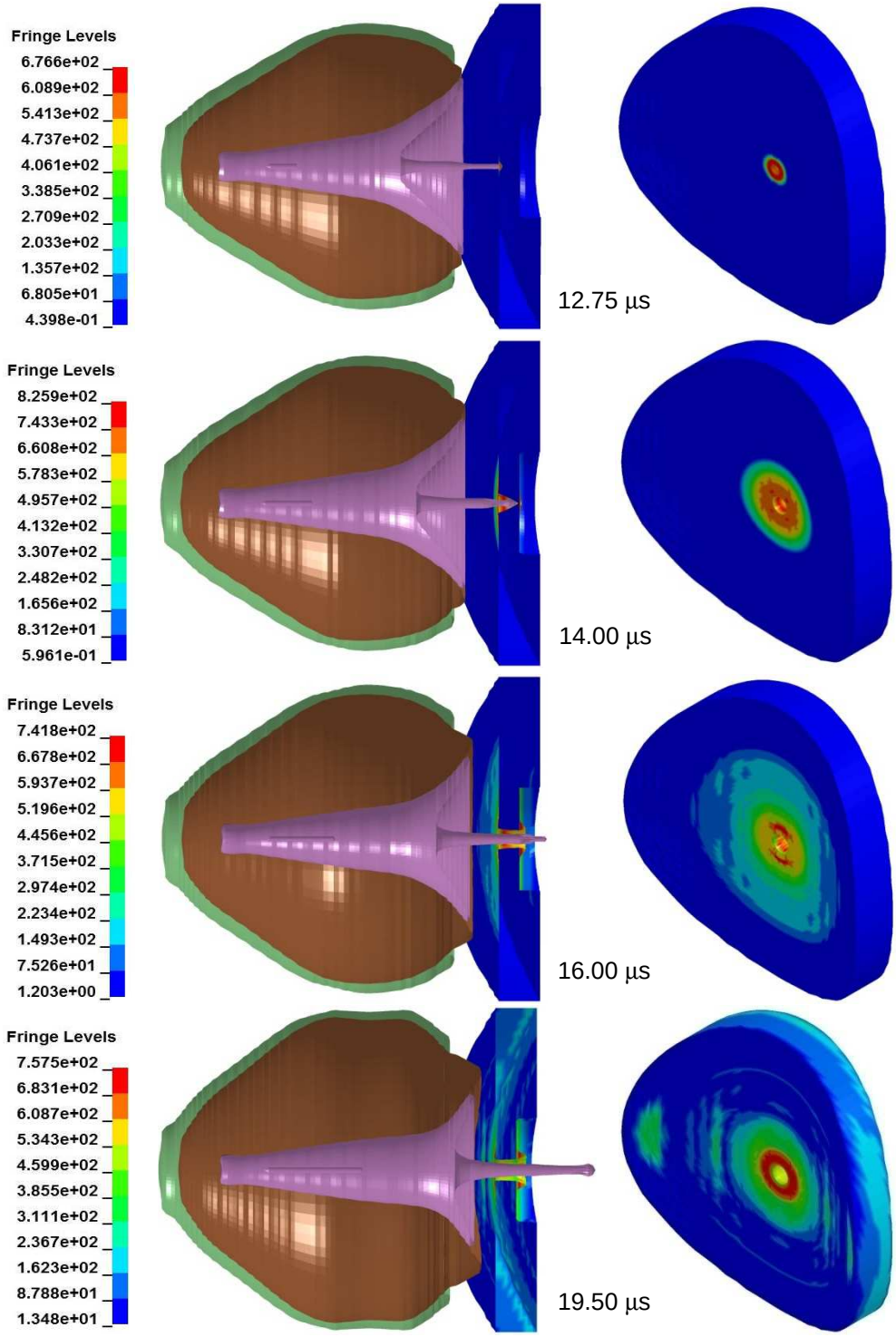

Figure 125. von Mises stress field [MPa] in the carrier at four different simulation times.

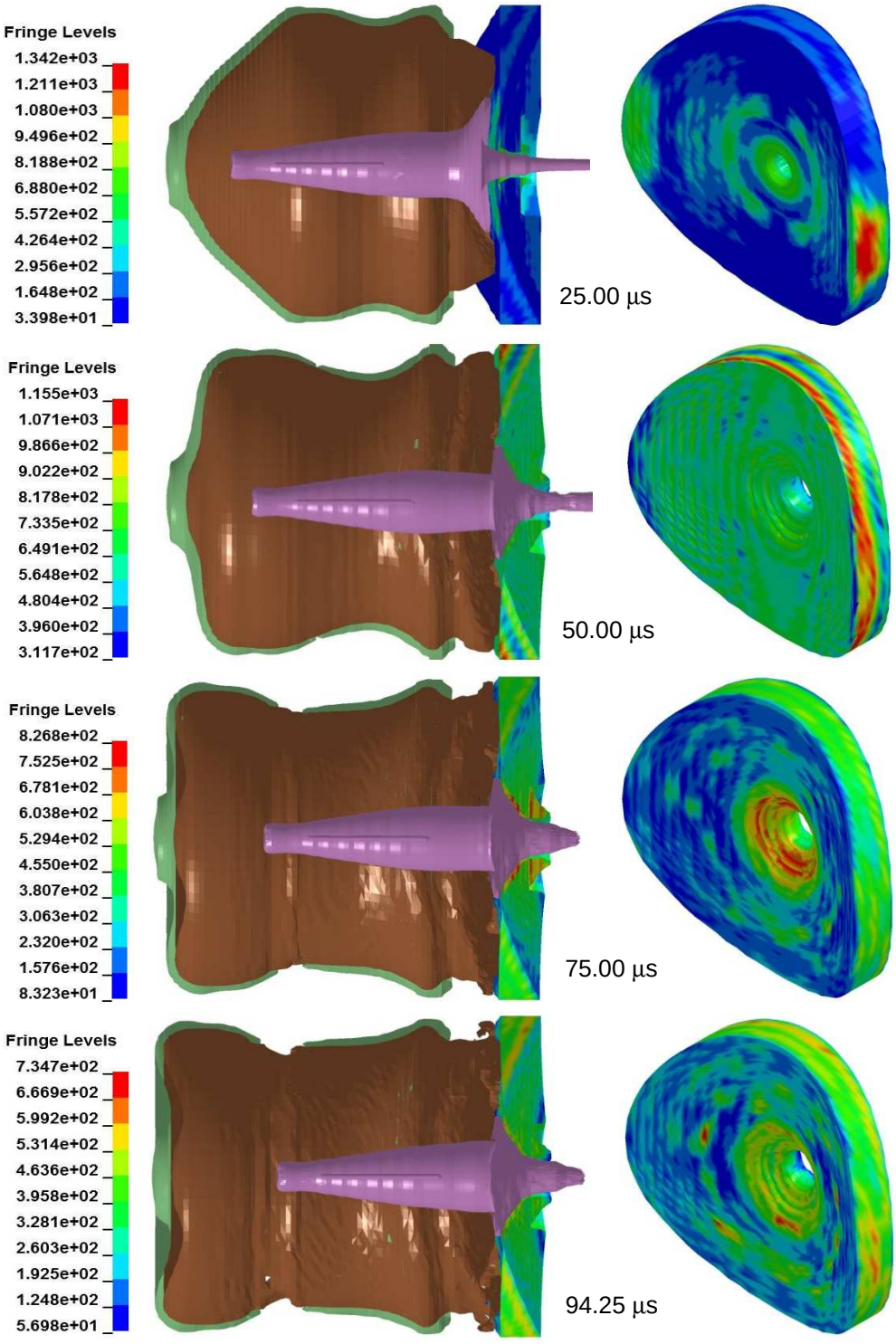

Figure 126. von Mises stress field [MPa] in the carrier at four different simulation times.

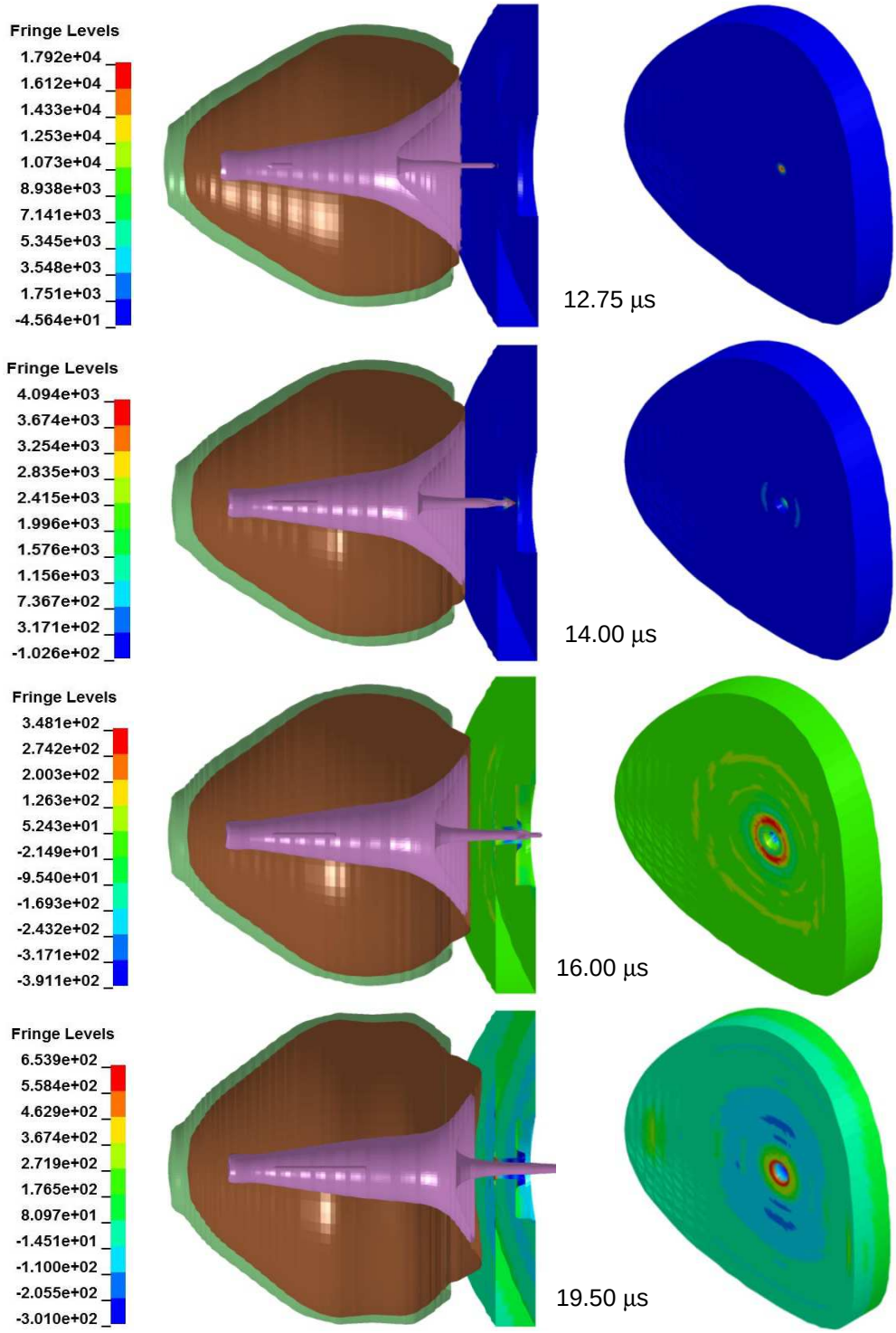

Figure 127. Pressure field [MPa] in the carrier at four different simulation times.

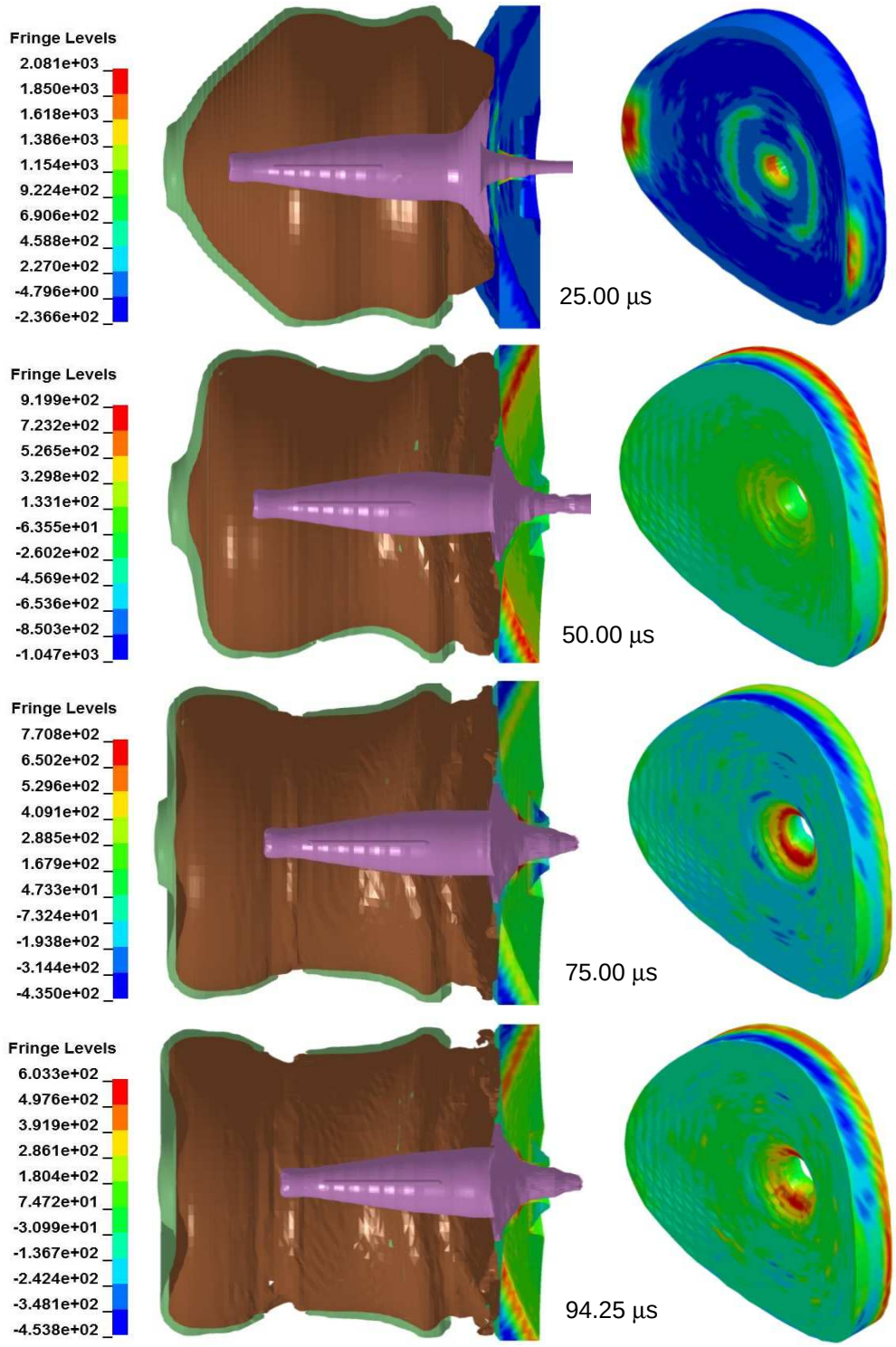

Figure 128. Pressure field [MPa] in the carrier at four different simulation times.

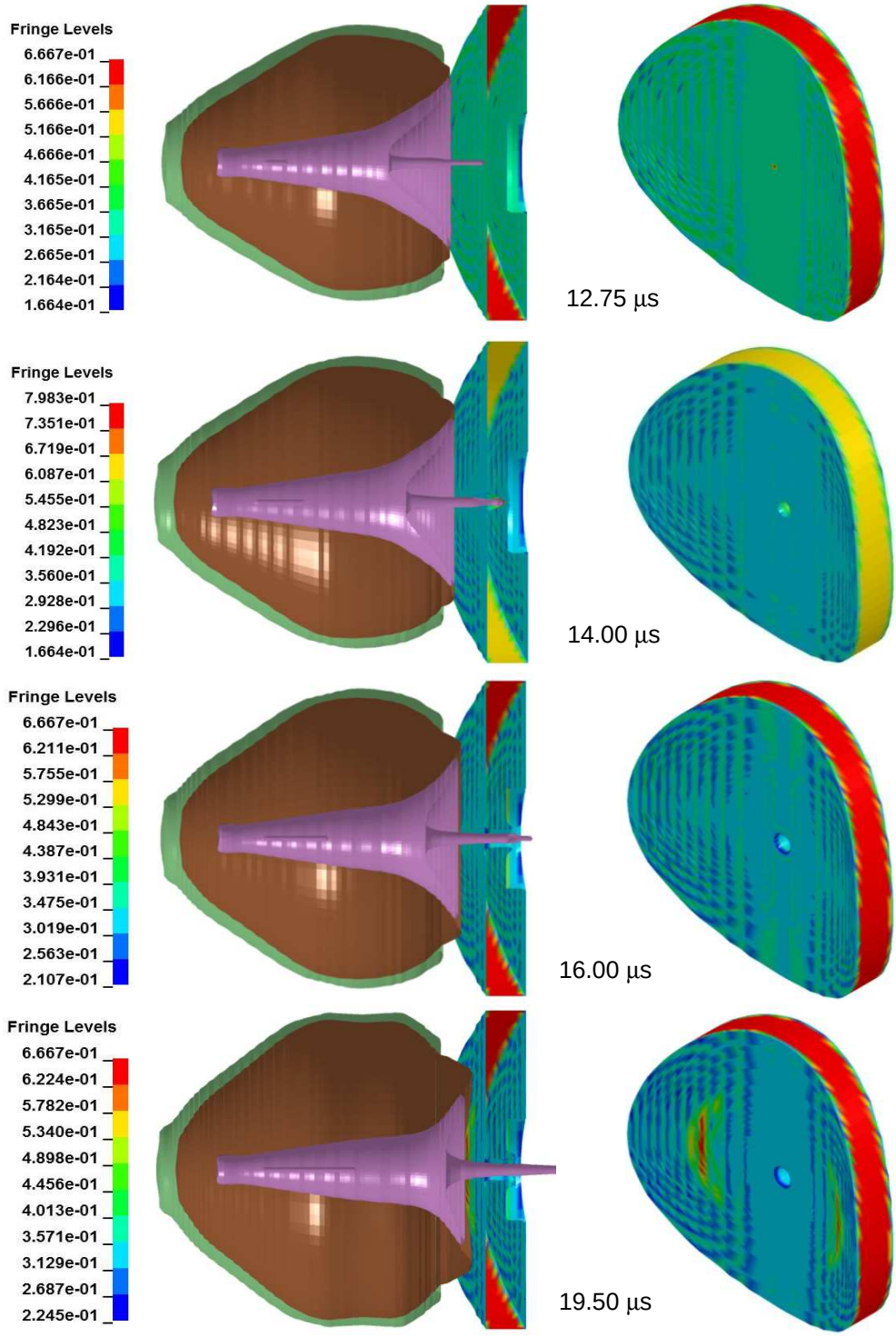

Figure 129. Equivalent plastic strain field in the carrier at four different simulation times.

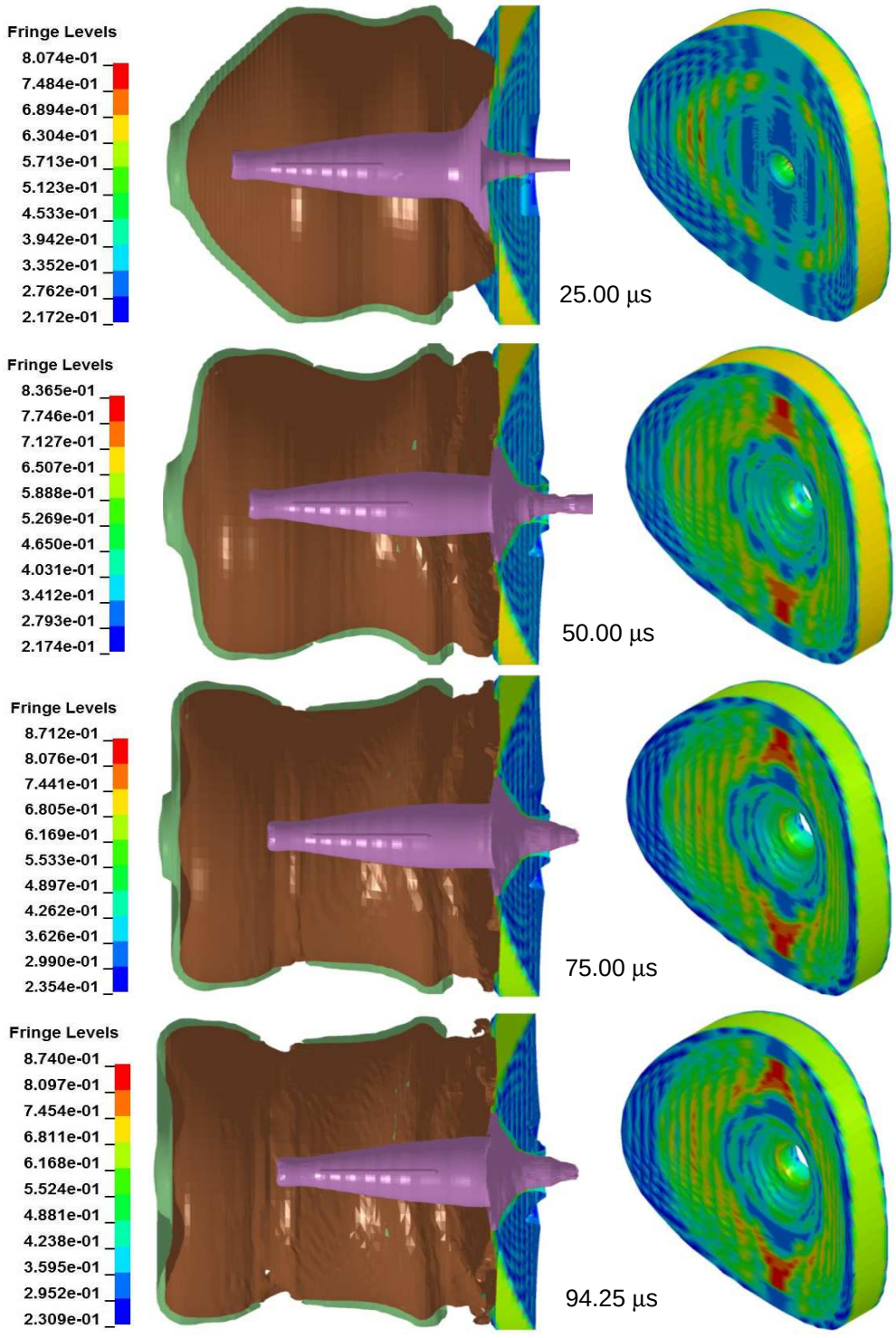

Figure 130. Equivalent plastic strain field in the carrier at four different simulation times.

In order to better assess the simulation results, the maximum and minimum values reached throughout the FEM analysis by the four considered variables are reported in following Table 44.

	MIN	MAX
Equivalent plastic strain rate [s^{-1}]	0	$2.865 \cdot 10^{6}$
Von Mises stress [MPa]	0	1379
Pressure [MPa]	-1082	17920
Equivalent plastic strain	0	0.874

Table 44
Maximum and minimum values for the four considered variables. It is recalled that in LS-DYNA positive pressures are intended as compressive and negative pressures as tensile.

Some considerations regarding the simulation results are made in the following, similarly to what previously done for the Lagrangian FEM results. Moreover, appropriate considerations about the comparison between the obtained Eulerian and Lagrangian outcomes are pointed-out.

Regarding the equivalent plastic strain rate, it is possible to see that, although very high values are involved, they are sensibly lower than those computed in the Lagrangian FEM simulations. The maximum equivalent plastic strain rate value reached through the Eulerian approach is about one order of magnitude lower than that computed with the Lagrangian approach, as readily noticeable by comparing the values reported in Tables 34 and 44. These very high equivalent plastic strain rate values are maintained throughout the piercing phase. Approximately, it may be said that this perforating phase happens at an equivalent plastic strain rate average value of about $1 \cdot 10^{6}$ s^{-1}, i.e. about an order of magnitude lower than what predicted by the Lagrangian FEM simulations. In this regard, it is also worthwhile to note that the impact between the liner and the carrier happens at a velocity of 4 km/s for the Lagrangian FEM simulations and at 5.524 km/s for the Eulerian FEM simulations. Nevertheless, the equivalent plastic strain rates in the Lagrangian FEM simulations are 1 order of magnitude higher. This aspect leads to the belief that the equivalent plastic strain rates computed in the Lagrangian FEM simulations may be strongly overestimated. This may be due to the fact that the Lagrangian FEM simulations considers the impact of a rigid liner, which actually does not correspond to the true physical phenomenon under analysis. Some references, such as Ambrosi and Briganti, 2010, stated that the liner may be coherently modeled as a rigid body, due to the huge velocity of the impact between the liner and the carrier. This approach considers that modeling the liner as a rigid body or as a deformable body should not comport sensible differences in the results computed on the carrier. On the basis of the results obtained here, such last consideration appears to be rather

untrue, at least for the evaluation of the equivalent plastic strain rates on the carrier. In view of this, it may be interesting to further investigate the role played by the deviatoric and volumetric resistances of the liner on the carrier overall response. In this regard, considerations about limit liner velocities at which its deviatoric resistance starts to play an important role are provided in Gooch et al., 2001.

As for the Lagrangian results, the highest equivalent plastic strain rate values are confined within a thin zone near the liner trajectory. Outside this zone, the equivalent plastic strain rate values appear to be sensibly lower, ranging from $2 \cdot 10^3$ s^{-1} to $2 \cdot 10^5$ s^{-1}, approximately. It is worthwhile to note that the lower value of this range is about twice the highest equivalent plastic strain rate value experimentally tested for the carrier steel, namely 1100 s^{-1}. After the perforation phase, the rear part of the liner and the detonation products begin to impact the carrier. Comparing to the effect of the tip of the liner, this second phase involves a much wider zone of the carrier. The resulting deformations occur at equivalent plastic strain rates ranging from $5 \cdot 10^3$ s^{-1} to $7 \cdot 10^4$ s^{-1}, approximately. As a matter of fact, very high equivalent plastic strain rates are involved in this second phase as well, although the values are quite lower comparing to those related to the first phase, namely when the front part of the liner pierces the carrier.

Temperature increments have been computed but they could not be plotted. However, it is known that temperature increments are computed only through Eq. (86). From the analysis of the obtained results, it can be said that the Eulerian equivalent plastic strain rates are approximately one order of magnitude lower than the Lagrangian ones. Assuming that the stress components computed in the Eulerian analysis do not strongly deviate from those calculated in the Lagrangian analysis, it can be said that the temperature increments involved in the Eulerian FEM analysis are about one order of magnitude lower than those involved in the Lagrangian FEM simulations. This assumption is due to the form of Eq. (86). Following these considerations, it can be said that the peak temperature increments involved in the Eulerian analysis may be around 1200 K, approximately, i.e. one order of magnitude lower than the peak temperature increments that arise in the Lagrangian FEM simulations. This aspect means that melting temperatures may never be reached during the Eulerian analysis. It is interesting to note how this point correlates particularly well with some experimental observations, reported in Yin et al., 2004, and Novokshanov and Ockendon, 2006, in which the presence of localized heating up to 1273 K was hypothesized. This assumption was related to the presence of some recrystallized austenite grains whose existence did imply the manifestation of such temperatures.

For what it concerns the von Mises stress, it is clear that the values here are heavily influenced by the equivalent plastic strain rates and by the temperatures, as ruled by the Johnson-Cook hardening function. The von Mises stress field appears

to present high values in a wider zone comparing to the very localized zone in which the higher equivalent plastic strain rates and temperatures are present. Comparing to the Lagrangian simulations, the von Mises stress field appears to present lower values but much more widespread throughout the carrier. This point is mainly due to the impact of the rear part of the liner and of the detonation products against the carrier.

Regarding the pressure, the highest compressive value reached on the carrier is equal to about 17.9 GPa. This value is much lower than the 263 GPa registered in the Lagrangian FEM simulations, and it is quite coherent with the expected results, i.e. a value at around 20 GPa. It is recalled that the pressure values have an important role also because they act directly in the computation of the Johnson-Cook damage, through the term in which the stress triaxiality is involved. As previously stated, the Mie-Grüneisen equation of state provides good modeling coherency up to compressive pressures of a few GPa. The values involved in this analysis are widely inside this range. As for the Lagrangian simulations, the highest compressive pressure values are reached in the first microseconds after the first liner impact with the carrier. After that, the compressive pressure appears to relax down to lower values. Similarly to what happens for the equivalent plastic strain rates, the highest compressive pressure values are confined in a tiny zone near the liner trajectory. Outside this zone, the compressive pressure values appear to lie between 0.1 GPa and 1 GPa, which are values one order of magnitude lower than those computed in the Lagrangian simulations, approximately. Regarding the tensile pressure, the highest value turns-out equal to about 1 GPa. This value is strongly lower than those reached in the Lagrangian simulations, which reach the imposed spall limit of 13 GPa. Thus, the Eulerian FEM simulations do not predict spall in the carrier.

Regarding the equivalent plastic strain, the piercing effect of the front part of the liner causes very localized effects, as predicted by the Lagrangian simulations. However, marked differences occur in the next phase, in which the rear part of the liner and the detonation products impact the carrier. Indeed, these two stressing factors determine a much severe and widespread deformation of the carrier, comparing to the very localized Lagrangian FEM results. First of all, the inner part of the carrier is heavily flared by the rear part of the liner. Second, the detonation products contribute to radially deform the carrier, resulting in a localized bulge. Furthermore, the Eulerian FEM maximum equivalent plastic strain is equal to about 0.854, while the Lagrangian FEM maximum is equal to 4.573. This aspect is due to the fact that the Lagrangian equivalent plastic strain are much more localized but also much higher, due to very severe deformations in some finite elements.

The Johnson-Cook damage variable has been computed but it is also not available for plotting. However, it can be said that results very similar to those of the

equivalent plastic strain are expected, due to the form of the Johnson-Cook damage and failure model, Eq. (69), as confirmed by the Lagrangian FEM simulations. The results obtained for the equivalent plastic strain are then considered to be very indicative of the values of the Johnson-Cook damage variable as well. It is also worthwhile to note that high positive stress triaxialities are no longer involved. Indeed, the maximum value is equal to about 1.3, thus not exceeding the limit value for the validity of the Johnson-Cook damage and failure model, i.e. 1.5. The positive stress triaxialities values are around one order of magnitude lower than those involved in the Lagrangian simulations. This aspect is mainly due to the fact that Eulerian tensile pressures are about one order of magnitude lower than those computed by the Lagrangian simulations.

Following Figs. 131 and 132 show the final equivalent plastic strain fields in the carrier for the Lagrangian and for the Eulerian simulations, in order to compare the deformations suffered by such component in the two cases.

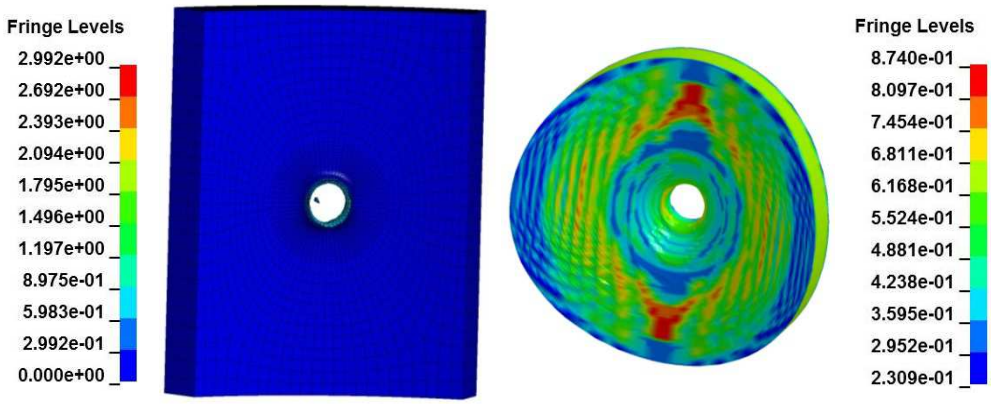

Figure 131. Lagrangian (left figure) and Eulerian (right figure) equivalent plastic strain fields in the carrier at the final instant of the simulations. The inner side is shown.

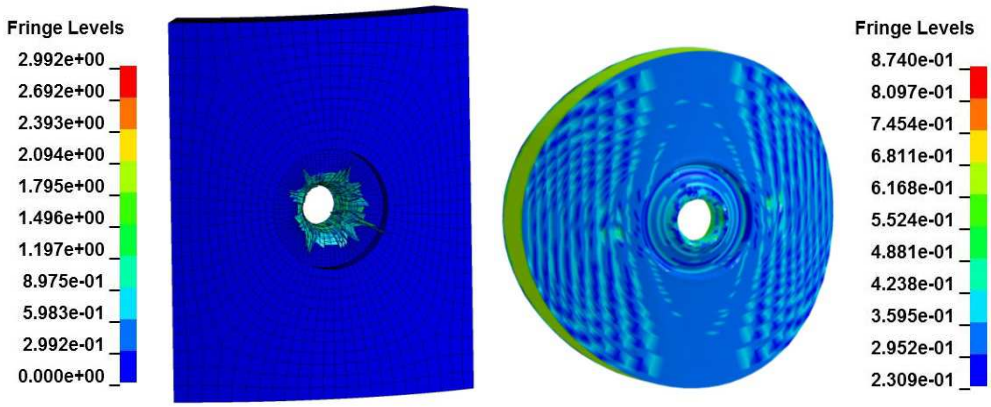

Figure 132. Lagrangian (left figure) and Eulerian (right figure) equivalent plastic strain fields in the carrier at the final instant of the simulations. The outer side is shown.

In general, it can be said that the piercing effect of the front part of the liner influences a very thin zone of the carrier, resulting in a very localized effect that takes place in a narrow band in the scallop zone, as previously stated for the Lagrangian FEM simulations. However, the Eulerian FEM simulations show that the rear part of the liner does play a role in stressing the carrier. The rear side of the liner impacts the carrier at lower velocities comparing to the tip, i.e. velocities in the range between 0.5 km/s and 1 km/s. As already discussed, the rear part of the liner causes the inner side of the exit hole to become heavily flared, and contributes also at stressing the carrier in the radial direction, resulting in a localized bulge. This last aspect is further strengthened by the subsequent action of the detonation products, which pushes radially on the carrier.

On the basis of the pointed-out considerations, it can be said that the carried-out Eulerian FEM simulations allow for investigating the firing of a perforating gun with much more coherency comparing to the Lagrangian FEM simulations. This last assumption is motivated by the good coherency of some of the obtained Eulerian FEM results to recorded experimental observations, such as the liner velocity, the compressive pressure that the liner produces on the carrier, the estimated temperatures and of course the final configuration of the carrier, which shows the produced exit hole and the localized bulge.

CONCLUSIONS

Some conclusive remarks are outlined in the following. Conclusions are presented by considering the three main parts treated in this work, i.e. the review of the constitutive modeling of large strain and high strain rate phenomena, the introduction of a new strength model and the analysis of a specific perforating gun device of industrial interest.

The first part of the thesis presented a brief review of the constitutive modeling of large strain and high strain rate phenomena, by introducing some basic considerations on strength models, equations of state and damage and failure models. Models extensively used in subsequent parts of the work have been investigated with specific attention. In particular, a detailed review of the Johnson-Cook strength model has been made. The specific interest on this model is due to its popularity and wide use in computational codes, together with the fact that it has been later used for the modeling of the industrial application analyzed in the present thesis.

An extensive, mainly original discussion of various calibration strategies of the Johnson-Cook model has been presented. Related issues and problematics have been investigated. Through a reasoned approach, five main calibration strategies have been identified, proposed and debated. These approaches have been then applied to a real material case, i.e. the determination of the Johnson-Cook parameters for a structural steel, based on experimental data from the literature. The obtained results have allowed to assess the strengths and weaknesses of the various calibration strategies, by directly evaluating the obtainable fittings of the considered experimental data. The outcomes of the Johnson-Cook model calibrated with the different strategies have been widely commented, by pointing-out the most important aspects and consequences of each calibration approach. It has been shown how choosing the different calibration strategies leads to quite different results, intended in terms of the produced errors relative to experimental data fittings. More in detail, average percentage yield stress root mean square errors spanning from 16.86% to 34.85% have been obtained.

The importance of the procedure adopted for calibrating the parameters of the Johnson-Cook model has been highlighted, by addressing how it may influence the aim of setting-up a strength model capable to reproduce a good coherency throughout the equivalent plastic strain, equivalent plastic strain rate and temperature ranges of interest. Due to its nature, the Johnson-Cook model comes with positive aspects, such as simplicity and readiness of implementation in FEM codes, but also weaknesses, i.e. incoherencies introduced into the modeling. The

choice of the calibration strategy allows to redistribute the errors according to different criteria, as extensively explained in this work. Such choice should be done by considering all the aspects exposed and explained, thus being aware of the nature and consequences of each selected calibration strategy.

The proposed considerations should provide a guideline in the process of determining the best Johnson-Cook parameters based on available experimental data, i.e. a set of hardening functions at different equivalent plastic strain rates and temperatures, depending on the quested target of the considered use of the model.

The second part of the work has regarded the introduction of a new strength model, named Split Johnson-Cook model, since it has been formulated as a generalization of the original Johnson-Cook model. Since the new model is a refinement of the Johnson-Cook model, it keeps a total empiric nature. The aims were those of improving the original Johnson-Cook hardening function, in order to mitigate shortcomings such as the fact that the equivalent plastic strain, the equivalent plastic strain rate and the temperature effects on the yield stress are totally independent from each other. More in detail, the Split Johnson-Cook model allows to separately model the dependence of the lower yield stress and of the plastic flow on the equivalent plastic strain rate and on the temperature. Furthermore, the Split Johnson-Cook model has been conceived in such a way capable of maintaining the same computational appeal of the original Johnson-Cook model. Indeed, it operates by requiring only the knowledge of the equivalent plastic strain, the equivalent plastic strain rate and the temperature, thus allowing to perfectly fit in the same computational framework of the original Johnson-Cook model.

The features of the new model have been widely discussed, together with a comprehensive discussion on its calibration strategies. Through a reasoned approach, three different calibration approaches have been presented. The new model has been also applied to the same real material case and results have been compared to those obtained through the original Johnson-Cook model. The replacement of the original Johnson-Cook model with the new model appears to almost exclusively introduce positive consequences. Negative implications, if any, appear to be very limited. Even though the model requires four extra parameters, the need of experimental data, the heaviness of calibration and the computational weight remain almost unchanged, comparing to the original Johnson-Cook model. Of course, the proposed model should be considered only when totally empiric approaches are under consideration. If the necessity to adopt more physically-based models becomes important, other strength models which specifically address this aspect should be taken into consideration. As a future development, the new model may be implemented in FEM codes. Structural results may then be compared to those provided by the original Johnson-Cook model, in particular by

considering some benchmark reference cases. For instance, the model may be implemented in the FEM code LS-DYNA, in order to allow for using the Split Johnson-Cook model in the perforating gun simulations carried-out in the present work and then achieve a possible refinement of the outcomes in quantitative terms.

The third and last part treated in the present work aimed at analyzing a perforating gun device proposed by the industrial partner that has co-sponsored the present research project. The main target was that of assessing the resistance of the carrier component, in particular when subjected to different stressing factors produced by the firing of the device.

First of all, perforating gun devices have been briefly described. Particular attention has been paid to the analysis of shaped charge explosions and the description of the resulting hyperfast liners, together with the main features and problematics related to the carrier. Afterwards, Lagrangian and Eulerian FEM simulations have been carried-out, by considering the firing of a specific perforating gun device. The main target of this investigation was that of assessing the performance of the carrier. For what it concerns the Lagrangian FEM simulations, single scallop and three scallop simulations have been carried-out. Eulerian FEM analyses have been carried-out for the single scallop configuration only, accordingly to the available computational capacities. The coherency of the obtained results has been assessed by considering the few available experimental data, specifically in terms of liner velocity, peak pressure at the first impact between the travelling liner and the carrier, and peak temperatures. Based on these findings, it is possible to state that the outcomes of the Eulerian FEM simulations appear to be much more reliable than those of the Lagrangian FEM simulations.

In particular, the present Lagrangian FEM simulations appear to greatly overestimate many key variables, such as the equivalent plastic strain rate, the temperature and the pressure. The obtained values are about one order of magnitude higher than the expected values. As previously stated, this aspect is believed to be strictly related to the strong simplifying hypotheses made for carrying-out the present Lagrangian FEM simulations, in particular for the taken assumption of a rigid liner. These aspects imply that the present Lagrangian FEM simulations may not actually model the true physical phenomenon under examination. All the listed negative aspects lead to the belief that the Lagrangian FEM results, in the present form, are not very reliable. Anyway, it is worthwhile to note that the carried-out Lagrangian FEM simulations appear to determine a considerable improvement comparing to those already presented in Ambrosi and Briganti, 2010, i.e. in the previous investigation on the carrier resistance conducted by the industrial partner. In particular, such improvements consist in the replacement of a linear equation of state with a Mie-Grüneisen EOS, in having tripled the number of finite elements on the carrier thickness, in a better

determination of the Johnson-Cook damage and failure parameters, and in all consequent outcomes.

Concerning the Eulerian FEM simulations, the obtained results appear to be much coherent, due to the good correlation of the outcomes with the few experimental values available and mentioned above. Furthermore, the final carrier deformed configuration appears to be quite coherent with the expected results. However, it is important to recall that both the carried-out Lagrangian and Eulerian FEM simulations are heavily influenced by lack of data, both geometrical and material. In particular, the lack of material data is quite evident. For the carrier, the Johnson-Cook hardening function has been calibrated with only two experimental observations in the equivalent plastic strain rate range, with a maximum value of 1100 s^{-1}, that is about three orders of magnitude lower than the peak values registered a posteriori in the Eulerian FEM simulations. Furthermore, no data have been provided for the calibration of the temperature term of the Johnson-Cook hardening function. Regarding the damage of the carrier, no data have been made available, resulting in the necessity to totally rely on literature values. Analogously, the Mie-Grüneisen EOS parameters for the carrier have not been calibrated and come from the literature, as for the spall strength limit. Similar considerations hold for the material parameters of the other components, i.e. the case, the explosive, the liner, the casing, the concrete coating and the soil. All these uncertainties shall exclude the possibility to consider the obtained Eulerian FEM results as truly quantitative. However, they shall be considered very valuable and probably innovative in qualitative terms. As a matter of fact, the present Eulerian FEM simulations appear to set as cutting-edge in the field of computational simulations of perforating gun devices. In particular, these simulations appear to be innovative for the fact of considering truly full tridimensional analyses. This aspect allows for future investigations regarding the simultaneous explosion and interaction of additional shaped charges, e.g. three shaped charges. Moreover, it may be said that the obtained Eulerian FEM results already allow to outline some interesting considerations on the operating phase and on the design of the considered perforating gun. For instance, by considering the fact that the analyzed carrier has resisted the firing process quite well, it may be proposed to diminish the thickness of the scallops, in order to achieve a higher liner velocity after having pierced the carrier. Other design tips may come by considering the strong flaring effect of the rear part of the liner on the inner side of the carrier. For instance, the inner part of the carrier may be somehow reinforced in the nearby of each scallop.

In order to further improve the coherency of the obtainable results, the first point to follow would be that of carrying-out further experimental tests on the considered materials, with specific attention to the carrier steel, considering that investigating the structural response of such component is set as a primary aim. In particular,

carrier plastic flow temperature behavior should be investigated. The use of other strength models may be considered as well. On the basis of the very high equivalent plastic strain rates involved, the adoption of the Steinberg-Cochran-Guinan or the Steinberg-Lund models may be attempted. In the case of enlarging the database of available experimental data, another interesting option would be that of improving the coherence of the simulations by replacing the Johnson-Cook hardening function with the enhanced Split Johnson-Cook model proposed in Chapter 3, after having implemented it into a FEM code.

Similarly to what stated for the carrier steel strength model, the Johnson-Cook damage and failure model needs to be calibrated in its five material parameters. Furthermore, a more coherent spall model may be introduced, even though the Eulerian FEM simulations do not appear to reveal the presence of very high tensile pressures in the carrier. However, the implementation of the Cochran-Banner spall model may be interesting to be pursued, together with an experimental investigation of the spall resistance of the steel carrier. Some other investigations may concern the use of equations of state different from the Mie-Grüneisen. As instance, the Tillotson EOS may be taken into consideration. In this regard, Lee, 2002, provided two dimensional Eulerian FEM simulations of a perforating gun by adopting a Tillotson equation of state for modeling the volumetric behavior of an oil shale, while the Mie-Grüneisen EOS was maintained for modeling the other components of the perforating gun device.

Beyond the carrier, the material parameters of all the other components should be better evaluated as well. Furthermore, the FEM simulations should rely on more specific geometrical parameters, with particular reference to those of the shaped charge and to the standoff distance. Another interesting point may be that of introducing in the simulations the support and detonation systems of the shaped charge. FEM simulations that considered also the shaped charge support are exposed in Grove et al., 2006.

The listed improvements should allow to obtain more quantitative results, which in turn shall permit to proceed with an optimization of some parameters of the perforating gun device. As instance, a strategy may be that of optimizing the carrier resistance, e.g. in terms of minimizing the bulging, together with an optimization of the penetration capacity, which may be assessed in terms of the length of perforated soil or of the liner velocity after having pierced the carrier. Another important point is that of maximizing the efficiency of the upcoming hydrocarbons flow toward the surface, which may be related to, e.g., the fact of having a larger hole in the casing and in the concrete coating, as suggested in Lee, 2002.

The variables on which act in order to achieve such optimization may be the geometrical parameters of the scallops, the material parameters of the carrier steel, the standoff distance, the shaped charge deployment strategy, the liner material

and many others. As instance, Han and Ference, 2010, provided interesting considerations regarding the effect of the shaped charge case material on the detonation of the main explosives and the resulting liners. Steel and zinc cases were considered, showing sensible differences in the pressures and temperatures due to the explosion. Another example of a reference in which some specific perforating gun parameters are investigated is provided in Jin et al., 2011, which presented a study on the effect of the liner cone angle on the produced liner, and therefore on the impact between the liner and the carrier. Furthermore, Lee, 2002, presented a study on the effect of adopting different external shaped charges diameters on the produced liners.

Of course, the optimization should also consider other technical parameters, such as the soil and rock properties, the difference of pressure between the reservoir and the well, the capacity to remove after detonation debris and so on. In this regard, some considerations may be found in Tariq, 1987, Behrmann and Elbel, 1991, Behrmann and Nolte, 1998, Baxter et al., 2009, and Burman et al., 2011, with particular reference to the analysis of the phenomenon of fracturing the carrier and the subsequent targets.

Beyond the FEM simulations obtained in this work, further investigations may be conducted as well. First of all, Eulerian simulations of a configuration with three shaped charges may be carried-out. The results should allow to evaluate the third stressing effect on the carrier, i.e. possible impacts with fragments or parts of the exploded shaped charges and their support and detonation systems. Furthermore, Eulerian three scallop simulations should allow to assess the possibility of synergic interactions of the stressing factors acting on the carrier, with particular reference to the actions of the explosives and the rear parts of the impacting liners. The possibility of the arising of splits and cracking may be assessed. It may also be interesting to further investigate the opportunity to carry-out simulations with the SPH method, that has been inquired only marginally in the present research project. This method may present problems related to the modeling of the detonation of the main explosive, but, on the other side, it may allow to carry-out more elaborated simulations. See, e.g., Swift et al., 1998, for an analysis carried-out with the SPH method.

Further investigations may also be conducted with the aim to evaluate the firing of the perforating gun in another ambient fluid. In particular, the air outside the carrier may be replaced by water, possibly at high pressures, in order to investigate underwater explosions of the device at various depths, i.e. at various water pressure.

As final conclusion, the results obtained and presented in this work are believed to satisfy both the academic and industrial sides involved in the present research program. The new proposed strength model may actually be considered as an

original scientific proposal. It appears capable in principle to improve the coherency of the original Johnson-Cook model and therefore it provides a theoretical and computational tool potentially useful in many practical situations. Furthermore, the obtained perforating gun FEM simulations appear to set as cutting-edge in the specific modeling field. They actually seem to be capable of providing detailed information on the process of industrial interest, i.e. the firing of a perforating gun device. Beyond all the possible future improvements, the FEM simulation results presented and discussed in this work appear to be useful for establishing some relevant considerations towards the design of the specific analyzed perforating gun device, although the investigations are still in an unfinished stage. In particular, important points regarding the structural resistance of the carrier have been clarified, i.e. the main target of the campaign of FEM simulations conducted and exposed in the present work. The obtained outcomes allow to point-out several considerations immediately usable in the optimization process of the device components. Indeed, this information is believed to be potentially helpful for the design and optimization processes of the analyzed industrial device.

BIBLIOGRAPHY

[1] Abu Al-Rub, R.K., Voyiadjis, G.Z., (2006), *A finite strain plastic-damage model for high velocity impact using combined viscosity and gradient localization limiters: Part I – Theoretical formulation*, International Journal of Damage Mechanics, 15(4), p. 293-334, SAGE Publications Ltd.

[2] Achenbach, J.D., (1973), *Wave Propagation in Elastic Solids, First Edition*, ISBN 9780720403251, monograph in the *North-Holland Series in Applied Mathematics and Mechanics*, Elsevier B.V.

[3] Al-Hassani, S.T.S., Chen, D., Sarumi, M.A., (1997), *A simple non-local spallation failure model*, International Journal of Impact Engineering, 19(5-6), p. 493-501, Elsevier B.V.

[4] Allen, D.J., Rule, W.K., Jones, S.E., (1997), *Optimizing material strength constants numerically extracted from Taylor impact data*, Experimental Mechanics, 37(3), p. 333-338, Springer Science+Business Media.

[5] Ambrosi, S., Briganti, D., (2010), *Modellazione e Simulazione di Dispositivi per la Perforazione di Pozzi Petroliferi*, Master Thesis, Advisors Corigliano, A., Mariani, S., Politecnico di Milano, Italy.

[6] Antoun, T., Curran, D.R., Razorenov, S.V., Seaman, L.K, Gennady, I., Utkin, A.V., (2003), *Spall Fracture, First Edition*, ISBN 0-387-95500-3, monograph in the series *Shock Wave and High Pressure Phenomena*, originally published as *High-Pressure Shock Compression of Condensed Matter*, Springer Science+Business Media.

[7] Aquelet, N., Souli, M., (2008), *2D to 3D ALE mapping*, Proceedings of the 10th International LS-DYNA Users Conference, June 8-10, 2008, Dearborn, Michigan, USA, Editor Mindle, W.L, published by Livermore Software Technology Corporation and DYNAmore GmbH at http://www.dynalook.com/.

[8] Asaro, R.J., Lubarda, V.A., (2006), *Mechanics of Solids and Materials, First Edition*, ISBN 0-511-14707-4, Cambridge University Press.

[9] Asay, J.R., Shahinpoor, M., (1993), *High-Pressure Shock Compression of Solids, First Edition*, Editors, ISBN 0-387-97964-6, anthological monograph in the series *Shock Wave and High Pressure Phenomena*, originally published as *High-Pressure Shock Compression of Condensed Matter*, Springer Science+Business Media.

[10] Bao, Y., Wierzbicki, T., (2004), *On fracture locus in the equivalent strain and stress triaxiality space*, International Journal of Mechanical Sciences, 46(1), p. 81-98, Elsevier B.V.

[11] Bao, Y., Wierzbicki, T., (2005), *On the cut-off value of negative triaxiality for fracture*, Engineering Fracture Mechanics, 72(7), p. 1049-1069, Elsevier B.V.

[12] Baudin, G., Serradeill, R., (2010), *Review of Jones-Wilkins-Lee Equation of state*, Proceedings of the Conference on New Models and Hydrocodes for Shock Wave Processes in Condensed Matter, May 24-28, 2010, Paris, Île-de-France, Editor Soulard, L., published by EPJ Web of Conferences at http://www.epjconferences.org.

[13] Baxter, D., Behrmann, L.A., Grove, B., Williams, H., Heiland, J., Hong, L.J., Khong, C.K., Martin, A., Mishra, V.K., Munro, J., Pizzolante, I., Safiin, N., Suppiah, R.R., (2009), *Perforating-When failure is the objective*, Oilfield Review, 21(3), p. 4-17, Schlumberger Ltd.

[14] Baytos, J.F., (1979), *Specific Heat and Thermal Conductivity of Explosives, Mixtures, and Plastic-Bonded Explosives Determined Experimentally*, Report LA-8034-MS, Los Alamos Scientific Laboratory, Los Alamos, New Mexico, USA.

[15] Behrmann, L.A., Elbel, J.L., (1991), *Effect of perforation on fracture initiation*, Journal of Petroleum Technology, 43(5), p. 608-615, Society of Petroleum Engineers (SPE).

[16] Behrmann, L.A., Nolte, K.G., (1998), *Perforating requirements for fracture simulations*, SPE Drilling and Completion, 14(4), p. 228-234, formerly known as SPE Drilling Engineering, Society of Petroleum Engineers (SPE).

[17] Belytschko, T., Liu, W.K., Moran, B., (2000), *Nonlinear Finite Elements for Continua and Structures, First Edition*, ISBN 0-471-98773-5, John Wiley & Sons Inc.

[18] Ben-Dor, G., (2007), *Shock Wave Reflection Phenomena, Second Edition*, ISBN 978-3-540-71381-4, monograph in the series *Shock Wave and High Pressure Phenomena*, originally published as *High-Pressure Shock Compression of Condensed Matter*, Springer Science+Business Media.

[19] Benson, D.J., (1991), *Computational methods in Lagrangian and Eulerian hydrocodes*, Computer Methods in Applied Mechanics and Engineering, 99(2-3), p. 235-394, Elsevier B.V.

[20] Benson, D.J., (1995), *A multi-material Eulerian formulation for the efficient solution of impact and penetration problems*, Computational Mechanics, 15(6), p. 558-571, Springer Science+Business Media.

[21] Benson, D.J., (1996), *A mixture theory for contact in multi-material Eulerian formulations*, Computer Methods in Applied Mechanics and Engineering, 140(1-2), p. 59-86, Elsevier B.V.

[22] Benson, D.J., (2000), *Raven: A Two-Dimensional, Multi-Material Eulerian Hydrocode with Heat Transfer*, Raven code manual, University of California at San Diego, La Jolla, California, USA.

[23] Benson, D.J., Nesterenko, V.F., Jónsdóttir, F., Meyers, M.A., (1997), *Quasi-static and dynamic regimes of granular material deformation under impulse loading*, Journal of the Mechanics and Physics of Solids, 45(11-12), p. 1955-1999, Elsevier B.V.

[24] Benson, D.J., Okazawa, S., (2004), *Contact in a multi-material Eulerian finite element formulation*, Computer Methods in Applied Mechanics and Engineering, 193(39-41, Special Issue), p. 4277-4298, Elsevier B.V.

[25] Benson, D.J., Stainier, L., (2000), *An Eulerian shell formulation for fluid-structure interaction*, Computer Methods in Applied Mechanics and Engineering, 187(3-4), p. 571-590, Elsevier B.V.

[26] Bigoni, D., (2012), *Nonlinear Solid Mechanics. Bifurcation Theory and Material Instability, First Edition*, ISBN 987-1-107-02541-7, Cambridge University Press.

[27] Bigoni, D., Hueckel, T., (1991), *Uniqueness and localization-I. Associative and non-associative elastoplasticity*, International Journal of Solids and Structures, 28(2), p. 197-213, Elsevier B.V.

[28] Bigoni, D., Hueckel, T., (1991), *Uniqueness and localization-II. Coupled elastoplasticity*, International Journal of Solids and Structures, 28(2), p. 215-224, Elsevier B.V.

[29] Bigoni, D., Zaccaria, D., (1993), *On strain localization analysis of elastoplastic materials at finite strains*, International Journal of Plasticity, 9(1), p. 21-33, Elsevier B.V.

[30] Birkhoff, G., MacDougall, D.P., Pugh, E.M., Taylor, G., (1948), *Explosives with lined cavities*, Journal of Applied Physics, 19(6), p. 563-582, American Institute of Physics Inc.

[31] Bojanowski, C., Kulak, R.F., (2010), *Comparison of Lagrangian, SPH and MM-ALE approaches for modeling large deformations in soil*, Proceedings of the 11th International LS-DYNA Users Conference, June 6-8, 2010, Dearborn, Michigan, USA, Editor Mindle, W.L, published by Livermore Software Technology Corporation and DYNAmore GmbH at http://www.dynalook.com/.

[32] Bonora, N., Ruggiero, A., Iannitti, G., (2010), *Caratterizzazione Meccanica in Regime di Deformazione Dinamico di Acciai per la Costruzione di Perforating Gun*, Report, TenarisDalmine, Dalmine, Italy.

[33] Børvik, T., Hopperstad, O.S., Berstad, T., (2003), *On the influence of stress triaxiality and strain rate on the behaviour of a structural steel. Part II. Numerical study*, European Journal of Mechanics, A/Solids, 22(1), p. 15-32, Elsevier B.V.

[34] Burman, J., Schoener-Scott, M., Le, C., Suire, D., (2011), *Designing completions after predicting wellbore dynamic-shock loads during perforating*, Proceedings of the Society of Petroleum Engineers (SPE) 2011 Brasil Offshore Conference, June 14-17, 2011, Macaé, Rio de Janeiro, Brazil, ISBN 9781618390189, Vol. 2, p. 845-858, published by Curran Associates, Inc.

[35] Burman, J., Schoener-Scott, M., Le, C., Suire, D., (2011), *Predicting wellbore dynamic-shock loads prior to perforating*, Proceedings of the Society of Petroleum Engineers (SPE) 2011 Digital Energy Conference & Exhibition, April 19-21, 2011, The Woodlands, Texas, USA, ISBN 9781617827419, p. 366-378, published by Curran Associates, Inc.

[36] Camacho, G.T., Ortiz, M., (1997), *Adaptive Lagrangian modelling of ballistic penetration of metallic targets*, Computer Methods in Applied Mechanics and Engineering, 142(3-4), p. 269-301, Elsevier B.V.

[37] Carol, I., Rizzi, E., Willam, K.J., (1994), *A unified theory of elastic degradation and damage based on a loading surface*, International Journal of Solids and Structures, 31(20), p. 2835-2865, Elsevier B.V.

[38] Carol, I., Rizzi, E., Willam, K.J., (2001), *On the formulation of anisotropic elastic degradation. I. Theory based on a pseudo-logarithmic damage tensor rate*, International Journal of Solids and Structures, 38(4), p. 491-518, Elsevier B.V.

[39] Carol, I., Rizzi, E., Willam, K.J., (2001), *On the formulation of anisotropic elastic degradation. II. Generalized pseudo-Rankine model for tensile damage*, International Journal of Solids and Structures, 38(4), p. 519-546, Elsevier B.V.

[40] Carol, I., Rizzi, E., Willam, K.J., (2002), *An 'extended' volumetric/deviatoric formulation of anisotropic damage based on a pseudo-log rate*, European Journal of Mechanics A/Solids, 21(5), p. 747-772, Elsevier B.V.

[41] Casadei, F., Halleux, J.P., (1995), *An algorithm for permanent fluid-structure interaction in explicit transient dynamics*, Computer Methods in Applied Mechanics and Engineering, 128(3-4), p. 231-289, Elsevier B.V.

[42] Casadei, F., Halleux, J.P., Sala, A., Chillè, F., (2001), *Transient fluid-structure interaction algorithms for large industrial applications*, Computer Methods in Applied Mechanics and Engineering, 190(24-25), p. 3081-3110, Elsevier B.V.

[43] Chapman, D.L., (1899), *On the rate of explosion in gases*, The London, Edinburgh, and Dublin Philosophical Magazine and Journal of Science, Volume XLVII, Number CCLXXXIV, p. 90-104, Taylor and Francis Group.

[44] Chen, D., Yu, Y., Yin, Z., Wang, H., Liu, G., Xie, S., (2005), *A modified Cochran-Banner spall model*, International Journal of Impact Engineering, 31(9), p. 1106-1116, Elsevier B.V.

[45] Chéret, R., (1999), *Chapman-Jouguet hypothesis 1899-1999: one century between myth and reality*, Shock Waves, 9(5), p. 295-299, Springer Science+Business Media.

[46] Clayton, J.D., (2003), *Modeling dynamic plasticity and spall fracture in high density polycrystalline alloys*, International Journal of Solids and Structures, 42(16-17), p. 4613-4640, Elsevier B.V.

[47] Cochran, S.G., Banner, D.L., (1977), *Spall studies in uranium*, Journal of Applied Physics, 48(7), p. 2729-2737, American Institute of Physics Inc.

[48] Coleburn, N.L., (1964), *Chapman-Jouguet Pressures of Several Pure and Mixed Explosives*, Report NOLTR 64-58, The Naval Ordnance Laboratory, White Oak, Maryland, USA.

[49] Coleman, T.F., Li, Y., (1994), *On the convergence of interior-reflective Newton methods for nonlinear minimization subjected to bounds*, Mathematical Programming, 67(1-3), p. 189-224, Springer Science+Business Media.

[50] Cooper, P.W., (1996), *Explosives Engineering, First Edition*, ISBN 0-471-18636-8, Wiley-VCH.

[51] Cortes, R., Elices, M., (1995), *Numerical modelling of ductile spall fracture*, International Journal of Impact Engineering, 16(2), p. 237-251, Elsevier B.V.

[52] Couque, H.R., Boulanger, R., Bornet, F., (1995), *A modified Johnson-Cook Model for strain rates ranging from 10^{-3} to 10^{5} s^{-1}*, Journal De Physique IV, 134, p. 87-93, EDP Sciences.

[53] Davison, L., (2008), *Fundamentals of Shock Wave Propagation in Solids, First Edition*, ISBN 978-3-540-74569-3, monograph in the series *Shock Wave and High Pressure Phenomena*, originally published as *High-Pressure Shock Compression of Condensed Matter*, Springer Science+Business Media.

[54] Davison, L., Grady, D.E., Shahinpoor, M., (1996), *High-Pressure Shock Compression of Solids II. Dynamic Fracture and Fragmentation, First Edition*, Editors, ISBN 0-387-94402-8 anthological monograph in the series *Shock Wave and High Pressure Phenomena*, originally published as *High-Pressure Shock Compression of Condensed Matter*, Springer Science+Business Media.

[55] Day, J., (2009), *Guidelines for ALE Modeling in LS-DYNA*, Report, Livermore Software Technology Corporation, Livermore, California, USA.

[56] De Souza Neto, E.A., Perić, D., Owen, D.R.J, (2008), *Computational Methods for Plasticity. Theory and Applications, First Edition*, ISBN 987-0-470-69452-7, John Wiley & Sons Inc.

[57] Duc-Toan, N., Tien-Long, B., Dong-Won, J., Seung-Han, Y., Young-Suk, K., (2012), *A modified Johnson-Cook Model to predict stress-strain curves of boron steel sheets at elevated and cooling temperatures*, High Temperature Materials and Processes, 31(1), p. 37-45, Begell House Inc.

[58] Eather, R.F., Griffiths, N., (1984), *Some Historical Aspects of the Development of Shaped Charges*, Report 2/84, Ministry of Defence, Royal Armament Research and Development Establishment, 2/84, London, Great Britain.

[59] Ehrart, T., (2011), *An overview of user-defined interfaces in LS-DYNA*, Proceedings of the 8th European LS-DYNA Users Conference, May 23-24, 2011, Strasbourg, Alsace, France, published by Livermore Software Technology Corporation and DYNAmore GmbH at http://www.dynalook.com/.

[60] Fickett, W., Davis, W.C., (2000), *Detonation. Theory and Experiment, Second Edition*, ISBN 0-486-41456-6, Dover Publications Inc.

[61] Field, J.E., Walley, S.M., Proud, W.G., Goldrein, H.T., Siviour, C.R., (2004), *Review of experimental techniques for high rate deformation and shock studies*, International Journal of Impact Engineering, 30(7), p. 725-775, Elsevier B.V.

[62] Fish, J., Belytschko, T., (2007), *A First Course in Finite Elements, First Edition*, ISBN 978-0-470-03580-1, John Wiley & Sons Inc.

[63] Fortov, V.E., Trunin, R.F., Al'tshuler, L.,V., Funtikov, A.I., (2004), *High-Pressure Shock Compression of Solids VII. Shock Waves and Extreme States of Matter, First Edition*, Editors, ISBN 0-387-20575-6, anthological monograph in the series *Shock Wave and High Pressure Phenomena*, originally published as *High-Pressure Shock Compression of Condensed Matter*, Springer Science+Business Media.

[64] Fugelso, E.L., Albright, J.N., Langner, G.C., Burns, K.L., (2004), *A Hypervelocity projectile launcher for well perforation*, International Journal of Impact Engineering, 10(1-4), p. 171-184, Elsevier B.V.

[65] Fung, Y.C., (1965), *Foundations of Solid Mechanics, First Edition*, Prentice-Hall Inc.

[66] Gooch, W.A., Burkins, M.S., Walters, W.P., Kozhushko, A.A., Sinani, A.B., (2001), *Target strength effect on penetration by shaped charge jets*, International Journal of Impact Engineering, 26(1-10), p. 243-248, Elsevier B.V.

[67] Graff, K.F., (1965), *Wave Motion in Elastic Solids, Second Edition*, Dover Publications Inc.

[68] Graham, R.A., (1993), *Solids Under High-Pressure Shock Compression. Mechanics, Physics and Chemistry, First Edition*, ISBN 0-387-97885-2, monograph in the series *Shock Wave and High Pressure Phenomena*, originally published as *High-Pressure Shock Compression of Condensed Matter*, Springer Science+Business Media.

[69] Grove, B.M., Werner, A., Han, C., (2006), *explosion-induced damage to oilwell perforating gun carriers*, WIT Transactions on the Built Environment, 87, p. 165-176, WIT Press.

[70] Grüneisen, E., (1912), *Theorie des festen zustandes einatomiger elemente*, Annalen der Physik, 344(12), p. 257-306, Wiley-VCH.

[71] Guinan, M.W., Steinberg, D.J., (1974), *Pressure and temperature derivatives of the isotropic polycristalline shear modulus for 65 elements*, Journal of Physics and Chemistry of Solids, 35(11), p. 1501-1512, Elsevier B.V.

[72] Gupta, A.K., Anirudh, V.K., Singh, S.K., (2013), *constitutive models to predict flow stress in austenitic stainless steel 316 at elevated temperatures*, Materials and Design, 43(2013), p. 410-418, Elsevier B.V.

[73] Gurtin, M.E., (1981), *An Introduction to Continuum Mechanics, First Edition*, ISBN 0-12-309750-9, monograph in the series *Mathematics in Science and Engineering*, Academic Press Inc.

[74] Gurtin, M.E., (1981), *Topics in Finite Elasticity, First Edition*, monograph in the series *CBMS-NSF Regional Conference Series in Applied Mathematics*, Society for Industrial and Applied Mathematics.

[75] Han, C., Du, M.H., Ference, B., (2010), *Effect of shaped charge case materials on perforating guns*, Proceedings of the Chinese Petroleum Society (CPS) and the Society of Petroleum Engineers (SPE) International Oil & Gas Conference and Exhibition in China, June 8-10, 2010, Beijing, China, Volume 1, p. 498-505, published by the Society of Petroleum Engineers (SPE).

[76] Heuzé, O., (2012), *General form of the Mie-Grüneisen equation of state*, Comptes Rendus Mecanique, 340(10), p. 679-687, Elsevier B.V.

[77] Hill, R., (1950), *The Mathematical Theory of Plasticity, First Edition*, Clarendon Press.

[78] Hill, R., (1978), *Aspects of invariance in solid mechanics*, Advances in Applied Mechanics, 18(C), p. 1-75, Academic Press Inc.

[79] Hirt, C.W., Amsden, A.A., Cook, J.L., (1974), *An arbitrary Lagrangian-Eulerian computing method for all flow speeds*, Journal of Computational Physics, 14(3), p. 227-253, Academic Press Inc.

[80] Hoge, K.G., Mukherjee, A.K., (1977), *The temperature and strain rate dependence of the flow stress of tantalum*, Journal of Materials Science, 12(8), p. 1666-1672, Springer Science+Business Media.

[81] Hoger, A., (1986), *The material time derivative of logarithmic strain*, International Journal of Solids and Structures, 22(9), p. 1019-1032, Elsevier B.V.

[82] Holmquist, T.J., Johnson, G.R., (1988), *Determination of constitutive model constants from cylinder impact tests*, Report NSWC TR 88-250, Naval Surface Warfare Center, Dahlgren, Virginia, USA.

[83] Holmquist, T.J., Johnson, G.R., (1991), *determination of constants and comparison of results for various constitutive models*, Journal de Physique IV, 1(C3), p. 853-860, EDP Sciences.

[84] Holzapfel, G.A., (2001), *Nonlinear Solid Mechanics. A Continuum Approach for Engineers, Second Edition*, ISBN 0-471-82319-8, John Wiley & Sons Inc.

[85] Hopperstad, O.S., Børvik, T., Langseth, M., Labibes, K., Albertini, C., (2003), *On the influence of stress triaxiality and strain rate on the behaviour of a*

structural steel. Part I. Experiments, European Journal of Mechanics, A/Solids, 22(1), p. 1-13, Elsevier B.V.

[86] Horie, Y., Davison, L., Thadhani, N.N., (2003), *High-Pressure Shock Compression of Solids VI. Old Paradigms and New Challenges, First Edition*, Editors, ISBN 0-387-95532-1, anthological monograph in the series *Shock Wave and High Pressure Phenomena*, originally published as *High-Pressure Shock Compression of Condensed Matter*, Springer Science+Business Media.

[87] Hou, Q.Y., Wang, J.T., (2010), *A modified Johnson-Cook constitutive model for Mg-Gd-Y alloy extended to a wide range of temperatures*, Computational Materials Science, 50(1), p. 147-152, Elsevier B.V.

[88] Hughes, T.J.R., (1987), *The Finite Element Method. Linear Static and Dynamic Finite Element Analysis, First Edition*, ISBN 0-13-317025-X, Prentice-Hall Inc.

[89] Hussain, G., Hameed, A.S.H., Hetherington, J.G., Barton, P.C., Malik, A.Q., (2013), *Hydrocode simulation with modified Johnson-Cook model and experimental analysis of explosively formed projectiles*, Journal of Energetic Materials, 31(2), p. 143-155, Taylor and Francis Group.

[90] Jiang, F., Vecchio, K.S., (2009), *Hopkinson bar loaded fracture experimental technique: a critical review of dynamic fracture toughness tests*, Applied Mechanics Reviews, 62(6), p. 1-39, American Society of Mechanical Engineers (ASME).

[91] Jin, Q., Shigui, Z., Ding, G., Yianjun, Binggui, C., (2002), *3D numerical simulations of penetration of oil-well perforator into concrete targets*, Proceedings of the 7th International LS-DYNA Users Conference, May 19-21, 2002, Dearborn, Michigan, USA, published by Livermore Software Technology Corporation and DYNAmore GmbH at http://www.dynalook.com/.

[92] Jin, W.W., Zhang, Z., Zhang, H.W., (2011), *Effect of liner cone angle on perforation and impact process of perforating guns*, Chinese Journal of Computational Mechanics, 28(1), p. 43-48, Editorial Office of Chinese Journal of Computational Mechanics.

[93] Jin, W.W., Zhang, Z., Zhang, H.W., Han, X.Q., (2010), *Numerical simulation of formation of shaped charge jet and cartridge design for perforating gun*, Journal

of Plasticity Engineering, 17(6), p. 121-126, Beijing Research Institute of Mechanical & Electrical Technology.

[94] Johnson, G.R., Cook, W.H., (1983), *A constitutive model and data for metals subjected to large strains, high strain rates and high temperatures*, Proceedings of the 7th International Symposium on Ballistics, April 19-21, 1983, The Hague, South Holland, The Netherlands, p. 541-547, published by the International Ballistics Society.

[95] Johnson, G.R., Cook, W.H., (1985), *Fracture characteristics of three metals subjected to various strains, strain rates, temperatures and pressures*, Engineering Fracture Mechanics, 21(1), p. 31-48, Elsevier B.V.

[96] Johnson, G.R., Holmquist, T.J., (1988), *Evaluation of cylinder-impact test data for constitutive model constants*, Journal of Applied Physics, 64(8), p. 3901-3910, American Institute of Physics Inc.

[97] Johnson, G.R., Holmquist, T.J., Anderson Jr., C.E., Nicholls, A.E., (2006), *Strain-rate effects for high-strain-rate computations*, Journal De Physique IV, 134, p. 391-396, EDP Sciences.

[98] Jones, H., (1947), *A theory of the dependence of the rate of detonation of solid explosives on the diameter of the charge*, Proceedings of the Royal Society A: Mathematical, Physical and Engineering Sciences, 189(1018), p. 415-426, The Royal Society.

[99] Jones, H., Miller, A.R., (1948), *The detonation of solid explosives: the equilibrium conditions in the detonation wave-front and the adiabatic expansion of the products of detonation*, Proceedings of the Royal Society A: Mathematical, Physical and Engineering Sciences, 194(1039), p. 480-507, The Royal Society.

[100] Kachanov, L.M., (1971), *Foundations of the Theory of Plasticity, English Translation of the Second Edition*, ISBN 0-7204-2363-5, monograph in the *North-Holland Series in Applied Mathematics and Mechanics*, Elsevier B.V.

[101] Kang, W.J., Cho, S.S., Huh, H., Chung, D.T., (1999), *Modified Johnson-Cook model for vehicle body crashworthiness simulation*, International Journal of Vehicle Design, 21(4-5, Special Issue), p. 424-435, Inderscience Enterprises Ltd.

[102] Kay, G., (2003), *Failure Modeling of Titanium 6Al-4V and Aluminum 2024-T3 with the Johnson-Cook Material Model*, Report DOT/FAA/AR-03/57, Lawrence Livermore National Laboratory, Livermore, California, USA, and U.S. Department of Transportation, Federal Aviation Administration, Office of Aviation Research, Washington, DC, USA.

[103] Kedrinskii, V.K., (2005), *Hydrodynamics of Explosion. Experiment and Models, English Translation of the First Edition*, ISBN 3-540-22481-5, monograph in the series *Shock Wave and High Pressure Phenomena*, originally published as *High-Pressure Shock Compression of Condensed Matter*, Springer Science+Business Media.

[104] Klepaczko, J.R., Rusinek, A., Rodríguez-Martínez, J.A., Pęcherski, R.B., Arias, A.M., (2009), *Modelling of thermo-viscoplastic behaviour of DH-36 and Weldox 460-E structural steels at wide ranges of strain rates and temperatures, comparison of constitutive relations for impact problems*, Mechanics of Materials, 41(5), p. 599-621, Elsevier B.V.

[105] Krafft, A., Sullivan, A.M., Tipper, C.F., (1954), *The effect of static and dynamic loading and temperature on the yield stress of iron and mild steel in compression*, Proceedings of the Royal Society A: Mathematical, Physical and Engineering Sciences, 221(1144), p. 114-127, The Royal Society.

[106] Krieg, R.D., (1972), *A Simple Constitutive Description for Cellular Concrete*, Report SC-DR-72-0883, Sandia National Laboratory, Albuquerque, New Mexico, USA.

[107] Kucher, V., Harrison, J., (1977), *Shaped Charge Jet Penetration of Discontinuous Media*, Report No. 1995, USA Armament Research and Development Command, USA Ballistic Research Laboratory, Aberdeen, Maryland, USA.

[108] Langrand, B., Geoffroy, P., Petitniot, J.L., Fabis, J., Markiéwicz, É., Drazétic, P., (1999), *Identification technique of constitutive model parameters for crashworthiness modelling*, Aerospace Science and Technology, 3(4), p. 215-227, Elsevier B.V.

[109] Lapoujade, V., Van Dorsselaer, N., Kevorkian, S., Cheval, K., (2010), *A study of mapping technique for air blast modeling*, Proceedings of the 11th International LS-DYNA Users Conference, June 6-8, 2010, Dearborn,

Michigan, USA, Editor Mindle, W.L, published by Livermore Software Technology Corporation and DYNAmore GmbH at http://www.dynalook.com/.

[110] Lee, E.L., Hornig, H.C., Kury, J.W., (1968), *Adiabatic Expansion of High Explosive Detonation Products*, Report UCRL-50422, University of California, Lawrence Radiation Laboratory, Livermore, California, USA.

[111] Lee, W.H., (2002), *Oil well perforator design using 2D Eulerian code*, International Journal of Impact Engineering, 27(5), p. 535-559, Elsevier B.V.

[112] Lemons, D.S., Lund, C.M., (1999), *Thermodynamics of high temperature, Mie-Grüneisen solids*, American Journal of Physics, 67(12), p. 1105-1108, American Association of Physics Teachers.

[113] Levi-Civita, T., (1926), *The Absolute Differential Calculus. Calculus of Tensors, English Translation of the First Edition*, ISBN 0-486-44637-9, Dover Publications Inc.

[114] Lieb, E.H., Simon, B., (1977), *The Thomas-Fermi theory of atoms, molecules and solids*, Advances in Mathematics, 23(1), p. 22-116, Academic Press Inc.

[115] Lin, Y.C., Chen, X.M., (2010), *A combined Johnson-Cook and Zerilli-Armstrong model for hot compressed typical high-strength alloy steel*, Computational Materials Science, 49(3), p. 628-633, Elsevier B.V.

[116] Lin, Y.C., Chen, X.M., (2010), *Erratum to: A combined Johnson-Cook and Zerilli-Armstrong model for hot compressed typical high-strength alloy steel [Computational Materials Science (2010) 49 (628-633)]*, Computational Materials Science, 50(10), p. 3073, Elsevier B.V.

[117] Lin, Y.C., Chen, X.M., Liu, G., (2010), *A modified Johnson-Cook model for tensile behaviors of typical high-strength alloy steel*, Materials Science and Engineering A, 527(26), p. 6980-6986, Elsevier B.V.

[118] Liu, M.B., Liu, G.R., Lam, K.Y., Zong, Z., (2003), *Meshfree particle simulation of the detonation process for high explosives in shaped charge unlined cavity configurations*, Shock Waves, 12(6), p. 509-520, Springer Science+Business Media.

[119] Livermore Software Technology Corporation (LSTC), (2006), *LS-DYNA Theory Manual*, LS-DYNA code manual, Livermore, California, USA.

[120] Livermore Software Technology Corporation (LSTC), (2012), *LS-DYNA Keywords User's Manual. Volume I*, LS-DYNA code manual, Livermore, California, USA.

[121] Livermore Software Technology Corporation (LSTC), (2012), *LS-DYNA Keywords User's Manual. Volume II. Material Models*, LS-DYNA code manual, Livermore, California, USA.

[122] Loret, B., Prévost, J.H., Deb, A., (1995), *Finite element simulation of dynamic strain-localization: a multi-scale problem*, Computer Methods in Applied Mechanics and Engineering, 120(3-4), p. 315-338, Elsevier B.V.

[123] Lu, Y., Wang, Z., (2006), *Characterization of structural effects from above-ground explosion using coupled numerical simulation*, Computers and Structures, 84(28), p. 1729-1742, Elsevier B.V.

[124] Lubarda, V.A., (2002), *Elastoplasticity Theory, First Edition*, ISBN 0-8493-1138-1, monograph in the series *Mechanical Engineering Series*, CRC Press.

[125] Lubliner, J., (2006), *Plasticity Theory, Revised Edition*, University of California at Berkeley, Berkeley, California, USA.

[126] Maheshwari, A.K., Pathak, K.K., Ramakrishnan, N., Narayan, S.P.A., (2009), *Modified Johnson-Cook material flow for hot deformation processing*, Journal of Material Sciences, 45(4), p. 859-864, Springer Science+Business Media.

[127] Malvern, L.E., (1969), *Introduction to the Mechanics of a Continuous Medium, First Edition*, ISBN 13-487603-2, Prentice-Hall Inc.

[128] Marsden, J.E., Hughes, T.J.R. (1983), *Mathematical Foundations of Elasticity, First Edition*, ISBN 0-13-5610-76-1, Prentice Hall Inc.

[129] Marsden, J.E., Ratiu, T., Abraham, R., (2007), *Manifolds, Tensor Analysis, and Applications, Third Edition*, ISBN 0-201-10168-S, Springer Science+Business Media.

[130] Mendoza, E., (1982), *The equation of state for solids 1843-1926*, European Journal of Physics, 3(3), p. 181-187, Institute of Physics Publishing.

[131] Menikoff, R., (2012), *Complete Mie-Grüneisen Equation of State*, Report LA-UR-12-22592, Los Alamos National Laboratory, Los Alamos, New Mexico, USA.

[132] Meyers, M.A., (1994), *Dynamic Behavior of Materials, First Edition*, ISBN 0-471-58262-X, John Wiley & Sons Inc.

[133] Meyers, M.A., Aimone, C.T., (1983), *Dynamic fracture (spall) of metals*, Progress in Materials Science, 28(1), p. 1-96, Elsevier B.V.

[134] Meyers, M.A., Benson, D.J., Vöhringer, O., Kad, B.K., Xue, Q., Fu, H.H., (2002), *Constitutive description of dynamic deformation: physically-based mechanisms*, Materials Science and Engineering A, 322(1-2), p. 194-216, Elsevier B.V.

[135] Mie, G., (1903), *Zur kinetischen theorie der einatomigen körper*, Annalen der Physik, 316(8), p. 657-697, Wiley-VCH.

[136] Milani, A.S., Dabboussi, W., Nemes, J.A., Abeyaratne, R.C., (2008), *An improved multi-objective identification of Johnson-Cook material parameters*, International Journal of Impact Engineering, 36(2), p. 294-302, Elsevier B.V.

[137] Molinari, J.F., (2002), *Finite elements simulation of shaped charge*, Finite Element in Analysis and Design, 38(10), p. 921-936, Elsevier B.V.

[138] Moon, P., Spencer, D.E., (1986), *Theory of Holors, First Edition*, ISBN 0-521-24585-0, Cambridge University Press.

[139] Moraes, R.F., Nicholson, D.W., (2000), *Implementation of constitutive equations for viscoplasticity with damage and thermal softening into the LS-DYNA FEM code, with application to dynamic fracture of ring-stiffened welded structures*, Proceedings of the 6th International LS-DYNA Users Conference, April 9-11, 2000, Dearborn, Michigan, USA, published by Livermore Software Technology Corporation and DYNAmore GmbH at http://www.dynalook.com/.

[140] Nagayama, K., (2011), *An Introduction to the Grüneisen Equation of State and Shock Thermodynamics, First Edition*, Amazon.com Inc.

[141] Nemat-Nasser, S., Guo, W.G., (2003), *Thermomechanical response of DH-36 structural steel over a wide range of strain rates and temperatures*, Mechanics of Materials, 35(11), p. 1023-1047, Elsevier B.V.

[142] Nemat-Nasser, S., Guo, W.G., Liu, M.Q., (1999), *Experimentally-based micromechanical modeling of dynamic response of molybdenum*, Scripta Materialia, 40(7), p. 859-872, Elsevier B.V.

[143] Nemat-Nasser, S., Isaacs, J.B., (1997), *Direct measurement of isothermal flow stress of metals at elevated temperatures and high strain rates with application to Ta and Ta-W alloys*, Acta Materialia, 45(3), p. 907-919, Elsevier B.V.

[144] Noble, J.P., Goldthorpe, B.D., Church, P.D., Harding, J.E., (1999), *The use of the Hopkinson bar to validate constitutive relations at high rates of strain*, Journal of the Mechanics and Physics of Solids, 47(5), p. 1187-1206, Elsevier B.V.

[145] Novokshanov, R., Ockendon, J., (2006), *Elastic-plastic modelling of shaped charge jet penetration*, Proceedings of the Royal Society A: Mathematical, Physical and Engineering Sciences, 462(2076), p. 3663-3681, The Royal Society.

[146] Pearson, J., Rinehart, J.S., (1952), *Deformation and fracturing of thick-walled steel cylinders under explosive attack*, Journal of Applied Physics, 23(4), p. 434-441, American Institute of Physics Inc.

[147] Rajendran, A.M., (1992), *High Strain Rate Behavior of Metals, Ceramics and Concrete*, Report WL-TR-92-4006, Materials Directorate, Wright Laboratory, Air Force Systems Command, Wright-Patterson Air Force Base, Dayton, Ohio, USA.

[148] Rajendran, A.M., Bless, S.J., (1985), *High Strain Rate Material Behavior*, Report AFWAL-TR-85-4009, Materials Laboratory, Air Force Wright Aeronautical Laboratories, Air Force System Command, Wright-Patterson Air Force Base, Dayton, Ohio, USA.

[149] Regalbuto, J.A., Gill, B.C., (1997), *Computer codes for oilwell-perforator design*, SPE Drilling and Completion, 12(3), p. 188-195, formerly known as SPE Drilling Engineering, Society of Petroleum Engineers (SPE).

[150] Rinehart, J.S., (1951), *Some experimental indications of the stresses produced in a body by an exploding charge*, Journal of Applied Physics, 22(9), p. 1178-1181, American Institute of Physics Inc.

[151] Rinehart, J.S., (1951), *Some quantitative data bearing on the scabbing of metals under explosive attack*, Journal of Applied Physics, 22(5), p. 555-560, American Institute of Physics Inc.

[152] Rinehart, J.S., (1952), *Scabbing of metals under explosive attack: multiple scabbing*, Journal of Applied Physics, 23(11), p. 1229-1233, American Institute of Physics Inc.

[153] Rizzi, E., (1995), *"Sulla Localizzazione delle Deformazioni in Materiali e Strutture"*, Doctoral Thesis, Advisors Maier, G., Willam, K., Politecnico di Milano, Department of Structural Engineering, Milano, Lombardy, Italy.

[154] Rizzi, E., Carol, I., (2001), *A formulation of anisotropic elastic damage using compact tensor formalism*, Journal of Elasticity, 64(2-3), p. 85-109, Springer Science+Business Media.

[155] Rizzi, E., Maier, G., Willam, K.J., (1996), *On failure indicators in multi-dissipative materials*, International Journal of Solids and Structures, 33(20-22), p. 3187-3214, Elsevier B.V.

[156] Rodríguez-Martínez, J.A., Rusinek, A., Chévrier, P., Bernier, R., Arias, A.M., (2010), *Temperature measurements on ES steel sheets subjected to perforation by hemispherical projectiles*, International Journal of Impact Engineering, 37(7), p. 828-841, Elsevier B.V.

[157] Rose, J.H., Smith, J.R., Guinea, F., Ferrante, J., (1984), *Universal feature of the equation of state of metals*, Physical Review B, 29(6), p. 2963-2969, American Institute of Physics.

[158] Rule, W.K., (1997), *A numerical scheme for extracting strength model coefficients from Taylor test data*, International Journal of Impact Engineering, 19(9-10), p. 797-810, Elsevier B.V.

[159] Rule, W.K., Jones, S.E., (1998), *A revised form for the Johnson-Cook strength model*, International Journal of Impact Engineering, 21(8), p. 609-624, Elsevier B.V.

[160] Rusinek, A., Rodríguez-Martínez, J.A., Klepaczko, J.R., Pęcherski, R.B., (2009), *Analysis of thermo-visco-plastic behaviour of six high strength steels*, Materials and Design, 30(5), p. 1748-1761, Elsevier B.V.

[161] Samantaray, D., Mandal, S., Bhaduri, A.K., (2009), *A comparative study on Johnson Cook, modified Zerilli-Armstrong and Arrhenius-Type constitutive models to predict elevated temperature flow behaviour in modified 9Cr-1Mo steel*, Computational Materials Science, 47(2), p. 568-576, Elsevier B.V.

[162] Scapin, M., Peroni, L., Peroni, M., (2012), *Parameters identification in strain-rate and thermal sensitive visco-plastic material model for an alumina dispersion strength*, International Journal of Impact Engineering, 40-41, p. 58-67, Elsevier B.V.

[163] Scheffler, D.R., Zukas, J.A., (2000), *Practical aspects of numerical simulations of dynamic events: material interfaces*, International Journal of Impact Engineering, 24(8), p. 821-842, Elsevier B.V.

[164] Schmidt, R.M., Davies, F.W., Lempriere, B.M., Holsapple, K.A., (1978), *Temperature dependent spall threshold of four metal alloys*, Journal of Physics and Chemistry of Solids, 39(4), p. 375-385, Elsevier B.V.

[165] Schwer, L.E., (2004), *Preliminary assessment of non-Lagrangian methods for penetration simulation*, Proceedings of the 8th International LS-DYNA Users Conference, May 2-4, Dearborn, Michigan, USA, published by Livermore Software Technology Corporation and DYNAmore GmbH at http://www.dynalook.com/.

[166] Schwer, L.E., (2004), *Optional strain-rate forms for the Johnson Cook constitutive model and the role of the parameter epsilon_0*[1], Proceedings of the 6th European LS-DYNA Users Conference, May 29-30, 2004, Gothenburg, Götaland, Sweden, published by Livermore Software Technology Corporation and DYNAmore GmbH at http://www.dynalook.com/.

[167] Segletes, S.B., (1991), *Erratum: thermodynamic stability of the Mie-Gruneisen equation of state, and its relevance to hydrocode computations [Journal of Applied Physics (1991) 70, (2489)]*, Journal of Applied Physics, 71(2), p. 1074, American Institute of Physics Inc.

[168] Segletes, S.B., (1991), *Thermodynamic stability of the Mie-Grüneisen equation of state, and its relevance to hydrocode computations*, Journal of Applied Physics, 70(5), p. 2489-2499, American Institute of Physics Inc.

[169] Simo, J.C., Hughes, T.J.R. (1998), *Computational Inelasticity, First Edition*, ISBN 0-387-97520-9, monograph in the series *Interdisciplinary Applied Mathematics*, Springer Science+Business Media.

[170] Souli, M., Olovsson, L., Do, I., (2002), *ALE and fluid-structure interaction capabilities in LS-DYNA*, Proceedings of the 7th International LS-DYNA Users Conference, May 19-21, 2002, Dearborn, Michigan, USA, published by Livermore Software Technology Corporation and DYNAmore GmbH at http://www.dynalook.com/.

[171] Steinberg, D.J., (1981), *The temperature independence of Grüneisen's gamma at high temperature*, Journal of Applied Physics, 52(10), p. 6415-6417, American Institute of Physics Inc.

[172] Steinberg, D.J., (1987), *Constitutive model used in computer simulation of time-resolved, shock-wave data*, International Journal of Impact Engineering, 5(1-4), p. 603-611, Elsevier B.V.

[173] Steinberg, D.J., (1987), *Spherical Explosions and the Equation of State of Water*, Report UCID-20974, Lawrence Livermore National Laboratory, Livermore, California, USA.

[174] Steinberg, D.J., (1996), *Equation of State and Strength Properties of Selected Materials*, Report UCRL-MA-106439 Change 1, Lawrence Livermore National Laboratory, Livermore, California, USA.

[175] Steinberg, D.J., Cochran, S.G., Guinan, M.W., (1980), *A constitutive model for metals applicable at high-strain rate*, International Journal of Impact Engineering, 5(1-4), p. 603-611, Elsevier B.V.

[176] Steinberg, D.J., Lund, C.M., (1988), *A constitutive model for strain rates from 10^{-4} to 10^{6} s^{-1}*, Journal of Applied Physics, 65(4), p. 1528-1533, American Institute of Physics Inc.

[177] Steinberg, D.J., Sharp Jr., R.W., (1988), *Interpretation of shock-wave data for beryllium and uranium with an elastic-viscoplastic constitutive model*, Journal of Applied Physics, 52(8), p. 5072-5083, American Institute of Physics Inc.

[178] Sternberg, H.M., (1970), *On the mathematical theory of the Chapman-Jouguet state*, Astronautica Acta, 15(5-6), p. 359-369, Pergamon Press Ltd.

[179] Struik, D.J., (1953), *Lecturès on Analytic and Projective Geometry, First Edition*, Addison-Wesley Publishing Company, Inc.

[180] Swift, R.P., Behrmann, L.A., Halleck, P.M., Krogh, K.E., (1998), *Micro-mechanical modeling of perforating shock damage*, Proceedings of the SPE International Symposium on Formation Damage Control, February 18-19, 1998, Lafayette, Louisiana, USA, published by Energy Resources Conservation Board (ERCB).

[181] Synge, J.L., Schild, A., (1969), *Tensor Calculus, Second Edition*, ISBN 0-486-63612-7, Dover Publications Inc.

[182] Tariq, S.M., (1987), *Evaluation of flow characteristics of perforations including nonlinear effects with the finite-element method*, SPE Production Engineering, 2(2), p. 104-112, continued as SPE Production and Facilities, Society of Petroleum Engineers (SPE).

[183] Taylor, G., (1948), *The use of flat-ended projectiles for determining dynamic yield stress. I. Theoretical considerations*, Proceedings of the Royal Society A: Mathematical, Physical and Engineering Sciences, 194(1038), p. 289-299, The Royal Society.

[184] Teng, X., (2004), *High Velocity Impact Fracture*, Report No: 134, Impact & Crashworthiness Laboratory, Massachusetts Institute of Technology, Cambridge, Massachusetts, USA.

[185] Teng, W., Wierzbicki, T., (2006), *Evaluation of six fracture models in high velocity perforation*, Engineering Fracture Mechanics, 73(12), p. 1653-1678, Elsevier B.V.

[186] Tillotson, J.H., (1962), *Metallic Equations of State for Hypervelocity Impact*, Report GA-3216, General Atomic, Division of General Dynamics, John Jay Hopkins Laboratory for Pure and Applied Science, San Diego, California, USA.

[187] Truesdell, C.A., Noll, W., (2004), *The Non-Linear Field Theories of Mechanics, Third Edition*, ISBN 3-540-022779-3, Springer Science+Business Media.

[188] Tu, Z., Lu, Y., (2008), *Evaluation of typical concrete material models used in hydrocodes for high dynamic response simulations*, International Journal of Impact Engineering, 36(1), p. 132-146, Elsevier B.V.

[189] Unosson, M., Buzaud, E., (2000), *Scalar and Vectorized User Defined Material Routines in LS-DYNA*, Report FOA-R--00-01502-311-SE, ISSN 1104-9154, FOA Defence Research Establishment, Weapons and Protection Division, Tumba, Svealand, Sweden.

[190] Van Dorsselaer, N., Lapoujade, V., (2008), *A Contribution to new ALE 2D method validation*, Proceedings of the 11th International LS-DYNA Users Conference, June 6-8, 2008, Dearborn, Michigan, USA, Editor Mindle, W.L, published by Livermore Software Technology Corporation and DYNAmore GmbH at http://www.dynalook.com/.

[191] Vitali, E., Benson, D.J., (2011), *Modeling localized failure with arbitrary Lagrangian Eulerian methods*, Computational Mechanics, 49(2), p. 197-212, Springer Science+Business Media.

[192] Voyiadjis, G.Z., Abu Al-Rub, R.K., (2006), *A finite strain plastic-damage model for high velocity impact using combined viscosity and gradient localization limiters: Part II – Numerical aspects and simulations*, International Journal of Damage Mechanics, 15(4), p. 335-373, SAGE Publications Ltd.

[193] Walters, W.P., (2008), *A Brief History of Shaped Charges*, Report ARL-RP-232, Army Research Laboratory, Aberdeen Proving Ground, Maryland, USA.

[194] Wang, L.L., (2007), *Foundations of Stress Waves, English Translation of the Second Edition*, ISBN 7-118-04015-0, Elsevier B.V.

[195] Wang, Y.P., Han, C.J., Wang, C., Li, S.K., (2011), *A modified Johnson-Cook model for 30Cr2Ni4MoV rotor steel over a wide range of temperature and strain rate*, Journal of Materials Science, 46(9), p. 2922-2927, Springer Science+Business Media.

[196] Weese, R.K., Burnham, A.K., Fontes, A.T., (2005), *An Investigation of Coefficient of Thermal Expansion, Decomposition Kinetics, and Reaction to*

Various Stimuli, Report UCRL-CONF-210860, Lawrence Livermore National Laboratory, Livermore, California, USA.

[197] Whiffin, A.C., (1948), *The use of flat-ended projectiles for determining dynamic yield stress. II. Tests on various metallic materials*, Proceedings of the Royal Society A: Mathematical, Physical and Engineering Sciences, 194(1038), p. 300-322, The Royal Society.

[198] Wierzbicki, T., Bao, Y., Lee, Y.W., Bai, Y., (2005), *Calibration and evaluation of seven fracture models*, International Journal of Mechanical Sciences, 47(4-5, Special Issue), p. 719-743, Elsevier B.V.

[199] Wilkins, M.L., (1963), *Calculation of Elastic-Plastic Flow*, Report UCRL-7322, University of California, Lawrence Radiation Laboratory, Livermore, California, USA.

[200] Wilkins, M.L., (1978), *Mechanics of penetration and perforation*, International Journal of Engineering Science, 16(11), p. 793-807, Elsevier B.V.

[201] Wilkins, M.L., Blum R.E., Cronshagen E., Grantham, P., (1974), *A Method for Computer Simulation of Problems in Solid Mechanics and Gas Dynamics in Three Dimensions and Time*, Report UCRL-51574, Lawrence Livermore National Laboratory, Livermore, California, USA.

[202] Wilkins, M.L., Guinan, M.W., (1973), *Impact of cylinders on a rigid boundary*, Journal of Applied Physics, 44(3), p. 1200-1206, American Institute of Physics Inc.

[203] Wilkins, M.L., Squier, B., Halperin, B., (1965), *equation of state for detonation products of PBX 9404 and LX04-01*, Proceedings of the Tenth Symposium (International) on Combustion, 10(1), p. 769-778, The Combustion Institute.

[204] Worsham, M., Kurtz, A., Shirley, A., Xiao, X., (2010), *Hypervelocity impact of spaced plates: simulation and comparison to data*, Proceedings of the IMPLAST 2010 Conference, October 12-14, Providence, Rhode Island, USA, published by Society for Experimental Mechanics Inc.

[205] Xi, L.G., (1995), *The simplified model for predicting shaped charge jet parameters*, Propellant, Explosives, Pyrotechnics, 20(5), p. 279-282, Wiley-VCH.

[206] Xue, L., Wierzbicki, (2006), *Verification of a new fracture criterion using LS-DYNA*, Proceedings of the 9th International LS-DYNA Users Conference, June 4-6, 2006, Dearborn, Michigan, USA, Editor Mindle, W.L, published by Livermore Software Technology Corporation and DYNAmore GmbH at http://www.dynalook.com/.

[207] Yin, Z.X., Ma, C.M., Li, S.X., Cheng, G.Q., (2004), *Perforation of an ultra-high strength steel penetrated by shaped charge jet*, Materials Science and Engineering A, 379(1-2), p. 443-447, Elsevier B.V.

[208] Zener, C., Hollomon, J.H., (1944), *Effect of strain rate upon plastic flow of steel*, Journal of Applied Physics, 15(1), p. 22-32, American Institute of Physics Inc.

[209] Zerilli, F.J., Armstrong, R.W., (1987), *Dislocation-mechanics-based constitutive relations for material dynamics calculations*, Journal of Applied Physics, 61(5), p. 1816-1825, American Institute of Physics Inc.

[210] Zhang, Z., Liu, Y.L., Hu, H.F., Kang, Z., Li, X.J., Zhang, H.W., Han, X.Q., (2008), *Numerical simulation of the perforation process and the parameter controls of the perforating gun*, Journal of Plasticity Engineering, 15(6), p. 151-156, Beijing Research Institute of Mechanical & Electrical Technology.

[211] Zocher, M.A., Maudlin, P.J., Chen, S.R, Flower-Maudlin, E.C., (2000), *An Evaluation of Several Hardening Models Using Taylor Cylinder Impact Data*, Report LA-UR-00-1192, Los Alamos National Laboratory, Los Alamos, New Mexico, USA.

[212] Zukas, J.A., (2004), *Introduction to Hydrocodes, First Edition*, ISBN 0-08-044348-6, monograph in the series *Studies in Applied Mechanics*, Elsevier B.V.

[213] Zukas, J.A., Scheffler, D.R., (2000), *Practical aspects of numerical simulations of dynamic events: effects of meshing*, International Journal of Impact Engineering, 24(9), p. 925-945, Elsevier B.V.